

Proceedings 2012 RII LA-SiGMA Symposium

July 23, 2012
Baton Rouge, LA



Louisiana EPSCoR

Sponsored by the National Science Foundation and Louisiana Board of Regents



Louisiana Alliance for Simulation-Guided Materials Applications

Welcome to the RII Symposium!

On behalf of Louisiana EPSCoR, I would like to welcome you to the 2012 LA EPSCoR RII LA-SiGMA Symposium. This is a great opportunity for everyone to become engaged in this trend-setting research/education initiative supported under the auspices of the National Science Foundation and the Louisiana Board of Regents. The objective of the project is to build the next generation of experimentally validated formalisms, algorithms, and codes for multiscale materials simulations; implementing them on present and next-generation supercomputers; and educating the next generation of a highly skilled workforce of materials scientists and engineers.

We are very proud of this project, a multidisciplinary initiative with participation by undergraduate/graduate students, post-doctoral researchers, and university research faculty from seven institutions across the State. I also welcome our distinguished participants and guests—individuals serving on our External Review Board, the Diversity Advisory Committee, EPSCoR Committee members, and university research administrators.

This Symposium features presentations on LA-SiGMA's achievements, a poster competition, and plenty of opportunities to network with your colleagues.

Thank you for participating in this Symposium, and I wish you all a productive and enjoyable meeting.

A handwritten signature in black ink, appearing to read "Michael Khonsari".

Michael Khonsari,
Louisiana EPSCoR Project Director and
Associate Commissioner for Sponsored Programs R&D, Louisiana Board of Regents

The research featured in this Symposium is supported by the National Science Foundation's Experimental Program to Stimulate Competitive Research (EPSCoR) under Grant No. EPS-1003897 and the Louisiana Board of Regents through its Board of Regents Support Fund.

Louisiana Board of Regents
Post Office Box 3677
Baton Rouge LA 70821-3677
225-342-4253
www.laregents.org

NSF EPSCoR Research Infrastructure Improvement (RII) Award 2012 LA-SiGMA RII Symposium

July 23, 2012
Marriott Hotel
5500 Hilton Avenue, Baton Rouge, Louisiana 70808

Agenda

7:00 – 8:00	Registration and Continental Breakfast
8:00 – 8:20	Welcoming Remarks, Project Update (Khonsari)
Science Drivers (SD) and CyberTools and CyberInfrastructure Group (CTCI)	
8:20 – 8:45	<i>Electronic and Magnetic Materials</i> (Bagayoko and Perdew)
8:45 – 9:10	<i>Materials for Energy storage and Generation</i> (Pratt and Mainardi)
9:10 – 9:35	<i>Biomolecular Materials</i> (Ashbaugh and Nikitopoulos)
9:35 – 10:00	<i>Computational Tools for Multiscale Simulations</i> (Bishop, Yun, Jarrell)
10:00 – 10:25	Break
Assessment and Broader Impacts	
10:25 - 10:45	<i>Diversity and Workforce Development</i> (Moreno and Hall)
10:45 - 11:00	<i>External Engagement and Sustainability</i> (Pesika and Domingue)
11:00 - 11:20	<i>Industrial Liaison</i> (Whittenburg and Cruthirds) Jeff Lynn (Louisiana Economic Development)
11:20 - 12:05	Presentations by invited recipients of EPSCoR awards: Carlos Montes (LA Tech) Laura Schrader (Tulane) Mark Merchant (McNeese)
12:05 – 2:30	Lunch and poster session
2:30 – 2:45	Data Management Plan (Joel Tohline and Lawrence Pratt)
2:45 – 3:00	Graduate Student Retreat (Chinedu Ekuma)
3:00 – 3:15	FIRST Training Program (Cynthia Sisson)
3:15 – 3:30	Evaluation and Assessment (Cindi Dunn)
3:30 – 3:45	Break
Planning Session	
3:45 – 4:45	Simultaneous sessions: ERB Deliberations DAC Deliberations LA-SiGMA members: Breakouts
4:45 – 5:00	DAC and ERB debriefing to LA-SiGMA
5:00	Concluding Remarks (Khonsari)

Table of Contents

Foreword	i
Agenda	ii
LA EPSCoR	vi
A DFT Study of the Reaction of Chlorinated Phenols with Copper Oxide Clusters.....	1
<i>Ab Initio</i> Molecular Dynamics Simulation of a Propylene Carbonate-filled Uncharged Nanotube Forest	5
Ab Initio Study of Iron Oxide Clusters and their Reactions with Phenol, 2-Chlorophenol and 4-Chlorophenol and Force Field Development for Copper Oxide Systems	9
Advanced Quantum Chemistry Approach to the Ground State Spin of Iron Oxide Clusters	13
Charge Transfer from a Carbon Nanotube Electrode to Tetramethyl Ammonium Ions Investigated by <i>Ab Initio</i> Molecular Dynamics Simulation.....	17
Dynamical Cluster Approximation – Typical Medium Theory Approach to Disordered Systems	21
Effect of Dopants in Dehydrogenation of NaMgH ₃ Core-Shell Nanoclusters	25
Efficient Hydrogen Saturation and Transfer Rate Simulation in Metallic Rods	29
Electrical Transport in a Magnetic Semiconductor Nanowire.....	33
Electronic and Conductive Properties of Polythiophene Containing Cobaltabisdicarbollide Structures	37
Everything You Always Wanted to Know about the van der Waals Interaction (But Were Afraid to Ask)	41
Exact Diagonalization of Disordered Anderson Model.....	45
Ferromagnetism in CuFeSb: Evidence of Competing Magnetic Interactions in Fe-based Superconductors.....	49
Geometric Analysis of DNA in Molecular Dynamics Simulation of Nucleosomes	53
GPGPU Performance Modeling	57
GPU Accelerated Hirsch-Fye Quantum Monte Carlo	61

Hybrid MD-continuum Simulation Methodology with Capability of Handling Two-Phase Flows with Application in Biomolecular Systems.....	65
Impedance Characterization of YSZ based NO _x Sensor	69
Investigations of RuO ₂ and SnO ₂ Nanoclusters as Potential Lithium Ion Battery Electrode Materials	73
Molecular Dynamics Simulation and Visualization of Thermal Barrier Coatings.....	77
Molecular Dynamics Simulation Study of the Effect of Electric Field on DNA Mononucleotides Dynamics in Nanoslits	81
Molecular Dynamics Simulations of the Interaction of a PLGA Nanoparticle with a Lipid Bilayer.....	85
Molecular Transport in Nanotubes	89
Multi-Spin Coding Parallel Tempering Monte Carlo Simulation of Ising Spin Glass with CUDA	93
Nanoparticle Uptake by Tumor Tissue through its Capillary Pores	97
Nucleosome binding in highly occupied sequences	101
Numerical Simulation of Hydrogen Absorption/Desorption in Metal-Hydride Reactors	105
Optimization of Electroless Deposition of CoNiFeB Thin Films for Application in Magnetic Recording Media.....	109
Preparation and Characterization of Amphiphilic, Biocompatible Cyclic Block Copolymers	113
Self-consistent Calculations of Electronic Properties of Systems with Energy or Band Gaps	117
Simulation of Propylene Carbonate Solutions for Electrochemical Double-layer Capacitors	121
Statistical Mechanics of a Hard Rod in the Hard Sphere Fluid	125
Structural Analysis of Bosch Heated Exhaust Gas Oxygen Sensors after Voltage Treatments.....	129
Study of the Hydrogen Storage Capability of KMgH ₃	133
Study of the Spin State of Localized Mn in (GaMn)As and (GaMn)N	137

Superparamagnetic Iron Oxide Nanoparticles with Variable Size and Iron Oxidation State: Synthesis and Relaxivity Studies	141
Thermal Collapse of N-Isopropyl Acrylamide in Aqueous Solution	145
Toward Improved Meta-Generalized Gradient Approximations: Variations on a Density Functional Theme	149
LA SiGMA Poster Session	153
REU/RET Poster Session.....	154
Registered Attendee List.....	155

What is EPSCoR?

The Experimental Program to Stimulate Competitive Research (EPSCoR) is a federal/state partnership established in 1978 by the National Science Foundation (NSF) with the goal of stimulating sustainable improvements in the research & development (R&D) capacity of states—like Louisiana—that historically have not received significant federal R&D funding. Since its initial establishment, EPSCoR programs are now supported by seven federal agencies.



Louisiana has participated in NSF EPSCoR since 1987, and has been the recipient of several competitively awarded Research Infrastructure Improvement (RII) awards. LA EPSCoR has served as the catalyst for transforming the way large-scale collaborative research is conducted in the State—from individual campuses competing for limited federal resources to one in which increased collaboration has enabled Louisiana to become more competitive for major R&D funding at the national level.

The major research component of the current RII award is the Louisiana Alliance for Simulation-Guided Materials Applications (LA-SiGMA). This ambitious initiative brings together seven academic institutions with the vision to make transformative advances in materials science research and education through a sustained multidisciplinary and multi-institutional alliance of researchers. LA-SiGMA research and education activities involve three areas of materials science, tied together with a common computational framework. The specific goals are:

Electronic and Magnetic Materials: To transform the field by extending many-body formalisms and first principles methods to much larger length scales than currently possible.

Materials for Energy Storage and Conversion: To develop and apply multi-scale computational tools to study materials for energy generation, storage, and conversion.

Biomolecular Materials: To develop, apply, and validate experimentally multi-scale computational tools for the design of novel vehicles for drug delivery and other applications.

Shared Computational Strategies: To develop multi-scale formalisms, algorithms, and codes for materials simulations and modeling; leverage existing tools and make optimum use of the next generation computing environments.

Tightly integrated with LA-SiGMA are a suite of programs offered by LA EPSCoR to the entire State's higher education and K-12 community. These programs are designed to improve Louisiana's research competitiveness, train a highly-education workforce, and promote greater public awareness and participation in science, technology, engineering, and mathematics (STEM). These programs include:

- Opportunities for Partnerships in Technology with Industry (OPT-IN)
- Supervised Undergraduate Research Experience (SURE)
- Pilot Funding for New Research (Pfund)
- Links with Industry, Research Centers, and National Labs (LINK)
- Travel Grants for Emerging Faculty (TGEF)
- Preliminary Planning Grants for Major Initiatives
- Planning Grants for Major Initiatives
- Grantwriting Workshops
- Faculty Expertise Database (SPINPlus, LA GENIUS, SMARTS)
- Speaking of Science (SOS) speakers' bureau

Participating Institutions

- **Grambling State University**
- **Louisiana State University**
- **Louisiana Tech University**
- **Southern University**
- **Tulane University**
- **University of New Orleans**
- **Xavier University**

External Review Board (ERB) members

- **B. Vincent McKoy**, Professor of Chemistry, California Institute of Technology (ERB Chair)
- **James Hoehn**, Executive Director of the EPSCoR/IDeA Foundation, National Science Foundation
- **William A. Lester Jr.**, Professor of the Graduate School, University of California, Berkeley
- **Susan B. Sinnott**, Professor of Materials Science and Engineering, University of Florida
- **Harold Silverman**, Senior Vice Provost, State University of New York System (retired)
- **Valerie E. Taylor**, Professor and Department Head, Computer Science, Texas A&M University

National Science Foundation EPSCoR

- **Jeanne Small**, NSF EPSCoR Program Director

Diversity Advisory Council (DAC) members

- **William A. Lester Jr.**, Professor of the Graduate School, University of California, Berkeley
- **DiOnetta Jones**, Associate Dean and Director, Office of the Dean for Undergraduate Education, Massachusetts Institute of Technology
- **Betsy Willis**, Director, Advising and Student Records, Gender Parity Initiative, Southern Methodist University
- **Stephanie Adams**, Associate Dean for Undergraduate Studies, Virginia Commonwealth University
- **Shelia Edwards Lange**, Vice President for Minority Affairs and Vice Provost for Diversity, University of Washington
- **Isiah Warner**, Vice Chancellor for Strategic Initiatives, Louisiana State University

- **Juana Moreno**, Assistant Professor of Physics, Louisiana State University
- **Jenna Carpenter**, Associate Dean for Administration & Strategic Initiatives, Louisiana Tech University

Project Evaluators

- **Cindi Dunn**, Office of Educational Innovation and Evaluation - Kansas State University (external evaluator)
- **Amy Hilgendorf**, Office of Educational Innovation and Evaluation - Kansas State University (external evaluator)
- **Judy Roth**, Office of Educational Innovation and Evaluation - Kansas State University, (external evaluator)

Louisiana EPSCoR Committee members

- **Les Guice** (Chair), Vice President for Research, Louisiana Tech University
- **Kevin Carman** (Vice Chair), Dean, College of Basic Sciences, Louisiana State University
- **Nicholas Altiero**, Dean, College of Science and Engineering and Professor of Biomedical Engineering, Tulane University
- **Diola Bagayoko**, Southern University System Distinguished Professor and Chair of Physics, Southern University - Baton Rouge, Chancellor's fellow, Director (Timbuktu Academy and M.S. Program), Associate Director (LaSPACE)
- **Geoffrey Cazes**, Vice President, Cyber Innovation Center, Bossier City
- **Henry Chu**, Director, School of Computing and Informatics, College of Sciences and Professor, Laboratory for Internet Computing, University of Louisiana at Lafayette (DEPSCoR Representative)
- **Gene D'Amour**, Senior Vice President for Resource Development, Xavier University of Louisiana
- **Kerry Davidson**, Deputy Commissioner for Sponsored Programs, Louisiana Board of Regents
- **Connie Fabré**, Executive Director, Greater Baton Rouge Industry Alliance
- **Robert Godke**, Boyd Professor, School of Animal Sciences, LSU Agricultural Center
- **Jeffrey Keller**, Executive Director for Basic Research, Pennington Biomedical Research Center
- **Michael Khonsari**, Associate Commissioner for Sponsored Programs R&D and LA EPSCoR Project Director and Dow Chemical Endowed Chair Professor of Mechanical Engineering, Louisiana State University
- **Kenneth Kratz**, Director, Office of Research Services and Professor of Cell Biology and Anatomy, LSU Health Sciences Center – New Orleans (NIH IDEA Representative)
- **Barry LeBlanc**, President, CEO, PamLab, L.L.C.

- **Laura Levy**, Associate Senior Vice President for Research and Professor of Microbiology and Immunology, Tulane University Health Sciences Center
 - **Sandra Roerig**, Dean for Graduate Studies and Research, LSU Health Sciences Center – Shreveport
 - **Hilary Thompson**, Adjunct Professor of Ophthalmology, Biometry, and Neuroscience, Director, Clinical Trials and Biometry Unit, School of Public Health, LSU Health Sciences Center – New Orleans
 - **Robert Twilley**, Vice President for Research, University of Louisiana at Lafayette
-
- **John Wefel**, Professor of Physics, Louisiana State University, (NASA EPSCoR Representative)
 - **Scott Whittenburg**, Vice Chancellor of Research and Sponsored Programs, Dean of the Graduate School, University of New Orleans
 - **Representative pending nomination**, Louisiana Economic Development

EPSCoR Staff

- **Michael Khonsari**, Project Director
- **Jim Gershey**, Project Administrator
- **Jessica Domingue**, EPSCoR Associate, Faculty Development Coordinator
- **Cindy Greer**, Grants and Contracts Coordinator
- **Susan Jernigan**, EPSCoR Associate
- **Karthik Poobalasubramanian**, IT Coordinator

A DFT Study of the Reaction of Chlorinated Phenols with Copper Oxide Clusters

Lucy W. Kiruri¹, Gyun Tack Bae², Barry Dellinger¹, Randall Hall^{1,3}

¹Department of Chemistry, Louisiana State University

²Department of Chemistry, Kansas State University

³Department of Natural Sciences and Mathematics, Dominican University of California

Abstract: *Ab initio* calculations of the reactions of copper oxide clusters (CuO)_n, (n=1-4) with chlorinated phenols were carried out to provide a physical insight into the formation of environmentally persistent free radicals (EPFRs). We employed the B3LYP functional to predict the reaction energies of the neutral copper oxide clusters with 2 and 4-monochlorinated phenol. First, the copper oxide surface was hydroxylated with water to create an “environmental reaction surface”. The chlorinated phenols were then added to the hydroxylated copper oxide surface. The most favorable reaction site had the most positive Bader charge. Two reaction pathways were investigated: (1) elimination of water and (2) elimination of hydrochloric acid gas. Local minimum structures, Bader charges, and reaction energies were calculated to help in understanding the role of metal oxides in EPFRs formation. The elimination of HCl is energetically more favorable over water.

Keywords: *Ab initio*, chlorinated phenols, EPFRs, copper oxide clusters

1. Introduction

Particles containing transition metal oxides have been shown to assist the formation of environmentally persistent free radicals (EPFRs) known to initiate adverse health impacts. Experimental studies show that ultrafine particles (< 0.1 μm diameter) cause more lung injuries than fine particles (0.1 – 0.25 μm) composed of the same material. [1] In general, ultrafine particles have a large surface area providing for more contact with the lung and hence have a profound effect. In addition, they are reported to penetrate deeper into the lungs than fine particles. Transition metal oxides are associated with particulate air pollution, (PM10) generated from combustion processes. These transition metals (Cu, Fe, Zn) have been shown to catalyze the formation of stable and highly reactive free radicals such as hydroxyl, ROS, superoxide, and hydrogen peroxide radicals. The bulk copper content in fly ash has been reported to contain 50% CuO and 30% Cu(OH)₂. [2] Copper is potentially carcinogenic. Copper oxide and hydroxide may catalyze the formation of poly-chlorinated dibenzodioxins/Furans (PCDD/Fs) in an incineration process. [3]

We have previously demonstrated phenols and chlorophenols chemisorb on metal oxide surfaces (particularly, Fe and Cu), and form EPFRs by electron transfer from the adsorbate to the metal ion, reducing the metal ion. This process occurs in postcombustion conditions at 150-400⁰C. Considering copper is typically the most abundant transition metal in airborne particles, the formation and stabilization of EPFRs involving reaction with copper is envisaged to contribute in understanding surface-mediated process. In this manuscript, we report results of a detailed density functional study of the geometrical structures of copper oxides clusters reactions with 2 and 4-chlorophenols, their energies and Bader partial charges. Monochlorophenol is a doubly substituted adsorbate and chemisorption can occur via reaction with both substituents through elimination of HCl and/or H₂O, respectively. [4] We have selected 4 clusters of copper oxides (CuO)_n, n=1-4, to demonstrate chemisorption process via either HCl or water elimination. Monochlorophenol is ubiquitous in combustion process containing chlorine such as hazardous wastes, fly ashes, and municipal incinerators. [5] The results of this and future studies using force fields developed by other LA-SIGMA researchers will help understand the reaction process on large clusters.

2. Computational Details

The Gaussian suite of programs has been used for all our calculations. All the geometries were optimized with the unrestricted version of the B3LYP hybrid density functional. An ECP basis set, LANL2DZ (Los Alamos National Laboratory 2 double ζ), was used for all the atoms. Vibrational frequencies were analyzed to confirm the nature of the minima energies for the geometries. The associated zero point energies and sum of electronic have been included to obtain the reaction energies. Our procedure calculated catalytic formation of EPFRs via three steps. First the structures and energetics of (CuO)_n clusters (n=1-4) were determined in order to find the minima structures and the lowest energy spin states. Second, since water is ubiquitous in the environment, it was added to each unique Cu atom in a cluster in order to find the most favorable hydroxylation site. Typically, addition of water resulted in formation of an O-H bond followed by transfer of an H atom to an adjacent O atom forming another O-H bond, hence our use of the term hydroxylation. Finally, chlorinated phenols (*ortho* and *para* substituted) were added to the hydroxylated copper oxide clusters. The energies and Bader charges of products involving the two pathways (1) elimination of water and (2) elimination of HCl were analyzed.

3. Results & Discussions

The electronic and structural properties of (CuO)_n (n=1-8) were previously investigated by Bae G. T. et al. using B3LYP (Becke's 3-Parameter exchange functional with Lee Yang Parr correlation) model chemistry and LANL2DZ basis set.[5] The geometries of hydroxylated (CuO)_n(OH)₂ with Bader charges on copper atom are shown in Figure 1. The spin states of the hydroxylated structures are doublet for (CuO cluster), singlet (Cu₂O₂ cluster), quartet (Cu₃O₃ cluster), and triplet (Cu₄O₄ cluster). The structures of CuO-water, Cu₂O₂-water, and Cu₃O₃-water are linear and the structure of Cu₄O₄-water is planar.

The surface of the copper oxide is typically hydroxylated in the environment. The water molecule was added to a copper atom with the largest positive Bader charge followed by an H-atom transfer to an adjacent O- atom. For

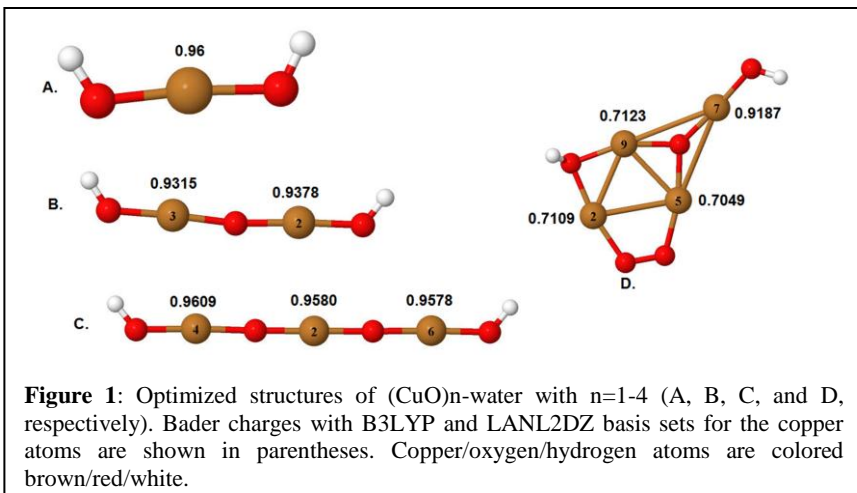


Figure 1: Optimized structures of $(\text{CuO})_n$ -water with $n=1-4$ (A, B, C, and D, respectively). Bader charges with B3LYP and LANL2DZ basis sets for the copper atoms are shown in parentheses. Copper/oxygen/hydrogen atoms are colored brown/red/white.

$n=1, 2,$ and $3,$ the structures are linear in shape. There is one reaction site for CuO . The reaction site for $n=2$ is the copper atom with 0.9378 Bader charge. The reaction site for $n=3$ is the copper atom with 0.9609 Bader charge. For $n=4,$ the three copper atoms forming a triangle has Bader charges of $0.7109, 0.7123,$ and 0.7049 . The reaction site has the largest Bader charge of 0.9187 . The reactions energies are exhibited in **Table 1** were

calculated as follows; $\Delta E = E(\text{Cu}_n\text{O}_n - \text{Water}) - (E(\text{Cu}_n\text{O}_n) + E(\text{Water}))$

4. Elimination of Water vs. Hydrochloric acid

Next monochlorophenol are reacted with the OH of hydroxylated copper oxide clusters resulting in either H_2O or HCl elimination. Table 2 (a & b) shows the reaction energies (in kcal/mol) of hydroxylated copper oxide with 2 and 4-monochlorophenol. The elimination of HCl is more favorable compared to water. Table 2a shows the reaction energies of CuO clusters with *ortho*-chlorinated phenols. The formation of EPFRs via water elimination has higher reaction energies. All the reaction energies are exothermic. The Cu_2O_2 cluster has lower energies for *ortho* and *para*- chlorophenols (-17.86 kcal/mol and -15.26 kcal/mol via HCl elimination, respectively).

5. Charge transfer

The knowledge of charge distribution has implications in the formation of EPFRs. Using Bader charge analysis, we calculated the change in electron density before and after reaction with chlorinated phenols. The electron transfer was anticipated to reduce copper (II) to copper (I). We calculated the Bader charges of the target Cu atom in CuO -water, CuO -*ortho*-chlorophenol, and *para*-chlorophenol in Figure 2. The Bader charges of CuO -water clusters are much higher than the CuO -chlorinated phenol.

6. Conclusion

We have investigated the stabilities and reactivities of copper oxide clusters using density functional theory. The reaction energies were calculated to investigate reaction energetics. It has been established that chlorinated phenols lead to formation of PCDD/Fs via surface-mediated processes. We find that the two processes (i.e. elimination of H_2O and HCl) are energetically possible. Elimination of HCl is a more favorable pathway. While

the magnitudes of the copper reduction are smaller than the full electron transfer expected to occur in a bulk system, there is evidence of electron transfer from the chlorophenol to the copper atom, as envisioned in the proposed mechanism.

Table 1. Reaction energies of CuO clusters with water

Cluster Size	ΔE (kcal/mol)
CuO-water	-55.94
Cu ₂ O ₂ - water	-41.73
Cu ₃ O ₃ - water	-37.28
Cu ₄ O ₄ - water	-56.32

Table 2a. Reaction energies of copper oxide clusters with ortho-chlorophenol

Cluster Size	Elimination of H ₂ O	Elimination of HCl
CuO	-5.80	-13.93
Cu ₂ O ₂	-9.27	-17.86
Cu ₃ O ₃	-6.15	-14.33
Cu ₄ O ₄	-5.91	-13.82

Table 2b. Reaction energies of copper oxide clusters with para-chlorophenol

Cluster Size	Elimination of H ₂ O	Elimination of HCl
CuO	-8.90	-11.31
Cu ₂ O ₂	-12.40	-15.26
Cu ₃ O ₃	-4.03	-12.04
Cu ₄ O ₄	-8.75	-11.26

8. References

- [1] Donaldson, K.; Li, X. Y.; MacNee, W., Ultrafine (nanometre) particle mediated lung injury. *Journal of Aerosol Science* **1998**, *29*, (5–6), 553-560.
- [2] Hsiao, M. C.; Wang, H. P.; Yang, Y. W., EXAFS and XANES Studies of Copper in a Solidified Fly Ash. *Environmental Science & Technology* **2001**, *35*, (12), 2532-2535.
- [3] Lomnicki, S.; Truong, H.; Vejerano, E.; Dellinger, B., Copper Oxide-Based Model of Persistent Free Radical Formation on Combustion-Derived Particulate Matter. *Environmental Science & Technology* **2008**, *42*, (13), 4982-4988.
- [4] Fine, P. M.; Cass, G. R.; Simoneit, B. R. T., Chemical Characterization of Fine Particle Emissions from Fireplace Combustion of Woods Grown in the Northeastern United States. *Environmental Science & Technology* **2001**, *35*, (13), 2665-2675.
- [5] Bae, G.-T.; Dellinger, B.; Hall, R. W., Density Functional Calculation of the Structure and Electronic Properties of CunOn (n = 1–8) Clusters. *The Journal of Physical Chemistry A* **2011**, *115*, (11), 2087-2095.

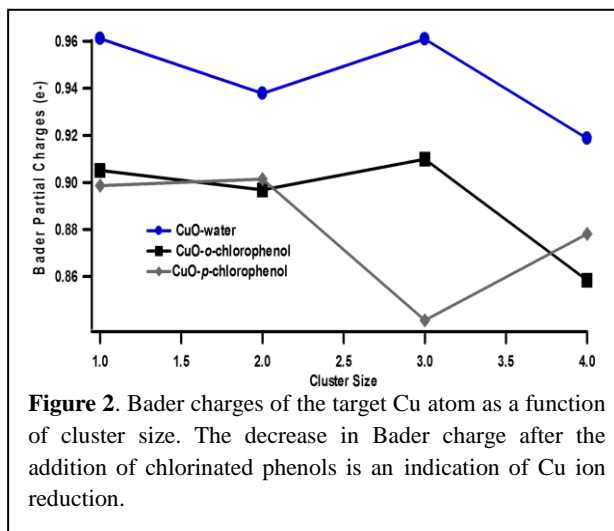


Figure 2. Bader charges of the target Cu atom as a function of cluster size. The decrease in Bader charge after the addition of chlorinated phenols is an indication of Cu ion reduction.

7. Acknowledgements

We gratefully acknowledge the support of this work under NSF-LASIGMA grant #EPS-1003897 and NIEHS-LSU Superfund Research Center grant #P42ES013648

***Ab Initio* Molecular Dynamics Simulation of a Propylene Carbonate-filled Uncharged Nanotube Forest**

G. G. Hoffman¹ and L. R. Pratt²

¹Department of Chemistry, Elizabethtown College

²Department of Chemical & Biomolecular Engineering, Tulane University

Abstract: *Ab initio* molecular dynamics simulation of propylene carbonate in a nanotube forest shows that this filling depends sensitively on attractive dispersion interactions not satisfactorily described by standard electron density functional models that are well-established and satisfactory for covalent interactions. Calculations reported previously with the PBE density functional are carried-out entirely over again with the dispersion corrected alternative PBE-D. The binding energies of the propylene carbonate molecules are now negative, and distributed approximately normally. This now agrees with observations of the PC-graphite contact angle reported previously. Collisional characteristics associated with the PC molecules are only slightly changed by this revision of electron density to address dispersion interactions specifically.

Keywords: propylene carbonate, AIMD simulation, nanotube forest

1. Introduction

We reported last year on *ab initio* molecular dynamics (AIMD) simulation of a propylene carbonate (PC) filled, uncharged carbon nanotube (CNT) forest [1]. What we learned from that work was that electron density functionals that are well-established and satisfactory for covalent interactions do not predict PC filling of the CNT forest, in apparent disagreement with our experimental assessment of PC-graphite interactions reflected by the observed contact angles. The suggested conclusion was that dispersion interactions are not adequately represented in the traditional electron density functionals. This possibility is becoming broadly appreciated in the arena of AIMD of molecular solutions.

Our previous report discussed the practical significance of these systems in the arena of electrical energy storage.

We also reemphasize here the crucial features of AIMD simulations. Those calculations treat the electronic structure of materials on-the-fly, within molecular dynamics simulations. They are feasible for condensed matter simulation on the basis of three enabling theoretical ingredients: (i) electron density functional theory, (ii) pseudo potentials that permit the calculation to focus only on outer, *e.g.*, valence, electrons, and (iii) suitability of plane wave basis sets for material simulation. AIMD calculations are several orders-of-magnitude more demanding than molecular simulations based on model molecular force-fields. AIMD calculations, relative to classic molecular dynamics, require severe compromises in times and length scales that may be addressed.

2. Methods

Our AIMD calculations used the CPMD package (<http://www.cpmo.org/>), with the PBE-D electron density

functional model [2], a norm-conserving pseudo-potential (NCPP), and a plane-wave basis set cut-off of 85 Ry. Periodic boundary conditions in all three spatial dimensions includes one 80-carbon-atom nanotube (with the implied images), 10 (13 atom) propylene carbonate molecules, 210 atoms in total. This is huge on the now-conventional electronic structure size-scale, but small on the now-conventional simulation size-scale. The present calculations were carried-out on LONI [3] and Xsede [4] and utilized about 2M service units.

Our report last year [1] discussed a tempering protocol that attempts to accomplish necessary aging of simulation configurations in view of the extreme relative cost of the AIMD calculations. Calculations were initiated at the high temperature of $T=600\text{K}$. Samples from that high T calculation were used to seed calculations at $T=300\text{K}$ with additional aging. In this way, the aging of low T calculations can be more effective, and the series of low T calculations might be more nearly independent. That tempering procedure was implemented in the revised calculations discussed here. In that way we collected 16 trajectories each 6 pfs in length. For the statistics below each of these trajectories was sampled at a rate of 2.0/ps.

The analysis of first interest here is based on the binding energies defined by

$$\varepsilon = U(n) - U(n-1) - U(1). \quad (1)$$

The distribution of binding energies ε provides the free energy of the fluid on the basis of the partition (thermal Green's) function formula

$$\exp(\beta\mu^{(ex)}) = \langle \exp(\beta\varepsilon) \rangle. \quad (2)$$

$\mu^{(ex)}$ is the interaction part of the chemical potential of Gibbs (partial molar Gibbs free energy) of the PC fluid; the brackets indicate the thermal average. Since there can be ten (the number of PC molecules) observations of a binding energy for each configuration, this data collection scheme produces $10 \times 12 \times 16 = 1920$ elementary data.

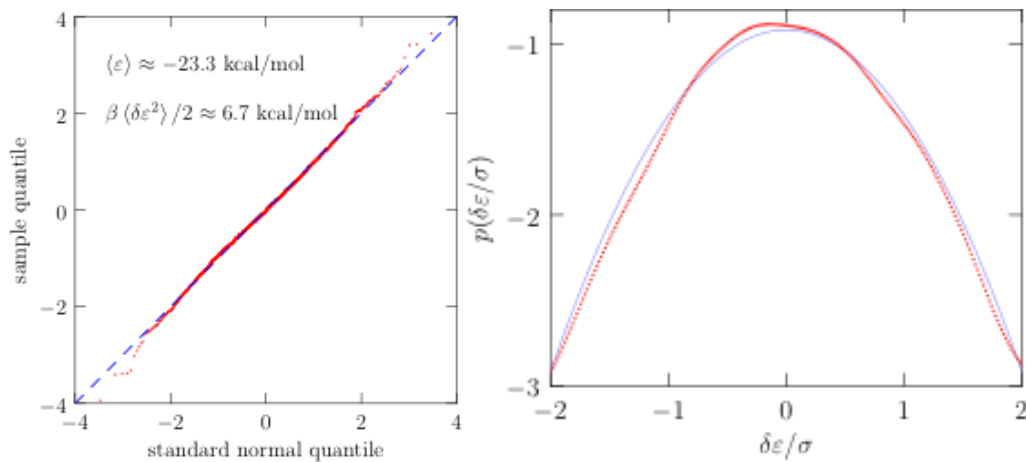


Figure 1: Distribution of binding energies. (left) The normal quantile-quantile plot indicates that the binding energies are distributed approximately normally. (right) The standardized comparison to a Gaussian probability density of ε gives an additional, rougher indication of that point.

3. Results

In contrast to the calculations reported last year [1] with the PBE functional, liquid PC is well-bound in the CNT forest when we use the PBE-D functional (Figure 1). This is consistent with the indication of healthy attractive interactions between PC and graphite on the basis of the observed contact angle [2]. We have also evaluated the Einstein frequency, $\Omega^2 = \langle F^2 \rangle / 3mkT$, for the central carbon atom of the PC molecule (Table 1). This characteristic changes insignificantly when we change PBE to PBE-D in the AIMD simulations.

4. Conclusions

Ab initio molecular dynamics simulation of propylene carbonate in a nanotube forest shows that this filling depends sensitively on attractive dispersion interactions not satisfactorily described by standard electron density functional models well-established and satisfactory for covalent interactions. Empirical dispersion-corrected models do a better job for those purposes.

Energy calculation →	PBE	PBE simulation, recalculation of energy at sampled points with PBE- D	PBE-D
$\langle \mathcal{E} \rangle$ (kcal/mol)	8.2	-21.3	-23.2
$\langle \mathcal{E} \rangle + \langle \delta \mathcal{E}^2 \rangle / 2kT$ (kcal/mol)	20.7	-11.9	-16.7
$\left(\frac{\langle F^2 \rangle}{3mkT} \right)^{-1/2}$ (fs)	43	-	42

Table 1: Comparison of energies and forces between PBE and PBE-D [2] AIMD calculations for PC in the CNT forest. The dispersion correction incorporated into PBE-D lowers the energy substantially. The energetic combination of the second row would be the interaction free energy of the PC material, if the distribution were precisely Gaussian. This gives an indication of the free energy but is typically not a sufficient theory without amendment. The force combination of the last row is associated with the central carbon atom of the PC. This parameter indicates a collisional time-scale, and that characteristic is only slightly changed between the two calculations.

5. Acknowledgments

The current work is funded by the NSF EPSCoR LA-SiGMA project under award #EPS-1003897.

6. References

- [1] G. G. Hoffman and L. R. Pratt, *Proceedings of the 2011 RII LA-SiGMA Symposium*, 13-16 (2011): “*Ab initio* molecular dynamics simulation of an uncharged propylene carbonate-filled nanotube forest”
- [2] S. Grimme, *Comput. Mol. Sci.* **1**, 211 (2011): “Density functional theory with London dispersion corrections”
- [3] www.loni.org/, Louisiana Optical Network Initiative
- [4] www.xsede.org/, “Extreme Science and Engineering Discovery Environment” ... “replaces and expands on the NSF TeraGrid project”

Ab Initio Study of Iron Oxide Clusters and their Reactions with Phenol, 2-Chlorophenol and 4-Chlorophenol and Force Field Development for Copper Oxide Systems

Cheri A. McFerrin¹, Barry Dellinger¹, and Randall W. Hall^{1,3}
Ramu Ramachandran² and Collin Wick²

¹Department of Chemistry, Louisiana State University, Baton Rouge, LA 70803

²Department of Chemistry, Louisiana Tech University, Ruston, LA 71272

³Department of Natural Sciences and Mathematics, Dominican University of California

Abstract: *Ab initio* calculations were used to study the structures and spin states of neutral iron oxide clusters, Fe_nO_n and $\text{Fe}_n\text{O}_{n+1}$ ($n=1-2$). The lowest energy structures of these neutral clusters were investigated using six all-electron basis sets and the BPW91, the M06 and the PBE0 density functionals. As a model for surface reactions on iron oxide nanoparticles, the FeO cluster was hydroxylated followed by reactions with phenol, 2-chlorophenol and 4-chlorophenol which condense water and HCl. Future work will apply the same procedure to the other iron oxide clusters examined in this work. Forcefield parameters have been determined such that larger copper oxide systems and their reaction with similar precursors may be studied. These studies will be used as part of LA-SiGMA's Science Driver 2 to validate and direct the development of force fields capable of studying the structure of larger metal oxide particles.

Keywords: Nanoparticles, catalysts, reaction thermodynamics, charge distributions.

1. Introduction

Copper and iron oxide nanostructured particles have been shown to be particularly effective catalysts for the formation of polychlorinated dibenzo-*p*-dioxins and dibenzofurans (PCDD/F) and other pollutants during combustion processes¹. Environmentally persistent free radicals form on combustion produced copper and iron oxide-containing nanoparticles, and these radicals have been shown to be intermediates in the formation of PCDD/F and be a possible cause of the observed health impacts of airborne fine particles.²⁻⁶ It has been shown that the metal atoms in these nanoparticles facilitate the formation of radicals via electron transfer from a physisorbed molecular precursor to a metal atom in the cluster.⁷ For this reason, we are studying the structures and reactivities of iron and copper oxide clusters. This involves accurate density functional calculations and the development of simple force fields capable of allowing calculations involving metal oxide clusters containing tens to hundreds of metal atoms. LA-SiGMA's focus on accurate density functionals and force fields is a critical component of understanding the mechanism for metal oxide catalysis of PCDD/Fs.

There are relatively few experimental and theoretical studies of how copper and iron oxide clusters catalyze or mediate the formation of pollutants in combustion systems or the environment. Estimates of the relevant cluster sizes range from a micrometer down to just a few metal atoms; therefore, this work studies the structures and energetics of small iron oxide clusters as a first step toward understanding the interactions between metal oxides and free radicals.⁷

2. Methods

Geometry optimizations for FeO and FeO₂ were done using three functionals (BPW91, PBE0, and M06) and six basis sets (6-31++G**, 6-311++G**, cc-pVDZ, cc-pVTZ, aug-cc-pVDZ, and aug-cc-pVTZ). All three functionals predict a quintet ground state for FeO while the BPW91 functional finds a triplet ground state for FeO₂. There was little qualitative disagreement between the different basis sets, so the all-electron basis set (aug-cc-pVDZ) was chosen for calculation of reaction energies since it includes polarization, diffuse functions, and is correlation-consistent. Each minimized geometry found has been verified as the global minimum using the Global Reaction Route Mapping algorithm⁸.

Our procedure will study the catalytic process in three steps. First the structures and energetics of Fe_nO_n and Fe_nO_{n+1} clusters (n=1-2) have been determined in order to find the lowest energy spin state. The lowest spin state for both Fe₂O₂ and Fe₂O₃ is a nonet. Second, since water is ubiquitous in the environment, it is expected that the surfaces of metal oxide clusters are hydroxylated; to model this, a water molecule will be added in turn to each unique iron atom in each cluster. For example, there are two non-equivalent Fe atoms in Fe₂O₃. Addition of water typically resulted in the formation of an O-H bond and the transfer of a hydrogen atom to an adjacent oxygen atom forming another O-H bond. Finally, phenol and substituted chlorinated phenols were added to the hydroxylated cluster and the reaction products (water and a phenoxyated cluster or HCl and a phenoxyated cluster) were analyzed for reaction energetics. Initial calculations for these reactions' thermodynamics (using M06/Lanl2DZ) for the addition of these molecular precursors indicate the number of oxygen atoms in a metal oxide cluster is directly proportional to the exothermicity of the reaction. It has already been experimentally shown the electron affinity of the neutral iron oxide clusters increases with the number of oxygen atoms.⁹

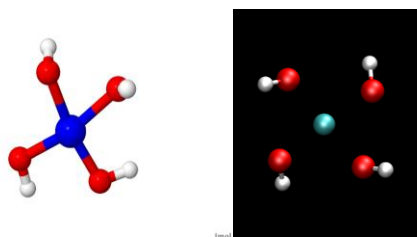


Figure 1: M06/cc-pVTZ optimized geometry (left) and model prediction (right) for CuO₄H₄.

to their low electronegativity. The LJ interactions of reproduce surface adsorption on oxide surfaces, and the copper LJ potential diameter was fit to the copper van der Waals radius, which was quite small. These interactions were all non-bonded interactions, but were present between all copper and oxygen atoms (hydrogens did not have non-bonded interactions with the oxygens they were bound to).

When copper and oxygen atoms came within 4 Å an additional binding potential was added to the

The force field for copper oxide was based on M06/cc-pVTZ calculations. Representative structures are shown in Figure 1. We parameterize our models to include electrostatic charges, point polarizabilities and Lennard-Jones (LJ) 12-6 potentials for each atom. The electrostatic charges were calculated from the *ab initio* calculations via a Bader charge analysis from different clusters, and the charges that most closely resembled the charge on each atom type were used. The point polarizabilities were taken from previous work of Applequist¹⁰ for oxygen atoms, and hydrogen atoms were considered to have no significant polarizable interactions due

oxygen were taken from other work, parameterized to

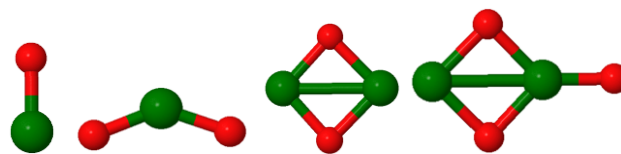


Figure 2. M06/aug-cc-pVDZ optimized clusters of Fe_nO_n and Fe_nO_{n+1}, n=1-2. Fe atoms are green; O atoms are red.

copper-oxygen interactions. This potential was harmonic with the force constant and distance minimum parameterized to reproduce the *ab initio* copper-oxygen distance versus energy in a cluster of one copper atom and four oxygens (Figure 1). For the described cluster, there are four copper-oxygen distances, with two of the stretches having different distances than the other two. Because of this, two harmonic bonded potentials were used. Furthermore, a harmonic bond bending potential was included between the oxygen-copper-oxygen bends. Since a single oxygen can interact with three other oxygens via the bond bending potential, two different potentials were used. One of them was between adjacent oxygen atoms, while a second was between oxygens that had greater angles than the other two. This second bond bending potential was required to reproduce the planar structure found with *ab initio* calculations.

3. Results

Figure 2 displays the optimized iron oxide clusters found using the M06/aug-cc-pVDZ model chemistry. These clusters coordination at the iron atoms ranges from 1-3.

Reaction thermodynamics (Table 1) in kcal/mol for the FeO cluster using PBE0/aug-cc-pVDZ and M06/aug-cc-pVDZ indicate the reactions are exoergic.

Reaction	PBE0	M06
$\text{FeO} + \text{HOH} \rightarrow \text{H}_2\text{O-Fe-O}$	-21.9	-30.7
$\text{H}_2\text{O-Fe-O} \rightarrow \text{HO-Fe-OH}$ (isomerization)	-54.6	-49.2
$\text{HO-Fe-OH} + \text{phenol} \rightarrow \text{HOH} + \text{HO-Fe-O-Phenyl}$	-3.3	-3.1
$\text{HO-Fe-OH} + 2\text{-Cl-Phenol} \rightarrow \text{HOH} + \text{HO-Fe-O-(2Cl-Phenyl)}$	-9.0	-12.2
$\text{HO-Fe-OH} + 4\text{-Cl-Phenol} \rightarrow \text{HOH} + \text{HO-Fe-O-(4-Cl-Phenyl)}$	-2.6	-3.5
$\text{HO-Fe-OH} + 2\text{-Cl-Phenol} \rightarrow \text{HCl} + \text{HO-Fe-O-(2-OH-Phenyl)}$	-9.3	-18.2
$\text{HO-Fe-OH} + 4\text{-Cl-Phenol} \rightarrow \text{HCl} + \text{HO-Fe-O-(4-OH-Phenyl)}$	-0.9	-7.8

As for the copper oxide force field model, while perfect agreement with *ab initio* energies and angles were not found, the general structure was reproduced well, and the copper-oxygen distances were well reproduced. The crystal parameters predicted by the model vs. experiment (using only the *ab initio* information from the clusters) are given in Table 2.

Parameter	Experimental	Model Prediction
α	90°	90.3°
β	99.6°	96.9°
γ	90°	91.0°
a (Angstroms)	4.68	4.56
b (Angstroms)	3.42	3.55
c (Angstroms)	5.13	5.03

4. Conclusion

We have begun to calculate reaction thermodynamics for iron oxide nanoparticles and their reactions with precursors such as phenol. We are also developing forcefield parameters for copper oxide nanoparticles using *ab initio* calculations and fits to non-bonded and harmonic potential energy functions. The model, once refined, will be used to model the structures of large copper oxide nanoparticles. Good agreement between *ab initio* and forcefield calculations is obtained using a harmonic forcefield for the angle bending potentials, harmonic bond stretching potential functions, and charge plus polarization non-bonded interactions. Two types of Cu-O bonds were found in the *ab initio* calculations and reproduced with the forcefield.

Future efforts will be to further refine the forcefield using calculations from larger clusters combined with Monte Carlo and molecular dynamics simulations. The goal is to construct a forcefield that will provide input structures for ONIOM or QM/MM calculations of the reactivities of larger clusters toward phenol and chlorinated phenols.

5. Acknowledgments

This work supported by NSF Award Number EPS-1003897, the Louisiana Optical Network Initiative (LONI) and the LSU Center for Computational Technology.

6. References

- [1] Ryan, S., Wikstrom, E., Gullett, B. K., Touati, A.; *Organohalogen Compd.*, 2004, 66, 1119-1125.
- [2] Dellinger, B., Pryor, W., Cueto, R., Squadrito, G., Hedge, V., Deutsch, W.; *Chem. Res. Toxicol.*, 2001, 14, 1371-1377.
- [3] Dellinger, B., Pryor, W., Cueto, R., Squadrito, G., Deutsch, W.; *Proc. Combust. Inst.*, 2000, 28, 2675-2681.
- [4] Shi, T., Knaapen, A., Begerow, J., Birmili, W., Borm, P., Schins, R.; *Occup. Environ. Med.*, 2003, 60, 315-321.
- [5] Li, N., Sioutas, C., Cho, A., Schmitz, D., Misra, C., Sempf, J., Wang, M., Oberley, T., Froines, J., Nel, A.; *Environ. Health Perspect.*, 2003, 111, 455-460.
- [6] Balakrishna, S.; Lomnicki, S.; McAvey, K. M.; Cole, R. B.; Dellinger, B.; Cormier, S. A.; *Part. Fibre Toxicol.*, 2009, 6, 11.
- [7] Vejerano, E.; Lomnicki, S.; Dellinger, B.; *Environ. Sci. Tech.*, 2011, 45 (2), 589-594.
- [8] Maeda, S., Ohno, K.; *J. Phys. Chem. A.*, 2005, 109, 5742-5753.
- [9] Wang, L., Wu, H.; Desai, S. R.; *Phys. Rev. Lett.*, 1996, 76 (25), 4853-4856.
- [10] Applequist, J., Carl, J.R., Fung, K.K.; *JACS*, 1972, 94, 2952.

Advanced Quantum Chemistry Approach to the Ground State Spin of Iron Oxide Clusters

J.M. Leveritt III,¹ V. Kolesnichenko,² G. Goloverda,² J.P. Perdew,³ A.L. Burin¹

¹Department of Chemistry, Tulane University;

²Department of Chemistry, Xavier University of Louisiana;

³Department of Physics, Tulane University

Abstract: We have continued the theoretical investigation of the ground state spin of the elementary iron oxide clusters derived from magnetite structures (see Fig. 1) using Gaussian¹ at PBE/PBE/LANL2DZ level. In the non-relativistic approximation we predict the high spin $S=12$ in the ground state. The excited states, $S=13$ and 9 are close in energy and therefore the relativistic interaction must be included, which is currently in progress.

Keywords: small molecular magnets, iron clusters, spinel-type, Fe-8, QM/MM

1. Introduction

Small molecular magnets, including Fe-8,² Manganese-12,³ cobalt (II) structures,⁴ and V-15 structures,⁵ are significant in quantum computations^{6,7} and information storage⁸. We consider the iron oxide cluster having a structure inherited from magnetite (see Fig. 1, the equatorial irons are terminated with the addition of water molecules). An important advantage of magnetite-structure is the strong highly anisotropic magnetic properties similarly to its crystalline counterpart. Also there is the opportunity to control the oxidation state of Fe changing the ligands.

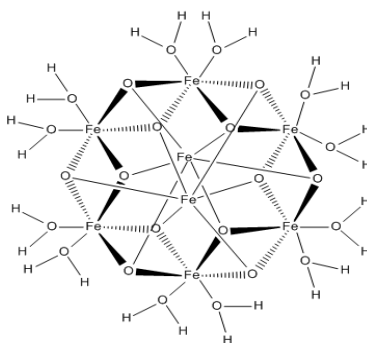


Figure 1 Structure of the spinel-type iron cluster analyzed in this study

2. Results

The analysis of iron oxide cluster ground state energy depending on the molecular spin has been performed using Gaussian 09¹. The calculations were performed at the PBEPBE/LANL2DZ theory level. The theory level has been chosen following previous work of other groups on iron clusters^{9,10} demonstrating relevance and success of *ab initio* approaches.

QM/MM methods have been used to perform basic geometry optimizations for various spin states ranging from S=0 to S=16. The inspiration using these methods comes from a recent review written by Bo and Maseras¹¹ and various references within that applied these methods to inorganic systems. The quantum mechanical method used is the pure DFT functional PBEPBE due to its ability to accurately calculate energies of systems with multiple metal centers¹². The molecular mechanics calculations were performed using the UFF force field, which is standard in QM/MM computations of inorganic systems¹¹. LANL2DZ is a common basis set used in computations of inorganic systems, and has recently been considered in Ref 13 and references within.

The energy of the geometry optimized ground state of the cluster that is different for each total molecular spin is shown in Fig. 2. Theory predicts the energy minimum to occur for the spin S=12, which is a signature of the molecular magnet behavior. The relative energies of other spin states exceeds the ground state by around 1.0-1.5 eV consistently with other studies,^{12,13} Since the PBEPBE/LANL2DZ theory level is more accurate than previously used B3LYP and mPWPW91 density functional theory methods we believe that the present estimate of ground state spin, S=12, is more accurate than the previous year estimate S=4.

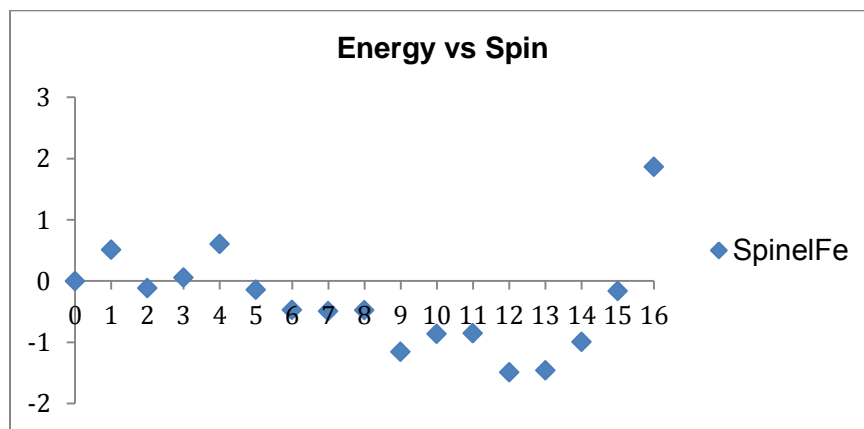


Figure 2 The plot shows the change in energy of the different optimized spin states relative to the singlet state. Energies are in eV

3. Conclusions

A high spin state ($S=12$) was determined to be the ground state when using the PBE as the functional treating exchange and correlation when all of the iron atoms are allowed to have an oxidation state of +3. This was achieved by comparing the energy values of each optimized spin state. Since Fe-8 is a similar system to that of these spinel-type iron oxide clusters we expected relatively similar ground spin states, and since Fe-8 is known to be $S=10$ this appears to be in reasonable agreement. A more detailed approach needs to be considered in Fe-8 and if a different approach is required to accurately calculate the ground spin state then that will be applied to these spinel-type iron oxide clusters.

An extension of theory to the relativistic approach is desirable to determine the true ground state and its anisotropy. We are currently working on this problem.

3. Acknowledgments

The current work is funded by the NSF EPSCoR LA-SiGMA project under award #EPS-1003897.

4. References

- [1] Frisch, M. J. et al. GAUSSIAN 09 Revision A.1, Gaussian, Inc. Wallingford CT 2009.
- [2] K Wiegardt, K Phol, I Jibril, G Huttner. Hydrolysis products of the monomeric amine complex $(C_6H_{15}N_3)FeCl_3$ – the structure of the octameric iron (III) cation of $[(C_6H_{15}N_3)_6Fe_8(u_3-O)_{12}Br_7(H_2O)]Br_8H_2O$. *Angewandte Chemie-International Ed. Engl.* 23, 77
- [3] T Lis. Preparation, structure, and magnetic properties of a dodecanuclear mixed-valence manganese carboxylate. *Acta Crystallogr. Soc. B* 36, 2042, 1980
- [4] M Murrie. Cobalt(II) single-molecule magnets. *Chemical Society Reviews*, 39, 6, 1986-1995, 2010
- [5] A Muller, J Doring. A novel heterocluster with d_3 -symmetry containing 21 core atoms – $[As_6(III)V_{15}(IV)O_{42}(H_2O)]^{6-}$. *Angewandte. Chemie-International. Ed. Engl.* 27, 1721, 1988
- [6] D Gatteschi, R Sessoli. Quantum Tunneling of Magnetization and Related Phenomena in Molecular Mterials. *Angewandte Chemie-International Ed.* 43, 3, 2003.
- [7] JA Jones. Fast searches with nuclear magnetic resonance computers. *Science*, 208, 5361, 229, 1998.
- [8] AV Postnikov, J Kortus, MR Pederson. Density functional studies of molecular magnets. *Physica Status Solidi (b)– Basic Solid State Physics*, 243, 11, 2006
- [9] M. Castro, D. R. Salahub, Density-functional calculations for small iron clusters: Fen , Fen^+ , and Fen^- for $n \leq 5$, *Phys. Rev. B* 49, 11842 (1994).

[10] G. L. Gutsev, C.W. Bauschlicher Jr., Electron Affinities, Ionization Energies, and Fragmentation Energies of Fen Clusters (n = 2–6): A Density Functional Theory Study, *J. Phys. Chem. A* 107, 7013 (2003).

[11] C Bo, F Maseras. QM/MM methods in inorganic chemistry. *Dalton Transactions*, 2911-2919, 2008

[12] JG Du, XY Sun, HY Wang. The confirmation of accurate combination of functional and basis set for transition-metal dimers: Fe-2, Co-2, Ni-2, Ru-2, Rh-2, Pd-2, Os-2, Ir-2, and Pt-2 *International Journal of Quantum Chemistry*, 108, 9, 1505-1517

[13] F Remacle, F Grandjean G. J. Long., A Density Functional Theory Calculation of the Electronic Properties of Several High-Spin and Low-Spin Iron(II) Pyrazolylborate Complexes. *Inorg. Chem.*, 2008, 47 (10), pp 4005–4014

Charge Transfer from a Carbon Nanotube Electrode to Tetramethyl Ammonium Ions Investigated by *Ab Initio* Molecular Dynamics Simulation

W. Zhang,¹ P. Wisdom,³ G. G. Hoffman,² S. W. Rick,³ and L. R. Pratt¹

¹Department of Chemical & Biomolecular Engineering, Tulane University

²Department of Chemistry, Elizabethtown College

³Department of Chemistry, University of New Orleans

Abstract: *Ab initio* molecular dynamics (AIMD) are carried-out on systems of a molecular ion, either tetramethylammonium cation (TMA^+) or tetrafluoroborate anion (BF_4^-), and a carbon nanotube (CNT) electrode in armchair configuration at several distinct charge states. ESP charges of the molecular ion are evaluated at the sampled configurations, and they are typically significantly reduced, reflecting electron donation from the CNT to the ion. The CNT electrode is thus an electron rich structure which typically donates electrons to nearby ions.

Keywords: supercapacitors, carbon nanotubes, tetramethylammonium (TMA^+), *ab initio* molecular dynamics (AIMD), charge transfer

1. Introduction

In recent years, carbon electrode materials of exotic type have become the basis of electrochemical double-layer capacitors (EDLCs) with impressive performance [1]. That performance will depend on the characteristics of the electrodes, the electrolyte solution, and the contacts between those subsystems, the so-called *double-layer*. Focusing for the moment on the liquid electrolyte solution, the molecular theory of electrolyte solutions is horrendously complicated and has degenerated into the disjoint activities [2]: (a) theory of primitive models in which the connection to experiments or simulation at a molecular level is not attempted, and (b) molecular simulation that does not address the physical issues that are basic to the theory which have been established albeit painfully. The challenge essential to re-animating the molecular understanding of these complex systems is achieving molecular realism on the basis of simulation while at the same time addressing the basic theoretical issues. For particular physical problems, a step in that re-animation is to secure the molecular-scale information that would be required for grounded theory. The present work attempts to follow that strategy for EDLCs based upon carbon nanotube (CNT) forests, and in particular evaluates charge transfer between CNT electrodes and the ions that might be present in realistic cases. The charges of the ions are possibly the most basic information required for serious statistical mechanical theory. Those theories will be sensitive to the ionic charges, and do not alternative sources of that information.

Here, specifically, we utilize *ab initio* molecular dynamics (AIMD) to treat ions involved in EDLCs, either the tetramethylammonium cation (TMA^+) or tetrafluoroborate anion (BF_4^-), and together with a CNT in armchair configuration at several electrode charges. We then evaluate the charges on the ions that would be relevant to statistical mechanical theories of these solutions and interfaces.

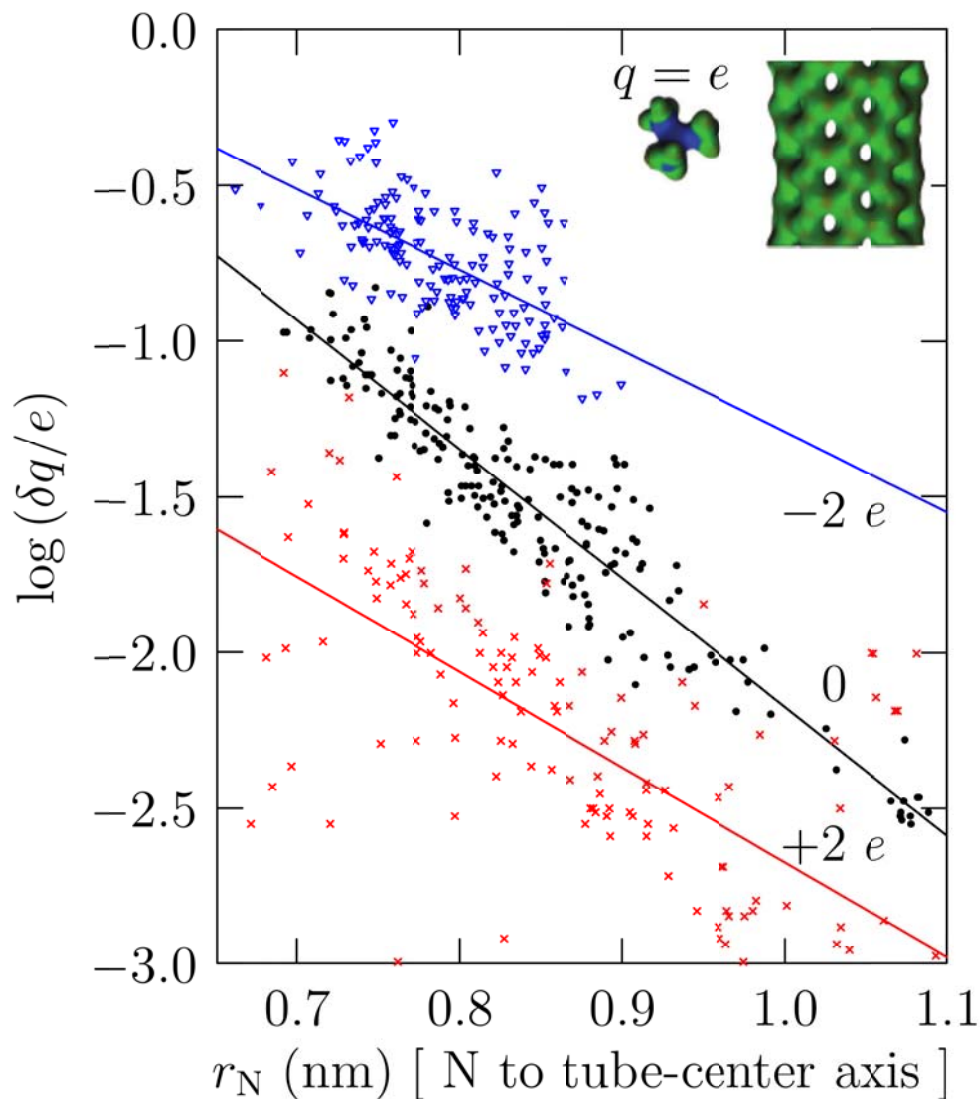


Figure 1: Electronic charge transferred to the TMA⁺ ion from the CNT at configurations sampled by the AIMD simulations, $q=e-\delta q$ with q the ESP charge on the ion. Blue: The CNT electrode is negatively charged, the system having an overall charge of $-e$. The TMA⁺ cation stays close to the CNT, and exhibits an ESP charge in the neighborhood of $0.6e$. Black: The CNT electrode is uncharged, but still donates substantial electron density to the TMA⁺ cation, as much as $0.3e$ as judged by the ESP charge. Red: The CNT is positively charged, the system having an overall charge of $+3e$. Here at the largest distances from the electrode, the ESP charge of the TMA⁺ cation approaches $+e$.

2. Methods

Our AIMD calculations and analysis used the CPMD package [3] with periodic boundary conditions in all three spatial dimensions. All the calculations utilized the PBE-D electron density functional model [4], a norm-conserving pseudo-potential (NCPP), and a plane-wave basis cut-off of 85 Ry. We carried out a standard AIMD trajectory for 10ps at the high temperature of $T=1200\text{K}$, thermalized using Nose-Hoover thermostat [3], to achieve broad configurational sampling. Deuterium (D) was used instead of protium (H) because propagation of the classical trajectories is slightly easier with smaller mass differences. We calculated the ESP charges [2,3] on the molecular ion at the configurations sampled by AIMD simulation.

All systems studied included an 80-carbon-atom nanotube (CNT) in armchair conformation and one molecular ion, either TMA^+ (97 atoms in all) or BF_4^- (85 atoms). We additionally studied cases with two more or two fewer electrons, corresponding prosaically to “ CNT^{2-} ” or “ CNT^{2+} ”. The system size was $L_x=L_y=1.8\text{nm}$, $L_z=1.05\text{nm}$. These simulation calculations were performed on LONI [7], and utilized about 200K service units.

Further *ab initio* calculations were carried for TMA^+ and BF_4^- to determine the amount of charge transfer between the ion pair. The program NWChem, version 6.1, was used [8]. For this relatively small system, a variety of quantum theories and electron partitioning schemes can be used. Calculations at the Hartree-Fock level as well as DFT with different functionals were used. All calculations used an aug-cc-pvdz basis set. The amount of charge transfer was determined using two methods, ESP, as for the CNT .. TMA^+ system, and Bader partitioning.[9]

3. Results

For TMA^+ (Figure 1), the CNT donates electrons to the molecular ion at all electrode charges considered. When the CNT is negatively charged (CNT^{2-}) likely cation-CNT distances are more probable (Figure 2), and the probability density more strongly structured than for the cases where the CNT has less charge.

Even for the BF_4^- anion, our results are consistent with the picture the CNT is an effective electron donor. Except for a possibly more complicated behavior of the BF_4^- .. CNT^{2+} , the anion can still acquire some electron density from the nanotube. The more complicated behavior of that BF_4^- anion will be discussed elsewhere, in circumstances that permit a more detailed analysis.

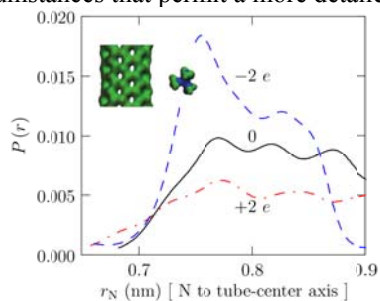


Figure 2: Probability density for the radial displacement of the N atom of the TMA^+ ion from the center axis of the CNT, for the AIMD sampling calculation at $T=1200\text{K}$. Labeling of the three curves is the same as in Figure 1. As expected, probable distances for the cation are most probable with CNT^{2-} tube, and least probable with

The results for the ion pair in its minimum energy structure, with a distance between ion centers equal to 0.437 nm, show (Table 1) more charge transfer predicted by DFT than by Hartree-Fock and more charge transfer when using ESP than Bader partitioning to determine charges. The results show less charge transfer between the ion pair than between TMA⁺ and the carbon nanotube.

Theory	TMA ⁺ charge, ESP (<i>e</i>)	TMA ⁺ charge, Bader (<i>e</i>)
Hartree-Fock	0.892	1.000
DFT, B3LYP	0.892	0.975
DFT, PBE0	0.890	0.977
DFT, XPBE96/CPBE96	0.879	0.962

Table 1: Charge of the TMA⁺ ion in contact with the BF₄⁻ ion.

4. Conclusions

The CNT is an electron-rich material that readily donates electrons to the TMA⁺ cation. At distances of closest approach to the neutral CNT electrode, a TMA⁺ cation has an ESP charge reduced to a value between 0.6-0.7*e*. For a negatively charged CNT electrode, a TMA⁺ cation in the corresponding probable configuration has an ESP charge reduced to values as low as 0.3*e*. There is charge transfer between the TMA⁺ and BF₄⁻ ions as well. These values will be of dominating concern for physical theories of the performance of electrochemical double-layer capacitance.

5. Acknowledgments

The current work is funded by the NSF EPSCoR LA-SiGMA project under award #EPS-1003897.

6. References

- [1] P. Simon and Y. Gogotsi, *Natural Materials* **7**, 845 (2008): "Materials for electrochemical capacitors"
- [2] D. M. Rogers, D. Jiao, L. R. Pratt, and S. B. Rempe, *Ann. Rep. Comp. Chem.* (in press 2012): "Structural Models and Molecular Thermodynamics of Hydration of Ions and Small Molecules"
- [3] <http://www.cpmid.org/>
- [4] S. Grimme, *Comput. Mol. Sci.* **1**, 211 (2011): "Density functional theory with London dispersion corrections",
- [5] F. L. Hirshfeld, *Theoret. Chim. Acta* **44**, 129 (1977): "Bonded-atom fragments for describing molecular charge densities"
- [6] U. C. Singh and P. A. Kollman, *J. Comput. Chem.* **5**, 129 (1984): "An approach to computing electrostatic charges for molecules"
- [7] www.loni.org/: Louisiana Optical Network Initiative
- [8] M. Valiev, E.J. Bylaska, N. Govind, K. Kowalski, T.P. Straatsma, H.J.J. van Dam, D. Wang, J. Nieplocha, E. Apra, T.L. Windus, W.A. de Jong, *Comput. Phys. Commun.* **181**, 1477 (2010): "NWChem: a comprehensive and scalable open-source solution for large scale molecular simulations"
- [9] R. F. W. Bader, *Atoms in Molecules- A Quantum Theory*, Oxford University Press, Oxford, 1990.

Dynamical Cluster Approximation – Typical Medium Theory Approach to Disordered System

C. E. Ekuma^{1,2}, Z. Y. Meng^{1,2}, H. Terletska^{1,4}, J. Moreno^{1,2}, M. Jarrell^{1,2}, and V. Dobrosavljević³

¹Center for Computation & Technology, Louisiana State University, Baton Rouge, LA 70803, USA

²Department of Physics & Astronomy, Louisiana State University, Baton Rouge, LA 70803, USA

³Department of Physics, Florida State University, Tallahassee, FL 32301, USA

⁴Brookhaven National Laboratory, Upton, New York 11973, USA

Abstract: Mean field theories like the coherent potential approximation (CPA) and its cluster extensions, including the dynamical cluster approximation (DCA), fail to describe the Anderson localization transition in disordered systems. This failure is intrinsic to these theories as the algebraically averaged quantities used in these theories always favor the metallic state, and hence cannot describe the localization transition. Here we extend the Typical Medium Theory (TMT), which replaces the average quantities with their corresponding typical (geometrically averaged) equivalents, to its cluster form such that non-local correlations can be incorporated systematically. Our DCA-TMT method, identifies the hybridization function ($\Gamma(\omega)$) as the order parameter for the metal-insulator-transition (MIT). Such an approach opens a new avenue to study localization effect both in model and in real materials.

Keywords: Disorder, Anderson Localization, MIT, DCA, CPA, Mean-field, TMT, DCA-TMT

1. Introduction

Over the past several decades, disorder-driven (Anderson) localization has been a subject of intensive theoretical, numerical, and experimental studies [1-5]. Quite generally, the study of disordered systems relies on the use of probability distribution functions (PDFs) to measure ‘random’ quantities of interest. The most significant quantity of interest in physical or statistical problems is usually the “typical” value of the ‘random’ variable which is the most probable value of the PDF [6]. In most physical systems of interest, the nature of the PDF is not known a priori; as such, limited information via the moments or cumulants is available. Unlike some systems where the first moment (the *arithmetic* average) is a good estimate of the random variable, the Anderson localization is not self-averaging, i.e., the electronic quantities fluctuate strongly and the corresponding PDF is so broad with long tails that infinitely many moments are needed to describe it [7]. In most cases, the corresponding moments might not even exist near the critical point [8]. The non-critical nature at the Anderson transition of the arithmetic average of random one-particle quantities masks the detection of the Anderson transition. This is the reason that most of the mean field theories like the coherent potential approximation [9], which is built upon the arithmetically averaged quantities, i.e. averaged local density of states (LDOS), fail to provide a proper order parameter to capture the Anderson localization transition.

In contrast to the arithmetic average, the *geometrical* (typical) mean [3,7,10], gives a better approximation of the most probable value of the local density of states (LDOS). In Ref. [3], Dobrosavljevic et al. proposed and

demonstrated that the typical density of states vanishes continuously as the disorder strength increases towards the localization critical point, and as such, it can be used as an order parameter for detecting the Anderson transition. In the original seminal paper of Anderson [1], the Anderson transition is defined as the absence of diffusion. In this work, we extend the typical medium theory [3] to its cluster version such that the non-local correlation effects can be included systematically. We propose a natural order parameter within the DCA-TMT framework which is the hybridization rate ($\Gamma(K, \omega)$) between the cluster and the typical medium. Γ measures the hopping amplitude (diffusion) of electron on site say i (in the cluster) with the typical medium (host) (c.f. Fig. 1). As a natural consequence, the point where this quantity vanishes corresponds to the absence of diffusion and as such, it detects the Anderson MIT.

In this work, we apply the DCA-TMT approach to the non-interacting Anderson model in one and two dimensions. We identify the hybridization rate as a natural order parameter for the Anderson transition. The rest of the paper is organized as follows: After this introduction in Section 1, the computational method used is given in Section 2. The results are given and discussed in Section 3. We will conclude in Section 4.

2. Theory and Computational Method

We consider a non-interacting Anderson model: $\hat{H} = -t \sum_{\langle i, j \rangle} |i\rangle \langle j| + \sum_i |i\rangle \varepsilon_i \langle i|$, where $|i\rangle$ is the ket for the Wannier orbital at position i on the lattice and $\langle i, j \rangle$ indicates that the sum is over the nearest-neighbor sites. The hopping matrix element, t is taken to be $4t = I$. This sets the energy scale. The site energies ε_i are taken from a uniform distribution (in $V_i = \pm V$) of independent quenched random numbers distributed according to some specified probability distribution $P(\varepsilon_i) = \frac{1}{2V} \Theta(V - |\varepsilon_i|)$, where V is the strength of the disorder, and Θ is a step function. The DCA-TMT involves the mapping of the (periodic) lattice with disorder, and in the thermodynamic limit, to a self-consistently embedded finite-sized cluster problem (an effective (typical) medium). The short length scale physics inside the cluster is treated explicitly via enumeration or sampling, and the long length scale physics is treated within mean-field (c.f. Fig. 1). For cluster size $N_c = 1$, the DCA-TMT is the same as the CPA and for $N_c = \infty$, the method becomes exact.

The DCA-TMT self-consistent loop combines the framework of the DCA self-consistent algorithm [4,5] and the average scheme of the single site TMT approach [3]. We will now describe it in detail. In the common mean field theories such as the CPA [9], the LDOS within a cluster is defined as $\rho^c(K, \omega) = -1/\pi \text{Im} G^c(K, \omega)$. However, given an effective medium within the DCA-TMT, the typical density of states (TDOS) is calculated as $\rho_{typ}^c(K, \omega) = \exp\left(\left\langle \ln(\rho(K, \omega)) \right\rangle_{dis_aver}\right)$. To obey causality of the Green function, we then perform the Hilbert transformation to obtain the typical Green function within the cluster $G_{typ}^c(K, \omega) = \int_{-\infty}^{+\infty} d\omega' \rho_{typ}^c(K, \omega') / (\omega - \omega')$ that will be used to continue the self-consistent loop. The DCA-TMT iteration procedure is the following: (1) The self-consistent iteration starts by proposing an initial impurity-averaged cluster self-energy (usually the bare one)

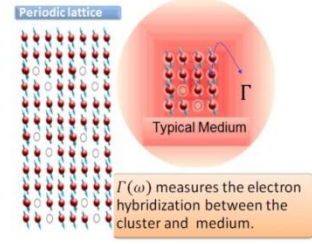


Fig. 1. Mapping of the periodic lattice problem (Left) into a cluster embedded in an effective typical medium (Right).

as $\Sigma_{\text{typ}}^c(K, \omega) = \bar{\Sigma}_{\text{typ}}(K, \omega) = N_c / N \sum_{\tilde{k}} \Sigma_{\text{typ}}(K + \tilde{k}, \omega)$, where \tilde{k} summation runs over N/N_c momenta of the cell about the cluster momentum \mathbf{K} . (2) This is used to calculate the coarse-grained Cluster Green function $\bar{G}_{\text{typ}}(K, \omega) = \frac{N_c}{N} \sum_{\tilde{k}} \frac{1}{\omega + \mu - \epsilon_{K+\tilde{k}} - \Sigma_{\text{typ}}^c(K, \omega)}$. (3) The cluster problem is now set-up by calculating the cluster-excluded Green function $G^{-1}(K, \omega) = \bar{G}_{\text{typ}}^{-1}(K, \omega) + \Sigma_{\text{typ}}^c(K, \omega)$ (Dyson's equation). This "cluster exclusion" procedure is to avoid over-counting of the contribution of the self-energy from interactions on the sites belonging to the cluster [5]. As explained in Ref. [5], this step determines the self-consistent embedding of the cluster. $G(K, \omega)$ is then Fourier transformed to its real space cluster representation $G_{n,m} = \sum_K G(K) \exp iK \cdot (r_n - r_m)$. (4) The cluster problem is solved using (Quantum) Monte-Carlo simulations to calculate a fully dressed cluster Green functions $G_{\text{typ}}^c(K, \omega)$. A new self-energy $\Sigma_{\text{typ}}^c(K, \omega) = G^{-1}(K, \omega) - (G_{\text{typ}}^c(K, \omega))^{-1}$ is then calculated using $G_{\text{typ}}^c(K, \omega)$. (5) The iteration is continued until convergence where $\bar{G}_{\text{typ}}(K, \omega) = G_{\text{typ}}^c(K, \omega)$ within the desired accuracy. Within the self-consistency loop, the hybridization rate $\Gamma(K, \omega)$ between the cluster and its host is calculated using $\Gamma(K, \omega) = \text{Im}(\bar{G}^{-1}(K, \omega) + \bar{\Sigma}(K, \omega))$.

3. Results and Discussions

Figure 2 shows the hybridization rate (function) $\Gamma(K, \omega)$ at the band center ($\omega = 0$) as a function of the disorder strength for 1D (c.f. Fig. 2c) and 2D (c.f. Fig. 2d) non-interacting Anderson model with uniform disorder. Here one can clearly see the superiority of the DCA-TMT over the DCA. Even though the DCA self-consistently takes

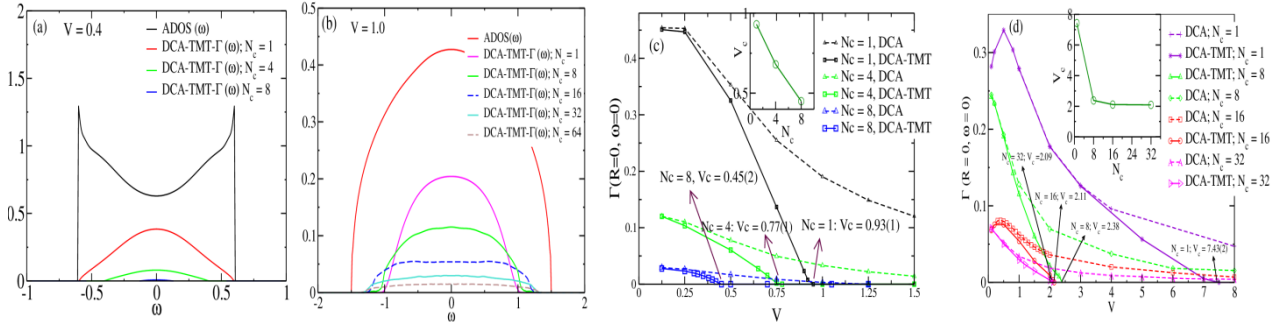


Fig.2. (a) The average DOS (ADOS) and hybridization rate $\Gamma(K, \omega)$ as a function of ω for 1D. (b) The average DOS and hybridization rate $\Gamma(K, \omega)$ as a function of ω for 2D. In both Fig. 2 (a) and (b), the ADOS integrates to one while $\Gamma(K, \omega)$ for a given disorder strength, decreases as the cluster size is increased. (c) The hybridization function, $\Gamma(\omega)$, at the band center as a function of the disorder strength V for 1D. (d) The hybridization function, $\Gamma(\omega)$, at the band center as a function of the disorder strength V for 2D. The insets in Fig. 2 c and d show the scaling of V_c with N_c . All the plots are for uniform disorder. The hybridization rate, $\Gamma(K, \omega)$, is the order parameter for the localization transition. It goes to zero at the critical disorder strength V_c . Above V_c , electrons become localized within the length scale of the cluster.

into account the short range non-local (spatial) correlations that are neglected in the local CPA, it cannot describe Anderson localization due to the fact that the LDOS is obtained via arithmetic averaging. Hence in both 1D and 2D, for all disorder strengths we have considered, the DCA hybridization functions remain finite even for very strong disorder strength V . On the other hand, $\Gamma(K, \omega)$ calculated from the DCA-TMT approach has critical disorder strength for each cluster size. Moreover, as the cluster size is systematically increased, the critical disorder strength V_c gradually decreases. In 1D, V_c decreases algebraically to zero as a function of cluster size (c.f. inset of Fig. 2c), and in 2D, V_c approaches zero logarithmically with cluster size (c.f. inset of Fig. 2d). The systematic approach of $\Gamma(K, \omega)$ to the critical point while the ADOS remains finite (always integrated to one) is shown in Fig. 2 a and b. For the 1D case, for disorder strength of 0.4, and cluster size of 8, $\Gamma(K, \omega)$ can already be seen to be practically zero. The same trend can be seen for 2D (c.f. Fig. 2b) where for disorder strength of 1.0, $\Gamma(K, \omega)$ approaches zero systematic as the cluster size is increased.

4. Conclusion

The DCA-TMT approach developed in this work is a self-consistent non-local correction to the local TMT for studying Anderson localization. It takes the hybridization function as the order parameter for identifying the localization transition. It is self-consistent hence; it provides a proper mean field description of Anderson localization. This particular study opens a new paradigm in the realization of *ab-initio study of localization* in real materials, and also provides a controlled method to study the interplay of disorder and the electronic correlations in strongly correlated systems. As for future investigations, we would first incorporate the interaction driven (Mott) effects into the present disorder driven (Anderson) localization. Then, we would combine the DCA-TMT with ab-initio computations (e.g., density functional theory (DFT) [11], such that we will be able to look at localization edge in real materials.

5. Acknowledgement

This work was supported by the National Science Foundation (NSF) [Award No. LA-SiGMA EPS-1003897, DMR-1005751], Department of Energy, DOE-CMCS N.

6. Reference

- [1] P. W. Anderson, Phys. Rev. **109**, 1492 (1958).
- [2] P. A. Lee et al., Rev. Mod. Phys. **57**, 287 (1985); B. Kramer et al., Rep. Prog. Phys. **56**, 1469 (1993); D. Belitz et al., Rev. Mod. Phys. **66**, 261 (1994); K. Slevin et al., Phys. Rev. Lett. **82**, 382 (1999); G. Schubert et al., Phys. Rev. B **81**, 155106 (2010).
- [3] V. Dobrosavljevic, et al., Europhys. Lett. **62** 76 (2003).
- [4] M. Jarrell and H. R. Krishnamurthy. Phys. Rev. B **63**, 125102 (2001).
- [5] M. H. Hettler et al., Phys. Rev. B **61**, 12739 (2000).
- [6] The most probable value of a random quantity is the mode, which is the value for which its PDF becomes maximal.
- [7] M. Janssen, Phys. Rep. **295**, 1 (1998); A. D. Mirlin and Y. V. Fyodorov, Phys. Rev. Lett. **72**, 526 (1994).
- [8] K. Byczuk, W. Hofstetter, and D. Vollhardt Phys. Rev. Lett. **94**, 056404 (2005).
- [9] R.J. Elliot, et al., Rev. Mod. Phys. **46**, 465 (1974); P. Soven, Phys. Rev. **156**, 809 (1967).
- [10] *Log-Normal Distribution—Theory and Applications*, edited by E. L. Crow and K. Shimizu (Marcel Dekker, Inc., New York, 1988).
- [11] P. Hohenberg and W. Kohn, Phys. Rev **136**, B 864, (1964); W. Kohn, Rev. Mod. Phys. **71**, 1253, (1999).

Effect of Dopants in Dehydrogenation of NaMgH₃ Core-Shell Nanoclusters

Fernando Soto¹, Daniela S. Mainardi^{1,2}

¹Institute for Manufacturing, Louisiana Tech University

²Institute for Manufacturing and Chemical Engineering, Louisiana Tech University

Abstract: NaMgH₃ is an attractive hydrogen storage material due to its 6 wt % hydrogen capacity and its hydrogenation/dehydrogenation reversibility. However, more fundamental understanding of the role of dopants in this hydride system is needed. Previous results show that clusters of hydrogen storage materials have a much lower desorption energy than their bulk counterparts; hence, they enable hydrogen desorption at lower temperatures. In this paper, 3d transition-metal doped NaMgH₃ nanoclusters with core-shell features are investigated using density functional theory to explore their cohesive energy and hydrogen desorption energy. These calculations provide a general trend for nanostructured manipulation of hydride systems geared towards reduction of current high-temperature hydrogen desorption barrier.

Keywords: hydrogen economy, hydrogen storage, DFT, nanoclusters, NaMgH₃

1. Introduction

Solid state hydrogen storage in the form of complex metal hydrides is considered in this study, due to their high gravimetric and volumetric hydrogen densities.¹ The attainment of high gravimetric hydrogen densities using solid state storage materials is favorable to compounds containing lightweight elements.² Magnesium is an abundant and inexpensive metal that can store up to 7.7 wt% hydrogen in its hydride form.³ However, its high thermodynamic stability and low de/hydrogenation rates deters the application of MgH₂ as a hydrogen storage medium.⁴ Recent research has been devoted to studying the stability of MgH₂ by reducing the size of the material via mechanical ball milling, quantum chemical studies and by alloying with early transition metals.^{5,6,3}

Perovskite structures such as NaMgH₃ may enhance kinetics and reversibility and inhibit toxic gas side products compared to the parents' borohydride, amide, and alanate compounds. Also, higher H mobility in this material due to their perovskite structure cause improved hydrogenation rates than the pure MgH₂.⁷ In this paper, a rational basis for NaMgH₃ nanoclusters is being developed through the systematic understanding of how nanostructuring and catalysts improve hydrogen storage properties for onboard mobile applications.

2. Methodology

All simulations conducted on these models were performed using Density for Molecules (Dmol₃), a numerical basis set-density functional theory (DFT) method available in the software package, Materials Studio 4.4 from Accelrys.⁸ The main setup parameters are given in Table 1. Zero-point energy (ZPE) corrections were not considered for this paper.

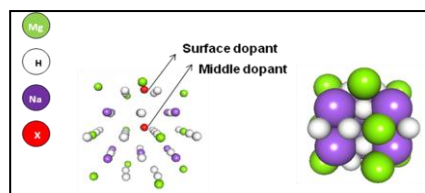
Table 1. Setup Parameters for Dmol₃ Calculation

Basis Set	DNP
Functional	GGA/PBE
Core-Treatment	DFT-Semicore Pseudopots
SCF Convergence	10⁻⁶
K-pt Set	Fine
Real Space Cutoff (Å)	4.4
Spin-Polarization	Restricted

2.1 Nanocluster Calculations

DFT calculations have been performed on pristine NaMgH₃ nanoclusters and on 3*d*-transition metal doped clusters with core/shell features. The pristine nanocluster was constructed from the NaMgH₃ unit cell⁹ with a radius of 5 Å for a total of 50 atoms. The core/shell features are explored to determine the optimal configuration that lowers hydrogen desorption energy. In the alloyed structures, all atoms of the 3*d* element block are placed at the bulk site with combinations of Ti, V, and Cr placed at a Na-substituted site (Figure 1).

Figure 1. Nanocluster Model, where x is a 3*d* Transition Metal Dopant and right figure is a CPK model of a 5 Å radius NaMgH₃-nanocluster



Cohesive energy (CE) and Hydrogen Desorption (HD) energy are calculated according to the following equations:

$$E_{CE} = E_{\text{total system}} - \sum E_{\text{free neutral atoms}} \quad (\text{Eq. 1})$$

$$E_{HD} = E(\text{Na}_{10}\text{Mg}_{10}\text{X}_2) + 15E(\text{H}_2) - E(\text{Na}_{10}\text{Mg}_{10}\text{X}_2\text{H}_{30}) \quad (\text{Eq. 2})$$

where X represents the 3*d* transition metal dopant. Also, CE is calculated relative to the pristine system.

3. Results and Discussions

The results for CE and HD are shown in Tables 2 and 3 respectively. With these results, we propose to form a design map that allows us to predict trends and binary combination of elements that result in lower

hydrogen desorption energies. As shown in Table 2, all values are negatives in relation to the pristine structure.

This indicates that the 3*d*-transition metal elements doped-nanoclusters are not stable in relation to the pristine structure. The results also show the relationship between CE and HD through a statistical correlation analysis, which showed a positive correlation of more than $r > 0.8$, indicating that CE is a factor that can predict HD energies in the nanocluster systems. This is in accordance with the findings reported by Wang et al. indicating that the CE is more important than the formation enthalpy for predicting dehydrogenation temperatures of complex metal hydrides¹⁰. In parallel, as shown in Table 3, HD energy in nanoclusters is lower than in the bulk models. This is in accordance with what had already been affirmed by Larsson et al.³ Similarly, choosing a more efficient catalyst for hydrogen storage materials is extremely important to improve thermodynamic and kinetic properties. In this sense, V is the most favorable element when doped at the surface Na site. HD energy values reach oscillates between 47 and 49 kJ mol⁻¹ H₂. These values are considerably lower than the values reported for MgH₂³. Vanadium is an early transition metal that bonds with Mg and H atoms due to the interaction of 3*d* states and H 1*s*-electrons. Of course, these structures must be studied to obtain detailed information on how to manipulate core/ shell nanoclusters. Despite this, these results provide information on the synergistic effects¹¹ that the 3*d* transition metals show in NaMgH₃ nanoclusters. As a future work, we intend to use a hybrid method of QM/MM which allows us to use larger size nanoclusters, while force fields such as ReaxFF will allow a more detailed study of chemical reactions that take place at the atomistic level. Similarly, future work includes studying the effects of graphene as a substrate which can break the links between Na and (MgHx) that exist in NaMgH₃ nanoclusters.

Table 2. Relative Cohesive Energy

		Relative Cohesive Energy (eV)			
		Surface Atoms			
Relative Cohesive Energy (eV)	Core Atoms	Elements	Ti	V	Cr
		Sc	-8.12	-7.38	-7.71
		Ti	0	-7.02	-7.35
		V	-8.09	0	-6.94
		Mn	-8.11	-6.15	-5.97
		Cu	-8.07	-5.64	-9.69
		Fe	-8.1	-5.08	-5.41
		Ni	-8.08	-4.47	-9.69
		Co	-8.09	-9.36	-4.8
		Cr	-8.08	-9.36	0
		Zn	-8.19	-9.36	-9.69

Table 3. Dehydrogenation Energy

		Dehydrogenation Energy (KJ mol/H ₂)			
		Surface Atoms			
Dehydrogenation Energy (KJ mol/H ₂)	Core Atoms	Elements	Ti	V	Cr
		Sc	-52.24	-50.23	-50.58
		Ti	0	-47.08	-50.76
		V	-51.54	0	-48.31
		Mn	-53.77	-54.09	-51.81
		Cu	-67.92	-49.36	-53.28
		Fe	-55.68	-53.21	-52.51
		Ni	-55.94	-54.09	-54.26
		Co	-55.89	-51.63	-66.16
		Cr	-55.88	-63.71	0
		Zn	-71.85	-67.73	-70.54

It is demonstrated that the cohesive energy of a complex metal hydride is a key predictor in determining the dehydrogenation energy of the nanocluster. Thus, a decrease in the energy required to break the atoms leads to a reduction in the dehydrogenation energy of the nanocluster. This is enhanced with the binary combination of Ti and V as the core/shell co-dopants, respectively. This superior synergism exhibited by the co-dopants can be explained by the superior electron sharing ability of *d*-electrons in Ti and the fact that early transition metals such as V suffer little loss of cohesive energy due to their 3*d* states interaction with 1*s*-state of hydrogen. These

findings provide invaluable information about the possible overall trends 3d-transition metals exhibit in NaMgH₃ nanoclusters.

4. Acknowledgments

This material is based upon work supported by the National Science Foundation under the NSF EPSCoR Cooperative Agreement No. EPS-1003897 with additional support from the Louisiana Board of Regents.

5. References

- [1] Alapati, S. V.; Johnson, K. J.; Scholl, D. S.; "Identification of Destabilized Metal Hydrides for Hydrogen Storage Using First Principles Calculations." *J. Phys. Chem. B.* 2006. 110. 8769-8776.
- [2] Choudhury, P.; Bhetanabotla, V.R.; Stefanakos, E.; "Manganese Borohydride as a Hydrogen –Storage Candidate: First-Principles Crystal Structure and Thermodynamic Properties." *J. Phys. Chem. C.* 2009. 113. 13416-13424.
- [3] Larsson, P.; Moyses Araujo, C.; Larsson, J.A.; Jena, P.; Ahuja, R.; "Role of Catalysts in dehydrogenation of MgH₂ Nanoclusters." *PNAS.* 2008.105. 8227-8231.
- [4] Hanada, N.; Ichikawa, T. ; Fujii, H.; " Catalytic Effect of Nanoparticle 3d- Transition Metals on Hydrogen Storage Properties in Magnesium Hydride MgH₂ Prepared by Mechanical Milling." *J. Phys. Chem. B.* 2005. 109. 7188-7194.
- [5] Choi, Y.J.; Lu. J.; Sohn, H.Y.; Fang, Z.Z.; R. E.; " Effect of Milling Parameters on the Dehydrogenation Properties of the Mg-Ti-H System." *J. Phys. Chem. C.* 2009. 113. 19344-19350.
- [6] Wagemans, R.W.P.; Van Lenthe, J.H.; de Jongh, P.E.; Jos van Dillen, A.; de Jong K.P.; "Hydrogen Storage in Magnesium Clusters: Quantum Chemical Study." *J. Am. Chem. Soc.* 2005. 127. 16675-16680.
- [7] Wu, H; Zhou, W.; Udovic, T.J.; Rush, J.J.;Yildirim, T.; " Crystal Chemistry of Perovskite-Type Hydride NaMgH₃ : Implications for Hydrogen Storage." *Chem. Mater.* 2008. 20. 2335-2342.
- [8] Accelrys. Materials Studio, version 4.0; Accelrys Software, Inc.: San Diego, CA, 2006.
- [9] Bouhadda, Y.; Boudouma, Y.; Fennineche, N.; Bentabet, A.; "Ab initio calculations study of the electronic,optical and thermodynamic properties of NaMgH₃, for hydrogen storage"; *J. of Physics and Chemistry of Solids.* 2010. 71. 1264-1268.
- [10] Wang, Y.; Liu, S.;Rong,L.;Wang,Y.; "A first principles study of the thermal stability of A_m(MH₄)_n light complex hydrides"; *J. Phys.:Condens. Matter.* 2010. 22. 1-7.
- [11] Wang, J.; Ebner, A.D., Zidan, R.; Ritter, J.A.; " Synergistic effects of co-dopants on the dehydrogenation kinetics of sodium aluminum hydride"; *J. of Alloys. Compd.* 2005. 391. 245-255.

Efficient Hydrogen Saturation and Transfer Rate Simulation in Metallic Rods

Weizhong Dai^{1,2}, Fei Han², David Howe

¹College of Engineering and Science, Louisiana Tech University

²Department of Mathematics, Louisiana Tech University

Abstract: Lanthanum Nickel (LaNi₅) has been shown to be an excellent candidate for efficient hydrogen storage and transportation. Experiments with these metallic rods have shown steady and contaminant-resistant absorption and desorption rates at relatively low temperatures (300-325K) [1]. Modeling of these and other rod's behavior in hydrogen rich environments over any significant time period or accuracy range have taken enormous computing power and wall-time, limiting the number of simulations for possible modifications to the LaNi₅ composition and other alloy testing. A parallel programming approach was used to drastically reduce the time necessary to model the hydrogen saturation at different radial distances from the edge of a LaNi₅ rod, as well as the absorption rates at the same points. Fortran 90 programming is being used in conjunction with MPI conventions on the LONI computer cluster to reduce the computing time from 32 hours to ~2 hours.

Keywords: Desorption, Lanthanum Nickel, Hydrogen Saturation, MPI, LONI

1. Introduction:

Hydrogen power was once heralded as the next generation in power production and liberator of nations from foreign fuel sources, but the fruition of such promises has been slow-coming in the past decade. Thus far, net energy production from hydrogen sources do not account for the amount of energy necessary to produce and transport the hydrogen itself, and therefore such generators are currently used only in large industrial and corporate situations, namely as reliable backup generators [2]. Cost-efficiency is also another necessary consideration that still has not met target ranges, both in storage options and within generators themselves. Four options present themselves for transportation of raw hydrogen, namely its gaseous and non-compressed form, liquid phase, compressed gas, and metallic hydride storage. Taking hydrogen in its gaseous form at atmospheric pressure presents multiple problems, from unreasonably large and costly tanks to high Hindenberg-type safety issues. Pressurizing the gas means very costly thick tanks and still presents safety issues. Liquefying hydrogen

and keeping it in this state during transport is extremely costly and reduces energy efficiency of production, as well as limiting the temperature range of generators. Metallic hydrides present a feasibly viable option for transport if low-cost metal alloys can be found and release rates can be effectively predicted. It is the purpose of this study to effectively map the density of hydrogen in these metallic rods and used such information to predict desorption rates at given initial temperatures. Our current serial code takes approximately 32 hours to run through its 10,800,000 time-steps to model three hours' worth of hydrogen absorption from a metallic rod. Distributing this process with MPI parallel programming would allow for tests of multiple hydrides and longer periods with less computational cost. Complexity arises in this approach through managing communication between processors and ensuring that the correct information is supplied to all processors in order to run calculations and then collected in meaningful configurations, which further must be optimized to ensure that this communication time does not negate the efficiency gained from distributing the calculations.

2. Procedure:

Extensive knowledge of Fortran 90, especially of the array features, was first necessary in order to begin writing basic functions to be integrated into the programming scheme. Basic Laplacian matrix programs using 60 by 60 meshes utilizing Jacobian iteration techniques were first formulated. Such a method's main computations took place in utilizing two DO-loops going from the 1st to 59th grid point (ie. the interior points of the matrix) and forming an two-dimensional array derived from ¼ of the summation of its surrounding points. The serial program consisted of 62 lines of code and was easily modified for larger meshes. Termination of this program relied on the difference between subsequent values at a specified grid point; if the difference between a value of the matrix between timestep n and $n+1$ fell underneath a specified tolerance, the program was terminated. Parallelizing this program utilized the MPI_REDUCE and MPI_BCAST functions in order to consolidate this difference information and ensure that the maximum difference in subsequent time-step values was measured against the set tolerance. Results of said programs (see section 3) suggest that similar techniques when applied to larger and more computationally varied situations could greatly reduce walltime needed for calculation of a hydrogen storage scheme. Such a program was developed that took the initial specific heat of both hydrogen and the metallic rod, their thermal conductivities, epsilon porosity, heat of formation for the reaction, permeability of the porous rod, dynamic viscosity of the hydrogen, and respective initial densities and temperatures and used said information and Jacobian iteration techniques it model the saturation of hydrogen at different column mesh points corresponding to radial distances from the edge of the rod. To split array computations between processors, two separate numerical schemes were developed to account for computations including and excluding the boundary points, respectively. For calculations involving boundary points, the columns were broken up in the following manner: $DO j = myid*(Nz/nprocs)+1, (myid+1)(Nz/nprocs)$

Where $nprocs$ is equivalent to the number of processors being utilized and $myid$ gives each processor a rank from zero to $nprocs-1$. Inspection confirms that this scheme successfully iterates all points between $j=1$ and Nz . In such a scheme each processor was responsible for calculating all of the rows for the columns it was assigned. For interior point calculations, such a basic scheme was not possible to include all mesh points between $j=2$ and $Nz-1$, so an IF-THEN-ELSE structure was used:

```

if (myid .eq. 0) then j=2,Nz/nprocs
else if (myid .eq. nprocs-1) then do j=(Nz/nprocs)*(nprocs-1)+1,Nz-1
else do j=myid*(Nz/nprocs)+1,(myid+1)*(Nz/nprocs)
    
```

By isolating both the first and last processors, which each are assigned one less computation than the other processors, the other processors could use the same scheme as before. The final mesh was 40 by 40, yet was programmed in such a way as to allow for differing lengths and widths of the rod. Our tested model had a rod length of .05 meters and a diameter of .03 meters. After such modifications and MPI communication devices were added to the program, the program totaled 2419 lines.

3. Results and Discussion

For our original test Laplacian 60 by 60 matrix the tolerance was set to 1E-5, which ran through 9042 iterations before terminating after .4 seconds. The parallel version of this test program, again set to a tolerance of 1E-5, completed in .0735 seconds, yielding a 544% speed increase. Buoyed by such results, comparable time increases were sought in measuring the effectiveness of Lanthanum Nickel as a viable hydrogen storage option. The serial version the developed code ran for upwards of 32 hours and stored data on the density of hydrogen in the rod, desorption rates, hydrogen pressure, velocity of the hydrogen, and temperature of the solid at ten minute intervals.

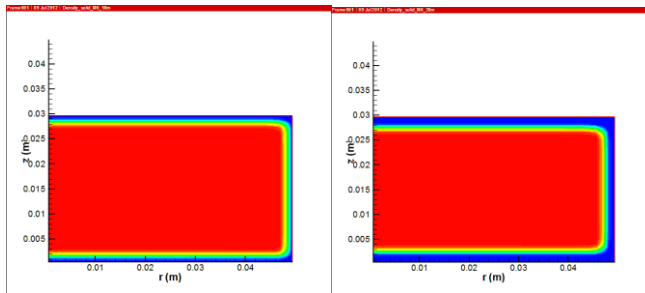


Fig.1

Density of Hydrogen (kg/m^3) at 10 and 20 minutes, respectively. Red corresponds to high concentrations of hydrogen, blue to low. Ranged between zero and 360 kg/m^3 . X and Y axes map the z and r components, respectively.

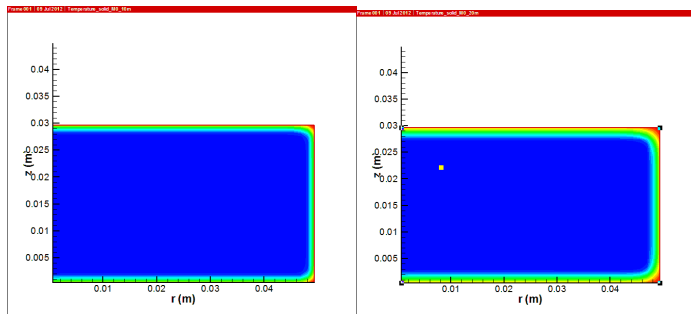


Fig. 2

Temperature (K) of Rod at 10 and 20 minutes, respectively. Red corresponds to high temperature, blue to low. Ranged between 297 and 317 K. X and Y axes map the z and r coordinates, respectively.

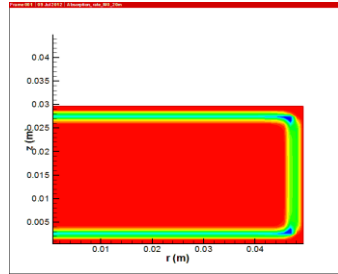


Fig. 3

Desorption of hydrogen (kg/sec). Maximum desorption at .206 kg/s. X and Y axes mark height and radius components, respectively.

Because of the consistently low temperatures within the rod at high hydrogen concentrations, Lanthanum Nickel is modeled to be much safer than other means of hydrogen transport. At a maximum concentration of 360 kg/m^3 , hydrogen packed within LaNi_5 is at the upper range of hydrogen saturation among other meta I hydrides [3]. Low surface desorption results in highly controllable reactions, though tests are still being done at higher initial temperatures to ensure this phenomenon is consistent. Though data has not yet been produced from a parallelized version of this code, this week will mark first tests of MPI implementations.

4. Conclusion

Lanthanum Nickel appears to be in the top range of candidates for hydrogen storage in metal hydrides. If MPI implementations can be successfully run on the LONI supercomputer cluster, this program could be used to model both different initial conditions and longer time periods for LaNi_5 but also can be used to get precise measurements for other metal hydrides without high computational costs. This technology will be beneficial in predicting which metals can reach standards of concentration of hydrogen per weight of rod to allow for cost-effective storage and transport of hydrogen.

5. Acknowledgements

The current work is funded by the NSF EPSCoR LA-SiGMA project under award #EPS-1003897.

6. References

- [1] Flanagan, T.B. and S. Tanaka. "Hydrogen storage by LaNi_5 - Fundamentals and applications"
<http://adsabs.harvard.edu/abs/1977empe.symp..470F>. Accessed July 8, 2012.
- [2] http://batteryuniversity.com/learn/article/fuel_cell_technology. Accessed July 9, 2012.
- [3] Ragheb, M. "Hydrides Alloys for Hydrogen Storage".
<https://netfiles.uiuc.edu/mragheb/www/NPRE%20498ES%20Energy%20Storage%20Systems/Metal%20Hydrides%20Alloys%20for%20Hydrogen%20Storage.pdf>. Accessed July 9, 2012.

Electrical Transport in a Magnetic Semiconductor Nanowire

D. J. Rebar¹, J. P. DeGrave², S. Jin², and J. F. DiTusa¹

¹Department of Physics and Astronomy, Louisiana State University

²Department of Chemistry, University of Wisconsin, Madison

Abstract: The transport properties of nanowires formed from the small band-gap insulator FeSi with cobalt dopants that produce metallic and magnetic behavior are explored at low temperatures to explore the role of finite size effects on this magnetic semiconductor. Preliminary measurements reveal strong effects of electron-electron interactions causing a power-law divergence of the resistivity below 5 K.

Keywords: Magnetic semiconductor, nanowire, electron-electron interaction effects

1. Introduction

Iron monosilicide is a small band-gap insulator that undergoes a metal-insulator transition with the partial substitution of cobalt for iron[1,2]. This cobalt substitution not only induces metallic behavior but also nucleates helimagnetism over most of the substitution series despite the fact that magnetism is not seen in either the insulating iron monosilicide or the semimetallic cobalt monosilicide parent compounds[1-3]. This helical phase is thought to stem from the non-centro-symmetric crystal structure (B20) that is typical of transition metal monosilicides and germanides where helical wavelengths can be as long as 90 nm. Our previous measurements on bulk crystals revealed a wide range of half metallic (spin-polarized electron gas) behavior below a doping-dependent Curie temperature that can be as high as 65 K[4,5]. We also showed that the low temperature electronic transport is dominated by electron-electron interactions similar to what observed in prototypical semiconductors, such as phosphorus doped silicon, when in proximity to an insulator-to-metal transition[4]. These disordered conductors are characterized by a highly diffusive electron transport and relatively poor electronic screening so that the Coulomb interactions between charge carriers is thought to create a square root singularity in the density of states at the Fermi energy[4,6]. Recently, interest in this material and several others having the B20 crystal structure has grown substantially as this material, $\text{Fe}_{1-x}\text{Co}_x\text{Si}$, was demonstrated to host a skyrmion lattice phase[7] over a thickness dependent range of field and temperature below its Curie point. This topologically interesting phase consists of tens of nanometer sized vortex like magnetic structures ordered into a hexagonal lattice.

The objective of this research is to probe electron transport in $\text{Fe}_{1-x}\text{Co}_x\text{Si}$ in a confined geometry such that transport is constrained to effectively one dimension with respect to inelastic processes. We hope to demonstrate that this constraint is realized in CVD-grown nanowires along with the expectation of long phase relaxation lengths typically found at temperatures below 1 K.

2. Experimental Details

Nanowires of $\text{Fe}_{1-x}\text{Co}_x\text{Si}$ were grown as described previously[8] and carefully deposited on a silicon wafer coated with its native oxide. Electron transport in these nanowires is to be characterized using four probe magnetoresistance measurements. To perform these measurements, various instruments in the CAMD cleanroom are utilized to pattern four electrical leads on single nanowires. The Mann 3600 Pattern Generator, 351 developer, and chrome etch are used to pattern a mask with an array of chip bonding pads and anti-static line elements. Silicon wafers are spin-coated with S1805 at the Headway Research PWM101 Light Duty Photoresist Spinner and aligned with the mask in the Quintel UL7000-OBS Aligner and DUV Exposure Station. After exposure, the wafers are developed with 351 developer, etched in the Bransen Plasma Asher, and metallized with the Temescal BJD-1800 E-Beam Deposition System. Wafers are divided into chips, and the Hitachi S-4500II Field Emission SEM with NPGS is used to pattern finer elements including nanowire leads on the chips using PMMA as a resist. After metallization, the chips are ready for wirebonding to cryostat pucks and four probe resistance measurement. Fig. 1 displays optical and electron beam microscopy images of one of our devices.

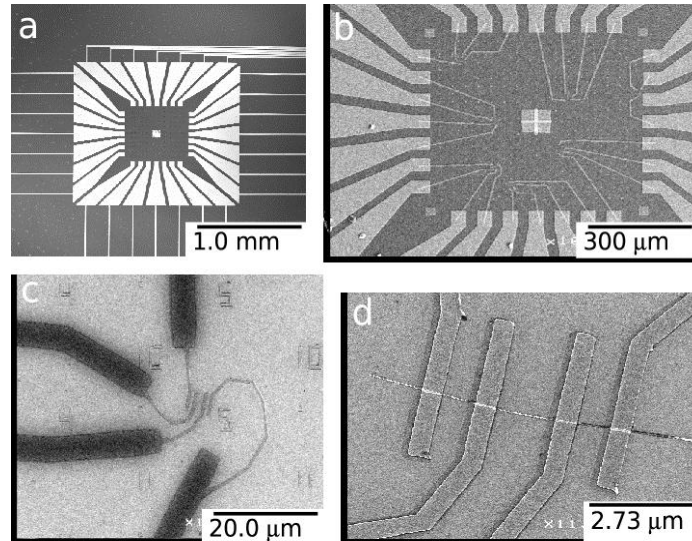


Figure 1: Lead arrangement for $\text{Fe}_{1-x}\text{Co}_x\text{Si}$ nanowire devices. Nanowires were located by optical microscopy and Cr/Au contacts were patterned by optical and electron beam lithographic techniques.

Low temperature measurements are performed on a Janis helium-3 cryostat equipped with a 5 T superconducting magnet. Measurements are performed with an ac excitation current of less than 10 nA to eliminate self heating effects at 300 mK.

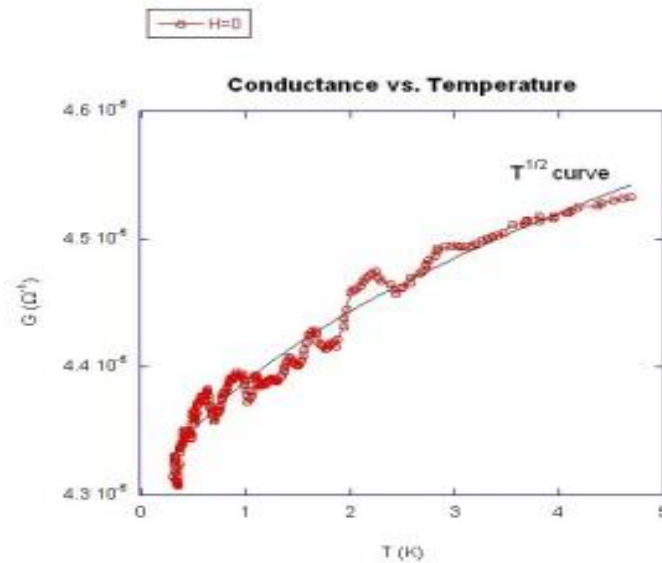


Figure 2: Conductance of a $Fe_{1-x}Co_xSi$ nanowire device at low temperature.

3. Preliminary Results

Preliminary measurements of the conductance of a two lead device is shown in Fig. 2. Here, the dominating effects of electron-electron interactions leads to a decreased conductance over the entire temperature range investigated as demonstrated by the square-root temperature dependence, solid line in the figure. Despite the large number of devices fabricated to date, a true four lead measurement has not been accomplished due to the low success rate for our electrical contacts.

4. Conclusions and Future Work

Thus far, we have demonstrated our ability to make high quality electrical contacts to the nanowires, albeit with a somewhat low success rate. We have also demonstrated that, just as in the bulk samples of this material, electron-electron interaction effects are responsible for creating a temperature dependent resistivity down to the lowest temperatures measured. In the future we plan to improve our technique for creating ohmic contacts to these nanowires to create four-terminal devices so that the magnetoresistance can be effectively characterized. Long term goals include the search for effects associated with the formation of a skyrmion lattice on the electrical transport properties of these devices.

5. Acknowledgments

This work is supported by the NSF EPSCoR Research Infrastructure Improvement (RII) Award # EPS-1003897 and the NSF through grant number DMR0804376 .

6. References

- [1] J. H. Wernick, G. K. Wertheim, and R. C. Sherwood *Mater. Res. Bull.* **7**, 1431-1441 (1972).
- [2] J. Beille, J. Voiron, and M. Roth, *Solid State Commun.* **47**, 399-402 (1983).
- [3] K. Ishimoto, M. Ohashi, H. Yamauchi, and Y. Yamaguchi, *J. Phys. Soc. Jpn.* **61**, 2503-2511 (1992).
- [4] N. Manyala, Y. Sidis, J. F. DiTusa, G. Aeppli, D. P. Young, and Z. Fisk, *Nature* **404**, 581-584 (2000).
- [5] N. Manyala, Y. Sidis, J. F. DiTusa, G. Aeppli, D. P. Young, and Z. Fisk, *Nature Materials* **3**, 255-262 (2004).
- [6] T. F. Rosenbaum, R. F. Milligan, M. A. Paalanen, G. A. Thomas, R. N. Bhatt, and W. Lin, *Phys. Rev. B* **27**, 7509-7523 (1983).
- [7] X. Z. Yu, Y. Onese, N. Kanazawa, J. H. Park, J. H. Han, Y. Matsui, N. Nagaosa, and Y. Tokura, *Nature* **465**, 901-904 (2010).
- [8] A. L. Schmidt, J. M. Higgins, and S. Jin, *Nano Letters* **8**, 810-815 (2008).

Electronic and Conductive Properties of Polythiophene Containing Cobaltabisdicarbollide Structures

Neelima Ranjitkar¹, Juana Moreno², Mark Jarrell², Pedro Derosa^{1,3}, B. R. Ramachandran⁴

¹Institute for Micromanufacturing, Louisiana Tech University

²Department of Physics and Astronomy and Center for Computation and Technology, Louisiana State University

³Department of Mathematics and Physics, Grambling State University

⁴Department of chemistry, Louisiana Tech University

Abstract: Magnetic, electrical, and electronic properties of organo metallic compounds consisting of carborane cages containing transition metal inserted in polythiophene chains were analyzed. The geometrical optimization of the compounds was conducted using Density Functional theory (DFT), and multiplicity was predicted using six different DFT functional including GGA, hybrid, and meta hybrid. Current versus voltage was calculated using Green's functions. Results were compared to available results on these systems with very good agreement.

Keywords: Carboranes, Organo metallic compounds, Transition metal, Functional, Basis set, Spin state, DFT

1. Introduction

Carborane is a closo boranes cage composed of boron and carbon atoms in which some boron atoms are replaced with carbon atoms[1]. Boron cages $C_2B_{10}H_{12}$ which are carboranes with two carbon atoms replacing two boron atoms, form an icosahedral structures and are stable[2]. A metal atom in the center between two of these cages is expected to highly affect the electronic and magnetic properties of the compound. Transition metal ions play a very significant role in the field of organometallic chemistry[3]. Highly stabilized transition metal derivatives of polyhedral borane anions, have unique applications like radio imaging agents. Computational methods like DFT can be used to compute and determine properties of such compounds [4]. DFT can be used to determine the electronic states of atoms, molecules, and materials in terms of the three dimensional electronic density of the system. Carboranes have unique properties, like electron withdrawing nature, as well as exceptional chemical, thermal, and optical stability[5]. Inserting these structures in polymer materials (such as poly-thiophenes), have shown to produce an improvement on their properties, this has been attributed to a more extended degree of conjugation than the parent oligothiophenes, these features indicate a significant electronic delocalization through the cobaltabisdicarbollide moiety[5]. The introduction of the ortho carborane in the monomer pattern yielded a more conjugated and more conducting material compared with those electrogenerated from the meta and para isomer, since ortho isomers are more stable than meta and para isomers[6].

Molecular orbital of the system containing one, two and three thiophene were calculated using B3LYP with LANL2DZ basis set and compared to the MO reported in reference[5] to ensure the geometries used in this work are consistent with those reported. A good agreement is observed (see Figure 2 in reference[5] and compare with the MOs presented in Figure 2 here).

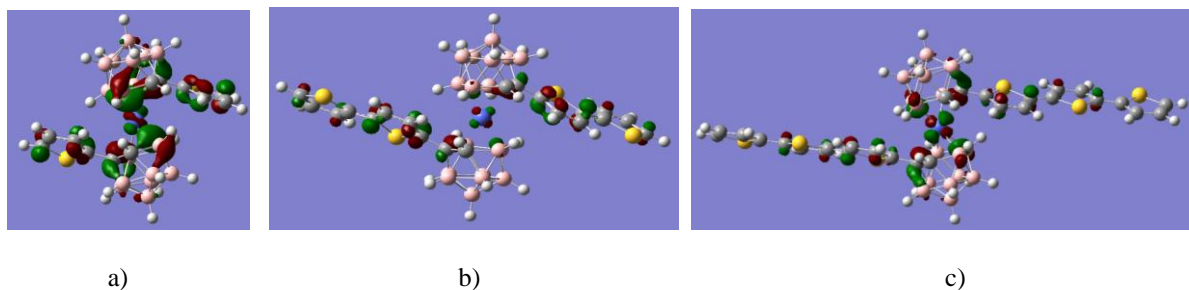


Figure 2: Molecular orbitals of cages with a)One, b) Two and c)Three thiophene monomers.

Figure 3 shows the current voltage throughout these systems, calculated for 1,2, and 3 thiophene oligomers (Figure 1). This was compared to published curves for equivalent systems[5]. There is also a very good agreement between the simulations and the experiment considering that the junction between the molecules and the contact (Au) is not known and probably would be different for every sample in the experimental study, so the main features are actually well captured by the calculations reported here.

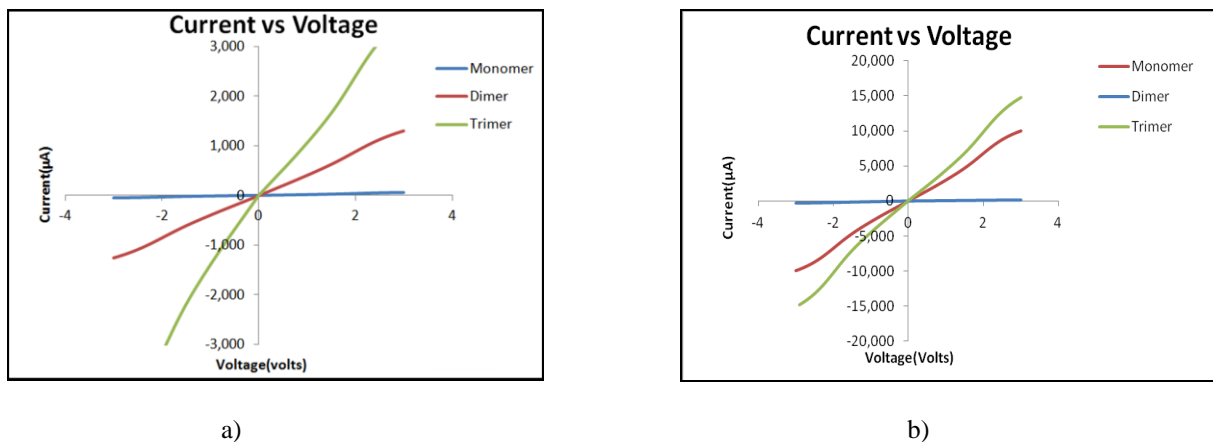


Figure 3: Current vs. Voltage curves for the structures described in Figure 1. a) Calculated with a DFT/Green functions model with Co b) Calculated with a DFT/Green functions model with Mn.

To show the effect of the metals, figure 3b shows the current vs. voltage when Mn is inserted between the two cages. These results are preliminary and under further study, but notice how conductivity significantly increases compared to the system with Co. The reason for which the dimer shows such a marginal conductivity are still under study, this may even be due to a problem in the way the contact with Au was setup. But the main conclusion, the different conductivity of the systems for different metal atoms is indeed relevant

4. Conclusion

Carborane cages as inserted in polythiophene chains were studied. Six different DFT functionals were used to study electronic, magnetic, and transport properties of a system with one, two, and three thiophene monomers. Results were compared to existing evidence with very good agreement. Predictions from all 6 functionals seem quite similar at least compared to available information. Current-voltages were calculated with a combined DFT/Green function model and predicted IV curves are also in good agreement with available information. Preliminary calculations with a second metal (Mn) show the effect of the central metal on the system properties. With the lessons learned from this study, the properties of similar systems but with Fe, Mn and Ti are currently under study.

5. Acknowledgments

The current work is funded by the NSF EPSCoR LA-SiGMA project under award #EPS-1003897. Computational resources from LONI are gratefully acknowledged.

6. References

- [1] Z. Z. Liang Deng, "A Journey from 12- Vertex to 14- Vertex Carboranes and to 15- Vertex Metallocarboranes," *American Chemical society*, vol. 26, pp. 1832-1845, 2007.
- [2] R. B. King, "Supraicosahedral polyhedra in carboranes and metallocarboranes; The role of local vertex environments in determining polyhedral topology," *Journal of organometallic chemistry*, vol. 692, p. 1773, 2006.
- [3] J. Koseki, *et al.*, "Quantum Monte Carlo study of porphyrin transition metal complexes," *The Journal of chemical physics*, vol. 129, p. 085103, 2008.
- [4] T. G. Williams and A. K. Wilson, "Importance of the quality of metal and ligand basis sets in transition metal species.," *The Journal of chemical physics*, vol. 129, p. 054108, 2008.
- [5] F. Bruno and E. Hao, "Polythiophenes Containing In Chain Cobaltabisdicarbollide," *ACS Appl. Mater. Interfaces*, vol. 2, pp. 691-702, 2010.
- [6] B. Fabre, *et al.*, "Electropolymerizable 2,2'-Carboranyldithiophenes. Structure-Property Investigations of the Corresponding Conducting Polymer Films by Electrochemistry, UV-Visible Spectroscopy and Conducting Probe Atomic Force Microscopy," *Macromolecules*, vol. 42, pp. 2981-2987, 2009.
- [7] J. M. Z. Seminario, A. G.; Tour, J. M., "Theoretical Interpretation of Conductivity Measurements of Thiitolane Sandwich. A Molecular Scale Electronic Controller.," *J. Am. Chem. Soc.*, vol. 120, pp. 3970-3974, 1998.

Everything You Always Wanted to Know about the van der Waals Interaction (But Were Afraid to Ask)

John P. Perdew¹, Adrienn Ruzsinszky¹, and Jianmin Tao¹

¹Department of Physics and Engineering Physics, Tulane University

Abstract: The van der Waals interaction is a long-ranged attraction between non-overlapped electron densities, typically expressed as an infinite series in inverse powers of the distance between them. It is important in physics, chemistry, and biology, where it can provide a weak binding between closed-shell objects such as typical molecules or nanostructures. Here we will describe the simple but realistic spherical-shell model for quasispherical objects (solid spheres for nanoclusters and even atoms, and hollow spheres for fullerenes), for which the van der Waals coefficients of all orders are determined analytically. We will apply this model to show that the van der Waals series may be summed to all orders. The formal sum has an unphysical divergence when the spheres touch, which may be removed without changing the asymptotic (large-separation) expansion to any order. There are two simple ways to add the long-range van der Waals interaction to theories which omit it, such as the Hartree-Fock and semilocal density functional approximations: atom-atom pair potentials and nonlocal correlation energy functionals of the Langreth-Lundqvist type. Our spherical-shell model shows that these approaches can give the right leading-order van der Waals coefficient for solid spheres, but not for hollow spheres such as large fullerenes. The asymptotic metallicity and abnormal atom distribution of a large fullerene combine to defy the conventional wisdom. The problem arises because the static dipole polarizability of a conducting sphere is a radically nonlocal functional of the electron density, depending only on the radius and not at all on what is inside the surface, for familiar classical-physics reasons.

Keywords: van der Waals interaction, van der Waals series, asymptotic expansion, nanostructure, fullerene, pair potential, density functional, nonlocality

1. Introduction

The van der Waals (vdW) interaction provides a long-range attraction between two objects with negligible density overlap between them. When the objects are spherical, without permanent electrostatic multipole moments, it can be the primary interaction between such objects. It can bind closed-shell molecules and nanostructures into complexes or molecular solids. In particular, the fullerene buckyball C₆₀ can form a molecular crystal with a high sublimation point. The vdW interaction arises via a Coulomb correlation between density fluctuations on each of the two objects. For two spherical objects separated by distance d between their centers, the vdW interaction has the non-retarded infinite asymptotic ($d \rightarrow \infty$) series

$$U(d) = -C_6/d^6 - C_8/d^8 - C_{10}/d^{10} - \dots \quad (1)$$

The vdW coefficients C_{2k} depend upon the dynamic multipole polarizabilities $\alpha_l(\omega)$ for each object A and B, describing the linear response of the 2^l multipole moment ($l=1$ dipole, 2 quadrupole, 3 octupole, etc.) to a weak applied uniform electric field oscillating at frequency ω . For example,

$$C_6 = \frac{3}{\pi} \int_0^\infty du \alpha_1^A(iu) \alpha_1^B(iu). \quad (2)$$

Casimir and Polder [1] have given similar expressions for all higher-order coefficients. $\alpha_l(iu)$ has a smooth and simple dependence upon u for the imaginary frequency $\omega = iu$. Typically only a few low-order coefficients are known, with uncertain accuracy, and only for pairs of atoms or small molecules. Here we will estimate the coefficients of all orders, even for pairs of large quasispherical objects, and so answer questions about the vdW interaction that could not be answered before.

2. Spherical-shell model

In previous work, we have establish several models for the dynamic multipole polarizabilities and vdW coefficients between spherical densities. All are designed to be exact for a conducting solid sphere [2-3], and the more recent ones [4-7] also for a conducting spherical shell.

Consider a conducting spherical shell, a system found in textbooks on classical electromagnetism. The shell has an outer radius R , an inner radius $R-t$, and a uniform electron density $\rho = N/\{(4\pi/3)[R^3 - (R-t)^3]\}$ between these radii, where N is the number of valence electrons. The dielectric function is $\varepsilon(iu) = 1 + \omega_p^2/u^2$ inside and 1 outside the shell, where $\omega_p = \sqrt{4\pi\rho}$ is the plasma frequency. Eq. (5) of Lucas et al. [8] then gives the exact multipole polarizability for this model:

$$\alpha_l(iu) = R^{2l+1} \frac{\omega_l^2}{\omega_l^2 + u^2} \frac{1 - \theta_l}{1 - \beta_l \theta_l}, \quad (3)$$

where

$$\beta_l = \frac{\omega_l^2 \tilde{\omega}_l^2}{(\omega_l^2 + u^2)(\tilde{\omega}_l^2 + u^2)}. \quad (4)$$

Here $\omega_l = \omega_p \sqrt{l/(2l+1)}$, $\tilde{\omega}_l = \omega_p \sqrt{(l+1)/(2l+1)}$, and $\theta_l = (1-t/R)^{2l+1}$.

Now the integrals like Eq. (2) can be evaluated analytically for the vdW coefficients of all orders. Note that

$$\alpha_l(0) = R^{2l+1} \quad (0 \leq t < R). \quad (5)$$

To apply this model to real systems, we fix $R = \alpha_1(0)^{1/3}$ from the static dipole polarizability, and in fullerenes we set $t = 2(R - R_n)$, where R_n is the known radius of the nuclear framework. The mean absolute relative error of the vdW coefficients against known values is about 8% for atom pairs, the clusters $\text{Na}_n\text{-Na}_n$, $\text{Si}_n\text{-Si}_n$, $\text{Na}_n\text{-C}_{60}$, and fullerenes $\text{C}_n\text{-C}_n$ [5]. Our neglect of energy-gap effects not in $\alpha_1(0)$ is justified in Ref. [7].

3. van der Waals Interaction as a Summable Asymptotic Series

For the spherical-shell model of section 2, we easily find for two identical objects [6]

$$C_{2k} = c_k(t/R) \sqrt{4\pi\rho} [(2R)]^{2k}. \quad (6)$$

The reduced coefficients $c_k(t/R)$ are found to tend to a constant $c_\infty = 0.011$ as $k \rightarrow \infty$, reminiscent of the geometric series $(1-z)^{-1} = 1 + z + z^2 + \dots$. Thus we can approximately sum the series in a way that will yield the first three terms of Eq. (1) while including the effect of $c_k \rightarrow c_\infty$:

$$U(d) = -\sqrt{4\pi\rho} [c_3(t/R)z^3 + c_4(t/R)z^4 + c_5(t/R)z^5 + c_\infty \{ (1-z)^{-1} - \sum_{k=0}^5 z^k \}], \quad (7)$$

where $z = (2R/d)^2$. Eq. (7) has an unphysical singularity as $d \rightarrow 2R$ (where the two spheres touch). This singularity is there when we sum the series of Eq. (1), but it is not there in reality because Eq. (1) is only asymptotic, for d so large that the quantum mechanical densities of the two objects have negligible overlap. We can remove the singularity via $U(z')$ where $z' = (2R/d')$ and for example $d' = d + g \exp([2R - d]/h)$ with g and h large enough to keep $d' > 2R$. This choice removes the singularity without changing the asymptotic series to any order in d^{-1} . For figures, see Ref. [6].

The $U(z')$ as defined above could provide a useful long-range correction to binding energy curves computed via the Hartree-Fock or semilocal density functional approximations.

4. Size-Dependence of vdW Coefficients: Fullerenes Defy Conventional Wisdom

Given two identical quasispherical nanostructures, each containing n atoms, how do the vdW coefficients C_{2k} grow with n ? In earlier work [5] based on the spherical-shell model, we found that C_6 grows like n^2 (the number of ways of pairing an atom in the first object with one in the second) for solid spheres, but much faster for fullerenes, and that the higher-order coefficients all grow much faster than n^2 .

The picture of atom-atom pair interaction would make [6] $C_{2k} \sim R^{2k} \sim n^{2k/3}$, so that $C_6 \sim n^2$, $C_8 \sim n^{8/3}$, etc. We have derived and confirmed [7] this behavior analytically and numerically for solid spheres from the spherical-shell model. But for single-walled fullerenes the spherical-shell model predicts [7] $C_{2k} \sim R^{2k-1/2} \sim n^{(2k-1/2)/2}$, so that $C_6 \sim n^{2.75}$, $C_8 \sim n^{3.75}$, etc. Thus the standard atom-atom pair interaction picture fails for large single-walled fullerenes. We have explained [7] this as a consequence of two effects: the asymptotic metallicity and abnormal atomic distribution of the fullerenes.

5. Conclusion

A simple spherical-shell model describes the polarizabilities of quasispherical nanostructures and even atoms. The van der Waals series of Eq. (1) is a summable asymptotic series with a removable singularity at small non-zero d . The size-dependences of the vdW coefficients between nanostructures show that the atom-atom pair-potential picture is essentially right for solid spheres, but fails for hollow spheres or large single-walled fullerenes. This failure is intimately related to Eq. (5): The static dipole polarizability of a conducting sphere depends only on the radius, and not on what is inside the surface, for good classical-physics reasons: The equilibrium charge density appears on the surface and cancels the applied electric field inside the conductor. For the same reason, standard nonlocal density functionals of the Langreth-Lundqvist type must fail for large single-walled fullerenes [7].

6. Acknowledgments

The current work is funded by the NSF EPSCoR LA-SiGMA project under award #EPS-1003897, and by NSF under Grant No. DMR-0854769.

7. References

- [1] H.B.G. Casimir and D. Polder, Phys. Rev. **73**, 360 (1948).
- [2] J. Tao, J.P. Perdew, and A. Ruzsinszky, Phys. Rev. B **81**, 233102 (2010).
- [3] J. Tao, J.P. Perdew, and A. Ruzsinszky, Proc. Nat. Acad. Sci. (USA) **109**, 18 (2012).
- [4] J.P. Perdew, J. Tao, P. Hao, A. Ruzsinszky, G.I. Csonka, and J.M. Pitarke, J. Phys.:Condens. Matter **24**, in press.
- [5] J. Tao and J.P. Perdew, submitted.
- [6] J.P. Perdew, A. Ruzsinszky, J. Sun, S. Glindmeyer, and G.I. Csonka, submitted.
- [7] A. Ruzsinszky, J.P. Perdew, J. Tao, G.I. Csonka, and J.M. Pitarke, submitted.
- [8] A.A. Lucas, L. Henrard, and Ph. Lambin, Phys. Rev. B **49**, 2888 (1994).

Exact Diagonalization of Disordered Anderson Model

C.W. Moore^{1,2}, H. Terletska^{1,3}, K. M. Tam¹, J. Moreno^{1,2}, M. Jarrell^{1,2}

¹Dept. of Physics and Astronomy, Louisiana State University, Baton Rouge, LA 70803

²Center for Computation and Technology, Louisiana State University, LA 70803

³Brookhaven National Laboratory, Upton, New York 11973

Abstract: We obtain exact diagonalization results of the geometrically averaged density of states and inverse participation ratio for the single band tight-binding model with diagonal disorder. These quantities are commonly used in the description of localized states in the disorder-driven metal insulator transition. Our exact results provide a validation for the methods used to incorporate disorder into DMFT and its cluster extensions [2,3] such as the DCA-TMT approach. This code is also used to study some physics of rare fluctuation events.

Keywords: Anderson Localization, Inverse Participation Ratio, Exact Diagonalization

1. Introduction

The metal-insulator transition can be driven either by electron-electron interactions or by the disorder present in the system [1]. The inclusion of disorder induced nonlocal correlations remains a challenging problem for quantum cluster theories [6], providing hints of localization, but unable to define a proper order parameter for the description of localization. Thus, an effort is underway in our group to combine DCA with Typical Medium Theory (TMT) [7] (see E. C. Ekuma *et al.* in these proceedings for further details). The difficulty in characterizing localized states is that the average Density of States (DOS) is not a proper order parameter and typical quantities must be used [7]. Another measure widely used to describe localization is the Inverse Participation Ratio (IPR) [5], and so we are developing an exact diagonalization code that calculates this well known quantity to compare with approximation methods. Furthermore, recent work [8] has shown interesting behavior in the IPR, even for a non-interacting system, where “rare fluctuation” events give rise to localized resonant tunneling states becoming a significant fraction of the total states, along with Anderson localized and extended states. One direction of this research is to investigate whether or not this phenomenon is observable within DCA-TMT.

2. Model and Method

We consider the single band tight binding Hamiltonian, written in second quantized notation,

$$H = \sum_i V_i \bar{c}_i c_i - t \sum_{\langle ij \rangle} \bar{c}_i c_j$$

where the disorder is introduced by setting the diagonal site energies, V_i , to values sampled from a uniform probability distribution of width equal to the disorder strength centered around zero. All data shown is for nearest neighbor site hopping of $t = 1$. A Hamiltonian is generated for each disorder realization, diagonalized and then all measurable quantities are averaged over each realization. For example, the IPR [5] is calculated for each eigenstate α of a realization via

$$IPR_\alpha = \sum_i |\Psi_i^\alpha|^4$$

and then averaged over each realization, where i indexes the site amplitude of the state.

3. Anderson Localization and Rare Fluctuation Events

The IPR can be understood as the average diameter of an electronic state [5] and serves as a canonical quantity used to study localization numerically [8]. The IPR is inversely proportional to the number of sites the typical electron wave function resides on, and provides a natural order parameter for localization of a particular eigenstate. For an extended (non-localized) state IPR decays as L^{-d} [5], and for the localized states below the mobility edge separating extended and localized states, the IPR remains finite in the thermodynamic limit. Recently, there has been a renewed interest towards the behavior of IPR in disordered systems due to the latest singular behavior observed in the band tail states (see Figure 2) by [8]. Our goal in this work is to verify using IPR whether or not such phenomenon can be captured within DCA-TMT cluster solver where geometrically instead of algebraic averaged quantities are used to describe localization. We hope our findings will link between these different characterizations of disorder and possibly even help develop a method to study these rare fluctuation events outside of exact methods, as rare fluctuations have been of significant interest since the discovery of the physics of dopants in semiconductors was understood to be such an effect [8].

4. Results and Discussions

The linearly and geometrically averaged DOS, shown in Figure 1, reproduce the behavior found in [4]. Rather than the linearly averaged density of state (right panel), the geometrically averaged DOS (left panel) is used in TMT-DCA. In Figure 2, we present the IPR, a more commonly used quantity for localization. The IPR increases as we move from the middle of the band ($E=0$) to the band edge, reaches some maximum value and then decreases. We also present results for the fraction of states beyond the maximum IPR in Figure 3. The result shows that these rare event resonant tunneling states become a significant fraction of the total states beyond some critical value of disorder [8].

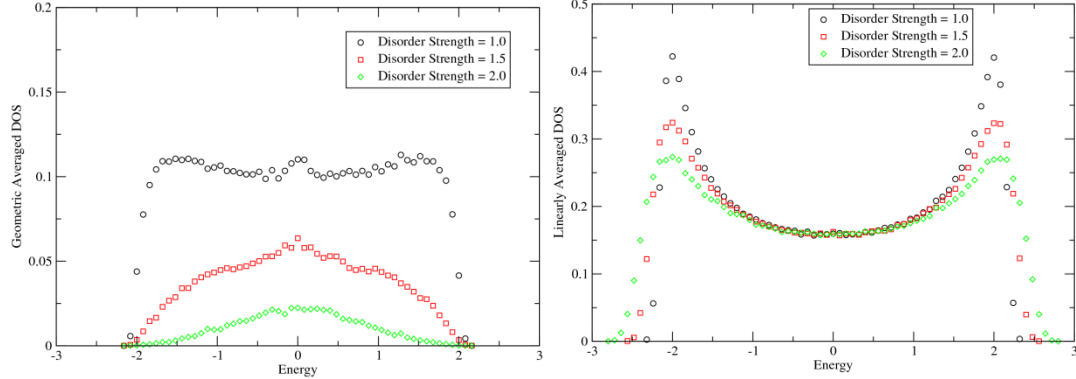


Figure 1 Geometrically (left) and linearly (right) averaged density of states plotted versus energy for three values of disorder strength. Both are plotted for a 1D lattice of 1000 sites, a bin width of 0.08 and 400 disorder realizations.

5. Conclusion and Future Work

Our exact diagonalization results for the density of states and IPR agree with those found in the literature. We believe the code will be invaluable as a reference to justify approximations made in current TMT-DCA approach, and its future extension to multi-orbitals. For example, verifying the behavior of the geometrically averaged DOS. Furthermore, finding a way to compare the exact results for the IPR to the DCA-TMT code in the presence of interactions could potentially elucidate the surprising results of the influence of rare fluctuation events that is demonstrated in the IPR calculations presented here.

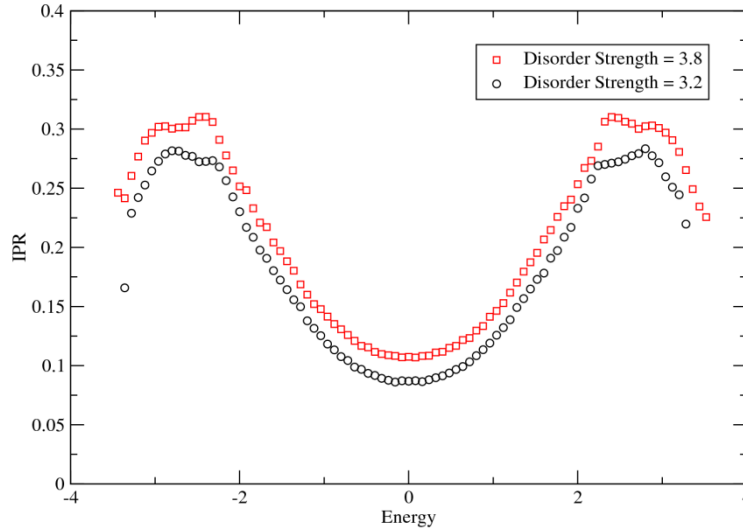


Figure 2: IPR plotted for two values of disorder strength. At some critical value of disorder strength maximum in the IPR on one side of the band changes from one peak to the next. This results in a sudden jump in the number of states that exist beyond the maximum IPR as illustrated in Figure 3

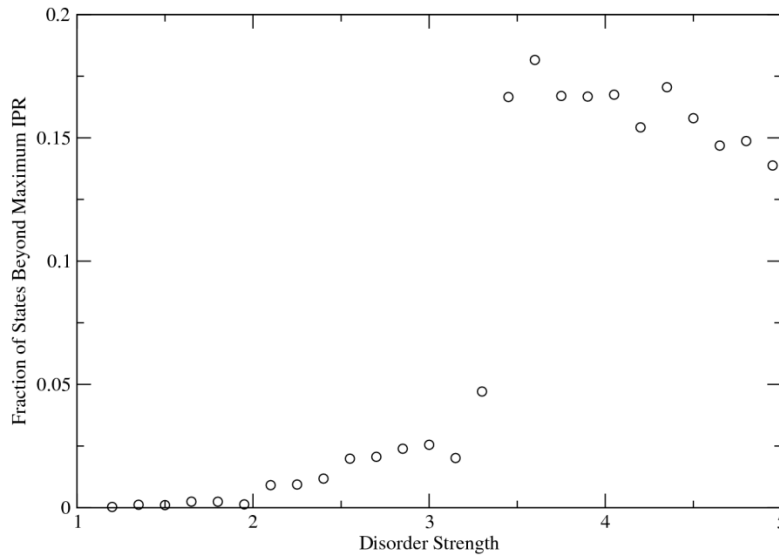


Figure 3: The number of states, corresponding to each energy in Figure 2 for a value of disorder strength, that exist beyond the maximum value of the IPR. This displays a sharp increase in the number of rare fluctuation events.

6. Acknowledgments

The current work is funded by the NSF EPSCoR LA-SiGMA project under award #EPS-1003897.

7. References

- [1] K. Byczuk et al. *Int. J. Mod. Phys. B* 24, 1727 (2010)
- [2] W. Metzner and D. Vollhardt. *Phys. Rev. Lett.*, 62:324–327, 1989.
- [3] Th. Maier, M. Jarrell, Th. Pruschke, and M. Hettler. *Reviews of Modern Physics*, 77:1027–1080, 2005.
- [4] Yun Song, W. A. Atkinson, and R. Wortis. *Phys. Rev. B*. 76, 045105 (2007)
- [5] B. Kramer, A. MacKinnon *Rep. Prog. Phys.* 56 1469-1564 (1993)
- [6] M. Jarrell and H.R. Krishnamurthy. *Phys. Rev. B*. 63 125102 (2001)
- [7] V. Dobrosavljevic et al. *Europhys. Lett.* 62, 76 (2003)
- [8] R.N. Bhatt, S. Johri *Int. J. Mod. Phys. Conference Series* (2012)

Ferromagnetism in CuFeSb: Evidence of Competing Magnetic Interactions in Fe-based Superconductors

B. Qian¹, J. Lee², J. Hu¹, G.C. Wang¹, T. J. Liu¹, D. Fobes¹, H. Pham³, L. Spinu³, M. Green⁴, S.H. Lee² and Z.Q. Mao^{1*}

¹ Department of Physics and Engineering Physics, Tulane University, New Orleans LA

² Department of Physics, University of Virginia, Charlottesville, VA

³ Advanced Material Research Institute and Physics Department, University of New Orleans

⁴ NIST Center for Neutron Research, Gaithersburg

Abstract: We have synthesized a new layered iron-pnictide CuFeSb which shares similar layered tetragonal structure with iron-based superconductors. CuFeSb differs remarkably from Fe-based superconductors in the height of anion Z_{anion} from the Fe plane. In contrast with the metallic antiferromagnetic or superconducting state of iron pnictides and chalcogenides, CuFeSb exhibits a metallic, ferromagnetic state with $T_c = 375$ K. This finding suggests that the competition between AFM and FM coupling may exist in Fe-based superconductors and that the nature of magnetic coupling within Fe plane is indeed dependent on the height of anion as predicted in theories.

Keywords: pnictides and chalcogenides, anion height, exchange and superexchange interactions

1. Introduction

Since superconductivity in iron pnictides and chalcogenides occurs in proximity to antiferromagnetically ordered states [1, 2], the superconducting pairing mechanism is suggested to be correlated to spin fluctuations [3]. Although iron pnictides and chalcogenides share similar layered structure and Fermi-surface (FS) topology, the antiferromagnetic (AFM) orders of their undoped parent compounds are distinct: the pnictides show a “single-stripe” AFM order with the in-plane wavevector being identical to the FS nesting wavevector (π, π) [4], while the chalcogenide Fe_{1+y}Te displays a “double-stripe” AFM order with the in-plane wavevector of $(\pi, 0)$ [5].

The distinct AFM structures between these two classes have triggered intensive debates over the origin of magnetism. The antiferromagnetism in iron pnictides has been suggested to be the spin-density wave induced by FS nesting [6]. Nevertheless, such mechanism cannot interpret the magnetism of Fe_{1+y}Te whose in-plane component of AFM wavevector is 90° rotated from the FS nesting direction. Various models based on local moment superexchange interactions have also been proposed [7]. Some recent works showed that the anion height from the Fe plane Z_{anion} plays important role in determining a magnetic ground state. Yin *et al.* proposed a unified microscopic model [8] which assumes coexistence of localized spins and itinerant electrons. The AFM superexchange coupling between localized spins competes with the double-exchange ferromagnetic (FM) interaction between the localized spins and itinerant electrons. Both “single-stripe” and “double-stripe” AFM orders can be well understood in light of different Z_{anion} . Besides, the first-principles calculations by Moon and Choi [9] showed that the magnetic state of Fe_{1+y}Te would switch from “double-stripe” to “single-stripe” as Z_{Te} was lowered below a critical value (~ 1.71 Å). This is consistent with the case of $\text{Fe}_{1+y}(\text{Te}_{1-x}\text{Se}_x)$ that the $(\pi, 0)$ magnetic correlation gradually weakens as the increase of Se content reduces $Z_{\text{Te/Se}}$, but the (π, π) magnetic correlation enhances accordingly [2]. Furthermore, the total energy calculation predicted a trend toward FM state

with further increase of Z_{anion} , although no such compound has been reported as far as we know. Here we report metallic ferromagnetic discovered in CuFeSb which is isostructural to Fe-based superconductors. The height of Sb, Z_{Sb} , is $\sim 1.84 \text{ \AA}$, much larger than Z_{As} (1.31-1.51 \AA) in FeAs compounds [4, 10] and Z_{Te} ($\sim 1.77 \text{ \AA}$) in Fe_{1+y}Te [5]. Our result is in a good agreement with the theoretical results stated above.

2. Experiment

Polycrystalline CuFeSb samples were synthesized using a self-flux method. The thoroughly mixed powder of Cu, Fe and Sb with stoichiometric ratio was pressed into pellets, sealed in an evacuated quartz tube and sintered at 700 °C for 24 h. The samples were then reground, pressed, and sintered again at 700 °C for 24 h to ensure homogeneity. Structural characterization was performed using x-ray diffraction and neutron scattering. Neutron scattering data were collected on 18 gram powder sample using high resolution powder diffractometer BT1 at the NIST Center for Neutron Research (NCNR), with Ge(311) monochromators giving wavelength 2.07820 \AA and collimation of 15 minutes. The crystal and magnetic structures of the sample were refined using FullProf [11]. The sample composition was analyzed using energy dispersive x-ray spectrometer (EDXS). The magnetization measurements were performed using a Quantum Design SQUID magnetometer. The resistivity was measured using a standard four probe method in a Physical Property Measurement System (PPMS, Quantum Design).

3. Results and discussion

Both x-ray diffraction and neutron scattering analyses show that the CuFeSb sample crystallizes in tetragonal structure with the space group $P4/nmm$. Figure 1a and b present neutron diffraction data collected at 400K and 20K, with results of structural refinement. Two minor phases FeSb (2.63(1)%) and Fe_3O_4 (0.74(1)%) are also observed. The refined lattice parameters at 400 K are $a = 3.93466(2) \text{ \AA}$ and $c = 6.25152(4) \text{ \AA}$. No structural transition was revealed at low temperatures. The stoichiometric composition was confirmed by EDXS.

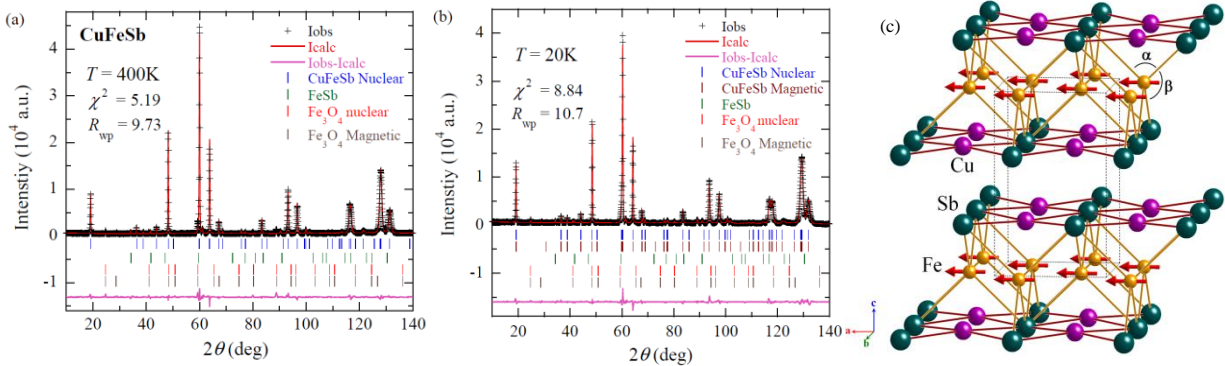


Fig. 1. Neutron powder diffraction spectra (+) of CuFeSb and the results of FullProf. refinements (solid line) at 400 K (a) and 20 K (b). The difference between the experimental data and the fitting line is shown at the bottom in both (a) and (b). Tick marks indicate nuclear Bragg diffraction peak positions of CuFeSb/minor impurity phases (FeSb and Fe_3O_4) and magnetic diffraction peaks of CuFeSb/minor Fe_3O_4 phase. (c) The crystal and magnetic structure of CuFeSb.

The crystal structure of CuFeSb is analogous to those of Fe-based superconductors, with particular similarity to LiFeAs [10] Fe square planar sheets form from the edge-sharing Fe-Sb tetrahedral network, and Cu ions occupy interstitial sites of Sb layers. In FeSb layers, Sb ions form a distorted tetrahedral arrangement around Fe ions,

giving rise to two distinct Sb–Fe–Sb bonding angles as indicated by α and β in Fig. 1c. α ($=93.860(5)^\circ$) and β ($=117.797(3)^\circ$) in CuFeSb are remarkably different from those for LiFeAs where $\alpha = 102.793(6)^\circ$ and $\beta = 112.910(3)^\circ$ [10]. Besides, the Fe–Sb bonding length (2.693 Å) is appreciably greater than the Fe–As bonding length (2.4162(1) Å). These differences lead the anion height of Sb, $Z_{\text{Sb}} (= 1.84 \text{ \AA})$ to be strikingly larger than Z_{As} in FeAs compounds or Z_{Te} in Fe_{1+y}Te (1.31–1.77 Å [4, 5, 10])

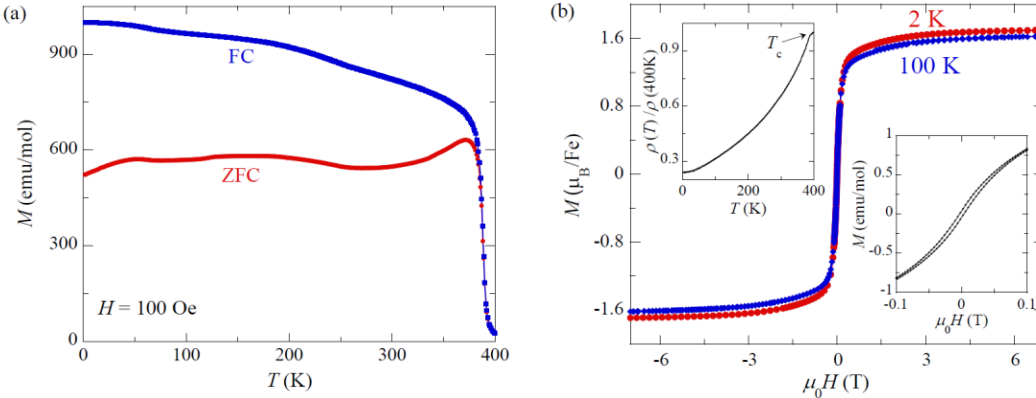


Fig. 2. (a) Magnetization as a function of temperature $M(T)$ of CuFeSb measured with ZFC and FC histories. (b) Magnetization as a function of magnetic field $M(H)$ of CuFeSb at 2 and 100 K. Left Inset: the temperature dependence of resistivity. Right inset: the magnetic hysteresis loop at 2 K.

Although CuFeSb shares similar structure with the iron pnictides and chalcogenides, it exhibits ferromagnetism as demonstrated by magnetization and neutron scattering measurements, in sharp contrast with antiferromagnetism and superconductivity observed in iron pnictides and chalcogenides. Figure 2a shows the magnetization M as a function of temperature for CuFeSb. A remarkable FM transition at 375 K is observed, with typical irreversible behavior between zero-field-cooling (ZFC) and field-cooling (FC) histories. Figure 2b displays the magnetization vs. magnetic field at 2 K and 100 K. The magnetization saturates at very low field, indicating small magneto-crystalline anisotropy. The saturation moments are 1.70 and 1.62 μ_{B}/Fe at 2 and 100 K, respectively. The coercive force is rather small as seen in the magnetic hysteresis loop at 2 K (Fig. 2b, right inset), indicating soft ferromagnetism. The temperature dependence of resistivity shows metallic behavior, as presented in Fig. 2b.

In neutron scattering measurements, as the temperature is decreased below T_c , we observed the increase of the magnetic Bragg intensities on top of the nuclear Bragg peaks, implying the magnetic propagation vector $Q_{\text{m}}=0$. The magnetic Bragg peaks can be best fit with the ferromagnetic spin alignment on the Fe plane (Fig.1b). The exact direction of the spin on the plane is indistinguishable in the case of powder measurements, and for the refinements, it was arbitrarily set to be parallel to the a -axis, as illustrated in Fig. 1c.

The origin of metallic ferromagnetism in CuFeSb would certainly be instrumental to the clarification of the magnetism mechanism of Fe-based superconductor parent compounds. According to the first principles calculation [9], the large Z_{Sb} in CuFeSb would cause the coupling between the Fe t_{2g} states and the Sb 5p states to become weak and thus increase the density of state at the Fermi level ($N(E_{\text{F}})$), leading to metallic ferromagnetism in terms of Stoner criterion. The trend toward ferromagnetism for $Z_{\text{anion}} > 1.82 \text{ \AA}$ has indeed been revealed in the DFT calculations for iron telluride [9]. Given $Z_{\text{Sb}}=1.84 \text{ \AA}$, the metallic ferromagnetism fits fairly well with this

theoretical result. Also, the ferromagnetism of CuFeSb can also be interpreted using the above-mentioned unified microscopic model proposed by Yin *et al.* [8]. AFM superexchange interaction of localized spins and the FM double-exchange interaction mediated by the Hund's rule coupling between localized spins and itinerant electrons coexist in iron pnictides/chalcogenides. Z_{anion} is a key parameter in tuning the relative strength of these two magnetic interactions, since the AFM superexchange interaction between localized spins at Fe sites occurs via the anions. When the anions are farther away from the Fe plane, the Fe-Fe superexchange interaction through the anions is naturally expected to weaken. Therefore the absence of antiferromagnetism in CuFeSb can be viewed as a natural consequence of the large Z_{Sb} . While we cannot exclude the possibility of the Stoner instability which gives rises of ferromagnetism, the double-exchange FM interaction is a reasonable alternative interpretation.

4. Conclusion

We have synthesized a new material CuFeSb, which crystalizes in layered tetragonal structure similar to those of Fe-based superconductors. We observed metallic ferromagnetism in this compound, in sharp contrast with the antiferromagnetism and superconductivity observed in other iron pnictides and chalcogenides. Analyses suggest that the large height of Sb from the Fe plane may play an important role in stabilizing a FM state in CuFeSb. Findings support the theoretical idea that the anion height controls the competing magnetic interactions in Fe-based superconductors.

5. Acknowledgments

Work is supported by the NSF under grant DMR-0645305 and the LA-SiGMA Award No. EPS-1003897. Work at UV and NCNR were partly supported by the US Department of Energy contract DE-FG02-10ER46384.

6. References

- [1] J. Zhao *et al.*, Nat. Mater. **7**, 953 (2008); H. Luetkens *et al.*, Nat. Mater. **8**, 305 (2009); A. J. Drew *et al.*, Nat. Mater. **8**, 310 (2009); H. Chen *et al.*, Europhys. Lett. **85**, 17006 (2009); J.-H. Chu *et al.*, Phys. Rev. B **79**, 014506 (2009); S. Nandi *et al.*, Phys. Rev. Lett **104**, 057006 (2010); N. Katayama *et al.*, J. Phys. Soc. Jpn. **79**, 113702 (2010).
- [2] T. J. Liu *et al.*, Nat. Mater. **9**, 718 (2010).
- [3] K. Ahilan *et al.*, Phys. Rev. B **78**, 100501 (2008); Y. Nakai *et al.*, J. Phys. Soc. Jpn. **77**, 073701 (2008); A. D. Christianson *et al.*, Nature **456**, 930 (2008); M. D. Lumsden *et al.*, Phys. Rev. Lett **102**, 107005 (2009); S. Chi *et al.*, Phys. Rev. Lett **102**, 107006 (2009); H. A. Mook *et al.*, arXiv:0904.2178 (2009); Y. Qiu *et al.*, Phys. Rev. Lett **103**, 067008 (2009).
- [4] C. de la Cruz *et al.*, Nature **453**, 899 (2008); Q. Huang *et al.*, Phys. Rev. Lett **101**, 257003 (2008).
- [5] W. Bao *et al.*, Phys. Rev. Lett **102**, 247001 (2009).
- [6] J. Dong *et al.*, Europhys. Lett. **83**, 27006 (2008); D. J. Singh, Phys. Rev. B **78**, 094511 (2008); V. Cvetkovic *et al.*, Europhys. Lett. **85**, 37002 (2009); I. I. Mazin, Nature **464**, 183 (2010).
- [7] F. Ma *et al.*, Phys. Rev. B **78**, 224517 (2008); Q. Si *et al.*, Phys. Rev. Lett **101**, 076401 (2008); T. Yildirim, Phys. Rev. Lett **101**, 057010 (2008); F. Ma *et al.*, Phys. Rev. Lett **102**, 177003 (2009); J. Hu *et al.*, Sci. Rep. **2**, 381 (2012).
- [8] W.-G. Yin *et al.*, Phys. Rev. Lett **105**, 107004 (2010).
- [9] C.-Y. Moon *et al.*, Phys. Rev. Lett **104**, 057003 (2010).
- [10] M. J. Pitcher *et al.*, Chem. Commun., 5918 (2008).
- [11] J. Rodríguez-Carvajal, Physica B **192**, 55 (1993).

Geometric Analysis of DNA in Molecular Dynamics Simulations of Nucleosomes

Rocky Brown¹, Victoria Bamburg², James Liman², James Solow²,
Thomas C. Bishop²

¹Department of Physics, Radford University

²Department of Chemistry and Physics, Louisiana Tech University

Abstract: There are specific DNA sequences that have a tendency to allow geometric conformations that either include or exclude nucleosomes. Since nucleosomes alter access to DNA, they are essential in regulating gene expressions. It is necessary that nucleosomes be properly understood in order to fully comprehend genomic function. By analyzing the geometric properties and possible peculiarities that specific DNA sequences contain, we hope to gain insight into why nucleosomes position as they do on DNA. Here, our goal is to analyze DNA helical parameter data obtained from molecular dynamic simulations of nucleosomes. From this analysis, we will determine if the helical parameters are conserved throughout the simulations or if the parameters are influenced by sequence. Furthermore, this will provide a metric for analysis methods that can be used in future simulations to identify and classify DNA sequence properties related to nucleosome positioning.

Keywords: Nucleosomes, Simulations, Helical parameters

1. Introduction

A nucleosome core particle (NCP) is a biomolecular complex of eight histone proteins around which is wrapped 147-base pair of DNA. Nucleosomes pack long lengths of DNA. This packing or folding influences genetic functions such as transcription, replication, regulation and repair. Nucleosome formation requires the 147bp of DNA to assume a specific superhelical conformation. Our goal is two fold: 1) determine if there is only one superhelical conformation or many separate conformational substates, and 2) determine if DNA sequence alters these findings.

For this purpose we have analyzed a collection of all atom molecular dynamic simulations (Bishop2005) of nucleosomes containing different sequences of DNA. These simulations provided DNA helical parameter data which we then used as a measure of conformation.

There are twelve DNA helical parameters. They consist of two types: base pair parameters and dimer step parameters. The base pair parameters- Shear, Stretch, Stagger, Buckle, Propeller, and Opening- are used to define the relative position and orientation of two bases in a pair with respect to each other, while the dimer step parameters- Shift, Slide, Rise, Tilt, Roll, and Twist- define the relative position and orientation of two base pairs

with respect to each other. In each case the relative orientation includes three rotations and three translations. In total, the helical parameters embody a complete description of DNA conformation that is equivalent to a Cartesian coordinate description. By using the helical parameters, we can quantify the influence of DNA sequences on the geometric properties of super-helical DNA in nucleosomes.

2. Methods of Analysis

2.1 Tools

In order to analyze the massive amount of the data that has been collected, it was necessary to generate computer programming software to assist in the task. Python was the language of choice due to its portability (operating system to operating system), its ability to execute high level functions such as Fourier Transforms, and its support of graphing and plotting utilities. To make the nucleosome simulation workflow more efficient, we developed a set of tools in Python, called HPTools, that can be used to analyze helical parameter data in near real time. This will allow for data processing to occur at nearly the same time as the simulations, and will convert the generated data into a reduced set of observations that are biologically relevant.

2.2 Dataset

The data to be analyzed was previously generated by running simulations of sequences found in the yeast genome. The simulations were executed in the molecular dynamics program NAMD using the same methods as previous experiments (Bishop2005). The simulations utilized 16 sequences (one from each chromosome of *S. cerevisiae*). The sequences correspond to the most highly occupied and least variable nucleosome footprint observed for each chromosome. In the molecular dynamics simulations, a 20bp window about the chosen position that included 10bp upstream and 10bp downstream was scanned. This gave us a 167bp sequence and 21 nucleosomes to simulate. In total, there were 336 systems that simulated. Every system was simulated for 20ns. Here, we only consider the last nanosecond and a subset of the 336 systems. Statistical analysis - mean, range, standard deviation and normality – were used to quantify the differences in conformation and determine whether or not conformations is independent of the sequence.

2.3 Process

It was previously demonstrated that twelve Fourier wavenumbers were both necessary and sufficient to model super-helical DNA in atomic resolution (Bishop2008) using the DNA helical parameters. The necessary and sufficient wavenumbers are: 1, 2, 3, 10, 11, 12, 13, 14, 15, 16. We will filter the simulation data for these wavenumbers to determine if the necessary and sufficient result is valid for our simulations with different sequences of DNA, or if DNA sequence somehow alters the Fourier spectra associated with super-helical DNA conformation.

3. Results and Discussions

The following graphs represent results from 21 separate simulations. Each line on the plots corresponds to one of the 21 positions associated with one of the 16 sequences that was “threaded” around the nucleosome. Below we

display only the mean values in a figure generated with our HPTools. The tools are sufficiently general and powerful to allow us to rapidly load, analyze and display virtually any data set associated with the 336 simulations, including routines to achieve the required Fourier analysis. From the images below it is clear that there remains a data formatting issue, note the spikes.

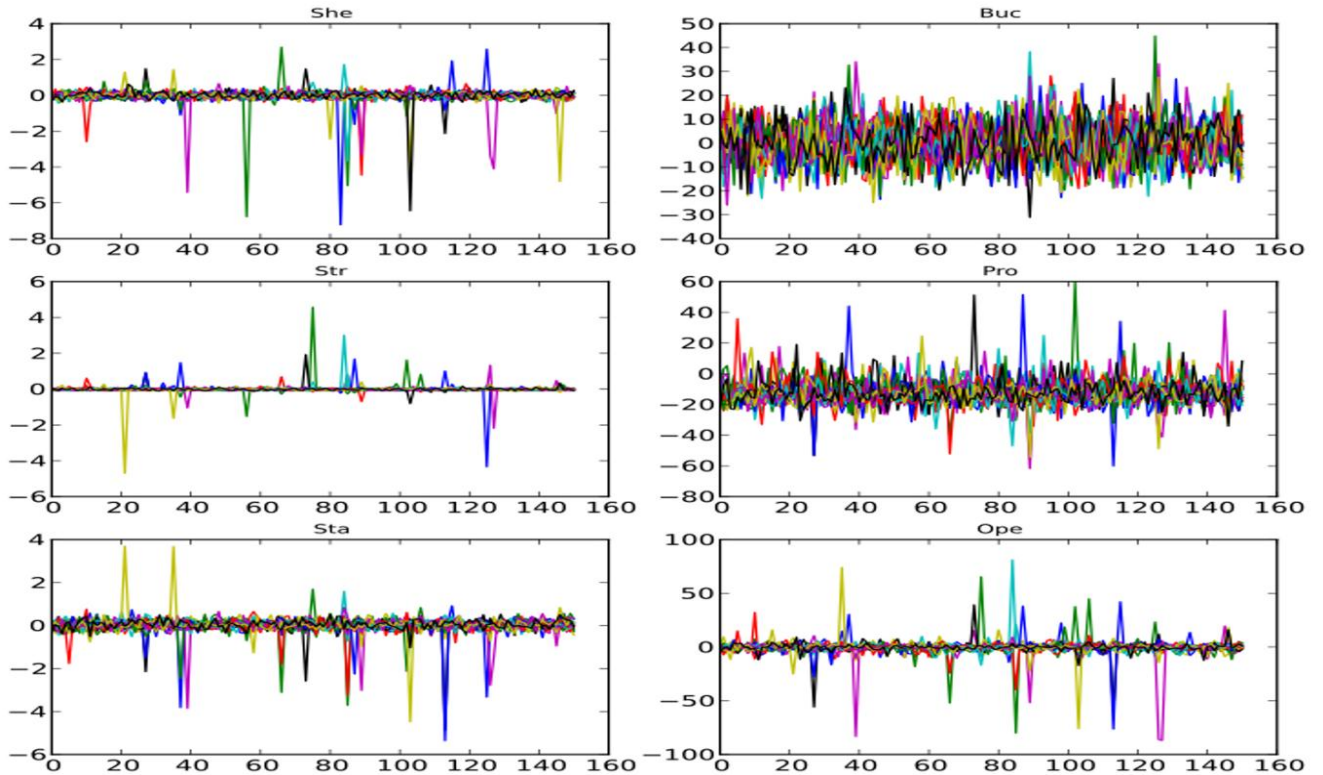


Fig. 1| Base Pair Parameters This is a graph of the mean values of the base pair parameters. As stated above, there are 21 separate systems here, each is represented by a different color. The peaks will be discussed in the conclusions.

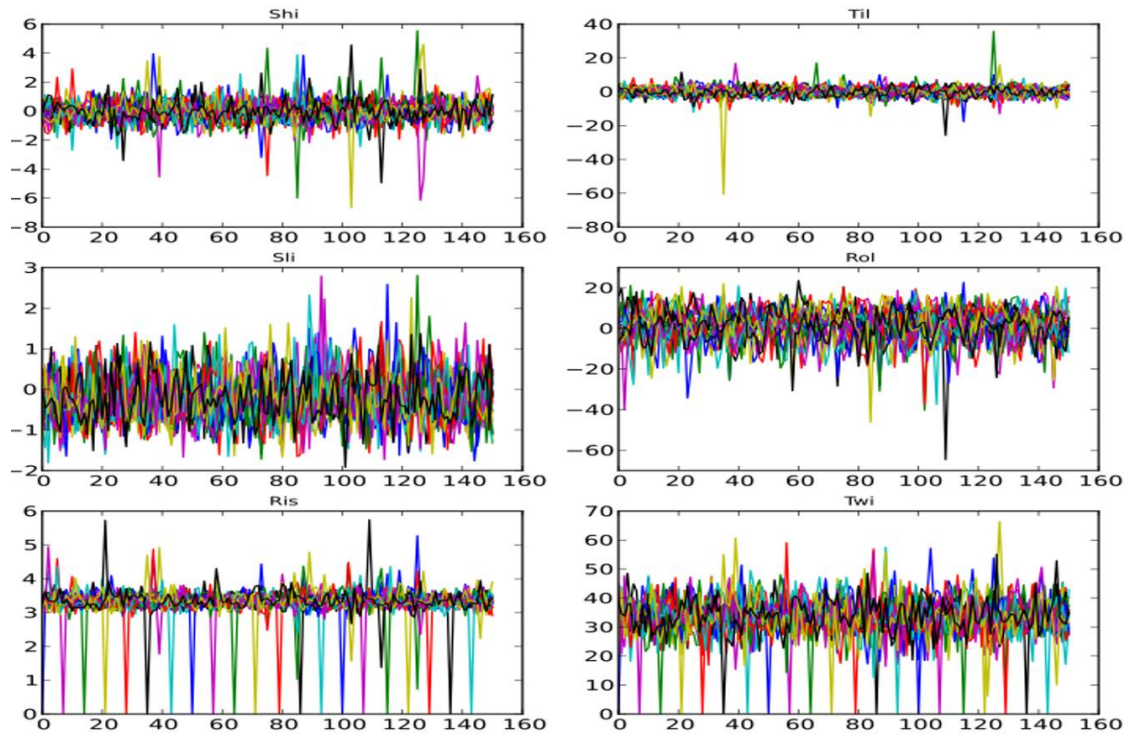


Fig. 2| Dimer Step Parameters This is a graph of the mean values of the dimer step parameters. As stated above, there are 21 separate systems here, each is represented by a different color. The peaks will be discussed in the conclusions.

4. Conclusions

The HPTools routines that we have developed have proven to be sufficiently fast, powerful, and generalizable to enable us to achieve data processing at the same time as the simulations. See our poster for applications of these tools.

5. Acknowledgments

The current work is funded by the NSF EPSCoR LA-SiGMA project under award #EPS-1003897.

6. References

- [1] Bishop. T.C. (2009). Geometry of the nucleosomal DNA superhelix. *Biophys J*, 95(3), 1007-1017.
- [2] Mukherjee, R., Bishop, T. C. (2011). Nucleosomal DNA: Kinked, Not Kinked, or Self-Healing Material?. *Frontiers Nucleic Acids*, 5, 69-92.

GPGPU Performance Modeling

Supada Laosooksathit, Chokchai Leangsuksun

College of Engineering & Science, Louisiana Tech University, Ruston, LA 71270

Abstract: Since GPUs have increasingly been deployed for non-graphic applications (as known as GPGPU), a performance model for GPGPU has become more critical in order to gain an insight into speed improvement issues from an HPC software development perspective. There are existing works that model GPGPU performance. However most of them assume that the number of clock cycles is the same for all memory instructions while it actually varies depending on the data types and the type of memory accesses. This paper proposes a performance model that aims to improve memory operation cost estimation by considering varied memory latencies. This is because the GPU memory model is one of the critical parameters that dictates performance outcome. The results show that our model is more accurate when the data set is practically large enough since an overlapping between two consecutive memory instructions is insignificant compared to the memory latency. On the other hand, there is a big impact to the model when the data set is significantly varied.

Keywords: GPGPU, Performance Modeling, HPC, Memory Latency.

1. Introduction

In order to gain an insight into speed improvement issues from an HPC software development perspective, performance model for GPGPU has become critical. By estimating the cost benefit, the performance model can help programmers to find ways to optimize their parallel program for a better use of the heterogeneous computing.

Although a GPU is considered as an accelerator for a CPU, the architectures between a GPU and a CPU are quite different [1][2]. In order to estimate an application completion-time, we need to know how long a GPU takes to execute a part of the program that is run on the GPU, which is called a kernel. Thus we can make a decision whether the GPU is worth participating in the computation and can further improve the heterogeneous computing application. In addition the performance model can also help increasing the efficiency of fault tolerance techniques for GPGPU, such as checkpoint/restart mechanisms, especially for a large GPU cluster.

In this paper, we propose a novel performance model that enhances Hong and Kim's model [3]. However, Hong and Kim's model is based on a limited assumption that a latency due to every global memory instruction is the same. Nonetheless, our empirical results reveal that the latencies are varied depending on the data type and the type of memory access. Figure Fig. 1 shows that a global memory write operation takes much longer than a global memory read operation in every case. Also, 4-byte word accesses take longer than 1-byte word accesses. Thus it is important to consider various memory access costs that will impact GPU performance outcome.

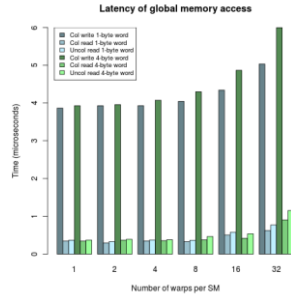


Fig. 1 Memory latency on GPU NVIDIA GeForce GTX 295

2. Performance Modeling

In this section, we define the important parameters in our performance. Then we describe the model notations in a general case and in cases with synchronization functions.

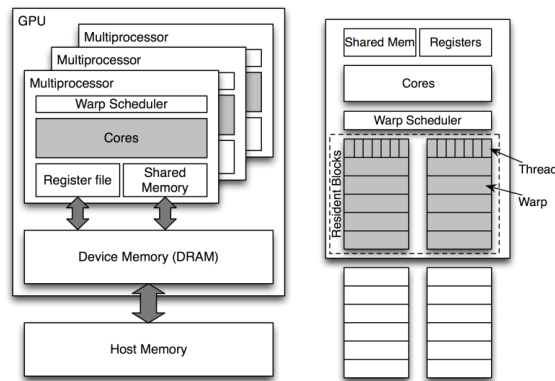


Fig. 2 GPU architecture: (a) programming model; (b) warp scheduling in an SM

In GPGPU programming, parallel instructions are executed by multiple threads. These threads are maintained as thread *blocks* that will be assigned to stream processors (SMs) as illustrated in figure Fig. 2(a). The thread blocks are also organized into a *grid* of a kernel. Moreover, figure Fig. 2(b) shows that threads in a block executed in an SM are managed in a group of parallel threads called a *warp*.

The parameters used in the model can be obtained by the specification of an underline hardware and code analysis. The details of how to obtain the following parameters can be found in [4].

N_{RW}	The number of resident warps
N_P	The number of groups of blocks assigned to an SM
T_C	Overall computing time
T_M	Overall global memory latency
T_{Syn}	Synchronization function cost

$T_{C,Syn}$ Computing time between the Sync function and memory instructions
 $T_{M,Syn}$ Memory latency cost by memory instructions adjacent to the synchronization function
 N_{Syn} Number of synchronization functions

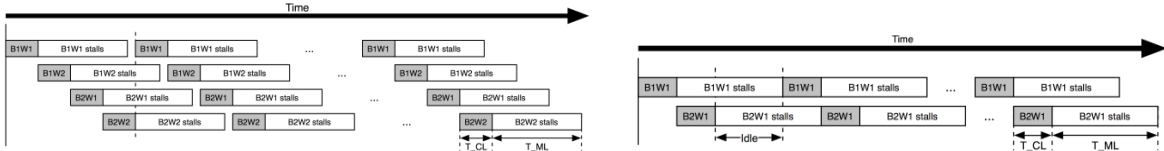


Fig. 3 Diagrams show the execution time when: (a) there is no idle time; (b) there is idle time. A shaded box indicates that the warp is being executed. A white box indicates that the warp is waiting for the memory access.

Figure Fig. 3(a) illustrates the case that T_C is longer than T_M , or N_{RW} is large enough to hide the idle time. The execution time of the kernel $T(K)$ can be defined as

$$T(K) = (T_{ML} + T_C N_{RW}) N_P \quad (1)$$

However, in Figure 3(b), N_{RW} is not large enough to fill the idle time [1][2]. Hence

$$T(K) = (T_M + T_C + T_{CL}(N_{RW} - 1)) N_P \quad (2)$$

To determine whether N_{RW} is large enough to hide the idle time, we subtract equation (2) from equation (1), to find the idle time and set it to zero. Then we have $N_{RW} = \frac{T_M - T_{ML}}{T_C - T_{CL}} + 1$. Therefore, if $N_{RW} \geq \left\lceil \frac{T_M - T_{ML}}{T_C - T_{CL}} \right\rceil + 1$, there will not be an idle time.

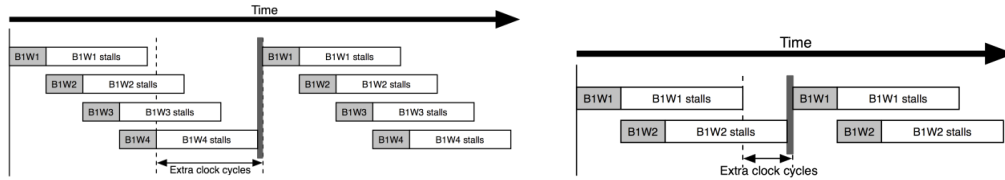


Fig. 4 (a) a synchronization function causes extra time between two consecutive computational instructions; (b) a synchronization function causes extra time between memory and computational instructions. Again, a shaded box indicates that the warp is being executed. A white box indicates that the warp is waiting for the memory access.

In case where there is a synchronization function, the function acts as a barrier at which threads in a block must wait until every thread hits this point before they are allowed to execute the next instruction [1]. In general, if $N_{RB} > 1$, the compiler will try to fill the idle clock cycles with warps from the other blocks. Therefore, we can omit the impact of the synchronization function. Nonetheless, if $N_{RB} = 1$, the number of execution time will be increased by the waiting time resulted by the synchronization function.

Figure Fig. 4(a) is the diagram extended from figure 3(a), which is the case that it originally does not have idle time. In this case, N_{Syn} synchronization functions generate extra time $(T_{Syn} + T_{M,Syn}) N_{Syn}$. Then the kernel execution time defined by equation (1) can be improved as follows

$$T(K) = [T_{ML} + T_C N_{RW} + (T_{Syn} + T_{M,Syn})N_{Syn}]N_P \quad (3)$$

Also figure 4(b) is the diagram modified from figure 3(b). It illustrates the extra time due to a synchronization function in case that it originally has idle time. The extra time generated by N_{Syn} synchronization functions is $(T_{Syn} + T_{C,Syn}(N_{RW} - 1))N_{Syn}$. Therefore the kernel execution time can be improved from equation (2) as

$$T(K) = [T_M + T_C + T_{CL}(N_{RW} - 1) + (T_{Syn} + T_{C,Syn}(N_{RW} - 1))N_{Syn}]N_P \quad (4)$$

3. Results

To validate our model we use naïve and tiled matrix multiplication as benchmarks. The sizes of squared matrices vary from 32×32 to 512×512 .

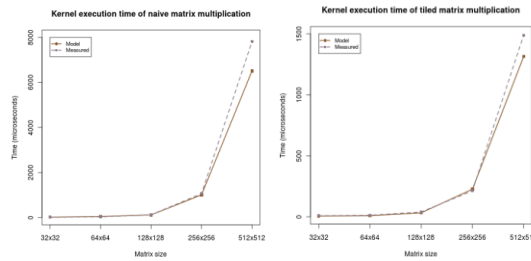


Fig. 5 The kernel execution time from the performance model compared to the measurement: (a) naïve matrix multiplication; (b) tiled matrix multiplication.

The GPU that is used in this experiment is NVIDIA GeForce GTX 295. The results shown in figure Fig. 5(a) and (b) indicate that the execution time from the model follows the measurement well. Also we observe that our model is more relatively accurate when the size of matrix is practically large enough.

4. Conclusion

This paper proposed the performance model that improved the kernel execution time estimation for a GPGPU application, which considered memory access types and the impacts of synchronization functions. We also showed that the global memory latency was varied depending on the type of memory.

5. Acknowledgments

The current work is funded by the NSF EPSCoR LA-SiGMA project under award #EPS-1003897.

6. References

- [1] NVIDIA, “CUDA C Programming Guide Version 4.0.” 06-May-2011.
- [2] NVIDIA, “CUDA C Best Practices Guide.” May-2011.
- [3] S. Hong and H. Kim, “Memory-level and Thread-level Parallelism Aware GPU Architecture Performance Analytical Model.”
- [4] S. Laosooksathit and C. Leangsuksun, “A Performance Model for Predicting Completion-time of a GPGPU Application,” Technical Report, 2012.

GPU Accelerated Hirsch-Fye Quantum Monte Carlo

C.W. Moore^{1,2}, S. AbuAsal^{2,3}, B.Thakur², Z.Yun², J. Moreno^{1,2}, J. Ramanujam^{2,3}, M. Jarrell^{1,2}

¹Department of Physics and Astronomy, Louisiana State University

²Center for Computation and Technology, Louisiana State University

³ECE Division, School of Electrical Engineering and Computer Science, Louisiana State University

Abstract We present the development of a Hirsch-Fye cluster solver on an NVIDIA Graphics Processing Unit (GPU) expected to accelerate the equilibration time of the Green function, required for the measurement routine of quantum cluster methods. The time spent in warm-up, equilibrating the Green function, is a major computational bottleneck of such many body calculations.

Keywords: GPU computing, Hirsch-Fye Monte Carlo

1. Introduction

Hirsch-Fye Quantum Monte Carlo (HFQMC) [1] is primarily used as the impurity or cluster solver in Dynamical Mean Field Theory (DMFT) or its cluster extensions such as the Dynamic Cluster Approximation (DCA) [2, 3]. The challenge of these calculations is incorporating the complexity of the electronic many-body interactions. HFQMC decouples the electron-electron interaction with an “Ising-like” field of up and down spins that is sampled with Monte Carlo, analogous to the classical Ising model. The Monte Carlo sampling is computationally intensive and requires a long equilibration time before taking measurements; fortunately, the linear algebra computations in the algorithm are especially suited for the architecture of the Graphics Processing Unit (GPU) from NVIDIA. In this work we describe how we have implemented GPU-accelerated HFQMC.

2. Hirsche-Fye Quantum Monte Carlo Algorithm and Computational Challenges

The Hirsh-Fye method works by decoupling the interaction of conduction electrons with an Ising decoupling field [1]. The interaction is mapped to electrons scattering off an $N \times L$ space and (imaginary) time-dependent decoupling field (Fig. 1), where N is the number of cluster sites and L is the number of time slices. A bottleneck for cluster methods is the time spent equilibrating the green function (an $(N \times L)^2$ square matrix) by exactly solving the quantum cluster problem. This is a problem that is not circumvented by simply increasing the number of independent Markov processes as this leads to the simulation being dominated by warm-up: more processes yield better statistics during the Monte Carlo, but do not decrease the equilibration time among processes. The procedure to accelerate the algorithm is to port the linear algebra operations of the FORTRAN code to the GPU.

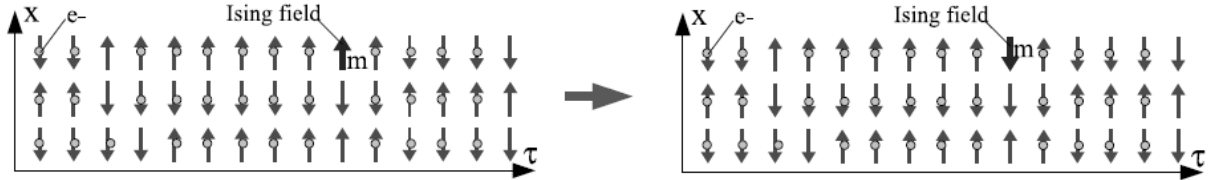


Fig. 1: A proposed Monte Carlo move for the Hirsch-Fye algorithm. Configurations of N cluster sites and L time slices of the decoupling field are sampled by proposing spin flips. A configuration's sampling weight is calculated from the diagonal element of the green function and is a relatively inexpensive calculation. This figure is taken from [4].

Proposed moves of each Markov process are computationally inexpensive to make, but the full update of the Green function is an expensive rank-1 update. This update incurs as many FLOPs as memory accesses with little data reuse; this is impractical for a GPU implementation as GPUs achieve their high performance by large number of concurrent calculations and large bandwidth to many shared memories, but have small data caches. An optimization of the update equation already implemented on CPU architecture is what is known as the "delayed update" [4] that collapses the rank-1 update (a sum of outer products) into a matrix multiplication (Fig. 2). This approach is desirable for the GPU as each data access is used many times, increasing the FLOPs.

$$G_{ij}^{(M)} = G_{ij}^{(1)} + \sum_{N=1}^M A_i^{(N)} B_j^{(N)} \rightarrow$$

Fig. 2: Rank-1 update rewritten as a thin-rectangular or panel-panel matrix multiplication of A and B which are $(N \times L) \times M$ matrices that are tiled by vectors that are rows and columns of the updated green function where M is the number of delays.

3. GPU Code Development

The Green function update is a data parallel operation and reading elements of the Green function while sweeping over the Ising decoupling field is a vector operation that can utilize the large global memory bandwidth available to CUDA threads on the GPU. Updating the diagonals of the Green function, to calculate the sampling weights, from a set of dependency equations is also a vector operation. Moreover, the panel-panel multiplication of the rows and columns read from the Green function is a natural data parallel operation with much potential for accelerating [5–7]. Such features make Hirsh-Fye a candidate for acceleration by GPUs. To avoid the overhead

of data movement back and forth between the host and device, we conduct all computation of the update equation on the GPU.

4. Results and Discussion

The execution time for the update as a function of delays is shown in Fig. 3. The execution time drops for both the CPU and the GPU as the number of delays is increased by decreasing the number of multiplications by substituting N rank-1 updates with N/M of thin rectangular multiplications that have more data reuse. Fig. 4(a) shows the drop in the overall execution time spent in `cublas_SGEMM` in the GPU version. Fig. 4(b) shows the overall execution time spent in execution of our GPU kernel with and without overhead.

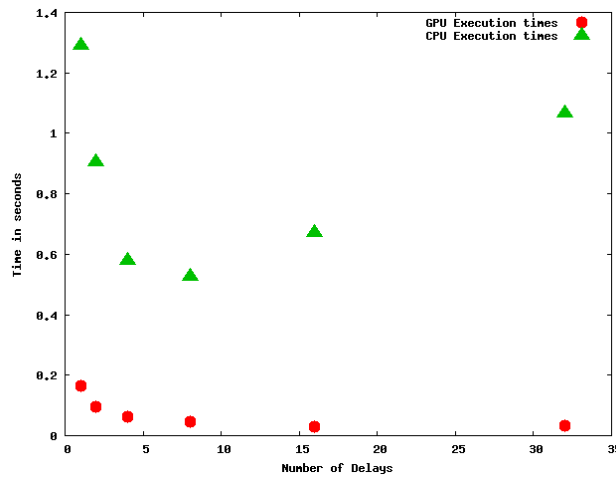


Fig. 3: Execution time for the CPU and GPU implementation. Note that the CPU implementation initially gets better with increasing number of delays but then starts to get worse, as the overhead of solving the dependency equations outweighs the advantage of the data re-use.

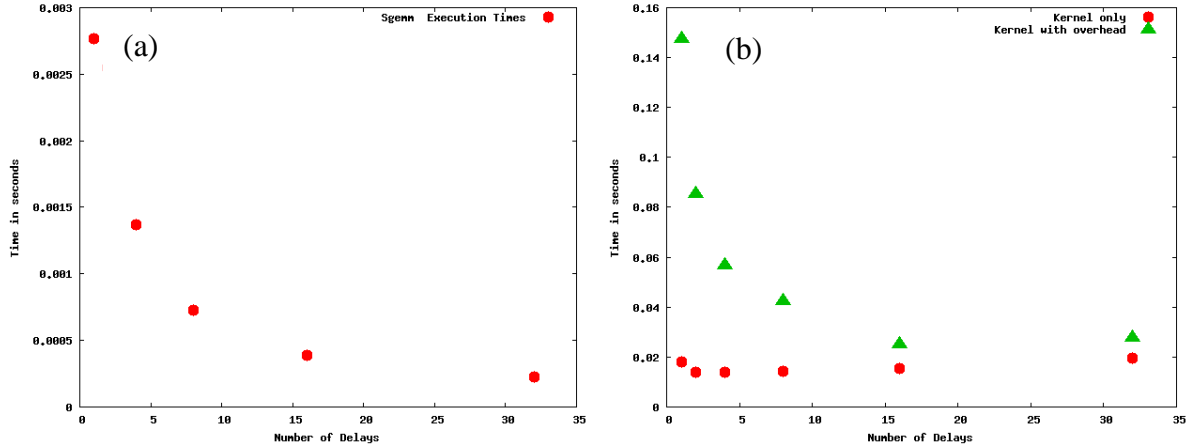


Fig. 4: (a) Execution time as a function of delays follows the behavior shown in [4]. (b) Kernel launch overhead (time); with increasing number of delays, the ratio of launch overhead to the overall execution time decreases.

5. Conclusions and Future Work

The results of Fig. 4(b) show a flaw in our code design where a kernel calls the `cublas_SGEMM` routine to update the green function. For a better performing code, kernel launches will be minimized by implementing both the multiplication and each block of M updates in the same kernel. Future work includes the addition of the blocked updating routine which, rather than increasing FLOPs, proposes moves which equilibrate the Green function quicker by blocking adjacent time slices together, incorporating strong correlations in time [4].

6. Acknowledgments

The current work is funded by the NSF EPSCoR LA-SiGMA project under award EPS-1003897.

7. References

- [1] J. E. Hirsch and R. M. Fye. *Phys. Rev. Lett.*, 56:2521–2564, 1986.
- [2] W. Metzner and D. Vollhardt. *Phys. Rev. Lett.*, 62:324–327, 1989.
- [3] Th. Maier, M. Jarrell, Th. Pruschke, and M. Hettler. *Reviews of Modern Physics*, 77:1027–1080, 2005.
- [4] M. Jarrell, A. Macridin, K. Tomko and E. D’Azevedo. *Optimizing QMC Algorithms for the Quantum Cluster Problem*.
- [5] G. Tan, L. Li, S. Triehle, E. Phillips, Y. Bao, and N. Sun. *Proceedings of the 2011 ACM/IEEE Conference on Supercomputing (SC '11)*. Article 35, 11 pages.
- [6] V. Volkov and J.W. Demmel. *Proceedings of the 2008 ACM/IEEE Conference on Supercomputing (SC '08)*. Article 31, 11 pages.
- [7] Y. Li, J. Dongarra, and S. Tomov. *Proceedings of the 9th International Conference on Computational Science: Part I*, 884–892, 2009.

Hybrid MD-continuum Simulation Methodology with Capability of Handling Two-Phase Flows with Application in Biomolecular Systems

K. Fattah-Hesary¹, N. Kim², B. Novak¹, S. Jha², D. Moldovan¹, and D. Nikitopoulos¹

¹Mechanical Engineering Department, LSU

²Centre Center for Computational & Technology, LSU

Abstract: A coupled CFD-MD scheme for simulating multi-scale (micro- and nano-) fluidic systems has been further developed. The coupling process involves three domains i.e. CFD, MD and an overlap hybrid region. A commercial continuum code, ANSYS/FLUENT is employed for the continuum part of the simulation, and LAMMPS is adopted for the MD part. Coupling schemes and data interfaces are implemented in ANSYS/FLUENT using its User Defined Function (UDF) capability. In the overlap region a file-based information exchange method is applied between atomistic and continuum fluidic information to define boundary conditions for the continuum region and the appropriate constraint for the atomistic one. The coupling is applied to a one-phase plane Couette flow where the fluid-solid interface is modeled at molecular level and by choosing suitable fluid-solid interaction parameters, the results are validated by comparing with analytical solution. Then, we study the physics of fluid-fluid planar interfaces under shear by modeling an atomistic binary liquid Couette flow to set the stage for applying the hybrid scheme to multiphase-multiscale systems. Discrepancies between available semi-analytic solution and atomistic results in two-phase simulation are explained by interfacial viscosity. This work will leverage force-field development efforts also under the LaSiGMA grant to enable multi-scale simulations involving interactions between biomaterials for which such force-field are unknown.

Keywords: Computational fluid dynamics, Molecular dynamics, Two-phase, Hybrid.

1. Introduction

Many interesting and significant phenomena in processes involving both purely biological and hybrid non-bio/bio systems occur at material interfaces and on the molecular level, while influenced by more “bulk” processes taking place on a much larger scale. Bio-molecules, such as mononucleotides or DNA fragments, interacting with natural, or functionalized/chemically modified wall surfaces in bio-analytical mixed-scale (micro/nano) fluidic instruments is a relevant example involving both bio and non-bio materials. To design such systems one must understand and resolve molecular interaction processes at interfaces, i.e. solid-fluid or fluid-fluid, where continuum description fails to describe proper physics, while resolving bulk transport and this necessitates the coupled simulation capabilities pursued by the present work.

The hybrid continuum and molecular dynamics (MD) approach is a simulation method which adopts the continuum hypothesis in capturing macroscopic features of a flow field and details atomistic inter-molecular interactions on interfaces of different materials by using the MD approach. This type of multiscale methods should have both the efficiency of the continuum model and the accuracy of the molecular model when necessary.

Several hybrid methods of this kind have been proposed in recent years which based on the information exchanged in overlapping region can be categorized into two main classes: 1) Exchanging velocity [1]: The velocity from the continuum model is imposed on the particle dynamics in the overlapping region, and the particle dynamics provides the velocity boundary condition for the continuum model. 2) Exchanging fluxes [2]: the fluxes of conserved quantities, including the mass flux, momentum flux and energy flux, are exchanged in the overlapping region.

In this paper we present a hybrid simulation by coupling a commercial continuum code, ANSYS/FLUENT, and an open source molecular dynamics code, LAMMPS [3], that builds on aforementioned works. The continuum solution is obtained by numerically integrating Navier-Stokes equations using ANSYS/FLUENT with the boundary information from MD implemented in ANSYS/FLUENT using its User Defined Function (UDF) capability. Modifications applied to LAMMPS include applying constrained dynamics which is imposed from solution of continuum part. The coupling is applied to a one-phase plane Couette flow where the fluid-solid interface is modeled at molecular level and by choosing suitable fluid-solid interaction parameters [4], the results are validated by comparing with analytical solution. Then, we study the physics of fluid-fluid planar interfaces under shear by modeling an atomistic binary liquid Couette flow to set the stage for applying the hybrid scheme to multiphase-multiscale systems.

2. Hybrid Method

Incompressible Navier-Stokes equations and the continuity equation are used to solve the flow in continuum region are written as, $\frac{\partial \vec{u}}{\partial t} + \vec{u} \cdot \nabla \vec{u} = -\frac{1}{\rho} \nabla p + \nu \nabla^2 \vec{u}$ and $\nabla \cdot \vec{u} = 0$ which are conservation of momentum and mass, respectively. Here u is the fluid velocity, p is the pressure and $\nu = \mu/\rho$ is the kinematic viscosity. These equations are solved numerically using Fractal Step method which is suitable for transient incompressible flows.

In the MD simulation to simulate the interaction of particles a Lennard-Jones potential $U^{LJ}(r) = 4\epsilon \left[\left(\frac{\sigma}{r} \right)^{12} - \left(\frac{\sigma}{r} \right)^6 \right]$ is used, where r is the pairwise distance between particles, ϵ and σ are the characteristic binding energy and length scales. The potential is truncated at $r = r_c = 2.2\sigma$, except when stated, and shifted to zero for computational efficiency [5]. The Verlet scheme is used for time integration of the interacting particles equation of motion to find the particles trajectories and the temperature of the fluid is maintained constant using a Berendsen thermostat [6]. Lennard-Jones units are used in the simulations, where ϵ , σ and m are the energy, length and molecular mass units exploited for non-dimensionalization.

3. Results and Discussion

We consider a sudden-start Couette flow which has been studied widely for the validation of a hybrid molecular-continuum solver [1,5]. Liquid Argon is confined between two parallel walls at $y = 0$ and $y = 52.1\sigma$ with periodic BC's imposed along x and z axes. We consider MD region on stationary (bottom) wall and continuum region on moving (top) wall. No-slip boundary conditions are imposed on the wall at the continuum level and the wall-fluid molecular interaction parameters are chosen such that yield a no-slip condition at walls in atomistic

region [4]. At constant temperature of $T = 1.1\epsilon/k_B$ and density $\rho = 0.81\sigma^{-3}$ the fluid is in a well-defined liquid phase with dynamic viscosity of $\mu = 2.14\epsilon\tau\sigma^{-3}$ [4]. The plots in Fig. 1 show the velocity profiles at different times from the initiation of the impulsive motion of one of the plates. At the latest times, the steady linear velocity profile is observed. It is obvious from Fig 1 (b) that the influence of the strong molecular interaction of the fluid with the wall material permeates into the continuum flow domain and it's this influence of fluid-wall interaction that pure continuum assumption is incapable of capturing.

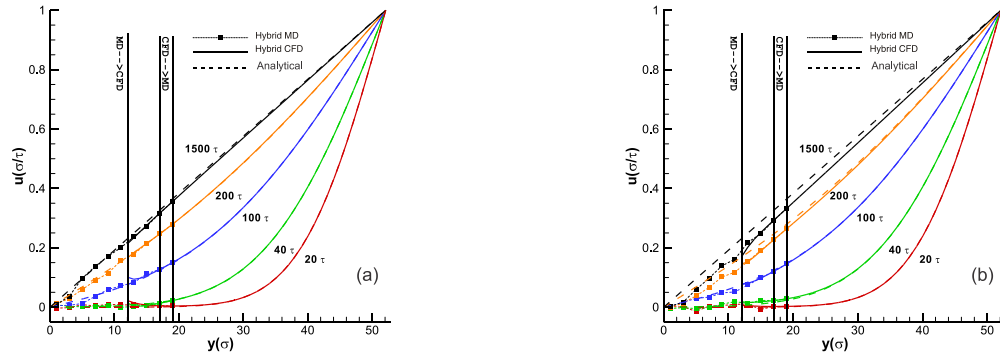


Fig 1. Velocity profiles at different times in CFD-MD hybrid simulation of sudden-start Couette flow with atomistic region on stationary (bottom) wall at two different value for the wall-fluid intermolecular interaction: (a) $\epsilon^{wf} = 0.6\epsilon$ and (b) $\epsilon^{wf} = 10\epsilon$

Next, a transient regime of a binary liquid Couette flow is studied in a purely atomistic simulation to set the stage for a multiphase atomistic-continuum simulation. The fluids are confined between two parallel walls at $y = 0$ and $y = h = 70\sigma$, and are chosen from LJ phase diagram to be in liquid state and well below the critical point.

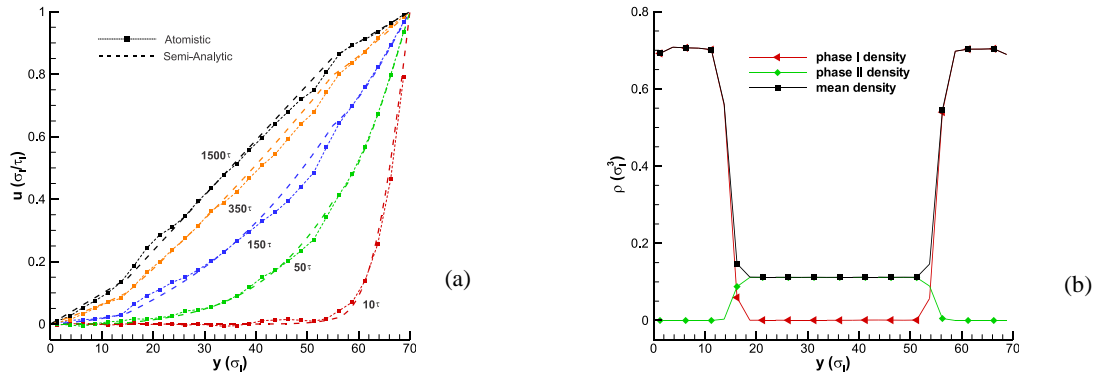


Fig 2. Comparing velocity profiles evolution with semi-analytic results (a) and density profile (b) in a two-phase Couette flow MD simulation (phase I = $[0, 15\sigma_I]$ and $[55\sigma_I, 70\sigma_I]$, phase II = $[15, 55]$).

The temperature of both liquids has been chosen $T = 1.1\epsilon/k_B$ and for this temperature the density of the phase I is chosen $\rho_I = 0.7\sigma_1^3$ while a density of $\rho_{II} = 0.85\sigma_{II}^3 (= 0.109\sigma_1^3)$, is chosen for phase II. The relation between LJ parameters of the phases can be obtained by considering that the real temperature and pressure are not

changing across the phases. Thus, choosing phase *I* parameters to be $\epsilon_I = \sigma_I = 1.0$, the phase *II* parameters are found to be $\epsilon_{II} = \epsilon_I T_I^* / T_{II}^* = 1.0 \epsilon_I$ and $\sigma_{II} = \sigma_I \sqrt{\rho_{II}^* \epsilon_{II} / \rho_I^* \epsilon_I} = 1.986 \sigma_I$. Dynamic viscosities of phase *I* and *II* are obtained to be $\mu_I = 1.21 \epsilon_I \tau_I \sigma_I^{-3}$ and $\mu_{II} = 2.63 \epsilon_{II} \tau_{II} \sigma_{II}^{-3} = 0.667 \epsilon_I \tau_I \sigma_I^{-3}$, respectively. Fig. 2(a) shows the comparison between atomistic and semi-analytic results for velocity time evolution across the field. There are noteworthy differences between the results can be explained in terms of the local viscosity in the vicinity of the fluid-fluid interface which different from that of the bulk viscosity. Thus, a partial slip can happen between two phases and cause the deviation from the semi-analytic results that are not capable of resolving this effect.

4. Conclusion and Future Work

A multiscale method for hybrid simulations of MD and CFD was presented. Navier-Stokes equations are solved where continuum assumption is accurate and MD simulations are used where atomistic description is important. MD and CFD are coupled via a flux continuity imposed in an overlap region. ANSYS/FLUENT is used for continuum simulation and LAMMPS adopted for MD region. The results of the Couette flow simulation show quantitative agreement with results from analytical solutions. An atomistic two-phase system was also set up to further expand the capability of the hybrid scheme in capturing the physics multiphase systems. The atomistic simulation of a binary Couette flow was presented and the results were compared with that of a semi-analytic solution. Significant discrepancies between simulation results and the semi-analytic solution in the vicinity of the fluid-fluid interface can be explained in terms of an interfacial viscosity which is different from the bulk. Next the stability of the fluid film in contact with wall and its critical thickness that makes it intact under the direct or indirect interaction of the wall and the other phase. Finally the hybrid scheme is applied to incorporate multiscale capability of the two-phase system.

5. Acknowledgments

This work is supported in part by LA-SiGMA, National Science Foundation (NSF) Award Number #EPS-1003897.

6. References

- [1] X. Nie, S. Chen, W. E and M. O. Robbins, A Continuum and Molecular Dynamics Hybrid Method for Micro- and Nano-Fluid Flow, *J. Fluid Mech.* 500, 55 (2004)
- [2] R. Delgado-Buscalioni and P. V. Coveney, Continuum-Particle Hybrid Coupling for Mass, Momentum, and Energy Transfers in Unsteady Fluid Flow, *Phys. Rev. E* 67, 046704 (2003)
- [3] S. Plimpton, Fast Parallel Algorithms for Short-Range Molecular Dynamics, *J Comp Phys*, 117, 1-19 (1995).
- [4] Thompson, P.A; Troian, S.M.; A general boundary condition for liquid flow at solid surfaces, *Nature*, 39, 360 (1997).
- [5] S. T. O'Connell and P. A. Thompson, Molecular Dynamics-Continuum Hybrid Computations: A Tool for Studying Complex Fluid Flows, *Phys. Rev. E* 52, 5792 (1995)
- [6] H. Berendsen, J. Postma, W.V. Gusteren, A. Dinola, J. Haak, Molecular Dynamics with coupling to an external bath, *J. Chem Phys*, 81, 3684-3690 (1984).

Impedance Characterization of YSZ based NO_x Sensor

Ling Cui and Erica P. Murray

Institute for Micromanufacturing, Louisiana Tech University

Abstract: Impedance spectroscopy was used to study the electrochemical response of NO_x exhaust gas sensors composed of Au electrodes and with a yttria-stabilized zirconia (YSZ) electrolyte. The sensor geometry was rectangular with a porous YSZ structure and Au wire electrodes. The porous YSZ electrolyte NO_x sensor has greater sensitivity compare to sensors with dense electrolyte structures. The impedancemetric response of the NO_x sensors was tested under various operating conditions where the temperature ranged from 600-700°C, and the concentrations of NO_x and O₂ were 0-100ppm, and 1.0-18.0%, respectively. Experiments were carried out under dry and humidified conditions. Data was collected over a frequency range of 0.1-1MHz. The impedance data for the NO response improved as the temperature increased, suggesting that electrochemical reactions proceeded more readily at higher temperature. The opposite response was observed for NO₂.

Keywords: Impedance spectroscopy, Gold electrode, Yttria-stabilized zirconia, NO_x , Porous phase, Gas sensor

1. Introduction

Automotive exhaust gas sensors are required to comply with governmental regulations for emission limits. Nitrogen monoxide (NO) and nitrogen dioxide (NO₂) (collectively referred as NO_x) are the more dangerous pollutants on air quality, particularly in high density urban areas. The Environmental Protection Agency (EPA) continues to issue new and more stringent standards for cars, light-duty and heavy-duty highway vehicles [1-2]. Advanced engines with better feedback control systems are being developed to reduce NO_x emissions and meet 2015 Tier 2, Bin 8 requirements established by the EPA [2]. These requirements drive the need for far more accurately measuring NO_x exhaust gas sensors that are capable of demonstrating greater stability, selectivity and sensitivity.

Impedancemetric NO_x sensing is a relatively new technique that appears to overcome the problems associated with amperometric and potentiometric sensors, which are more established sensing methods. In addition, impedancemetric NO_x sensors based on a porous YSZ electrolyte (instead of the traditional dense YSZ electrolyte structure) have demonstrated greater sensitivity toward NO_x. However, there are a limited number of studies concerning the mechanisms governing the electrochemical behavior of porous YSZ electrolyte and NO_x sensing. The aim of this study is to characterize the electrochemical response of NO_x sensors using porous YSZ in order to

better understand the kinetic reactions impacting NO_x sensing. Such knowledge will contribute to the advancement of NO_x sensor development.

2 Experimental

Rectangular slabs (give the dimensions) of porous YSZ were fabricated using slurry of YSZ (8 mol % Y_2O_3 -doped ZrO_2) powder, mixed with ethanol, dispersant, binders and graphite pore forms. Slab samples were sintered in air at 1100°C for 2 hours. The sensors consisted of four YSZ slabs with 2 cm Au wire in the middle and Au wire loops around the cross section [7]. This sample was dip coated with YSZ slurry in room temperature and fired in air at 1000°C for 1 hr. Figure 1a shows the top view of the sample. Figure 1b shows a simplified representation of the cross section of the sensor. Figure 2 shows the SEM image of sample surface, the interconnected network of 100 nm diameter YSZ particles. The surface area of the sample is around $10.5 \text{ m}^2/\text{g}$ and did not change after long time testing. This type of material has high stability.

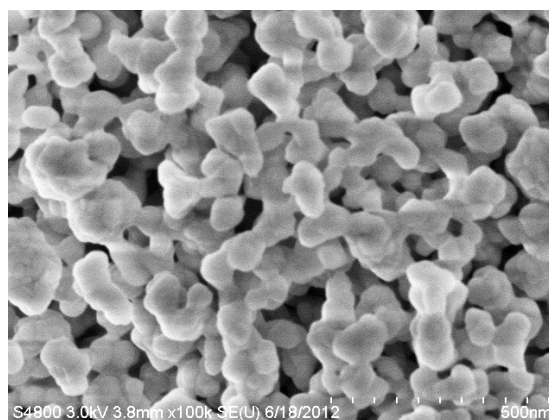
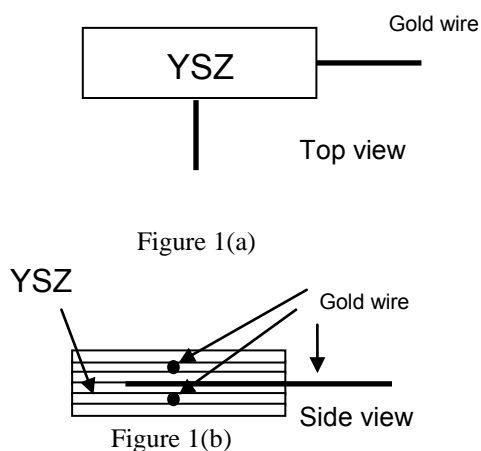


Figure 2

Figure 1. Top and side view of sample. Figure 2. SEM image of sample surface, the interconnected network of 100 nm diameter YSZ particles.

Data were collected in a quartz tube that was placed inside a tube furnace where both electrode and electrolyte were exposed at same environment. Samples were tested at temperatures ranging from $600\text{--}700^\circ\text{C}$ in NO and NO_2 atmospheres of 0-100 ppm with 1.0-18.0% O_2 , respectively, under both dry and humidified conditions. A standard gas system equipped with thermal mass flow controllers was used to control the gas flow. The study involved impedance spectroscopy using a Gamry Reference 600 that was capable of scanning over frequency of 1 MHz to 1 Hz at 10 steps per decade with an excitation voltage of 50 mV. Impedance spectra were analyzed using Gamry software.

3 Results and Discussion

The electrochemical response of the NO_x sensor is described by the impedance data shown in figure 3. The impedance is the electrical response that results from applying a sinusoidal voltage perturbation across the sensor. Using a small amplitude sine wave perturbation enables frequency analysis of a transfer function. The high frequency arc describes reactions within the electrolyte, such as oxygen ion conductivity, bulk and grain boundary resistance. There are two arc in the result data, the first part is low frequency arc (LFA) and the other is high frequency arc (HFA). There are two arc in the result data, the first part is low frequency arc and the other is high frequency arc. As expected, the high frequency data does not depend on the NO_x concentration. Whereas, the low frequency does depict NO_x dependence. Figure 3 indicates the impedance for NO is larger than that for NO_2 for $T = 600^\circ\text{C}$. Interestingly, as the temperature increased the impedance response for NO and NO_2 became more similar, as seen in the data collected at 650°C ; and then at 700°C the impedance for NO was slightly smaller than that of NO_2 . This suggests that reactions associated with NO (e.g., adsorption, dissociation, diffusion, charge transfer) may become more rapid with increasing temperature. The porous YSZ structure provides greater surface area and potentially additional pathways for reactions to proceed. In other NO_x studies with a porous YSZ electrolyte, NO and NO_2 reactions have been associated with different reaction pathways, but the mechanisms associated with these reactions were not well understood [4]. The present data may indicate a temperature dependence associated with those pathways.

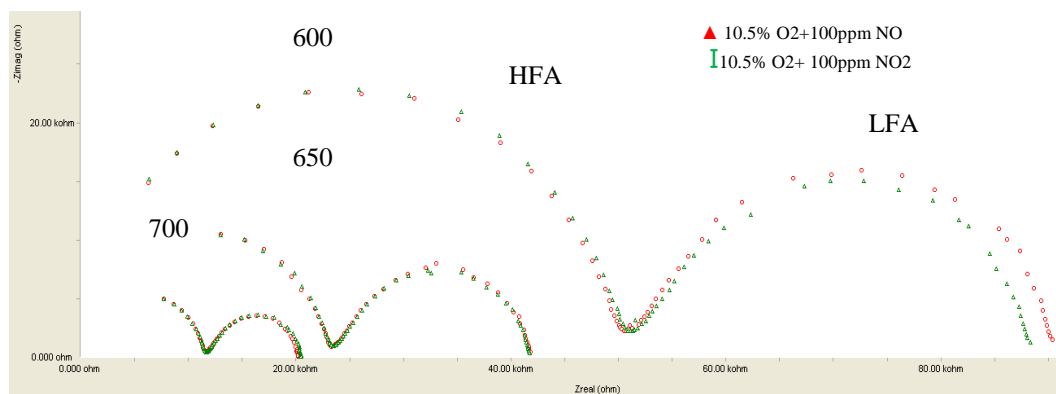


Figure 3

Figure 3. The impedance arc of NO is larger than NO_2 at 600°C and this phenomena changed at 700°C . NO_x sensor has greater sensitivity at low frequency (<100 Hz). Data collected under dry conditions.

The data for the O₂ and NO_x response shows that the impedance is slightly reduced under humidified conditions, suggesting that reactions proceed more readily when H₂O is present. The cross-sensitivity to water is undesirable as it indicates that water can change the NO_x response. Other data suggests that operating at T > 650°C can avoid this cross sensitivity. However, there may be a way to control water cross-sensitivity by modifying the available surface area (i.e., vary the porosity of the electrolyte) for reactions to take place.

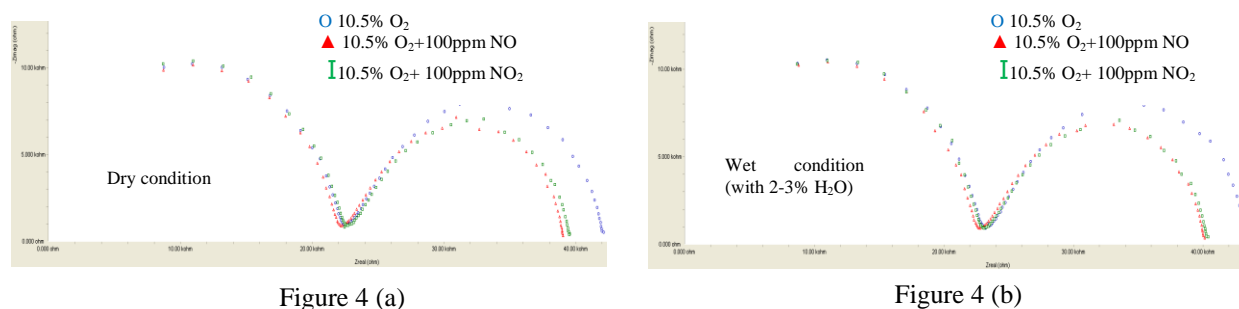


Figure 4. Difference between NO impedance and NO₂ is smaller at wet condition compared with dry condition at 650°C.

4. Conclusion

The impedance data indicated the NO_x response is temperature dependent. Additionally, cross-sensitivity to water impacts the NO_x response. To further understand impact of the electrolyte structure on the NO_x sensor electrochemical behavior, it is necessary to fabricate additional sensors with varied porosity. Changing the porosity will change the surface area with is directly related to the reactions sites available for NO_x reactions to take place. Comparing the sensors with different porosity under various operating conditions will provide valuable data that can be used to further interpret the NO_x sensor behavior.

5. Acknowledgments

The current work is funded by the NSF EPSCoR LA-SiGMA project under award #EPS-1003897.

6. References

- [1] United States Environmental Protection Agency, 2007 Progress Report: Vehicle and Engine Compliance Activities, EPA-420-R-10-022, Aug 2010.
- [2] United States Environmental Protection Agency, EPA's Program for Cleaner Vehicles and Cleaner Gasoline, EPA420-F-99-051, Dec 1999.
- [3] C. O. Park and N. Miura, *Sens. Actuators B*, Vol. 316, 113, 2006
- [4] L. Y. Woo, and L. P. Martin, *et al.*, *The Electrochemical Society*, 154 (4), 2007

Investigations of RuO₂ and SnO₂ Nanoclusters as Potential Lithium Ion Battery Electrode Materials

Aditya Das,^{1*} Ayorinde Hassan,¹ Ramu Ramachandran,¹ Collin Wick,¹
Anantharamulu Navulla² and Lamartine Meda²

¹Louisiana Tech University, Ruston, LA 71270;

²Xavier University of Louisiana, New Orleans, LA 70125

Abstract: Considerable effort is currently being expended in developing electrode materials in an attempt to improve the cycle life of Li-ion batteries, while preserving high energy and power density of the electrode material. Actualizing the full potential of using Li-ion batteries in everyday micro- and nano- scale devices, and even electric vehicles demands the development of new stable, safe electrode materials with high electron density. We present a computational investigation of nanoparticles of RuO₂ as a potential material to achieve this goal. Nanoparticles of SnO₂ are also studied in this work to ascertain the origin of the structural instability of SnO₂ as an electrode material when subjected to charge and discharge cycles in Li-ion batteries. Using molecular orbital based density functional theory, the voltages for Li ion adsorption on the metal oxide nanoparticles are calculated and the resulting structural changes examined.

Keywords: Li-ion batteries, metal oxide nanoparticles, anode coatings, voltages

1. Introduction

Li-ion batteries are considered to be the next generation in battery technology compared to other conventional battery technologies such as Nickel-Cadmium. The development of a wide array of mobile consumer electronics such as notebooks PCs, smartphones, PDAs, pocketsize calculators, camcorders, and portable liquid crystal TVs lead to an ever-present need for the use of batteries, and demand for batteries with longer life cycles. The increase in cyclability of Li-ion batteries will also be very important in transportation applications, such as electric vehicles, and hybrid electric vehicles. In fact, Li-ion batteries are being aggressively researched and implemented, albeit at a rudimentary extent in this area.

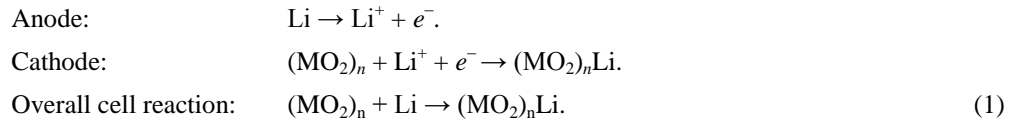
Of current research interest is the use of nanoscale crystalline thin-film electrode materials in improving the electrochemical performance of Li-ion batteries. Tin (Sn) oxide is one such material, as it has been shown to be a high Li-ion storage compound. It has twice the gravimetric capacity of carbon, and three times the volumetric capacity of carbon, hence it can store more than twice as much Li⁺ as graphite, the most common commercially

* LA-SiGMA REU student; Current Address: Carnegie Mellon University, Pittsburgh, PA 15289

available anode. However, it has significantly less cyclability because of structural instabilities in the oxide layer that develop over time.^{1,2}

We are also interested in examining RuO₂ as a possible Li-ion storage compound with desirable capacity and good cyclability. RuO₂ may be a good candidate for electrode materials due to its low resistivity (~40 μΩ m), good thermal stability up to 800 °C and chemical stability.³

We adopt the approach of the Ceder group⁴ to calculate the voltage of the two metal oxides against a Li|Li⁺ anode, which implies the following cell reactions:



The free energy changes for the cell reaction is used to calculate the cell voltage from the Nernst relationship:⁴

$$E(\text{V}) = \frac{\left[G_{(\text{MO}_2)_n}^\circ + G_{\text{Li}}^\circ - G_{(\text{MO}_2)_n\text{Li}}^\circ \right] \text{J mol}^{-1}}{xF(\text{C mol}^{-1})}, \quad (2)$$

where x is the number of electrons involved in the reaction, and F is the Faraday.

2. Computational Methods

Molecular orbital calculations in the framework of Kohn-Sham density functional theory (DFT)⁵ has been utilized for all calculations reported. The preferred structure, energetics, and electronic properties of (SnO₂)₆ and (RuO₂)₆ clusters were assessed by the recently developed M06 DFT functional of Zhao and Truhlar.⁶ The Los Alamos National Laboratory double ζ effective core potential (LANL2dz)⁷ basis sets have been employed. Geometries were optimized without any symmetry constraints, and harmonic vibrational frequency calculations were performed at the same level of theory to confirm the structures as minima on their respective potential energy hypersurface. All calculations were performed on LONI computers using the Gaussian 09 suite of programs. We considered the nanoparticles with chemical formula Ru₆O₁₂ and Sn₆O₁₂, respectively.

3. Results and Discussions

Several geometric possibilities for Li-ion chemisorption were assessed. The adsorption sites for Li^+ deposition in both nanoclusters are shown in Figure 1. Both Ru_6O_{12} and Sn_6O_{12} can be considered as hexamers of RuO_2 and SnO_2 respectively. The trigonal planar co-ordination of oxygen is more common in SnO_2 than RuO_2 ; hence RuO_2 has a more varied structure than SnO_2 , giving it more isoforms to consider.

For the $(\text{RuO}_2)_6$ cluster, we found that Li adsorption on its surface favors the corner (C and C' in figure 1) and

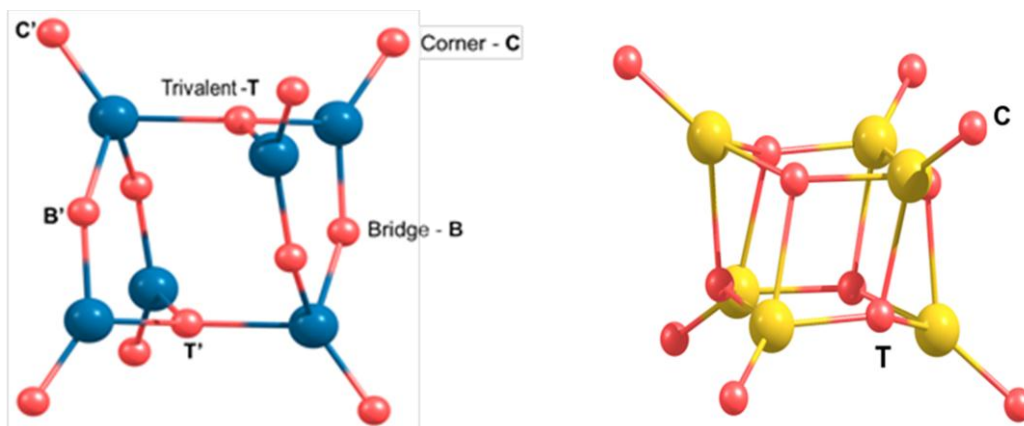
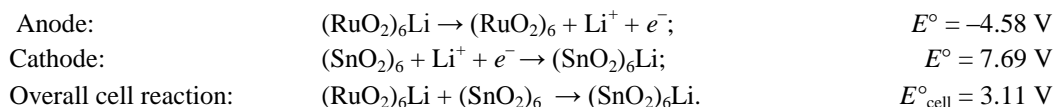


Figure 1: Nanoparticles of RuO_2 (left) and SnO_2 (right) showing the labeling used for various Li adsorption sites. Each nanoparticle has the chemical formula $(\text{MO}_2)_6$, where $M = \text{Ru}$ or Sn .

trivalent (T and T') sites. The placement of Li in the center of the cluster is highly unfavorable, and the Li atom gets pushed out from the cluster during optimization. We have calculated the voltages for the net reaction in an electrochemical process using Eq. (2), which implies that the reference is the $\text{Li}|\text{Li}^+$ anode. For Li adsorption on the C-T sites in each case, the voltages are calculated to be 4.58 V for Ru_6O_{12} , compared to 7.69 V for Sn_6O_{12} .

While the voltage for Ru_6O_{12} is not as high as that of Sn_6O_{12} , the obtained value for Ru_6O_{12} suggest that it could be a prospective anode coating material especially due to its stability, and potential to suffer less from capacity

fading/poor cyclability. In fact, from the results obtained thus far, one could construct a hypothetical cell with nanostructured metal oxide electrodes as follows:



4. Summary and Future work

The interaction of Li ions with transition metal oxide thin film nanoparticle surfaces is being studied with density functional theory. The high unfavorability of Li placement in the middle of the Ru_6O_{12} cluster appears to be a promising result because intercalation of Li^+ leading to large structural change is a problem in Sn and Sb anodes.

We are studying these small nanoclusters as models for nanoscale domains, we intend to increase the size and geometry of the cluster. To this end, we are currently examining the results of our Gaussian basis sets calculations against double numerical basis sets with polarization (DNP) as implemented in DMol3 module of the Materials studio suite of program. This will allow us to assess the reliability of GGA(PBE)/DNP level of theory, and afford us the ability to extend our cluster size to as large as 200 atoms. We hope to gain enough insight into the energetics and electronic properties of these systems to be able to develop a methodology to compare many different potential electrode materials for optimized structural and voltage properties for lithium ion oxidation/reduction.

5. Acknowledgments

This material is based upon work supported by the National Science Foundation under the NSF EPSCoR Cooperative Agreement No. EPS-1003897 with additional support from the Louisiana Board of Regents.

6. References

- [1] Li, N.; Martin, C. R.; Scrosati, B. *Electrochem. Solid-State Lett.* **2000**, *3*, 316.
- [2] Brousse, T.; Retoux, R.; Herterich, U.; Schleich, D. M. *J. Electrochem. Soc.* **1998**, *145*, 1.
- [3] Krusin-Elbaum, L.; Wittmer, M.; Yee, D. S. *Applied Physics Letters* **1987**, *50*, 1879.
- [4] Mueller, T.; Hautier, G.; Jain, A.; Ceder, G. *Chemistry of Materials* **2011**, *23*, 3854.
- [5] Parr, R.G.; Yang, W. *Density-Functional Theory of Atoms and Molecules*. Oxford University Press: New York, 1989.
- [6] Zhao, Y.; Truhlar, D. *Theor. Chem. Acc* **2008**, *120*, 215.
- [7] Hay, P. J.; Wadt, W. R. *J. Chem. Phys* **1985**, *82*, 270.

Molecular Dynamics Simulation and Visualization of Thermal Barrier Coatings

Sanjay Kodiyalam¹, Michael G. Benissan¹, Stephen Akwaboa¹, Partick Mensah¹, Amitava Jana¹, Diola Bagayoko²

Department of Mechanical Engineering¹/Physics², Southern University Baton Rouge
sanjay_kodiyalam@subr.edu, mykkellg@gmail.com, stephen_akwaboa@subr.edu, patrick_mensah@subr.edu,
amitava_jana@subr.edu, Bagayoko@aol.com

Abstract: Parallel molecular dynamics code for simulating the interface of Yittria stabilized Zirconia and the thermally grown oxide (α -Alumina) is developed using empirical potentials available in the literature. With only short (finite) ranged interactions the CPU time varies linearly with the number of atoms number per CPU and is roughly constant with proportionally increase in system size and number of CPU. This scaling has been verified up to 512 CPU of the LONI machine Queenbee and is preserved with only the real space part of the long (infinite) ranged Coulomb interactions as they are cutoff at a fixed atomic separation and are therefore effectively short ranged. Inclusion of the reciprocal space part of the long ranged interactions, with the same fixed cutoff in real space, increases the CPU time significantly: It scales, as expected, as the square of number of atoms per CPU. The corresponding large increase in CPU time suggests constructing empirical potentials with screened Coulomb interactions to preserve linear scaling. Moving atoms with bonds are visualized stereographically using CAVE library-based code.

Keywords: Yittria stabilized Zirconia, Alumina, Ewald sums, CAVE

1. Introduction

Thermal barrier coatings (TBCs) are used in high temperature applications like turbine blades (Fig. 1) to increase the operating temperature beyond the melting point of the substrates. The coating is of a material with low thermal conductivity such as Yittria stabilized Zirconia (YSZ). A bond cote, typically an alloy M-Cr-Al-Y, between the substrate and the TBC is used to aid in the adhesion of the TBC to the substrate [1]. During the deposition of the TBC as well as during the high-temperature operation of the turbine a thermally grown oxide (TGO) layer, of α -Alumina, develops due to diffusion of oxygen through YSZ [2]. Of interest therefore are thermal properties of YSZ, Alumina, and the bond coat. These include the thermal conductivity of the individual components as well as the thermal resistance of the interfaces. The longer time-scale process of oxygen diffusion through YSZ and Alumina is also of interest in the context of TGO growth as it is the primary mechanism of TBC failure by spallation. As part of a multi-scale approach to studying TBC's molecular dynamics (MD) code is developed to focus on short length scales complementary to continuum simulations at longer length scales [3]. The initial focus is on simulating α -Alumina (Al_2O_3) and Ω -YSZ ($\text{Zr}_5\text{Y}_2\text{O}_{13}$). While the mole percentage of Y_2O_3 in Ω -YSZ (17%) is much higher than in TBC's (6%) it is chosen here for comparing to results in literature.

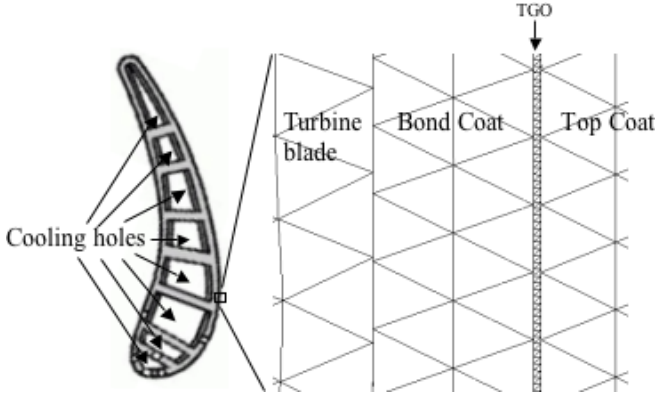


Fig. 1. Schematic [4] of a turbine blade. The enlarged view shows the top coat (the TBC), TGO, and bond coat. The typical length scale for the three layers together is $\sim 500 \mu\text{m}$.

2. Molecular dynamics Simulations

2.1 Empirical Potentials

Empirical potentials for both YSZ and Alumina are adopted from literature. The potential for Alumina [5] has two body terms corresponding to steric repulsion, Coulomb, charge-dipole, and van Der Walls interactions, and three body terms corresponding to bond-bending and stretching. This potential was developed to simulate solid, molten, and amorphous Alumina and its interface with ceramics. An important feature of this potential, from the point of view of computations, is that the Coulomb and charge-dipole interactions are screened and all terms in the potential are then cutoff beyond an atomic separation of 6 \AA . The potential for YSZ [6] has only two body terms of the Born-Meyer-Buckingham type with terms accounting for Pauli repulsion and van Der Walls interactions. In addition there are long (infinite) ranged Coulomb interactions.

2.2 Ewald summation

Long ranged Coulomb interactions lead to infinite sums for the interaction energy E between any two ions separated by a distance \vec{r} due to periodic boundary conditions. These interactions are handled via Ewald summation [7]:

$$E(\vec{r}) = \Gamma_{0.5}^{-1} \epsilon \left[\sum_{\vec{R}} \frac{\Gamma(0.5, (\epsilon |\vec{r} + \vec{R}|)^2)}{(\epsilon |\vec{r} + \vec{R}|)} \right] + \frac{\Gamma_{0.5}^{-1} \epsilon^{-2} \pi^{1.5}}{V} \left[\sum_{\vec{G}} \frac{\Gamma(1, (|\vec{G}/2\epsilon|)^2)}{(|\vec{G}/2\epsilon|)^2} \right] \quad \text{where } \vec{R} \text{ are}$$

multiples of the vectors defining the extent MD system and \vec{G} are multiples of the corresponding reciprocal basis. As in [6], the real space terms are cutoff at the same distance at which other, short ranged, terms in the empirical potential vanish: 10 \AA . The minimum system size is larger than this cutoff and this results is only the $\vec{R} = \mathbf{0}$ term in the real space (R-space) summation. The allowed error due to cutting of the real space sum then determines the convergence parameter ϵ . This error is chosen to be $10^{-8} \text{ eV per atom}$. The same error choice in reciprocal space then determines the cutoff magnitude of \vec{G} . The constant cutoff in real space is expected to make the CPU time required for computing this part of the interaction proportional to the total number of ions - exactly as that for short ranged interactions. This constant cutoff together with a constant density of ions results in a constant ϵ , independent of the total number of atoms. The magnitude of the cutoff in reciprocal space is therefore constant. However as the density of \vec{G} vectors increases with the total system size the CPU time required for computing the reciprocal space (G-space) sum is expected to be proportional to the square of the number of ions per CPU. Both these trends are seen the results. Evaluation of all terms in the summation, and of other short-ranged terms in the empirical potential, is via 2nd order interpolation of the tabulated exact values.

3. Results and Discussions

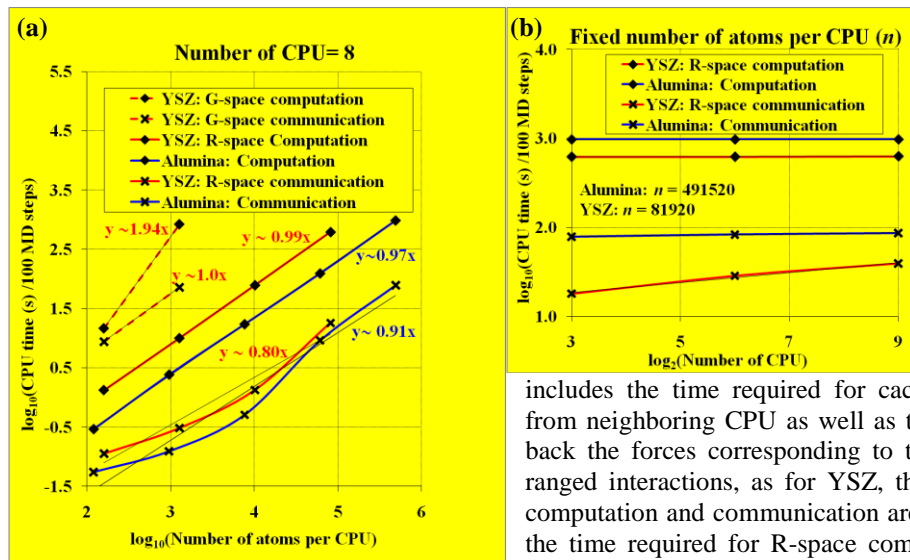


Fig. 2. Log-log plots of the computation and communication time versus the number of atoms per CPU (a), and the number of CPU (b). The computation time includes the time required for computing the global stress and for the MD evolution. The communication time

includes the time required for caching the atomic coordinates from neighboring CPU as well as the time required for sending back the forces corresponding to the cached atoms. With long ranged interactions, as for YSZ, the time required for G-space computation and communication are separately considered while the time required for R-space computation and communication include the times for handling the other short (finite) ranged interactions also.

Figure 2a shows the variation of the CPU time required for computation and communication with the number of CPU fixed at 8. With only the R-space terms of the long ranged interactions in YSZ, the computation time scales linearly with the number of atoms per CPU – exactly similar to that of Alumina. The difference between the two cases can be accounted for simply by the number of neighbors per atom in the two cases and the additional R-space computations due the long ranged interactions in YSZ. The communication time in all cases with short ranged interactions, even with increasing the number of CPU (Fig. 2b), is much smaller than the computation time leading the parallel efficiencies > 90%. However, the deviation in the variation of the communication time from the power law of $(\text{Number of atoms per CPU})^{2/3}$ shows that more precise accounting of this time is needed together with a further simplification of the communication algorithm to avoid steps proportional to the number of atoms per CPU. Inclusion of the G-space terms of the long ranged interactions increases the communication and computation time enormously – varying respectively linearly and as the square with the number of atoms per CPU (Fig. 2a) thereby making these terms the primary bottleneck in the parallel MD simulations at scales larger than ~1000 atoms per CPU. While not evident in Fig.2, even with a fixed number of atoms per CPU, a larger total number of atoms will proportionally increase the computation and communication time required for handling these G-space terms.

4. Visualization of MD configurations

CAVE-library based code to stereographically visualize atomic configurations develop earlier [8] has been used to visualize the melting of α -Alumina (Fig. 3). Moving atoms with bonds have been visualized by reading saved

atomic configurations in the main loop of the CAVE library that runs asynchronously relative to the display loop(s). Currently, systems with ~1000 atoms can be visualized interactively.

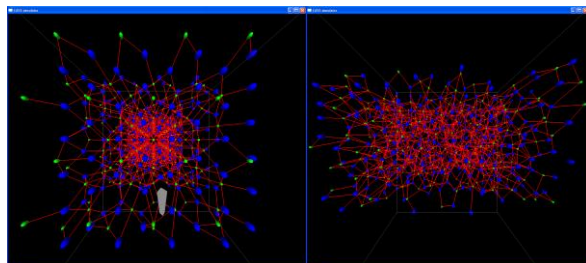


Fig. 3. Perspective views of crystalline (left) and liquid (right) Alumina visualized using the CAVE-library based code. Aluminium atoms are shown smaller in green while Oxygen atoms are shown in blue. Bonds are shown in red.

5. Conclusion and future work

Parallel molecular dynamics code for simulating two components of thermal barrier coated systems has been developed. In the absence of long ranged Coulomb interactions the code can handle ~0.1-0.5 million atoms per CPU – with roughly constant execution time up to 512 CPU. The scaling is preserved with only the real space part of the Coulomb interactions. Inclusion of the reciprocal space terms of the Coulomb interaction increases the CPU time significantly and limits studies at comparable execution speed to ~1000 atoms per CPU and a total size of ~10,000 atoms. The code may be used to study matched interfaces in the thermal barrier coated systems while mismatch systems, and those including nano-sized structures as cracks and nano-crystals, will required much larges system sizes beyond the reach of the current code. Other algorithms such as Fast Fourier Transforms and Fast Multipole Method need to be explored for efficient simulation of larger numbers of atoms. Alternatively, modification of the empirical potentials, by screening the Coulomb interations, is needed. The efficiency of the visualization code is being further developed [9] to interactively more than the current limit of ~1000 atoms.

6. Acknowledgments

The work is funded by the NSF EPSCoR LA-SiGMA project under award #EPS-1003897 and NASA EPSCoR grant NNX09AP72A.

7. References

- [1] W.O. Soboyejo, P. Mensah, R. Diwan, J. Crowe, and S. Akwaboa, *Mater. Sci. Eng. A* 528, 2223 (2011).
- [2] K.A. Marino, B. Hinnemann, and E.A. Carter, *Proc. Natl. Acad. Sci. U.S.A.*, **108**, 5480 (2011).
- [3] S. Akwaboa, S. Kodiyalam, A. Jana, P. Mensah, and R. Diwan, *Proceedings of the 19th Annual International Conference on Composites or Nano Engineering*, Shanghai, China, July 2011.
- [4] From http://www.mmlab.mech.tuat.ac.jp/mmlab/fig/fig_01.jpg
- [5] P. Vashishta, R.K. Kalia, A. Nakono, and J.P. Rino, *J. Appl. Phys.* 103, 083504 (2008).
- [6] K.C. Lau, and B.I. Dunlap, *J. Phys.: condens. Mater* 23, 035401 (2011).
- [7] M.P. Allen, and D. J. Tildesley, *computer Simulation of Liquids*, Oxford Science Publications, (1991).
- [8] G.R. Wright, S. Kodiyalam, A. Jana, LA-SiGMA REU report, July 2011.
- [9] C. Vanderlick, S. Kodiyalam, A. Jana, Ongoing LA-SiGMA REU June-July 2012.

Molecular Dynamics Simulation Study of the Effect of Electric Field on DNA Mononucleotides Dynamics in Nanoslits

Kai Xia¹, Brian Novak¹, Dimitris Nikitopoulos¹, Steven Soper² and Dorel Moldovan¹

¹Department of Mechanical Engineering, Louisiana State University, Baton Rouge, LA 70803

²Department of Biomedical Engineering and Department of Chemistry, University of North Carolina, Chapel Hill, NC 27599

Abstract: Transport of DNA mononucleotides through nanochannels might be used to distinguish them by comparing their flight times over a fixed distance. Using nonequilibrium molecular dynamics (MD) simulations we investigate the dynamics of DNA mononucleotides moving through hydrophobic nanoslits driven by electric fields. Our simulations show that during the translocation process all four nucleotides adsorb and desorb from the slit-walls multiple times. The mechanism of absorption/ desorption events was studied by monitoring the angle of the nucleotide bases with the walls. Various nucleotide properties such as their velocity and their association with sodium ions depend on whether or not the nucleotide is adsorbed on the walls and on the strength of the electric field. The association of sodium ions with the phosphate group of the nucleotides has a great influence on nucleotide velocity along the direction of the applied field and their mean velocity increases nonlinearly with the electric field.

Keywords: Molecular dynamics, DNA sequencing, nanoslit, sodium-nucleotide association

1. Introduction

Interesting new nanotechnologies are being developed for sequencing hetero-polymers such as DNA. This paper addresses an approach to DNA sequencing which combines sequential DNA disassembly and subsequent transport of mononucleotides through a nanochannel sensor. The four kinds of mononucleotides that result from DNA disassembly can be distinguished by measuring their flight time during their translocation through a nanochannel of a given length. The basic idea is that every kind of mononucleotide has a specific flight time which depends on its molecular identity and on the specificity of interaction with the channel walls. The advantage of the proposed sequencing methodology is that in practice only the presence of the mononucleotides rather than their identity needs to be detected. The realization of this device for directly reading structural information from DNA requires a fundamental understanding of the transport dynamics of mononucleotides through nanochannels and the characteristics of the interaction between mononucleotides and nanochannel walls.

2. Simulation Method

To help understand the dynamics of mononucleotide travelling through a nanochannel, equilibrium and non-equilibrium molecular dynamics simulation were performed with LAMMPS [1] software package. The CHARMM27 force field [2] was used to describe the interactions of the mononucleotides. The interaction of water molecules is described by CHARMM TIP3P model. The simulation system consists of a single mononucleotide (dAMP, dCMP, dGMP or dTMP) in water-NaCl solution of 89 mM concentration located between two slabs composed of Lennard-Jones atoms distributed randomly in the slabs and tethered to their original positions. The 1.2 nm thick slit walls are placed 3 nm away from each other. Only the wall atoms were thermostatted at 300K using the Berendsen thermostat method [3]. The flow in the slit was generated by applying an external electric field. The electrostatic interactions were evaluated by using the 3-dimensional particle-particle particle-mesh (PPPM) method [4] corrected for slab geometry. The box length in the non-periodic direction was taken to be three times the simulation box length in the direction along which the electric field was applied. The simulation system is shown in Fig. 1. Several different electric fields (0.6, 0.3, 0.1 and 0.0144V/nm) are applied.

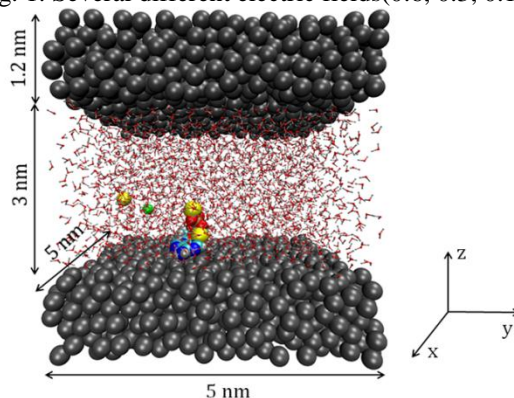


Fig. 1. The simulation system consisting of a mononucleotide, sodium chloride, water and walls. The walls are composed of tethered Lennard-Jones atoms thermostatted at 300K. The green sphere represents a chloride ion, yellow represents sodium ions, red represents non-water oxygen atoms, blue represents nitrogen atoms and water molecules are the smaller background molecules (red and white). Periodic boundary conditions were applied in x and y directions

3. Results and Discussions

The simulations show that the phosphate group of the mononucleotides on which the net charge is $-2e$ (e = electronic charge) can be associated with sodium ions due to the electrostatic interaction. This association significantly influences the traveling velocity of mononucleotides. The mononucleotides are driven by electric field and the driving force is proportional to the net charge on it. Therefore, the more sodium ions that are associated with a mononucleotide, the lower the net charge the complex has and the slower its motion. Fig. 2 shows the association number and the position of dTMP in the direction of the electric field versus time. This

show that indeed the mononucleotide moves slower when the association number is 1 than when no sodium ion is associated. As illustrated in Fig. 2, in the 40 ns to 50 ns interval, the average association number is equal to 2 and accordingly the mononucleotide hardly moves forward.

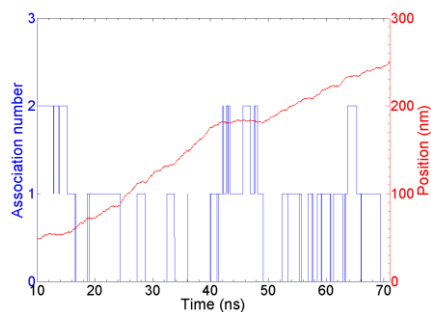


Fig. 2. Time dependence of the association number and the coordinate along the direction of the applied electric field (x) for a dTMP molecule moving in the slit. When one or two sodium ions are associated with the ionic phosphate group, the velocity of the nucleotide decreases significantly.

In both no-flow (equilibrium) and flow simulations the nucleotides are adsorbed and desorbed from the wall multiple times. In the adsorbed state the hydrophobic base part of the nucleotides tends to sit on the surface while the hydrophilic phosphate group points away from the surface. All four nucleotides once they are adsorbed on the wall they stay on wall for a while. Fig. 3 shows the z position of dTMP versus time. This clearly shows that the dTMP is adsorbed and desorbed from the wall several times during the 60ns interval.

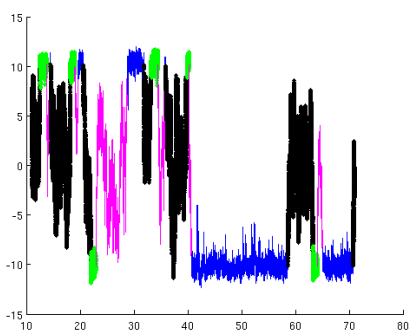


Fig. 3. A 60 ns trajectory segment of a dTMP depicting the time dependence of the z -coordinate of the mononucleotide center of mass. The green and blue lines represent adsorption periods, black and pink lines represent desorption periods.

The average velocity along the direction of the applied field for dTMP in adsorbed and desorbed states at two states of ionic association is given in Table 1. The nucleotide and the ions are driven electrophoretically by an electric field $E = 0.1$ V/nm. The MD simulations show that the velocity of the dTMP in both states of association ($N=0$ and $N=1$) is smaller in the adsorbed state than in the desorbed state. Moreover, the ionic association leads to large decrease of the average velocity in both adsorbed and desorbed states.

Association number	Nucleotide velocity	
	V _{adsorbed} (m/s)	V _{desorbed} (m/s)
0	4.92	5.83
1	1.65	2.07

Table. 1. The average nucleotide velocity of dTMP in adsorbed and desorbed states at two states of ionic association.

4. Conclusion

Using MD simulations we investigated the translocation of DNA nucleotides through 3 nm wide slits in the presence of an electric field. Our simulations indicate that during the translocation process the phosphate group of the nucleotide bases may associate with one or two neutralizing sodium ions. This association process has a strong impact on the nucleotide motion in the nanoslit. When one or two sodium ions associate with the ionic phosphate group of the nucleotide, the velocity of the nucleotide decreases significantly in both adsorbed and desorbed states. The increase of the externally applied electric field leads to an increase of the nucleotide average velocity; the velocity increase is nonlinear with the strength of the electric field.

5. Acknowledgments

Work supported in part by NSF-EPSCoR Grant # EPS-1003897. Computer resources were provided by LONI and HPC @ LSU.

6. References

- [1] S. Plimpton, *J. Comput. Phys.* 117, 1, 1995.
- [2] N. Foloppe, and A. D. MacKerell, *J. Comput. Chem.* 21, 86, 2000.
- [3] H. J. C. Berendsen et al., *J. Chem. Phys.* 81, 3684 (1984).
- [4] R. W. Hockney and J. W. Eastwood, "Computer Simulation Using Particles", Adam Hilger, 1989.

Molecular Dynamics Simulations of the Interaction of a PLGA Nanoparticle with a Lipid Bilayer

Brian Novak¹, Cristina Sabliov², Carlos Astete², Dorel Moldovan¹

¹Department of Mechanical Engineering, Louisiana State University, Baton Rouge

²Department of Biological and Agricultural Engineering, Louisiana State University, Baton Rouge

Abstract: Poly(lactic-co-glycolic acid) or PLGA is a biodegradable polymer which is being used for drug delivery. Preliminary potential energy parameters were used in a molecular dynamics simulation of a 3 nm particle in contact with a DMPC lipid bilayer. This simulation showed that the particle interacted strongly with the bilayer. It caused a local change in the lipid orientation, indented the bilayer, and caused a local thinning of the bilayer.

Keywords: Poly(lactic-co-glycolic acid), DMPC lipid bilayer, drug delivery

1. Introduction

Poly(lactic-co-glycolic acid) (PLGA) is a polyester copolymer composed of lactic and glycolic acid units. It is synthesized by a ring opening reaction of the cyclic dimers of lactic and glycolic acid. PLGA degrades slowly by hydrolysis. This degradation and the fact that the monomer units have a low toxicity make PLGA useful for encapsulation and delivery of drugs. Figures 1 a) and b) show the structure and chemistry of PLGA.

In order for a drug delivery vehicle to be useful, it must get the drugs across the cell membrane. This might be accomplished if the entire assembly is taken into a cell or if the drug molecules are released near the cell membrane and only they are taken into the cell. In either case, the interaction of the assembly with the cell membrane is important. The cell membrane is composed largely of lipids; therefore we used a lipid bilayer as a model for a cell membrane. Molecular dynamics (MD) simulations were used to study the interaction of a PLGA particle with a diameter of about 3 nanometers with a dimyristoylphosphatidylcholine (DMPC) bilayer in aqueous solution. Figure 1 c) shows the structure of DMPC.

2. Simulation Methodology

In classical molecular dynamics simulations, the interactions between atoms are usually specified by a set of analytical potential energy functions. The functions and the parameters in them constitute a force field. For our simulations, the GROMOS 54a7 united atom force field[1] was used for the DMPC, ions, and PLGA along with the SPC water model. There were existing parameters for the DMPC and ions, but none for the PLGA. To get parameters for the PLGA, the Automated Topology Builder (ATB) web server[2] was used on four different molecules in order to obtain the parameters for end and middle units for both lactic acid and glycolic acid type units. See Fig. 1 d). The only modification made to the ATB parameters was to modify the partial charges slightly

so that there was zero overall charge on every type of monomer. This ATB parameter set for PLGA has not yet been tested against any experimental data.

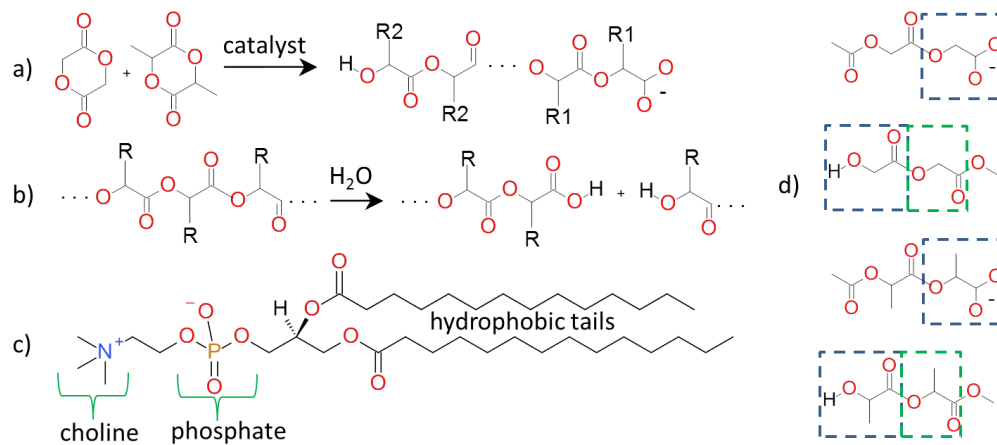


Fig. 1. Structures and chemistry of PLGA and DMPC. a) Synthesis of PLGA. b) Hydrolysis of PLGA. c) DMPC structure. d) Molecules used to obtain force field parameters for PLGA. The different types of monomer units are enclosed in boxes with dashed lines.

The following is an explanation of how the PLGA particle was constructed. Using the average molecular weight of real PLGA (55,000 g/mol), the approximate density of real nanoparticles,[3] the assumption that all of the charged groups will be found on the surface of the particle, and using the same surface charge density that would be found in real nanoparticles led to the conclusion that for a 3 nm particle there should be 8 polymer molecules with 20 monomer units in each molecule. One molecule was constructed with 50% glycolic acid and 50% lactic acid units, and 8 of these molecules were used in the particle. It was assumed that the stereochemistry of the two units of the cyclic dimers of lactic acid was the same, but that a racemic mixture (50% R, 50% S) of the dimers was used for synthesis. The nanoparticle was constructed from the 8 polymer molecules using the following steps: 1) Placed the 8 molecules in a 4.5 X 4.5 X 4.5 nm box with random orientation using packmol.[4] 2) Added water molecules in a 9.6 X 9.6 X 9.6 nm box with random orientation using the GROMACS[5] genbox utility. 3) Removed a sphere of water centered on the PLGA with a radius of 3.90 nm using VMD,[6] 4) Used the GROMACS[5] genion utility to replace 8 water molecules with 8 sodium ions to balance the charge on the PLGA. 5) Restraints were added to the water oxygen atoms. 6) Energy minimization. 7) The average solvent temperature was kept at 350 K, and the average PLGA temperature was kept at 800 K for 2.34 ns while continuously decreasing the simulation box size in all directions at a rate of -0.006 nm/ps. The time step was 1.0 fs. The restraint positions of the oxygens were scaled as the box size was decreased. 8) The same as step 7, except that the time was 2.49 ns, the temperature of the PLGA was 750 K, and the time step was 0.75 fs. 9)

Constant temperature of 300 K and constant pressure of 1.0 bar for 3.0 ns. 10) The same as step 9, except with the restraints on water oxygen atoms removed. Steps 6-10 were performed with GROMACS 4.5.3.[5]

The particle from step 10 above was placed either in contact with a bilayer or such that the minimum distance in the bilayer normal direction between a PLGA atom and a lipid atom was 0.7 nm. The DMPC bilayer was taken from a configuration on the ATB website[2] containing 128 lipid molecules. Water and sodium ions were added to the PLGA + DMPC system using packmol[4] to get a box dimension in the bilayer normal direction of about 11.0 nm. A picture of the final system is shown in Fig. 2 a). The simulations of this system consisted of restraining the DMPC and PLGA for energy minimization and equilibration of the solvent for 3.0 ns at a temperature of 323.0 K and constant volume, removing the restraints, and simulating at a temperature of 323.0 K and a pressure of 1.0 bar using semi-isotropic pressure coupling. The time step for the MD simulations was 2.0 fs.

3. Results

When the PLGA particle was started 0.7 nm from the bilayer, the particle moved away from the bilayer. This is an indication that there is a free energy barrier for the particle to come in contact with the bilayer. This is likely due to the ordered water molecules near the bilayer and particle which have to be rearranged when the particle and bilayer come in contact with each other.

When the particle was started in contact with the bilayer, it interacted strongly with it and induced local changes in the bilayer structure. Properties were averaged over 8 ns, after 24 ns of equilibration. Fig. 2 b) is a plot of the probability of observing a choline nitrogen (N) atom or a phosphate phosphorus (P) atom as a function of distance in the plane of the bilayer from the center of mass of the particle ($d_{xy,PLGA}$). Since the PLGA is negatively charged, there is a depletion of P and an excess of N at the particle center. There is also ordering of the P atoms further out, which is indicated by the oscillations in the probability. Fig. 2c) is a plot of the bilayer thickness as a function of $d_{xy,PLGA}$. The particle sinks into the bilayer, causing a local thinning. Fig. 2 d) is a plot of the angle of the P-N vector with the outward bilayer normal (Fig. 2e) as a function of $d_{xy,PN-PLGA}$, where the reference is the P-N geometric center. The particle causes the lipid heads to locally point more inward on the side of the bilayer that the particle directly interacts with and causes the lipid heads to locally point more outward on the other side.

4. Conclusion

An adsorbed 3 nm PLGA particle has a significant local effect on the structure of a DMPC bilayer. The particle indents the bilayer and has an effect on lipid head orientation, even on the side of the bilayer not in direct contact with the particle. Future work will include validation of the force field, use of slightly larger particles and making certain they have a solid core, and comparison of the interaction of PLGA (negatively charged) particles, with those of trimethyl chitosan (a positively charged polymer) coated PLGA particles.

5. Acknowledgments

The current work is funded by the NSF EPSCoR LA-SiGMA project under award #EPS-1003897. Computational resources were provided by LONI and HPC @ LSU.

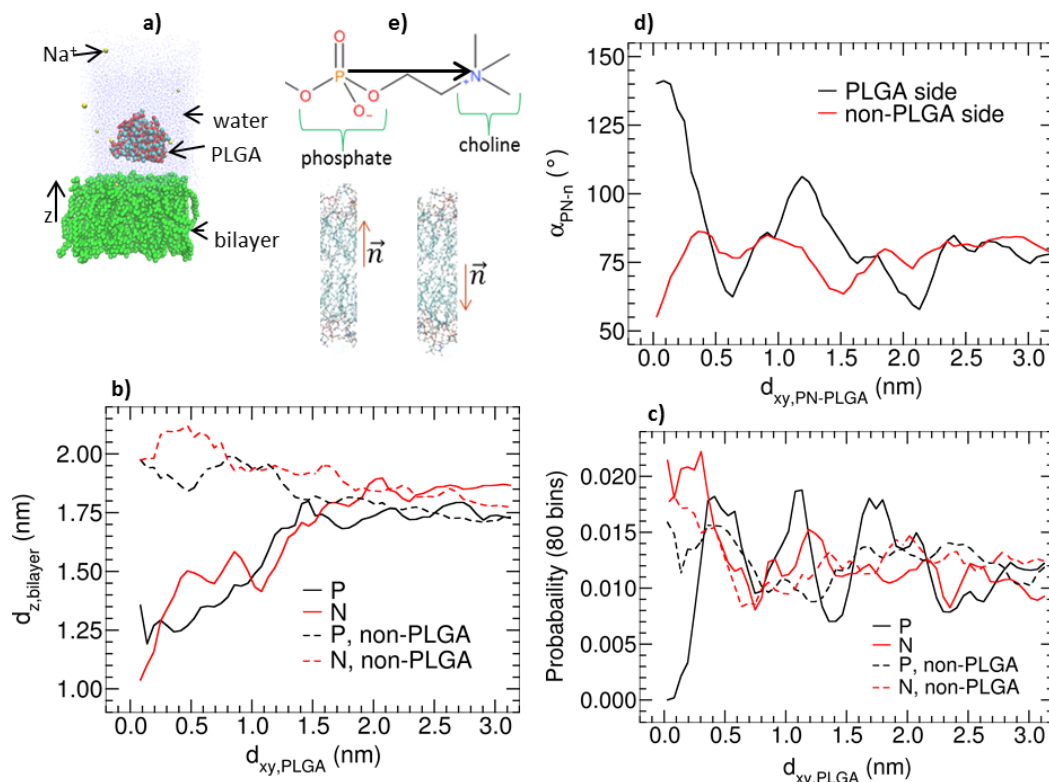


Fig. 2. Simulation system and results. a) Simulation system. b) Distance from the bilayer center in the bilayer normal direction (z) of the phosphorus (P) and nitrogen (N) atoms in the lipids versus the distance in the bilayer plane (xy) from the PLGA center of mass ($d_{xy,PLGA}$). c) Probability versus $d_{xy,PLGA}$. d) Angle between the outward bilayer normal and the P-N vector of the lipid heads versus distance in the bilayer plane (xy) from the P-N geometric center to the PLGA center of mass. e) Definitions of the P-N vector and outward bilayer normal. The non-PLGA side refers to the side of the bilayer that PLGA does not directly interact with.

6. References

- [1] N. Schmid, *et al.*, *Eur. Biophys. J. Biophys. Lett.*, Vol. 40, No. 7, 843-856, 2011.
- [2] A. K. Malde, *et al.*, *J. Chem. Theory Comput.*, Vol. 7, No. 12, 4026-4037, 2011.
- [3] C. Vauthier, C. Schmidt, P. Couvreur, *J. Nanopart. Res.*, Vol. 1, No. 3, 411-418, 1999.
- [4] L. Martinez, *et al.*, *J. Comput. Chem.*, Vol. 30, No. 13, 2157-2164, 2009.
- [5] B. Hess, *et al.*, *J. Chem. Theory Comput.*, Vol. 4, No. 3, 435-447, 2008.
- [6] W. Humphrey, A. Dalke, K. Schulten, *J. Mol. Graphics*, Vol. 14, No. 1, 33-38, 1996.

Molecular Transport in Nanotubes

Divya Narayan Elumalai¹, Anil Thapa¹, Elshad Abdullayev¹, Yuri Lvov¹, Pedro Derosa^{1,2}

¹Institute for Micromanufacturing, Louisiana Tech University

²Department of Mathematics and Physics, Grambling State University

Abstract: Nanotubes show exceptional properties that make them promising candidates for applications that require the transport of fluids or the storage of Molecular systems. Halloysite clay nanotubes are investigated as a tubular container for applications such as rust coatings, self healing composites and selective delivery of drugs. Variable release rates of molecules from halloysite nanotubes, in the range of 20 – 50 hours, are enabled by the formation of end stoppers at the tube openings. These stoppers are utilized to aid in controlling the release rates of molecules from nanotubes.

Keywords: Diffusion, Nanotubes, Nanostructures, Halloysite, Sustained Release, Corrosion Inhibitors, Self Healing, End Stoppers

1. Introduction

Many interesting applications have been designed and developed using nanotubes. Applications like the selective delivery of anti cancer drugs to specific cancer cell types,[1, 2] self healing composites[3] and the prolongation of rust coatings on metal surfaces in extremely hazardous environments,[4] require the controlled diffusion of molecules. Several methods have been proposed to make self-healing composites, including self-healing induced by mechanical stimulation, such as filled hollow glass fibers,[5] microcapsules[6] and microvascular networks[7, 8] most often containing healing agents that react with catalysts in the matrix or viscoelastic ionic polymers that reseal after a ballistic puncture. [9] It is our endeavor in this paper to present a computational model to predict the release-rate of healing and anticorrosion agents from clay nanotubes fitted with end stoppers made of material such as starch. This work will help design self-healing “smart” polymeric composite materials doped with clay nanotubes filled with healing and anticorrosion agents. Naturally occurring halloysite clay tubes are aluminum-silicate hollow cylinders with a length of 1 μm , an outer diameter of 50 nm, and a lumen of 15 nm[10]. The healing agents are loaded into the nanotubes and slowly released in the damaged locations (such as cracks) to suppress the defect propagation, followed by a slow release stage lasting from 20 to 50 hours. Doping loaded clay nanotubes into polymeric matrix provides a ceramic “skeleton” within the coating layer; these “bones” are loaded with functional chemicals (like real bones are loaded with marrow). This skeleton also improves the coating strength and adhesiveness. In this study the approach has been to study the effect of a number of interactions between particles and nanotube on the out diffusion of the healing and anticorrosion agents.

2. Experimental Procedure

Clay nanotubes (halloysites) are used for loading and sustained release of corrosion inhibitors and healing agents.[4, 11] In this work it is demonstrated that the nanotubes entrap anticorrosion agents in the inner lumen and release them in the coating defect points where they are exposed to humid environment as in cracks. Inhibitors may be retained inside the tubes doped into the paint or composite for infinitely long periods. The inhibitors are released in the coating defect spots with an initial burst to suppress the corrosion process, followed by 20-50 hours curing. Longer release times can be achieved through the addition of tube openings stopper.[12] Mechanisms of slowing the release from halloysite are studied in terms of pore size of the stopper. The self-healing effect in the metal coating doped with inhibitor loaded halloysite nanotubes is studied in-situ with the scanning vibrating microelectrode technique monitoring the corrosion spots anodic activity. Doping of paint with 5 % of halloysite nanotubes not only adds anticorrosion functionality but also increases the strength and hardness of the coating. The assembly of the stoppers at the tube's ends further perfects these nanocontainers. By variation of internal fluidic properties and creation of smart caps at the tube's ends, it is possible to develop a wide range of release rates. In this transformative research, the focus is on novel abundantly available coating material with integrated nano and micro features. All suggested processes are "green", occur in aqueous solutions and under mild conditions. When the most efficient chromate based anticorrosion coatings are forbidden because of their carcinogenic effects, development of smart nanocontainers for efficient environmentally friendly chelate agents (e.g. benzotriazole) is especially important and for that reason this compound is selected in this work.

2.1 Simulations

A Monte Carlo model implementing a forced random-walk algorithm is used to model the diffusion of particulate entities from the nanotubes. In this study the diffusion of particles in tubular nanostructures is modeled as a function of the interaction between particles and the nanotube walls; it is hypothesized that the delay in the diffusion rate is dependent on particle-particle interaction in the confined interiors of nanotubes and a strong interaction between the nanotube walls and the particles. Our algorithm generates combinations of the most probable motion of the particles in the nanotubes which are then streamlined to predict the diffusion paths and times. The overall energy of the system is calculated with contributions from particle-wall and particle-particle interactions. The wall-particle interactions are modeled by summing up the contributions from dipole-charge interactions, shielded Columbic interactions coupled with Van Der Waals interactions at short distances. Particle-particle interactions are modeled primarily by taking into consideration columbic interactions, Van Der Waals contributions are also considered. The shielding is introduced by implementing a modified Debye-Huckel screening model. The stoppers at the tube ends are modeled as doughnut shaped barriers with impervious walls and a permeable pore (center). The results from the experiments conducted on halloysite nanotubes are presented in figure 1. As can be seen there is a delay in diffusion or release of the anticorrosive agents from the nanotubes.

3. Results and Discussions

Halloysite admixing to polar plastics at 3-5 % usually doubles the composite strength. With silica as its outermost layer, it is well suited for mixing with epoxy resins. It has been shown that halloysite clay is biocompatible for most applications[13].

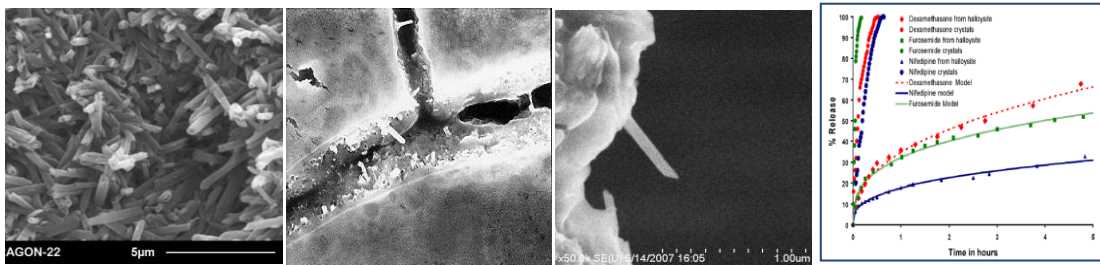


Fig.1. SEM image of the halloysite sample (a), and cracks in dry layer of the composite with inclusion of 5 wt % halloysite nanotubes (a general view and a larger magnification of single tube) (b-c). (d) Experimental release profile of Dexamethasone, Nifedipine and Furosemide from clay nanotube.[14]

Healing agent loaded inside the halloysite is released when cracks, such as the one shown in figure 1b occur, sealing them and preventing further defect propagation. Halloysite is readily mixed with a variety of epoxy resins. Incorporation of 2-10 % of halloysite in epoxy resins results in 30-100 % strength increase. From the point of view of composite healing, an optimal loading of 10-12 wt % will provide enough healing materials to seal micro-cracks.

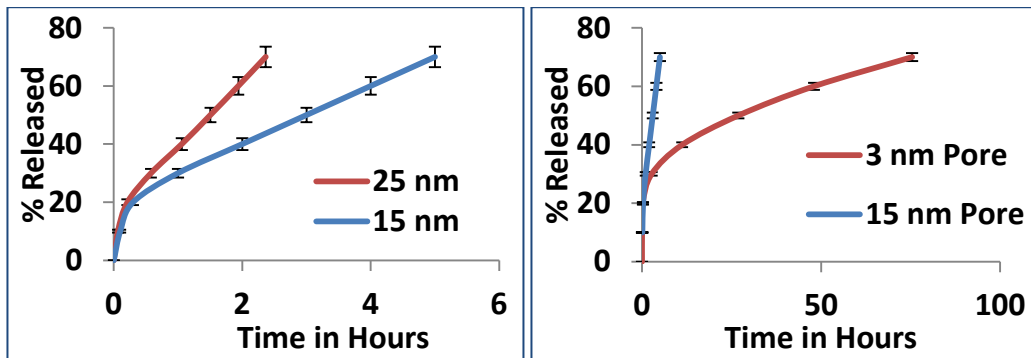


Fig.2. (a) Release profiles of Dexamethasone for 2 different Radii the blue curve is for 15 nm (b) Release profiles of Dexamethasone for 2 different pore openings the blue curve is for 15 nm.

For fixed values of temperature, particle size and maximum jump distance, and considering an attractive interaction between the particles and the wall (as is the case), the particles experience a pull towards the walls. Figure 2a shows how the release profiles of Dexamethasone changes as a function of the tube's radius, as it can

be seen, the smaller the nanotube radii the slower is the out diffusion of the particles. When end stoppers are added, the effect becomes more pronounced as is seen in figure 2b, the 15nm pore (figure 2b) correspond to no stopper, and it is the same as the blue curve in figure 2a. The effect in this case is due to the smaller opening at the tube ends, these smaller opening lead to a decreased diffusivity, and a slower release of the drug from the nanotube. This results in a marked increases in release times enabling a more sustained and controlled release of the drug from the nanotubes.

4. Conclusion

Simulation results show a marked delay in diffusion of Dexamethasone from halloysite when end stoppers are introduced when compared to normal release profiles and instantaneous powder dissolution. Simulation studies show that a particle-wall attraction lead to a delay in the diffusion of species, i.e. the rate of diffusion is decreased. A simple columbic interaction, shielded by a dielectric media, seems to be enough to explain the diffusion delay. This work lays out the ground for furthers studies aiming and not only understanding the diffusion but controlling its rate, a proposed use is in fields such as drug delivery and self-healing composites. This study is expected to lead to a recipe where the diffusion rate can be then controlled as needed.

5. Acknowledgments

The current work is funded by the NSF EPSCoR LA-SiGMA project under award #EPS-1003897.

6. References

- [1] Lay, C.L., J. Liu, and Y. Liu, *Functionalized carbon nanotubes for anticancer drug delivery*. Expert Rev Med Devices, 2011. **8**(5): p. 561-6.
- [2] Liu, Z., et al., *Preparation of carbon nanotube bioconjugates for biomedical applications*. Nat Protoc, 2009. **4**(9): p. 1372-82.
- [3] Abdullayev, E., et al., *Natural tubule clay template synthesis of silver nanorods for antibacterial composite coating*. ACS Appl Mater Interfaces, 2011. **3**(10): p. 4040-6.
- [4] Abdullayev, E. and Y. Lvov, *Halloysite clay nanotubes for controlled release of protective agents*. J Nanosci Nanotechnol, 2011. **11**(11): p. 10007-26.
- [5] Bleay, S.M., et al., *A smart repair system for polymer matrix composites*. Composites Part A: Applied Science and Manufacturing, 2001. **32**(12): p. 1767-1776.
- [6] Yang, J., et al., *Microencapsulation of Isocyanates for Self-Healing Polymers*. Macromolecules, 2008. **41**(24): p. 9650-9655.
- [7] Kessler, M.R., *Self-healing: A new paradigm in materials design*. Proceedings of the Institution of Mechanical Engineers, Part G: Journal of Aerospace Engineering, 2007. **221**(4): p. 479-495.
- [8] Toohey, K.S., et al., *Self-healing materials with microvascular networks*. Nat Mater, 2007. **6**(8): p. 581-5.
- [9] Wool, R.P., *Self-healing materials: a review*. Soft Matter, 2008. **4**(3): p. 400-418.
- [10] Theng, B.K.G., et al., *Surface properties of allophane, halloysite, imogolite*. Clays and Clay Minerals, 1982. **30**(2): p. 143-149.
- [11] Abdullayev, E., et al., *Halloysite tubes as nanocontainers for anticorrosion coating with benzotriazole*. ACS Appl Mater Interfaces, 2009. **1**(7): p. 1437-43.
- [12] Abdullayev, E. and Y. Lvov, *Clay nanotubes for corrosion inhibitor encapsulation: release control with end stoppers*. Journal of Materials Chemistry, 2010. **20**(32): p. 6681-6687.
- [13] Vergaro, V., et al., *Cytocompatibility and Uptake of Halloysite Clay Nanotubes*. Biomacromolecules, 2010. **11**(3): p. 820-826.
- [14] Veerabadran, N.G., R. Price, and Lvov.Y. M., *Clay nanaotubes for encapsulations and sustained release of drugs*. NANO, 2007. **2**(2): p. 115-120.

Multi-spin Coding Parallel Tempering Monte Carlo Simulation of Ising Spin Glass with CUDA

Sheng Feng^{1,2}, Ye Fang^{2,3}, Ka-Ming Tam^{1,2},
Bhupender Thakur², Zhifeng Yun², Ariane Papke¹, Sean Hall¹, Cade Thomasson^{1,2},
Juana Moreno^{1,2}, J. Ramanujam^{2,3}, Mark Jarrell^{1,2}

¹Department of Physics and Astronomy, Louisiana State University

²Center for Computation and Technology, Louisiana State University

³ECE Division, School of Electrical Engineering and Computer Science, Louisiana State University

Abstract: We implement the Monte Carlo method for the Edwards-Anderson model in the Graphics Processing Units architecture. The multi-spin coding method is used to accommodate memory size requirements and the parallel-tempering method is used to accelerate the thermalization of the Monte Carlo simulation. The code provides substantial speed up compared to that for the CPU and approaches around fifty percent of the speed attained by the field programmable gate array architecture.

Keywords: Spin Glass, Ising Model, Parallel Tempering, GPU, CUDA, Multi-spin Coding

1. Introduction

The discovery of unusual magnetic behavior in disordered materials initiated the field of glassy systems.¹ Spin glasses are beyond the conventional description of ferromagnets. Some of their features, including their frequency-dependent susceptibilities and the discrepancy between zero-field and field cooling measurements, suggest that spin glasses have very slow dynamics. Randomness and frustration seem to be present in most of the spin glass systems. In real materials, the dilution introduces randomness, and directional or distance-dependent coupling, such as dipolar coupling in insulating systems and the Ruderman-Kittel-Kasuya-Yoshida coupling^{2,3,4} in metallic systems, introduces frustration. The simplest model which captures the consequences of disorder is an Ising model with quenched random disorder couplings. This model was first proposed by Edwards and Anderson.⁵ The mean field solution of the Edwards-Anderson model for infinite dimensions was first attempted by Sherrington and Kirkpatrick.⁶ However, the mean field solution was found to be unstable below the Almeida-Thouless line.⁷ The difficulty of obtaining a stable solution was solved by Parisi with his replica symmetry breaking ansatz.^{8,9} Although the mean field solution has been proven to be the correct description of the spin glass phase^{10,11} in infinite dimensions, the spin glass physics in finite dimensions, which presumably is more relevant to experiments, is still not fully understood. Indeed, it had been debated for a long time whether spin glass phase at finite temperature exists in three dimensions.

The Edwards-Anderson model may be deceptively simple. Since it is a classical spin model one may think that its numerical study can be simply carried out by Monte Carlo methods. However, one of the defining signatures of spin glass systems is their long relaxation time. Moreover, it has been proved that finding the ground state of the three dimensional Edwards-Anderson model is an NP-hard problem.¹² For sufficiently low temperature, the system become very sluggish and equilibration is prohibitively difficult to obtain even for modest systems sizes.

The breakthrough in the numerical study of spin glass systems came along with the introduction of the parallel tempering method, which allows the study of larger system sizes at lower temperature than the simple single spin flip Monte Carlo method.^{13,14,15,16} Combined with the improved scheme for finite size scaling, it is now widely believed that the thermodynamic finite temperature spin glass phase does exist in the Edwards-Anderson model for three dimensions.¹⁷

The upper critical dimension of the Edwards-Anderson spin glass model is six. A prominent question in the study of spin glasses is what is the nature of the spin glass phase below the upper critical dimension. In particular if the spin glass can still be described by the replica symmetry breaking scenario, there should be an Almeida-Thouless line below the upper critical dimension. One of the possible tests on whether the Almeida-Thouless line exists is to determine whether a spin glass phase exists under an external magnetic field. Recent studies on this problem do not come to a universal consensus. By using the correlation length scaling analysis, the data seem to suggest the absence of the spin glass phase.¹⁸ On the other hand, a recent study in four-dimensional lattices suggests that by using a different quantity for the finite size scaling analysis, a spin glass phase can be revealed.¹⁹

Given the importance of spin glasses and the on-going controversy on the nature of the spin glass phase below the upper critical dimension, it is desirable to implement an efficient parallel-tempering (PT) Monte Carlo algorithm that utilizes the architecture of graphics processing units (GPU). In this work we will show that using the multi-spin coding method, the Monte Carlo algorithm can be implemented efficiently in the GPU.^{20,21} The code provides substantial speed up compared to other GPU implementations, and approaches close to fifty percent of the speed achieved on special-purpose field programmable gate array (FPGA) architectures.²²

2. Algorithm

The algorithm is simply the single spin flip Monte Carlo Metropolis update. The system is a three-dimensional cubic lattice with a dimension of L , therefore the lattice has L^3 sites. On each site, there is a +1 or -1 spin, and the spins interact with the following Hamiltonian: $H = \sum_{\langle i,j \rangle} J_{ij} S_i S_j + \sum_i h S_i$, where J_{ij} is a random interaction energy and $\langle i,j \rangle$ stands for nearest neighbors.

For the problem we are studying, the energy landscape is rugged and complicated. It is difficult for the system, especially at very low temperatures, to get through the energy barriers and travel from one local minimum to another. In order to help the system explore the phase space more efficiently, the parallel tempering or replica exchange method is used. For each of the disorder realizations, we need to do N_B different replicas, with temperatures ranging from above to below the critical temperature. During the simulation, we propose to exchange the configuration of two replicas with a probability $P = e^{\Delta E \Delta \beta}$. Throughout the simulation, the spin configuration of systems with different temperatures will be swapped frequently.

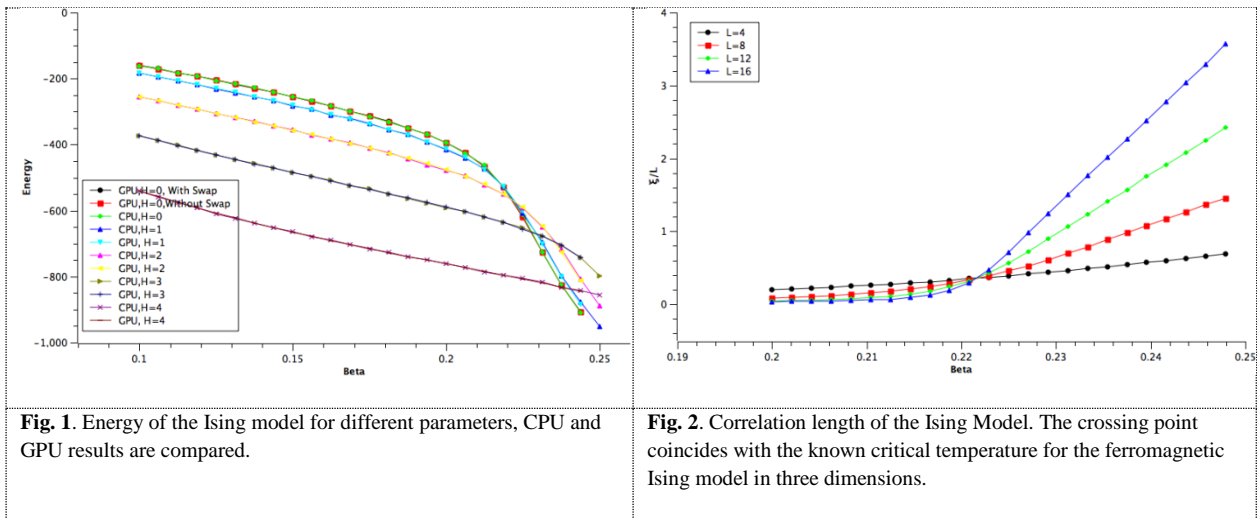
3. Implementation

To do the parallel tempering, frequent exchange between configurations is required, and therefore it is necessary to fit N_B replicas into one thread block of the CUDA model. Within each thread block, N_t threads are assigned to update the configuration of the lattice in a checkerboard pattern in order to meet the dependency requirements. Different thread blocks, which will be executed in parallel on different multiprocessors of the GPU, are assigned to simulate different disorder configurations of J_{ij} .

To make the most out of the fast shared memory on NVIDIA GPUs, the multi-spin coding technique is adopted to reduce the memory requirement for storing the configurations and also to boost the performance. We also tested the performance of several different forms of multi-spin coding and proposed a new form: the Asynchronous Compact Multi-Spin Coding (ACMSC), which will be elaborated in a future publication.

4. Results

We tested our code with both the simple ferromagnetic Ising model and the Edwards-Anderson spin glass model. Some of the results are shown in Figures 1-3. In Figure 1, our results from the GPU code are consistent with the results from the CPU code for the ferromagnetic Ising model, both with and without the external magnetic field. We can compare the results with and without parallel tempering as a check to determine whether the parallel tempering swap is performed correctly. We find that the results with and without parallel tempering swap are consistent with each other. In Figure 2, we plot the Binder ratio for the ferromagnetic Ising model in three dimensions, the crossing point for the Binder ratio coincides with the known critical temperature for the ferromagnetic ordering.



For the Edwards-Anderson model we calculated the Binder ratio of the system and compared it with published results, as shown in Fig. 3. The results match the published data.

Our present GPU code achieves 39 picoseconds per spin flip attempt for the three-dimensional Edwards-Anderson Ising model with parallel tempering. This is substantially faster than any other GPU implementation and around fifty percent of the speed achieved by special-purpose FPGA implementations.²² See Fig. 4 for comparison of the performance of different implementations.

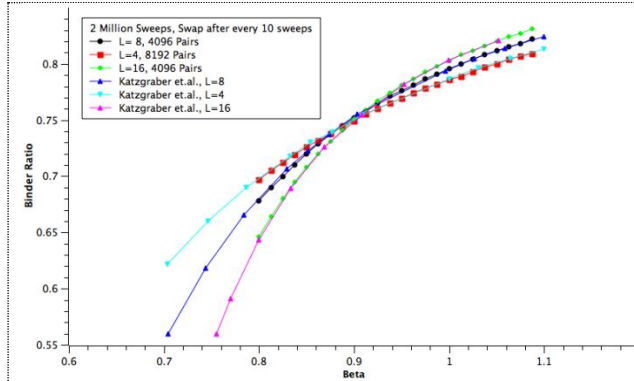


Fig. 3. Binder Ratio of Edwards-Anderson model compared with Katzgraber et al.²³

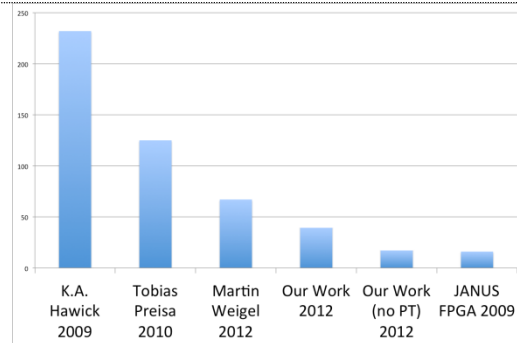


Fig. 4. Comparison of performance with several similar projects (measured in picoseconds/spin). Lower is better.

5. Acknowledgments

This work is funded by the NSF EPSCoR LA-SiGMA project under award number EPS-1003897.

6. References

- [1] K. Binder and A. P. Young, *Rev. Mod. Phys.* **58**, 801 (1996).
- [2] M. A. Ruderman and C. Kittel, *Phys. Rev.* **96**, 99 (1954).
- [3] T. Kasuya, *Prog. Theor. Phys.* **16**, 45 (1956).
- [4] K. Yosida, *Phys. Rev.* **106**, 893 (1957).
- [5] S. F. Edwards and P. W. Anderson, *J. Phys. F: Met. Phys.* **5**, 965 (1975).
- [6] D. Sherrington and S. Kirkpatrick, *Phys. Rev. Lett.* **35**, 1792 (1975).
- [7] J. R. L. de Almeida and D. J. Thouless, *J. Phys. C*: **11**, 983 (1978).
- [8] G. Parisi, *J. Phys. A: Math. Gen.* **13**, 1101 (1980).
- [9] M. Mezard, G. Parisi, and M. A. Virasoro, “Spin glass theory and beyond”, Singapore: World Scientific.
- [10] M. Talagrand, *Ann. Probab.* **28**, 1018 (2000).
- [11] F. Guerra and F. L. Toninelli, *Commun. Math. Phys.* **230**, 71 (2002).
- [12] F. Barahona, *J. Phys. A* **15** (1982) 3241.
- [13] R. H. Swendsen and J.-S. Wang, *Phys. Rev. Lett.* **57**, 2607 (1986).
- [14] C. J. Geyer, *Computing Science and Statistics: Proceedings of the 23rd Symposium of the Interface*, 156 (1991).
- [15] E. Marinari and G. Parisi, *Europhys. Lett.* **19**, 451 (1992).
- [16] K. Hukushima and K. Nemoto, *J. Phys. Soc. Jpn.* **65**, 1604 (1996).
- [17] H. G. Ballesteros, A. Cruz, L. A. Fernández, et al., *Phys. Rev. B* **62**, 14237 (2000).
- [18] A. P. Young and H. G. Katzgraber, *Phys. Rev. Lett.* **93**, 207203 (2004).
- [19] Janus Collaboration: R. A. Baños, A. Cruz, L.A. Fernandez, et al., *Proc. Natl. Acad. Sci. USA*, **109**, 6452 (2012).
- [20] M. Creutz, L. Jacobs, and C. Rebbi., *Phys. Rev. Lett.* **42**, 1390 (1979).
- [21] C. Rebbi and R. H. Swendsen, *Phys. Rev. B* **21**, 4094 (1980).
- [22] Janus Collaboration: F. Belletti, I. Campos, A. Cruz, et al. *Computing in Science & Engineering* **8**, 41 (2006).
- [23] H. G. Katzgraber, M. Koerner, and A. P. Young, *Phys. Rev. B* **73**, 224432 (2006).

Nanoparticle Uptake by Tumor Tissue through its Capillary Pores

Vishwa Priya Podduturi¹, Pedro Derosa^{1,2}

¹Institute for Micromanufacturing, Louisiana Tech University

²Physics Department, Grambling State University

Abstract: Nanoparticles are used as drug delivery vehicles to efficiently deliver the drug in treating cancer. The study of the uptake of nanoparticles by the tumor as a function of time can help understand the factors that control the mechanisms of delivery and guide physicians in the administration of appropriate drug dose to the body. The selective delivery of nanoparticles to cancer over healthy tissue, can be achieved due to the unique physiology of the tumor blood vessels which contain larger pores than regular tissue. In this work, a section of the capillary wall with a single pore is simulated. The pore in the capillary is simulated in the size range of 100-600 nm diameter, which is within the size range reported for this type of tissue[1]. The nanoparticles are assumed to move with the velocity of the blood in the capillary with Brownian motion, contributed by the collisions of the nanoparticle with other particles in the blood stream, superimposed. A specific concentration of nanoparticles is introduced into the capillary and the uptake of the nanoparticles by the tumor with time is studied.

Keywords: Nanoparticle delivery, Tumor, Capillary wall, Concentration.

1. Introduction

Nanoparticles can be used as drug delivery vehicles provided they are not toxic to the body and that they remain for long-enough time in the blood circulation so that they have a better chance to reach the tumor[2]. Polymeric nanoparticles, polymeric micelles, dendrimers, liposomes, and viral nanoparticles are some of the nanoparticles being studied as potential drug delivery vehicles[3]. Doxorubicin, Myocet, and Daunorubicin are used in the treatment of metastatic breast cancer [4-6]. Many other nanoparticle-based drugs are still in clinical trials. When the Nanoparticles are introduced intravenously in the body, they enter the blood circulation including the tumor tissue blood vessels. Once the nanoparticles are in the tumor capillary, to be effective, they have to leave the circulation to enter the tumor through the pores in the capillary wall. To achieve an efficient delivery, the uptake of the nanoparticles by the tumor should be optimized. In this paper, the nanoparticle flow in the tumor capillary is

simulated and the uptake of them by the tumor with time is studied. By studying the different factor affecting delivery, it is possible to optimize the process.

2. Methodology

The model was introduced in our previous paper[7]. In short, the velocity profile of the Pressure driven flow of blood plasma in a cylindrical tube, represented by a power law (equation 1) [8] is used to describe the component of the particle motion due to fluid drag. The velocity profile of the nanoparticles due to equation 1 is shown in figure 1a.

$$V = \left(\frac{P}{2 \times k \times l} \right)^{\frac{1}{n}} \times \left(\frac{n}{n+1} \right) \times \left(R^{\frac{n+1}{n}} - x^{\frac{n+1}{n}} \right) \quad (1)$$

Where V= velocity of the nanoparticle, P= Pressure drop across the blood capillary, R= Radius of the blood capillary, x= distance of the nanoparticles from the centre of the blood capillary, l = length of the blood capillary, k= flow consistency index, n= flow behavior index.

The effect of the pore on the capillary pressure is studied using COMSOL [9]. Figure 1-b shows the pressure profile in the capillary near the pore. Based on the effect of the pore, the capillary is divided into three zones. Zone 1 has a high pressure gradient and hence the nanoparticles entering this zone are assumed to leave the blood stream through the pore with all certainty. The pressure gradient in zone 2 is intermediate between that in zone 1 and the regular pressure in the capillary and nanoparticle are considered to have a chance of missing the pore. The nanoparticle's velocity in this zone has two components, one due to the pressure gradient at the pore and the other due to the pressure gradient along the capillary. Both velocities components are calculated from equation 1. The pressure values for the velocity component in the direction of the pore is obtained from COMSOL.

3. Results

The interstitial pressure in the tumor is higher than the normal tissues[10] but its value is not well defined in the literature, hence simulations were performed for three different values of this pressure. Case 1, 2 and 3 with a pressure difference of 0.5 mm Hg, 5 mm Hg and 13 mm Hg are studied. Case 1 represent a case where possibly high concentration of particles in the tumor decreases uptake due to saturation, Case 2 occurs when the tumor has an elevated interstitial pressure which is still less than the blood pressure value in the capillary. Case 3 occurs if the tumor have an normal interstitial pressure like in healthy tissues[11].

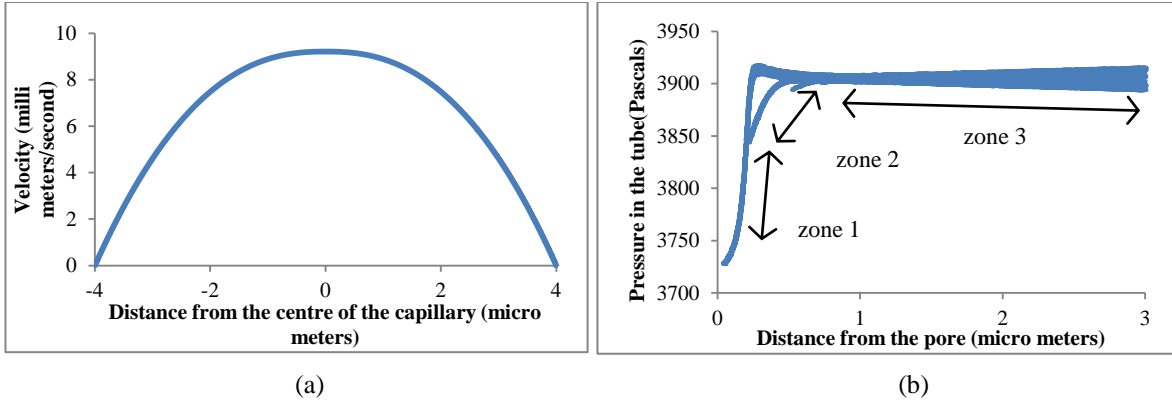


Figure 1: a) Velocity profile of nanoparticles obtained from equation 1 b) change in the blood capillary pressure due to the pore obtained from COMSOL

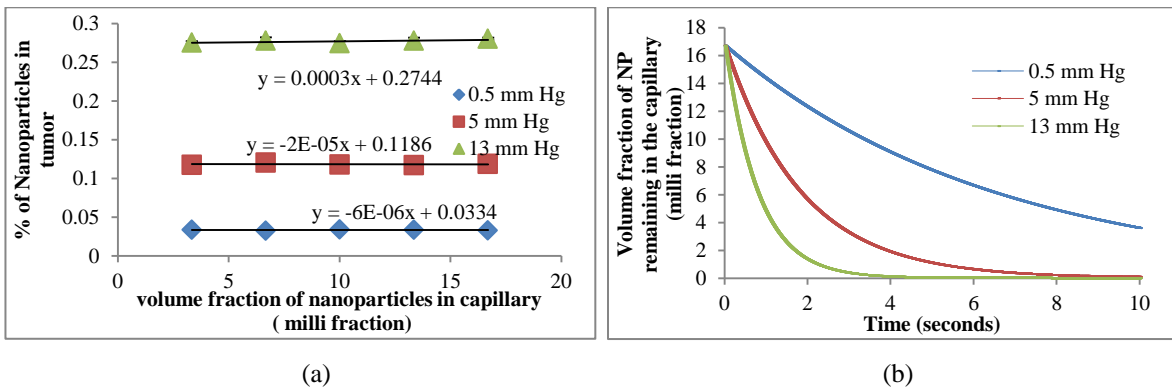


Figure 2: a) percent of nanoparticles entering the pore as a function of the volume fraction of nanoparticles in the capillary b) volume fraction of nanoparticles remaining in the blood capillary as a function of time.

Simulations are performed as a function of nanoparticle concentration in blood. Figure 2-a shows the effect of the nanoparticle concentration in blood on their delivery. The nanoparticle diameter is 200 nm and the pore diameter is 400 nm. The results show that the percent of the nanoparticle delivered is constant for all the three cases. Figure 2-b shows the volume fraction of nanoparticles remaining in the capillary with time for the three cases. The uptake of nanoparticles by the tumor is high at the beginning and slowly decreases with time due to the lower availability of nanoparticles in the blood stream. As expected, the volume of nanoparticles remaining in the capillary decreases more rapidly in case 3 compared to the other 2 cases. The effect of saturation of the tumor

tissue is not considered in the results presented here, at this point joint work with experimentalist Dr. Patrick O'Neal and his group is being carried out to validate and better parameterize this model. It has already been determined that the uptake curves (figure 2-b) agreed qualitatively with experimental results although the experimental curves show a much larger time scale due to the time it takes for the nanoparticles to circle around the body and get back to the tumor.

4. Conclusion

From the results, it can be stated that increasing nanoparticle concentration in blood does not improve the efficiency of delivery (% of nanoparticles delivered), however, an increased concentration (larger dose), increases the total number of particles delivered in each cycle and allows nanoparticles to remain in blood circulation for more time and hence have more chances of entering the tumor capillary thereby increasing the tumor uptake over time.

5. Acknowledgments

The current work is funded by the NSF EPSCoR LA-SiGMA project under award #EPS-1003897.

6. References

- [1] S.K. Hobbs, *et al.*, " Regulation of Transport Pathways in Tumor Vessels: Role of Tumor Type and Microenvironment," *Proceedings of the National Academy of Sciences*, Vol. 95, pp. 4607-4612, 1998.
- [2] C. Li, "Poly(-glutamic acid)-anticancer drug conjugates," *Advanced Drug Delivery Reviews*, vol. 54, pp. 695-713, 2002.
- [3] K. Cho, *et al.*, "Therapeutic Nanoparticles for Drug Delivery in Cancer," *Clinical Cancer Research*, vol. 14, pp. 1310-1316, March 1, 2008 2008.
- [4] M. Markman, "Pegylated liposomal doxorubicin in the treatment of cancers of the breast and ovary," *Expert Opin Pharmacother*, vol. 7, pp. 1469-74, Aug 2006.
- [5] E. Rivera, "Current Status of Liposomal Anthracycline Therapy in Metastatic Breast Cancer," *Clinical Breast Cancer*, vol. 4, pp. S76-S83, 2003.
- [6] E. Rosenthal, *et al.*, "Phase IV Study of Liposomal Daunorubicin (DaunoXome) in AIDS-Related Kaposi Sarcoma," *American Journal of Clinical Oncology*, vol. 25, pp. 57-59, 2002.
- [7] V. P. Podduturi, *et al.*, " Simulating Nanoparticle Movement in Tumor Tissue Blood Vessels," *Proceedings of Louisiana EPSCoR RII LA-SiGMA Symposium*, 2011.
- [8] G. A. Truskey, *et al.*, *Transport phenomena in biological systems*, 2nd ed. Upper Saddle River, N.J.: Pearson Prentice Hall, 2009.
- [9] www.comsol.com.
- [10] R. K. Jain, "Physiological Barriers to Delivery of Monoclonal Antibodies and Other Macromolecules in Tumors," *Cancer Research*, vol.50, pp. 814-819, 1990.
- [11] A. C. Guyton, *et al.*, *Textbook of Medical Physiology*, 11 th ed. Saunders, 2006.

Nucleosome Binding in Highly Occupied Sequences

Victoria Bamburg¹, James Solow², Ronald Brown³, James Lineman¹, Thomas C. Bishop⁴

¹Department of Biomedical Engineering, Louisiana Tech University

²Department of Computational Analysis and Modeling, Louisiana Tech University

³Department of Physics, Ratford University

⁴Department of Physics and Chemistry, Louisiana Tech University

Abstract: In higher organisms, DNA is packed in the nucleus by histones. Eight histones wrap 147bp long segments of DNA into a left-handed superhelix forming a nucleosome. The location of nucleosomes within the genome plays a crucial role in all genomic processes because it regulates the accessibility of DNA. DNA sequence can influence the location of nucleosomes within the genome by one of two criteria; the DNA internal energy or the interaction energy between DNA and the environment. Internal energy is the associated energy with DNA and the conformation. Interaction of DNA with the environment is between the solvent or histone and the DNA. It is unclear which energy dominates and how differences in these energies compare to other energy considerations within the cell. We analyzed molecular dynamics simulations of nucleosomes containing DNA sequences from *S. cerevisiae* corresponding to highly occupied sequences to determine the behavior of selected DNA. DNA self interaction and interaction between DNA and environment (histones & solvent) were calculated to see if these energies as observed in Molecular Dynamics (MD) correspond with known positions in *S. cerevisiae*. Lower energy areas or areas with high environmental factors were noted as potential nucleosome bind sites. Our results were compared to previously found experimental and theoretical nucleosome bind sites.

Keywords: Nucleosome, self-energy, molecular dynamics

1. Introduction

Interaction between functional DNA sites with non-histone proteins influence a nucleosome positioning and may play a role in determining nucleosome location [1]. Energy differences as function of DNA sequence should tell us about the nucleosome positioning determination. Thermodynamically the relative population of two locations on a given sequence is determined by the ratio of the energies associated with the two nucleosomes; however, these simple thermodynamic arguments can be overridden by cellular machinery or other processes (eg. remodeling proteins) which utilize ATP (i.e. energy) to affect reorganization of chromatin or even nucleosome-nucleosome interactions. In the simulations, sequences of DNA, corresponding to known nucleosome positions are thread, base pair by base pair, around a histone core. From the simulations internal energies as well as external energies are calculated to determine if these molecular dynamics energies correspond to experimentally determined positions on *S. cerevisiae*. Any discrepancies in location can be examined more closely so that we can determine why they are located elsewhere and how this affects the structure and expression of the sequence.

2. Methods

The yeast genome database provides maps of all nucleosomes in the yeast genome based on experimentally determined locations; theoretical predictions are also provided. It must be noted that there is variation in the observed nucleosome positions. We selected sequences corresponding to highly occupied and least variable nucleosome locations from each chromosome. This provides 16 sequences (one from each chromosome of *S. cerevisiae*). In the MD simulations a 20 basepair window about these positions with 10 basepair upstream and 10 basepair downstream was scanned. This gave us a 167 basepair sequence and 21 nucleosomes to simulate. In total, there were 16 sequences by 21 simulations giving 336 systems that were simulated. Since there are 147 basepair in a nucleosome, each set of simulations contained a single 127 basepair subsequence kernel. Each system was simulated for 20ns equal to 6.720μs of nucleosome dynamics. Here we look at only the last nanosecond from a subset of the 336 sequences.

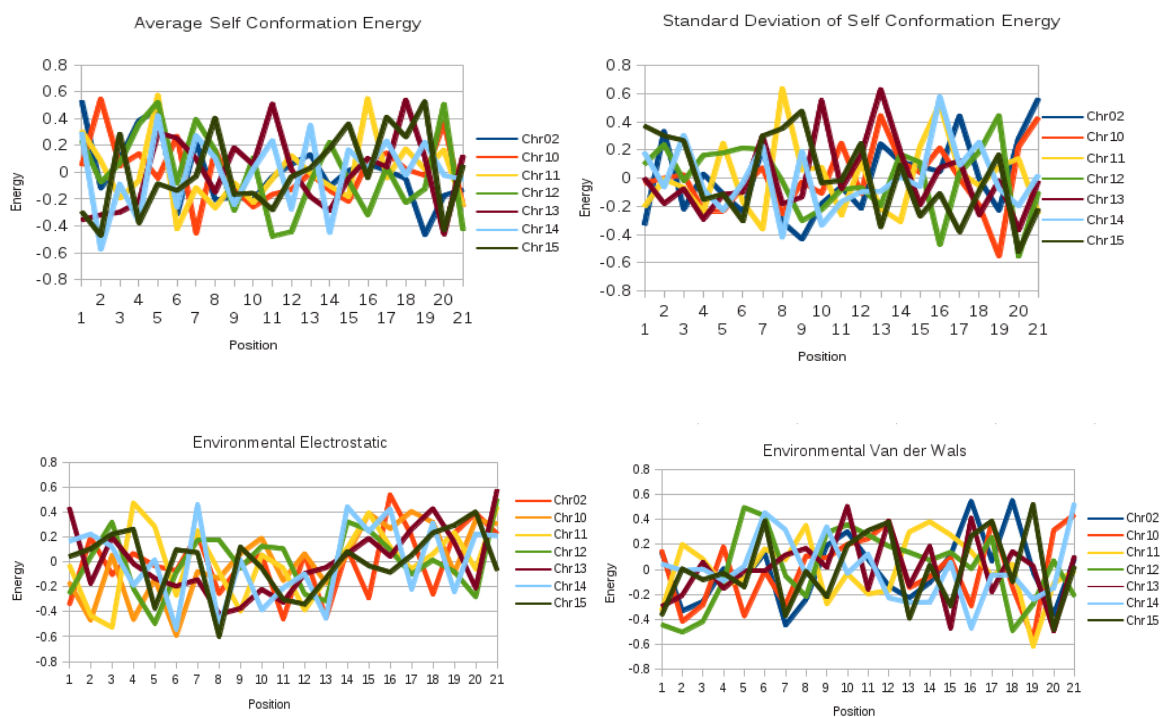
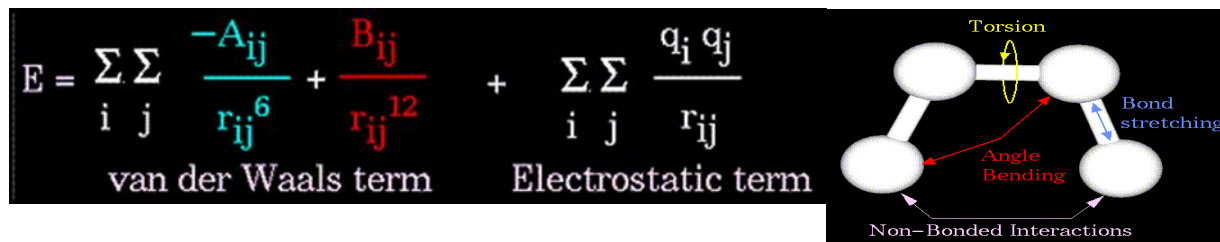
2.1 Simulations

The NAMD energy plug-in for VMD (23) was used to calculate Coulomb and van der Waals interaction energies between the histone core and DNA for 127 basepair. A total of 100 equally spaced snapshots from each last nanosecond trajectory were evaluated. For this analysis the water and ions were stripped from the snapshots and a dielectric constant of 80 was used as an ad hoc method of approximating solvent screening. For all energy calculations a cutoff of 400 Å was used with switching that began 300 Å and no periodic boundaries. This provided a complete accounting of the long range Coulomb interactions in our analysis. Note that during the simulations PME with periodic boundaries and a 10-12 Å switching function was utilized to determine long range interactions. Bishop and Mukherjee had 336 nucleosomes each simulated for 20ns. Here we consider only energy from the last nanosecond (time period 19ns to 20ns) for a subset of the 336. Energies in a molecular dynamics experiment are defined by potential energy functions. The DNA self-energy includes bonded and non-bonded, DNA interaction only included the non-bonded terms.

$$E = \sum_{\text{torsions}} A [1 + \cos(n\tau - \phi)]$$

$$E = \sum_{\text{angles}} k_{\theta} (\theta - \theta_o)^2$$

$$E = \sum_{\text{bonds}} k_b (r - r_o)^2$$



3. Results and Discussions

Figure 1. Shows the average self conformation energy that has been 'normalized by applying $(x-\text{avg})/(\text{max}-\text{min})$ '. The Self conformation energy is the sum of the energy terms.

Figure 2. Shows the normalized standard deviation of the self conformation energy.

Figure 3. Shows the average Environmental Electrostatic energy normalized by the previously stated method (figure 1).

Figure 4. Shows the average van der Waals normalized energy.

Neither the DNA self-energy nor the environmental energy exhibited a pattern consistent with a single well positioned nucleosome between the location of the nucleosome and energy fluctuations. Only seven sets out of the sixteen sequences DNA sequences have been analyzed.

4. Conclusion

Reasons that the data analyzed did not offer any conclusive results are many and include: The physical laws regulating nucleosome occupancy and variability in yeast nucleosome are not governed by DNA sequence. Our simulations may not yet have equilibrated. Our data must be more carefully scrutinized and plots analyzed more extensively to determine if trends do in fact exist. Even if DNA sequence does govern positioning we may not be able to see it with the techniques employed here.

5. Acknowledgments

The current work is funded by the NSF EPSCoR LA-SiGMA project under award #EPS-1003897.

6. References

- [1] Miele, V., Vaillant, C., d'Aubenton-Carafa, Y., Thermes, C., Grange, T., DNA physical properties determine nucleosome occupancy from yeast to fly. *Nucleic Acids Research*, 36:3746–3756, 2008.
- [2] Fernandez M, Fujii S, Kono H, Sarai A. Evaluation of DNA intramolecular interactions for nucleosome positioning in yeast. *Genome Informatics. International Conference On Genome Informatics* [serial online]. October 2009;23(1):13-20. Available from: MEDLINE, Ipswich, MA.
- [3] Kaplan, N., Hughes, T., Lieb, J., Widom, J., & Segal, E. (2010). Contribution of histone sequence preferences to nucleosome organization: proposed definitions and methodology. *Genome Biology*, 11(11), 140.
- [4] Bishop. T.C. (2009). Geometry of the nucleosomal DNA superhelix. *Biophys J*, 95(3), 1007-1017.
- [5] Mukherjee, R., Bishop, T. C. (2011). Nucleosomal DNA: Kinked, Not Kinked, or Self-Healing Material?. *Frontiers Nucleic Acids*, 5, 69-92.

Numerical Simulation of Hydrogen Absorption/Desorption in Metal-Hydride Reactors

Fei Han and Weizhong Dai

Mathematics & Statistics, College of Engineering & Science, Louisiana Tech University

Abstract: Studying hydrogen absorption/desorption in metal-hydrogen reactors is important for the usage and commercialization of hydrogen energy. In this article, we consider a cylindrical metal-H₂ reactor and present a finite-difference scheme for simulating the heat and mass transfer between LaNi₅ and H₂ during the absorption and desorption of hydrogen in the reactor, by using a two-dimensional (2D) mathematical model. Numerical results including temperature, gas and solid densities are obtained.

Keywords: metal-hydrogen reactor, absorption, desorption, mass and heat transfer, mathematical model, finite difference method

1. Introduction

Hydrogen energy is the best alternative to fossil fuels due to its high calorific value and being environmentally friendly. Hydrogen produces more energy per unit weight than any other fuel. However, storage problem of hydrogen prevents its wide usage and commercialization because of the low density of hydrogen, which creates several storage problems such as high pressure and large volume requirements, weight and safety risks [1]. Metal-hydrogen reaction has attracted researchers' attention in recent years because it attains relatively large amount of hydrogen at a relatively low pressure at near normal temperature, and under certain conditions hydride can desorb hydrogen quickly. Thus, understanding of mass and heat transfer between metal and H₂ in the reactor is important for optimizing the design of metal hydrogen storage systems. There are numerous experimental and theoretical studies in the literatures to study the details of hydrating/dehydrating process. Lucas and Richards [2] developed a 1D mathematical model for investigating the heat and mass transfer of the storage system. Mayer and Gopal et al. [3] also developed a 1D mathematical model for studying the transient heat and mass transfer in the reaction tank and compared the results with the experimental data. However, the experimental data clearly showed that the temperature varies along both r -direction and z -direction. Jemni et al. [4,5,6] presented two-dimensional models for simulating the heat and mass transfer in a cylindrical tank during the absorption and desorption processes. Furthermore, Jemni et al. [7] conducted an experimental and numerical study to determine the effective thermal conductivity, the equilibrium pressure, and reaction kinetics. Their numerical results reasonably match their experimental results. Based on the continuum model in [4-7,8], Mat et al. [9,10] investigated the parameter affection on the hydrating process and extended the model to three-dimensional cases. They reported that hydride formation enhances at regions with lower equilibrium pressure. In particular, Jemni et al. [5] presented a 2D mathematical model to describe the mass and heat transfer between metal and H₂ in a tank during the desorption

process, and later, Dhaou et al. [11] experimentally validated the mathematical model in a closed reactor. Since most of the numerical results were obtained using the commercial software, the motivation of our research is to develop our own numerical scheme so that we can determine some critical parameters later on by using the inverse computation from our scheme.

2. Mathematical Model

Consider a cylindrical metal-hydrogen reactor as shown in Fig. 1(a). The reactor can be heated/cooled from boundary walls. To study the mass and heat transfer between metal and H₂ in the reactor during absorption and desorption processes, we assume that the temperatures of hydrogen and hydride are the same, the hydrogen is ideal from thermodynamic view, and heat transfer by radiation is negligible. Thus, the mass balance equation for hydrogen and hydride can be expressed as [12]

$$\varepsilon \frac{\partial \rho_g}{\partial t} + \frac{1}{r} \frac{\partial}{\partial r} (r \rho_g u_r) + \frac{\partial}{\partial z} (\rho_g u_z) = -\dot{m}, \quad (1)$$

$$(1 - \varepsilon) \frac{\partial \rho_s}{\partial t} = -\dot{m}, \quad (2)$$

where ε is porosity, ρ_g is the density of hydrogen, ρ_s is the density of hydride, u_r, u_z are the velocities of hydrogen in the r and z directions, respectively, and \dot{m} is the reaction rate in the reactor. For the absorption process, the reaction rate is given by $\dot{m} = C_a \exp[-\frac{E_a}{R_g T}] \ln(\frac{P_g}{P_{eq}}) [\rho_{ss} - \rho_s]$, where ρ_{ss} is the density of the solid phase at saturation, C_a is a material dependent constant, E_a is the absorption activation energy, R_g is the ideal gas constant, P_g is pressure of hydrogen, and T is the temperature of hydrogen/hydride. Here, P_{eq} is the equilibrium pressure calculated using the van's Hoff relationship, $\ln(P_{eq}) = A - \frac{B}{T}$. For the desorption process,

the reaction rate is given by $\dot{m} = C_d \exp(-\frac{E_d}{R_g T}) \frac{P_g - P_{eq}}{P_{eq}} \rho_{H_2M}$, where C_d is a material-dependent constant, E_d is the desorption activation energy, ρ_{H_2M} is the mass of hydrogen in the hydride divided by the volume of reactor. On the other hand, the energy equation can be expressed as [12]

$$(\rho C_p)_e \frac{\partial T}{\partial t} = \frac{1}{r} \frac{\partial}{\partial r} [r \lambda_e \frac{\partial T}{\partial r}] + \frac{\partial}{\partial z} [r \lambda_e \frac{\partial T}{\partial z}] - \rho_g C_{pg} u_r \frac{\partial T}{\partial r} - \rho_g C_{pg} u_z \frac{\partial T}{\partial z} - \dot{m} [\Delta H^0 - T(C_{pg} - C_{ps})]. \quad (3)$$

The hydrogen velocity is calculated by Darcy's law, $\vec{V} = -\frac{K}{\mu_g} \text{grad}(P_g)$, where K is permeability of the porous

and μ_g is hydrogen dynamic viscosity. The above equations coupled with initial and boundary conditions frame our mathematical model for mass and heat transfer between metal and H₂ in the reactor during absorption and desorption processes. Because of the complex and nonlinearity of the mathematical model, it must be solved

numerically. Here, we develop a finite difference scheme in a staggered mesh for the mathematical model. The detailed scheme and mesh will not be presented here due to the page limitation.

3. Numerical Examples

To test the applicability of the developed numerical scheme, we first simulated the hydrogen absorption in a cylindrical $\text{LaNi}_5\text{-H}_2$ reactor that has a height of 0.5 m and a radius of 0.1 m with the radius of inlet to be 0.01 m, as shown in Fig. 1(a). The reactor was filled with grains of LaNi_5 alloy and the hydrogen was charged to the reactor from the top through a circular inlet. The reactor was cooled on top, lateral and bottom walls. The pressure at the inlet was kept a constant. Three meshes of 50×100 , 75×150 , and 100×200 in the (r, z) plane were used in order to test the convergence of the scheme. The time increment was chosen to be 0.001s. Figure 1 (b)-1(d) show contours of the hydride density distribution changing with time. Because the hydrogen gas comes from the top inlet, there is a stronger reaction (red color) between the gas and the hydride near the top region, implying that the hydrogen gas near the top zone was absorbed most by the hydride.

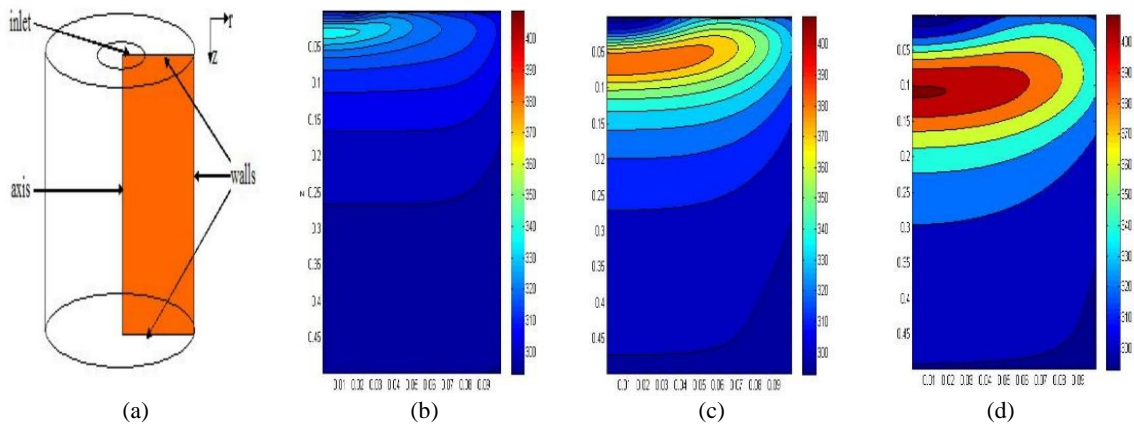


Fig. 1 (a) Reactor and cross section, and contours of hydride density distribution at times (b) 10 min, (c) 30 min, and (d) 60 min.

We then simulated the hydrogen desorption in a cylindrical $\text{LaNi}_5\text{-H}_2$ reactor with a height of 0.03 m and a radius of 0.05 m, as shown in Fig. 2(a). The reactor was first filled with $\text{LaNi}_5\text{-H}_2$ hydride and then heated from lateral and bottom walls. During the desorption process, it needs a space to store the discharged hydrogen gas. Thus, the cross section was considered to be the one without the outlet portion and the hydrogen was discharged from the top surface. The pressure at the top surface was assumed to be constant. Three meshes of 20×20 , 40×40 , and 80×80 in the (r, z) plane were used to test the convergence of the scheme. The time increment was chosen to be 0.001s. Figure 2 (b)-2(d) show contours of the hydrogen density in the hydride changing with time. Because the reactor was heated from lateral and bottom walls, the reaction took place first near the edge and then gradually toward to the core of the reactor. Region in blue color indicates that most of the hydrogen in the hydride has been discharged.

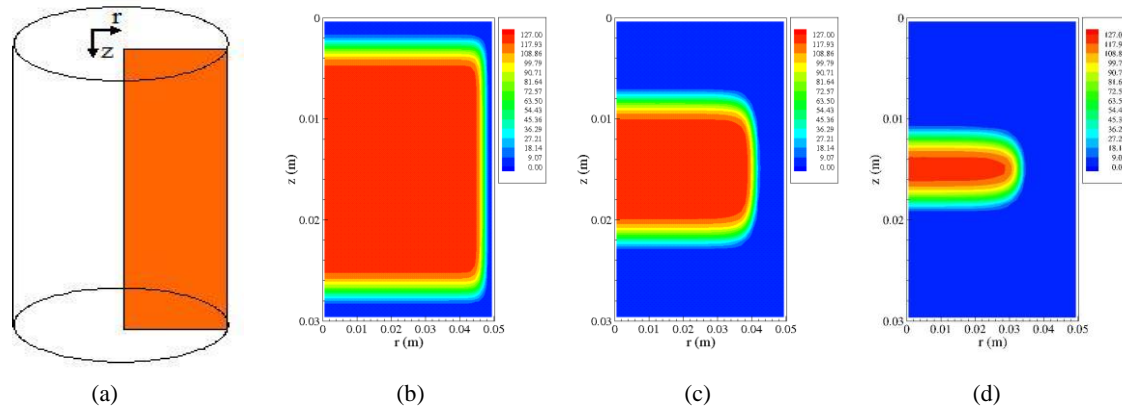


Fig. 2 (a) Reactor and cross section, and contours of density distribution in hydride at times (b) 10 min, (c) 30 min, and (d) 120 min.

4. Conclusion

We have developed a finite difference method in a staggered mesh for simulating both hydrogen absorption and desorption processes in cylindrical $\text{LaNi}_5\text{-H}_2$ reactors.

5. Acknowledgments

The current work is funded by the NSF EPSCoR LA-SiGMA project under award #EPS-1003897.

6. References

- [1] A. Demircan, M. Demiralp, Y. Kaplan, M. D. Mat, T. N. Veziroglu, *Int. J. Hydrogen Energy*, 30: 1437-1446, 2005.
- [2] G. G. Lucas, W. L. Richards, *Int. J. Hydrogen Energy*, 9: 225-231, 1984.
- [3] U. Mayer, M. Groll, W. Wupper, *Journal of the Less Common Metals*, 131: 235-244, 1987.
- [4] A. Jemni, S. B. Nasrallah, *Int. J. Hydrogen Energy*, 20: 43-52, 1995.
- [5] A. Jemni, S. B. Nasrallah, *Int. J. Hydrogen Energy*, 20: 881-891, 1995.
- [6] A. Jemni, S. B. Nasrallah, *Int. J. Hydrogen Energy*, 22: 67-76, 1997.
- [7] A. Jemni, S. B. Nasrallah, J. Lamloumi, *Int. J. Hydrogen Energy*, 24: 631-644, 1999.
- [8] A. Lopez-Suarez, J. Rickared, L. R. Trejo, *Int. J. Hydrogen Energy*, 28: 1107-1113, 2003.
- [9] M. Mat, Y. Kaplan, *Int. J. Hydrogen Energy*, 26: 957-963, 2001.
- [10] M. Mat, Y. Kaplan, K. Aldas, *Int. J. Hydrogen Energy*, 27: 973-986, 2002.
- [11] H. Dhaou, S. Mellouli, F. Askri, A. Jemni, S. B. Nasrallah, *Int. J. Hydrogen Energy*, 32: 1922-1927, 2007.
- [12] Y. Kaplan, T. N. Veziroglu, *Int. J. Hydrogen Energy*, 27: 1027-1038, 2002.

Optimization of Electroless Deposition of CoNiFeB Thin Films for Application in Magnetic Recording Media

Amin Azizi¹, Amin Yourdkhani², David Cutting¹, Noshir S Pesika¹, Gabriel Caruntu²

¹ Department of Chemical and Biomolecular Engineering, Tulane University

² Advanced Materials Research Institute, Department of Chemistry, University of New Orleans

Abstract: In today's rapid technological progress, magnetic recording media like hard disc drives (HDDs) have gained considerable attention because of their advantages in capacity, speed, and fabrication cost. In order to increase the areal density of HDDs, attempts have been made to make the read-write head smaller and the head-medium spacing smaller. Soft magnetic thin films with high saturation magnetic flux density (B_s) and low coercivity (H_c) are used as core materials of high-density recording heads. Electroless deposition method is a promising method for fabrication of magnetic thin films with such benefits as capability of uniform coatings fabrication on the substrates with fine and complex geometries. Recent developments of fabrication of high-performance CoNiFeB soft magnetic thin films applicable to the recording head cores are presented in this work. Effects of electroless bath conditions on the coating quality, crystal structure, composition, magnetic properties and deposition rate are rigorously investigated. Increase in the pH of the bath showed both the raise in the deposition rate and the BCC(110)/FCC(111) phase ratio of the synthesized samples. It was understood that magnetic properties of the samples have a reasonable relationship with their BCC(110)/FCC(111) phase ratio which can be controlled by optimizing the bath conditions.

Keywords: Thin Films, Magnetic Recording Heads, Electroless Deposition, Crystal Structure, Magnetic Properties

1. Introduction

Magnetic recording medium is a key information supportive technology in everyday human life. High-density magnetic recording gadgets are used as the storage devices of personal computers. Increase in the areal density of hard disk drives (HDDs) has been achieved via developments in the magnetic thin film materials. Soft magnetic thin films are used as core materials of high-density recording heads [1]. Low coercivity (H_c), high saturation magnetic flux density (B_s), and high electrical resistivity (ρ), are most important requirements for high performance of these magnetic recording heads [1-3]. Many soft magnetic films of such transition metals as Fe, Co and Ni and their alloys have been recently introduced for head core applications. NiFe alloys [4] have desirable characteristics including low coercivity (<2 Oe) and high saturation flux density (B_s) which increase

their thin film applications [4], while cobalt containing alloys like CoNiFe [5] and FeCo [6] have recently grown due to their higher saturation magnetization values [7].

The most common technique for the fabrication of magnetic devices such as writing head-cores having high aspect-ratio is electrodeposition. This method is, however, unable to coat non-conductive surfaces and create films with uniform thickness and composition in the sub-micrometer scale. The electroless deposition method has benefits like potential of uniform coatings fabrication on the substrates with fine and complex geometries, as this method does not suffer from the problems associated with current density distribution [2,7-9].

Although the earlier attempts to produce CoNiFeB coatings by electroless deposition method [5,7] have reported interesting results on synthesis of CoNiFeB thin film, they have not given precise details of the impact of the electroless bath condition on the coating quality and the thin film properties. This study describes the most recent findings achieved by rigorous investigation on the optimization of bath condition and its influence on the film thickness, morphology, composition, crystal structure and magnetic behavior.

2. Experimental Procedure

CoNiFeB thin films were deposited on an n-type silicon wafer via an electroless deposition method. Prior to the deposition, the silicon substrates were degreased with acetone for 5min to remove the dust and the organic substances. Samples were rinsed by double distilled water after each stage. A 100-nm gold layer was then sputtered onto the silicon surface to act as a catalytic surface for electroless deposition [5]. The gold sputtered silicon substrate was then dipped into an electroless plating bath for 60 seconds. The bath was alkaline in nature and contained sulfates of nickel, cobalt and iron as the sources of metallic raw ions and dimethylamine borane (DMAB) as the reducing agent. The temperature of the bath was kept at 70°C, and the pH was altered from 8 to 9.5. The electroless CoNiFeB coatings were obtained from different solutions in order to explore the effects of the pH of the bath on characteristics of the samples. Topography and thickness of the samples were characterized using atomic force microscopy (AFM). X-ray diffraction (XRD) was utilized to determine the crystal structure of the samples. The compositions of the films were obtained by energy dispersive X-ray spectrometry (EDS). A vibrating sample magnetometer (VSM) was applied to measure the magnetic properties of CoNiFeB coatings.

3. Results and Discussions

AFM measurements (Fig.1a) show that the thickness of the CoNiFeB films coated by electroless deposition are about 60, 68, 74 and 93 nm for the samples synthesized from the bath with pH 8, 8.5, 9, and 9.5, respectively. Composition variation of the CoNiFeB coatings with the pH of the bath (Fig.1b) indicates that the Ni content of the coatings increases with the pH of the bath. Co content of the coatings is, however, not significantly changed by the alteration of pH. Increase in Ni content (wt%) of the coatings is, hence, almost equal to decrease in Fe content (wt%) of the films. XRD results presented in Fig.1c show an interesting relationship between the crystal structure of the films and the bath condition and film composition. A decrease in BCC(110)/FCC(111) phase ratio

can be observed by increasing the pH of the bath in such a way that the BCC single-phase film deposited at pH 8 goes to the FCC single-phase film by increasing the pH of the bath to 9.5.

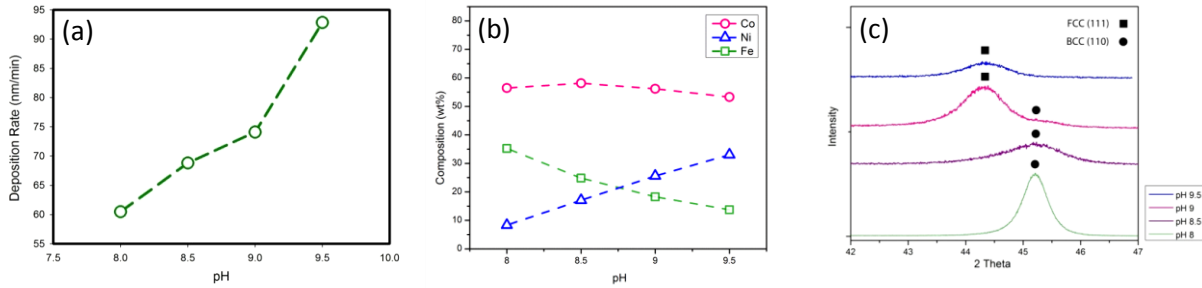


Fig.1. a) The deposition rate vs. pH of the bath, b) The composition of the films vs. pH of the bath, and c) XRD results of the electroless CoNiFeB films from the bath with different pH.

Fig. 2 shows the AFM images of the electroless CoNiFeB films fabricated from the solutions with different pH. As is seen, all the samples are very uniform and the average size of the particulates becomes smaller by increasing the pH which can be attributed to the increase in the deposition rate. However, the sample deposited at pH 9 has the smallest particulate size which can be ascribed to its crystal structure having the mixture of BCC/FCC phases. AFM results also indicated that the surfaces of the films are obviously smooth; showing RMS of 2.542, 1.598, 1.595, and 3.719 for the samples deposited at pH 8, 8.5, 9, and 9.5, respectively. A reasonable relationship between the magnetic properties of the samples and their crystal structure was found. Many other factors such as grain size, surface roughness, stress and thickness also influence on magnetic properties of thin films [7]. However, as VSM results (Fig.3) reveal, the saturation magnetization (B_s) of the films decreases when the pH of the bath increases which can be ascribed to the decrease of the BCC phase ratio in the samples [10]. High saturation magnetization and large coercivity (H_c) for the sample synthesized from the bath with pH 8 is the results of its BCC structure [10]. The low coercivity of the sample deposited at pH 9.5, on the other hand, can be attributed to the higher Ni content of the coating and its FCC structure.

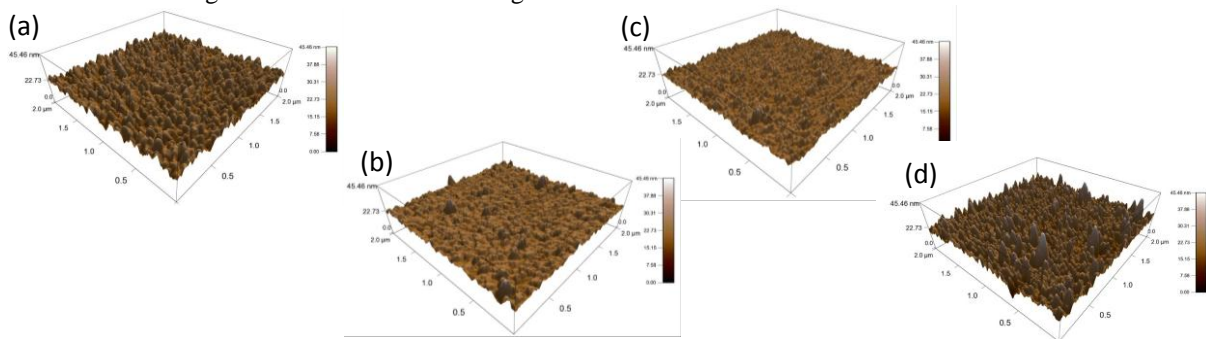


Fig. 2. AFM images of the electroless CoNiFeB films from the bath with the pH of: (a) 8, (b) 8.5, (c) 9, and (c) 9.5.

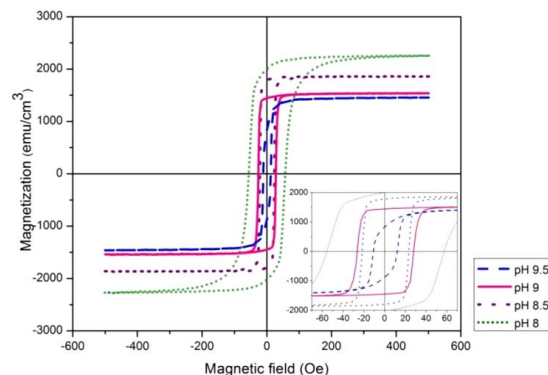


Fig.3. Magnetization curves of the electroless CoNiFeB films from the baths with different pH.

4. Conclusion

Homogenous and high quality CoNiFeB thin films with desirable magnetic properties suitable for recording head core applications were synthesized by an optimized electroless plating method. Increase in the pH of the bath resulted in rise in the deposition rate, and the BCC(110)/FCC(111) phase ratio in the samples was decreased by a rise in the pH of the bath. Magnetic properties of the films showed a reasonable relationship with their BCC(110)/FCC(111) phase ratio which can be controlled by optimizing the bath condition.

5. Acknowledgments

The current work is funded by the NSF EPSCoR LA-SiGMA project under award #EPS-1003897

6. References

- [1] T. Osaka¹, *et al.*, *Nature*, Vol. 392, 796-798. 1998.
- [2] T. Yokoshima, *et al.*, *J. Electroanal. Chem*, Vol. 491, 197–202. 2000.
- [3] T. Osaka, *et al.*, *Electrochim. Acta*, Vol. 50, 4576–4585. 2005.
- [4] Y. Zhou, *et al.*, *J. Magn. Magn. Mater*, Vol. 320, 963–966. 2008.
- [5] Y.K. Takahashi, *et al.*, *J. Magn. Magn. Mater*, Vol. 320, 490–495. 2008.
- [6] A. Hashimoto, *et al.*, *J. Magn. Magn. Mater*, Vol. 320, 3008–3010. 2008.
- [7] J.F. Rohan, *et al.*, *Electrochim. Acta*, Vol. 54, 1851–1856. 2009.
- [8] M. Mohammadi, *et al.*, *J. Coat. Technol. Res*, Vol. 7, 697-702. 2010.
- [9] A. Azizi, *et al.*, *Mater Lett*, Vol. 65, 289-292. 2011.
- [10] M. Saito, *et al.*, *J. Electrochem. Soc*, Vol. 149, C642-C647. 2002.

Preparation and Characterization of Amphiphilic, Biocompatible Cyclic Block Copolymers

Boyu Zhang, Scott M. Grayson

Department of Chemistry, Tulane University, New Orleans, LA 70118

Abstract: While amphiphilic block copolymers are of importance because their self-assembled aggregates can be used for drug delivery, the behavior of cyclic block copolymers remains largely unexplored. In order to investigate their behavior, cyclic amphiphilic poly(ethylene glycol)-polycaprolactone c-(PEG-PCL) was synthesized by a combination of ring opening polymerization (ROP) and click chemistry. In addition, exactly analogous linear block copolymers have been prepared as a control sample to better understand the effect that polymer architecture plays in self-assembly. The micellation and degradation behavior have been investigated and revealed unique differences that are related to the changes in architecture.

Keywords: Amphiphilic, cyclic polymer, self-assembly, drug delivery

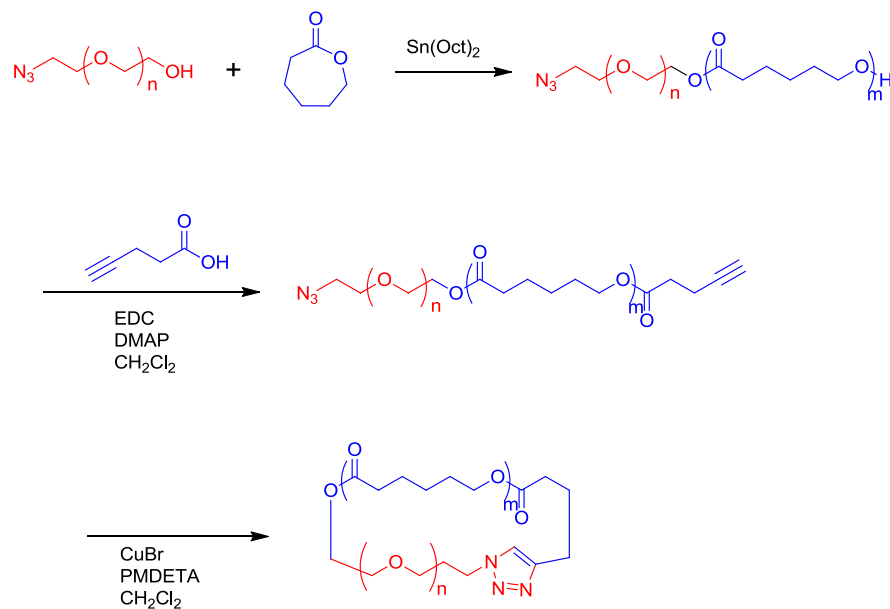
1. Introduction

Amphiphilic polymers are of interest for a range of applications because of their inherent ability to self-assemble into discrete objects. Controlling the size and stability of such aggregates is particularly important for drug delivery applications, as the size is one of the most critical features in determining its biodistribution, and the stability can be utilized to enable a controlled release of a therapeutic payload. A substantial body of work has already been carried out by numerous investigators in order to define and control the parameters of simple linear block copolymers,^[1] (those containing a series of repeat units that are polar, attached to a second series of repeat units that are non-polar.) However, only a limited amount of work has focused on cyclic polymers, owing to the difficulty in preparing such macromolecules in high purity.^[2] Recently, our research group has reported an efficient technique for preparing cyclic polymers using the highly efficient copper-catalyzed azide-alkyne cycloaddition reaction (CuAAC) in order to link the end groups of a linear polymer.^[3] The relative ease of this technique has already enabled the preparation of cyclic block copolymers.^[3] but in order to investigate the biological applications of these macromolecules, a biocompatible and biodegradable cyclic polymer has been investigated, based on blocks of poly(ethylene glycol) and poly(caprolactone).

2. Experiment section

2.1 Synthesis and characterization of the amphiphilic cyclic polymers

The cyclic polymers were prepared by the route described in scheme 1. α -hydroxy- ω -azido poly(ethylene glycol) was purchased from a commercial supplier (Polymer Source) and used to initiate the tin octanoate catalyzed ring opening polymerization of ϵ -caprolactone. The purity of both the starting material and the linear



Scheme 1. Synthetic route for preparing biocompatible cyclic block copolymers from poly(ethylene glycol) and poly(caprolactone).

block copolymer could be confirmed by the MALDI-TOF mass spectra (figure 1) and the gel permeation chromatography. Next, it is critical that the terminal hydroxyl of the polymer is converted quantitatively to the required alkyne functionality, otherwise the subsequent cyclization reaction cannot be quantitative, and the resulting linear impurities are extremely difficult to remove from the desired cyclic product. In order to assure that the alkyne functionalization occurs quantitatively, the terminal alcohol is esterified with pentynoic acid using EDC, a powerful esterification catalyst. The resulting diblock copolymer displays the required complimentary functionalities on opposite ends to enable the CuAAC cyclization. In order to ensure that cyclization is favored, rather than oligomerization, the cyclization had to be carried out under highly dilute conditions, that were achieved by a slow dropwise addition of the linear precursor to copper catalyst over multiple hours.

The purity of the cyclic product was confirmed by analyzing the both the matrix assisted laser desorption ionization-time of flight (MALDI-TOF) mass spectral data (figure 1) verifying that the average molecular weight of the cyclic product remains unchanged, and comparing to the gel permeation chromatograms (GPC) (figure 2), which exhibit a distinct shift in molecular size, characteristic of the shift in size caused by cyclization. Further evidence of the near quantitative cyclization of the block copolymer could be obtained by examination of the Fourier-transform infrared spectra (FTIR) (figure 3), which show a loss of the characteristic azide resonance (2200 cm^{-1}) which confirms the end group has been completely consumed in the cyclization reaction.

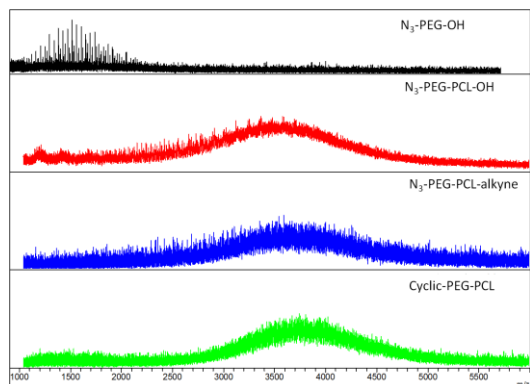


Figure 1. MALDI data the PEG starting material (black, top), the PEG-PCL diblock (red, second), the linear diblock α -azido- ω -alkynyl precursor (blue, third), and the cyclic diblock (green, bottom).

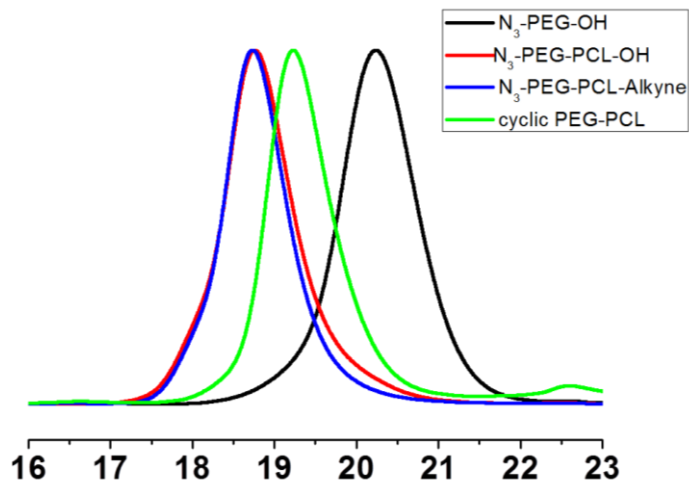


Figure 2. GPC data the PEG starting material (black), the PEG-PCL diblock (red), the linear diblock α -azido- ω -alkynyl precursor (blue), and the cyclic diblock (green).

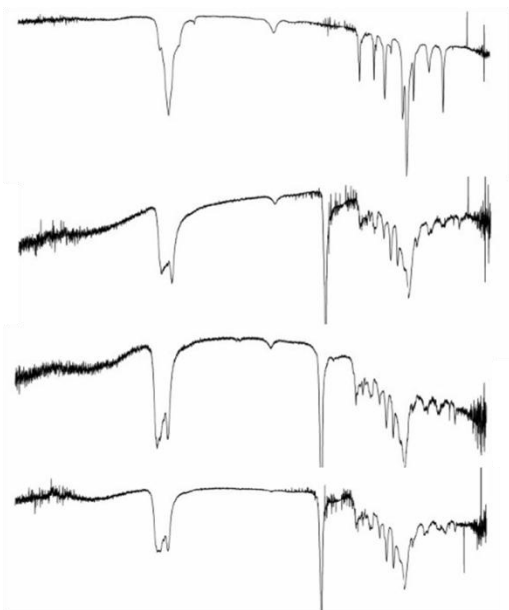


Figure 3. FTIR data the PEG starting material (top), the PEG-PCL diblock (second), the linear diblock α -azido- ω -alkynyl precursor (third), and the cyclic diblock (bottom).

3. Result and discussion

3.1 Characterization of amphiphile self-assembly by dynamic light scattering (DLS)

Upon confirming the purity of the cyclic polymer, both the linear PCL-PEG amphiphile and the cyclic analog were characterized using light scatter (figure 4). Both exhibit the formation of well-defined aggregates, with relatively narrow size distribution, but the cyclic polymer exhibited aggregates that were distinctly smaller than their linear analogs. It should be stressed that these both samples have the exact same molecular weight, dispersity, etc., but differ only in architecture.

N₃-PEG-OH

N₃-PEG-PCL-OH

N₃-PEG-PCL-alkyne

Cyclic PEG-PCL

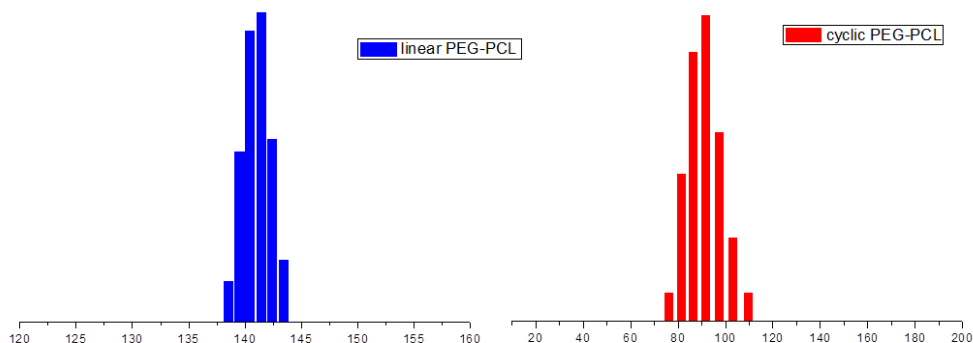


Figure 3. Size distributions of the self-assembled aggregates of the linear PEG-PCL (blue, left) and the exactly analogous cyclic PEG-PCL (red, right) confirm that the cyclic polymers exhibit a smaller overall aggregate size.

4. Conclusion

Amphiphilic cyclic polymers can be prepared with relative ease using the CuAAC cyclization procedure previously demonstrated for a range of non-amphiphilic homopolymers. Although detailed studies of their properties are ongoing, preliminary data confirms that the amphiphilic cyclic polymers exhibit unique behavior relative to linear analogs during their self-assembly into aggregates, in particular a smaller size for the cyclic relative to exact linear analogs. Further studies are ongoing to better understand both the physical properties of these materials, and their potential applications.

5. Acknowledgments

The current work is funded by the NSF EPSCoR LA-SiGMA project under award #EPS-1003897.

6. References

- [1] Torchilin, V. P. *J. Controlled Release* **2001**, *73*, 137-172.
- [2] Honda, S.; Yamamoto, T.; Tezuka, Y. *J. Am. Chem. Soc.* **2010**, *132*, 10251–10253.
- [3] Laurent, B. A.; Grayson, S. M. *J. Am. Chem. Soc.* **2006**, *128*, 4238-4239.
- [4] Eugene, D. M.; Grayson, S. M. *Macromolecules* **2008**, *41*, 5082-5084.

Self-consistent Calculations of Electronic Properties of Systems with Energy or Band Gaps

Diola Bagayoko,¹ Lashounda Franklin,¹ and Chinedu E. Ekuma²

¹Department of Physics, Southern University and A&M College, Baton Rouge, Louisiana

²Department of Physics and Astronomy, Louisiana State University, Baton Rouge, Louisiana

Abstract: We re-examine the process of performing *ab-initio*, self consistent calculations of electronic and related properties of semiconductors. This work applies to calculations utilizing density functional theory (DFT) and X_α potentials and to other computations that entail solving *a system of inherently coupled equations*. In particular, the local density approximation (LDA) and the generalized gradient approximation (GGA) of DFT are defined by *a system of equations* that reduces to the Kohn Sham equation and the equation giving the ground state charge density in terms of the wave functions of the occupied states – upon the selection of an exchange correlation potential. We discuss difficulties associated with single trial basis set calculations that *do not verifiably obtain the minima of the occupied energies of the material under study. These minima are truly self-consistent solutions, with physics content, of the system of equations*. We describe how the Bagayoko, Zhao, and Williams (BZW) method solves self consistently the relevant system of equations to obtain the minima of the occupied energies. The resulting, calculated, electronic properties are in agreement with corresponding experimental ones. The enhancement of this method by the work of Ekuma and Franklin (EF) leads to results in **excellent agreement** with experimental ones. In the methodical increase in size and enrichment of the basis set in our calculations, *this enhancement generally leads to adding p , d , and f orbitals, for a given principal quantum number, before adding the s orbitals*. The resulting BZW-EF method produced excellent results for rutile TiO_2 , w-ZnO, c-SrTiO₃, and zb-InP. Unquestionably, the BZW-EF method is profoundly transformative as (a) it provides accurate, electronic, structural, transport, optical, and related properties of semiconductors, including band gaps, and (b) it ushers in an era of *ab-initio*, self-consistent, and accurate predictions of properties of novel materials. **Hence, BZW-EF calculations can inform and guide the design and fabrication of devices based on finite or crystalline materials with energy or band gaps, respectively.**

Keywords: DFT potentials, *ab-initio*, self consistent, BZW-EF method, energy and band gaps

1. Introduction

From their introduction in the first half of the 20th century to 2012, quantum mechanical calculations of properties of materials have made significant progress. From the onset, however, obtaining an accurate potential describing various systems has been a challenge. In 1964, Hohenberg and Kohn [1] introduced density functional theory (DFT) that has since been widely utilized to obtain potentials that are a unique functional of the electronic charge

densities of the materials under study. The local density approximation (LDA) [2] and the generalized gradient approximation (GGA) [3] potentials of DFT are presently the most widely used. These potentials were found to describe metals rather well. Up to 1997-98, first principle calculations utilizing these potentials mostly led to woeful underestimates, by 30 to 50% or more, of the measured band gaps of semiconductors and insulators. Several, non ab-initio potentials have been constructed, using LDA or GGA potentials, in attempts to solve this band gap problem. A feature of many of these potentials, including the ones from LDA+ C, LDA+U, GGA +U+V, and many versions of hybrid functional potentials, etc., is that they are essentially ad hoc in nature and often depend on adjustable parameters that vary from one material to the next. It appears that a large segment of the scientific, publishing, and funding communities is satisfied with this situation that takes us away from ab-initio, predictive solutions. With this continuing proliferation of non ab-initio schemes, the band gap problem has become a band gap catastrophe, in the view of some observers.

The aim of this work is to present a mathematically rigorous computational method that indicates that much of the earlier failures of DFT in describing energy or band gaps could be ascribed to computational shortfalls as opposed to intrinsic limitations of DFT potentials. A second motivation is to describe our computational method that appears to have resolved most of the energy and band gap problem while yielding electronic and related properties in excellent agreement with corresponding, experimental ones.

2. The BZW-EF Method

Upon the selection of an exchange correlation potential, the single-particle Kohn-Sham (KS) equation, in the local density approximation (LDA), is:

$$\left[-\frac{1}{2}\nabla^2 + V(\vec{r}) + \int \frac{n(\vec{r}')}{|\vec{r}-\vec{r}'|} d\vec{r}' + V_{xc}(n(\vec{r})) \right] \psi_i(\vec{r}) = \varepsilon_i \psi_i(\vec{r}),$$

where $V_{xc}(n(\vec{r}))$ is a functional derivative of the exchange correlation energy with respect to the charge density given by $n(\vec{r}) = \sum_{i=1}^N \psi_i^*(\vec{r})\psi_i(\vec{r})$, a sum over wave functions of *occupied* states only.

With the selection of the potential, the system of equations defining LDA (or GGA) is reduced to the two above. The second equation (for the charge density) is like a constraint of the first, the KS equation. The variational derivation of the KS equation dictates that the physically acceptable solution to it be obtained with a charge density that best approximates that of the real system, on the one hand, and *that leads, verifiably, to the minima of the occupied energies*, on the other hand. With localized orbitals (i.e., exponential or Gaussian orbitals), there is an added requirement that the corresponding basis set must not be over-complete. *Clearly, a single trial basis set, irrespective of its judicious selection, can generally not lead, verifiably, to the minima of the occupied energies. Further, we know of no scheme for establishing that such a basis set is not over complete.* We described below a method that circumvents these difficulties.

In the original Bagayoko, Zhao, and Williams (BZW) method [4-5], one starts the self-consistent calculations for a system by utilizing the minimal basis (MB) set, i.e., the basis set that is just large enough to account for all the electrons in the material. It is understood that the output from this self consistent calculation does not provide a physical description of the material. A second calculation is performed with a basis set that includes the MB set plus one additional orbital from an excited state of one of the atomic or ionic species present in the material. Depending on the angular symmetry of that state, and taking spin into account, this addition leads to an increase of 2, 6, 10, or 14 functions for s, p, d, or f states, respectively. The occupied energies of Calculations I and II are compared and are generally found to be different, with those from II generally lower than their corresponding ones from Calculation I. A third calculation is therefore necessary, after augmenting the basis set as described above. Again, the occupied energies of Calculations II and III are compared. This process of augmenting the basis set and of performing self consistent calculations continues until one finds a calculation, say N, to have the same occupied energies as Calculation (N+1). Given that the occupied energies have already converged to their minima in Calculation N, the outputs of this calculation provide the physical description of the system under study. The basis set for this calculation is referred to as the optimal basis set. Calculations with basis sets obtained by augmenting the optimal one lead to the same charge density, potential, Hamiltonian, and occupied energies as Calculation N – even though they often lead to some further lowering of some unoccupied energies. Out of some fundamental misunderstanding, some have argued that those lower conduction bands are more converged than the one obtained with the optimal basis set. In the absence of any change in the Hamiltonian, the extra-lowering cannot be ascribed to a physical interaction. Further, the Rayleigh theorem explains the extra lowering of unoccupied energies as a mathematical artifact. As described above, the BZW method can be thought of as systematic sampling of Hilbert space to determine the optimal basis set.

Recent works by Ekuma and Franklin led to the realization that, for valence electrons in binary molecules and any other system containing two (2) or more atomic or ionic species, polarization (p, d, and f orbitals) has primacy over spherical symmetry (s orbitals). Consequently, in the methodical augmentation of the basis set beyond the minimum one, we generally add p, d, and f orbitals, if applicable, before the s orbital of the same principal quantum number. While the BZW method has resolved the band gap problem [4-7], as compared to most other ab-initio DFT calculations, it still often leads to results that are 0.1 to 0.3 eV smaller than the measured band gaps. With the BZW-EF method, this small underestimation vanishes and the resulting widths of the occupied bands are also in excellent agreement with measured ones. The same is true for the optical properties (i.e., dielectric functions and optical conductivities), electron effective masses, peaks in the total densities of states (DOS), and structural and elastic properties. Hence, as per the results, the BZW-EF method [8-10] has resolved not only the band gap problem, but also the general problem of inaccurate, first principle, calculated properties of materials with an energy or a band gap.

3. Results

Numerous, quantitative results from the application of the BZW and BZW-EF methods are provided in references [4] through [10]. In particular, our predictions for cubic Si_3N_4 [6] and InN [7] have been confirmed by experiment [11-12] and [13], respectively. Our recent, BZW-EF results for CdS [8], TiO_2 [9], SrTiO_3 [10] are available in the literature while those for Ge , ZnO , and zb-InP are under peer review.

4. Conclusion

The mathematical rigor and ab-initio nature (parameter-free) of the BZW-EF method and the excellent agreements between our calculated, electronic and related properties of materials clearly indicate that we have solved a problem that dates from the inception of quantum mechanics. *This solution, it should be underscored, ushers in an era of ab-initio, self consistent, accurate, descriptive and predictive calculations of electronic and related properties of materials.* In this sense, it marks the dawn of transformative computations of properties of materials.

5. Acknowledgments

The current work is funded by the NSF EPSCoR LA-SiGMA project under Award # EPS-1003897 and NSF (2010-15)-RII-SUBR.

6. References

- [1] P. Hohenberg and W. Kohn, Phys. Rev 136, No.3B, B 864, 1964.
- [2] W. Kohn, Rev. Mod. Phys. 71, 1253, 1999.
- [3] John P. Perdew, Kieron Burke, and Matthias Ernzerhof, Phys. Rev. Lett. 77, 3865, 1996.
- [4] D. Bagayoko, G. L. Zhao, J. D. Fan, and J. T. Wang, J. of Phys.: Cond. Matter, 10, 5645, 1998.
- [5] G. L. Zhao, D. Bagayoko, and T. D. Williams, Physical Review B 60, 1563, 1999.
- [6] D. Bagayoko and G. L. Zhao, Physica C364-365, Pages 261-264, 2001.
- [7] D. Bagayoko, L. Franklin, and G. L. Zhao, J. Appl. Phys. 96, 4297, 2004.
- [8] C. E. Ekuma, L. Franklin, G. L. Zhao, J. T. Wang, and D. Bagayoko. Can. J. Phys. Vol. 89, 319-324, 2011.
- [9] C. E. Ekuma and D. Bagayoko, Japanese Journal of Applied Physics (JJAP), 50, 101103 (2011).
- [10] C. E. Ekuma, M. Jarrell, J. Moreno, and D. Bagayoko, AIP Advances 2, 012189 (2012).
- [11] R. G. Egdell, V. E. Henrich, R. Bowdler, and T. Sekine, J. Appl. Phys 94, 6611, 2003.
- [12] J. Z. Jiang, H. Lindelov, L. Gerward, K. Stahl, J. M. Recio, P. Mori-Sanchez, S. Carlson, M. Mezouar, E. Dooryhee, A. Fitch, and D. J. Frost, Phys. Rev. B, Rapid Communications, 65, 161202(R), 2002.
- [13] J. Schörmann, D. J. As, K. Lischka, P. Schley, R. Goldhahn, S. F. Li, W. Löffler, M. Hetterich, and H. Kalt, Appl. Phys. Lett. 89, 261903, 2006.

Simulation of Propylene Carbonate Solutions for Electrochemical Double-layer Capacitors

X. You,¹ K. M. Aritakula,² N. Pesika,¹ L. R. Pratt,¹ and S. W. Rick²

¹Department of Chemical & Biomolecular Engineering, Tulane University

²Department of Chemistry, University of New Orleans

Abstract: Validation, adjustment, and characterization of simulation models on the basis of interfacial characteristics have laid the basis for recently initiated dynamical simulation of filling of a nanotube forest by propylene carbonate (PC) tetraethylammonium-tetrafluoroborate (TEABF₄) solutions. Revised simulation models agree with measure contact angles of PC on graphite. Simulations of liquid films produce accurate values of the PC liquid-vapor tension, and then specific superficial excess entropy and internal energy. The density profiles of PC:TEABF₄ solutions are strongly structured at the low temperature of T=300K, but not at T=400K. Simulations of PC droplets, designed to study curvature dependence of surface thermodynamics, exhibit non-classic fragmentation processes for metastable droplets.

Keywords: propylene carbonate (PC), tetraethylammonium-tetrafluoroborate (TEABF₄), molecular dynamics simulation, graphite, contact angles, interface thermodynamics, droplet fragmentation

1. Introduction

We reported last year [1] on validation of molecular models of electrochemical double-layer capacitors, or *supercapacitors*. Validated models enable dynamical simulation of the filling of a carbon nanotube forest with propylene carbonate (PC) tetraethylammonium-tetrafluoroborate (TEABF₄) solutions. That system has realistic chemistry and a well-defined microstructure that makes fully molecular simulation both realistic and worthwhile, though a severe challenge.

Validation of molecular simulations requires effective interaction between experiment and simulation. What is more, it requires assessment of what is possible for experiment and for simulation, and good judgment for what comparisons are informative. We have focused on contact angles of solution droplets on graphite as a model electrode material. Charge-discharge cycling of a supercapacitor is expected to lead to bubble formation that can be an important mechanism for mechanical damage. Therefore interface properties associated with the contact angles are highly significant.

The observed contact angle of PC on graphite (Figure 1, upper panel) was reported last year [1]. The corresponding initial simulation results [1] showed complete wetting of the graphite by PC for the off-the-shelf force-field model, qualitatively different from the experimental result. Adjustment of the dispersion attractions between the PC molecules and graphite now reproduces the experimental contact angle (Figure 1, lower panel). Specifically, all graphite-PC dispersion interactions were reduced by a factor of 0.4.

Ongoing work is characterizing the system-size dependence of these simulation results, investigating the *line tension* associated with three phase contact, the dependence on electrolyte composition, and response to electrode charging. This direct success has been followed-up with more detailed studies of the specific interfacial properties of these fluid phases.

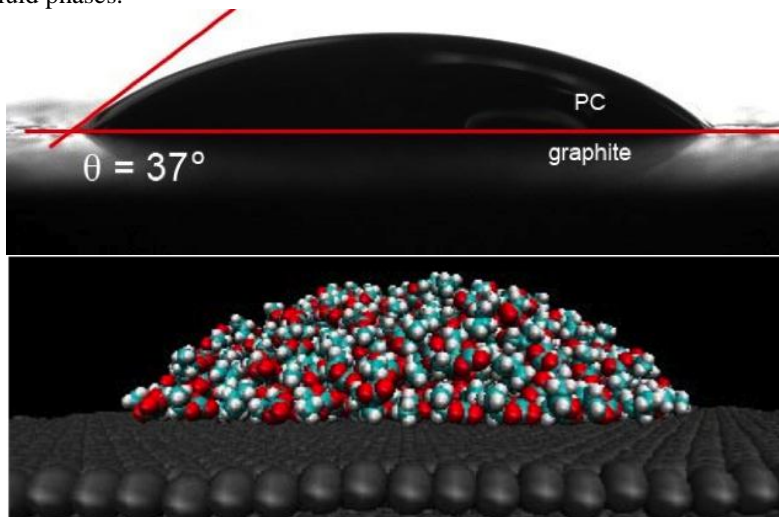


Figure 1: Propylene carbonate (PC) droplet on graphite. (upper panel) The low observed contact angle indicates good wetting behavior, and suggests that PC should effectively fill nanotube forests. (lower panel) Simulated PC droplet on model graphite. The attractive interactions between the PC molecules and the graphite are adjusted empirically to match the experimental result.

2. Bulk liquid PC

Bulk liquid simulations provide basic data for construction of accurate thermophysical information that assist in device-level modeling of electrochemical double-layer capacitors. We summarize our previous results [1] with a generalized AMBER force-field (GAFF): The dielectric constant of the liquid and its temperature derivative, the density and the compressibility of the bulk liquid are in satisfactory agreement with experiment

3. PC liquid-vapor interfaces

Interfacial characteristics of these solutions were investigated by molecular simulation of liquid-vapor, two-phase systems in standard slab geometry (**Figure 2**). In this geometry, the interfacial tension, $\gamma = \bar{A}^{(s)}$ (the specific superficial excess Helmholtz free energy referenced to the Gibbs equimolar surface), can be evaluated by differencing interfacial stresses in the standard way; for the PC solvent we obtained $\gamma = 40.8$ and 29.9 erg/cm^2 at T

= 300K and 400K, respectively. (At 20C, the experimental value is 41.1 erg/cm².) Estimating the temperature derivative provides specific superficial excess entropy, $\bar{S}^{(s)} = (-)dy / dT \approx 0.11$ erg/cm² K, a quantitative

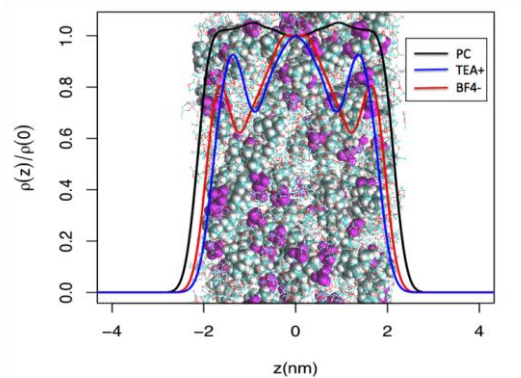


Figure 2: Molecular simulation of a PC:TEABF₄ liquid slab in coexistence with vapor of T=300K. Here $n_{PC}=1000$, $n_{TEABF_4}=85$, and $\tau(\text{observation time}) = 20\text{ns}$. The black curve is the density of the PC atoms, the blue curve is the density of the N atom in TEA⁺, and the red curve is the density of the B atom of BF₄⁻.

indication of the (dis)ordering of the PC molecules at these interfaces. The specific superficial excess internal energy is then $\bar{U}^{(s)} = \bar{A}^{(s)} + T\bar{S}^{(s)} \approx 74$ erg/cm².

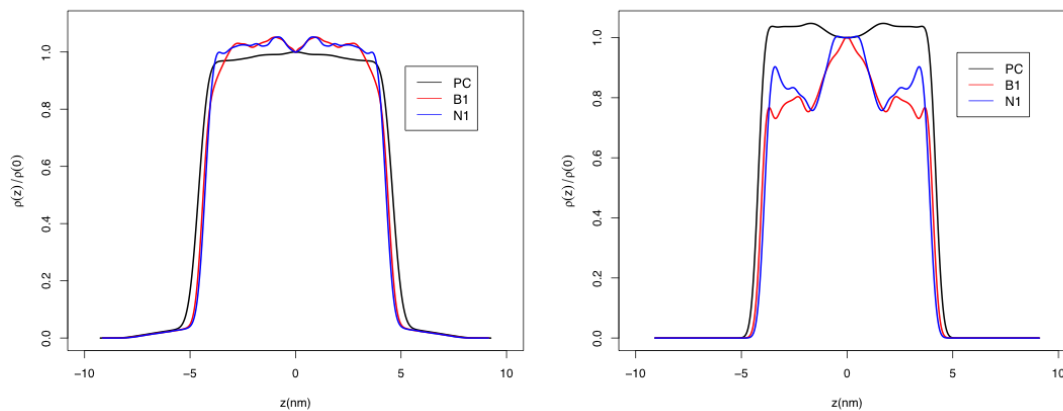


Figure 3: Density profiles for saturated PC:TEABF₄ solutions at T=300K (right) and T=400K (left); $n_{PC} = 2000$, $n_{TEABF_4} = 170$, and $\tau(\text{observation time}) = 50\text{ns}$.

The liquid-vapor interfaces of the solutions, including ions, (Figures 2 and 3) are significantly structured at the low temperature of $T = 300\text{K}$, but not at the higher temperature $T = 400\text{K}$. This is similar to observations for ionic liquids, but not yet well-explained in broader physical terms. The results so far indicate that the ions do not appreciably change the surface tension from the solvent-only value.

4. Simulation of PC droplets

Understanding the curvature dependence of these surface tensions should help in treating the physical issues of droplet/bubble formation in nanoscopic pores. The thermodynamic theory for that curvature dependence seems well-established. Implementation of that classic theory requires simulation of droplets coexisting with their vapor phase [2,3]. Droplets have a higher vapor pressure than the macroscopic liquid. But in the standard view, that vapor pressure difference provides information on curvature dependence of the surface thermodynamics. In attempting to follow that classic line of reasoning with simulation calculations, we have made the original observation that these droplets do not equilibrate by a simple mechanism of condensation/evaporation of individual molecules. Instead long simulations invariably ended with spontaneous formation of a fluid neck that pinches off to divide the droplet into two similar sized fragments (Figure 4).

5. Conclusions

Validation, adjustment, and characterization of simulation models on the basis of interfacial characteristics have laid the basis for recently initiated dynamical simulation of filling of a nanotube forest by PC:TEABF₄ solutions. Simulations of PC droplets have provided direct observations of droplet break-up that suggests a non-classic mechanism for equilibration of droplets with a vapor phase.

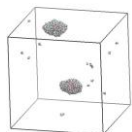


Figure 4: Snapshot of the debris after a droplet break-up. Here $n_{PC}=1200$ and $T=300\text{K}$. These break-ups typically occur after several nanoseconds of simulation but are then complete in less than a nanosecond.

6. Acknowledgments

The current work is funded by the NSF EPSCoR LA-SiGMA project under award #EPS-1003897.

7. References

- [1] G. G. Hoffman, R. Mariano, N. Pesika, L. R. Pratt, S. W. Rick, X. You, *Proceedings of the 2011 RII LA-SiGMA Symposium*, 101-104 (2011)
- [2] J. G. Powles, *J. Phys. A: Math. Gen.* **18**, 1551 (1985): "On the validity of the Kelvin equation"
- [3] J. G. Powles, R. F. Fowler, and W. A. B. Evans, *Chem. Phys. Letts.* **96**, 289 (1983): "A new method for computing surface tension using a drop of the liquid"

Statistical Mechanics of a Hard Rod in the Hard Sphere Fluid

L. R. Pratt,¹ and H. S. Ashbaugh¹

¹Department of Chemical & Biomolecular Engineering, Tulane University

Abstract: Evaluation of the statistical thermodynamics of a *long-thin* hard rod in a hard-sphere solvent proceeds on the basis of general quasi-chemical methods, and is simple and successful. This result will be a helpful ingredient to general development of scaled-particle theories of these systems, with intended utility in describing the statistical thermodynamics of solution-filled carbon nanotube forests.

Keywords: carbon nanotube forests, van der Waals theory, quasi-chemical theory, scaled-particle theory, statistical thermodynamics, Monte Carlo calculations

1. Introduction

This contribution is directed toward basic statistical mechanics problems underlying composite fluid materials involving rod structures. Systems of specific interest are solution-filled carbon nanotube (CNT) forests. We treat systems composed of hard-core molecules because they foundational to the theory of liquids [1-3]. For hard-core molecules the intermolecular interactions are either infinite (when the molecules overlap), or zero.

A superficial perspective on these difficult statistical mechanical problems is that hard-core systems are merely models. Real systems are susceptible to simulation, and are not hard-core systems. More seriously, however, quasi-chemical theory [4] re-instates hard-core, or *packing*, problems as an integral contribution to free energies generally considered (Figure 1). Thus, ultimate assessment and understanding of solution free energies for real systems requires assessment of packing contributions. Not only are those packing contributions essential, assessment of those packing contribution is the most severe of the challenges (Figure 1) to implementation of quasi-chemical theory to molecular liquids.

$$\beta\mu^{(ex)} = -\ln p^{(0)}(n_\lambda = 0) + \ln \langle e^{\beta\epsilon} | n_\lambda = 0 \rangle + \ln p(n_\lambda = 0)$$

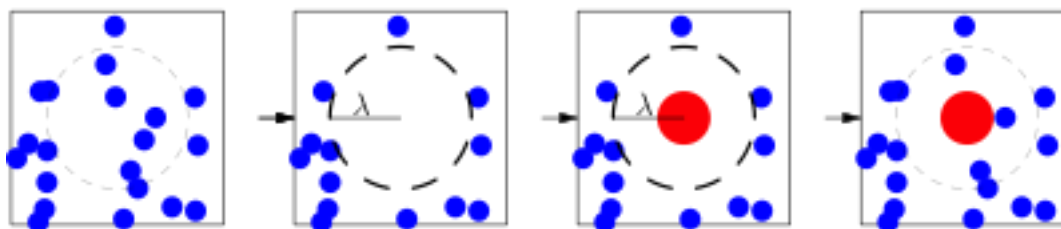


Figure 1: General quasi-chemical partitioning of solution free energies, from left to right: Packing, outer-shell, and chemical contributions [4]. The left-most or packing contribution is defined by hard-core interactions between the designated molecule, a hard-rod solute in the present study.

2. Methods

Scaled-particle theory [5-6] is the most effective and physically instructive general approach to modeling of those packing contributions. Here we report initial steps in implementing a scaled-particle theory for a system of a hard rod in a bath of hard-sphere solvent molecules.

A characteristic feature of scaled-particle theories is the analysis of solution free energies in limiting extremes of scale of a distinguished solute, here the hard rod. Denoting the rod length as L and the rod cross-sectional radius λ , then an interesting limiting-scale problem is the *long-thin* (or needle) limit $L : \infty, \lambda : 0$. [This is not the only interesting limiting-scale problem for rod in a hard-sphere solvent!]

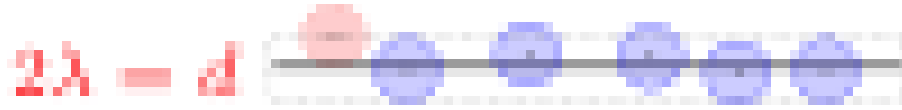


Figure 2: Geometry for the partition function calculation essential to the *long-thin* limit as formulated in quasi-chemical theory for hard-core problems [7-8]. The pink sphere illustrates the geometry of closest approach of a hard sphere to the needle. The dashed rectangle is the excluded-volume silhouette for the cylindrical rod that is infinitely long.

Here we apply the hard-core version [7-8] of quasi-chemical theory to solve that limiting *long-thin* problem. The essential task is the evaluation a grand canonical partition function of hard-spheres confined to the excluded volume footprint of the rod (Figure 2):

$$1 + \sum_{n \geq 1} \zeta^n K_n = e^{\beta \mu_{rod}^{(ex)}} \quad (1)$$

Here ζ is an activity, or occupancy mean-field, that permits adjusting the occupancy of the excluded volume to the expected value $\langle n \rangle = L(\pi\lambda^2)\rho$, with ρ the thermodynamic density of the solvent. K_n is a canonical partition function for n hard spheres in that *long-thin* volume. The required partition function can be exactly evaluated on the basis of the following ideas: (a) further mean-field contributions are irrelevant in the *long-thin* limit because neither longitudinal or transverse forces can play a significant role in this geometry; and (b) the partition function for hard spheres on a line is exactly soluble in the thermodynamic limit [9-10].

3. Results

The result of those considerations is

$$\frac{L(\pi\lambda^2)\rho}{1-d(\pi\lambda^2)\rho} : \beta\mu_{rod}^{(ex)} = -\ln p_0(\lambda) \quad (2)$$

Notice that this free energy is strictly proportional to L in this approximation. The last equality introduces a structural interpretation of this thermodynamic free energy: $p_0(\lambda)$ is the probability that a random insertion of the rod would not overlap any sphere [5]. See also Figure 1. Further structural consequences are

$$\frac{\partial\beta\mu_{rod}^{(ex)}}{\partial\lambda} = 2\pi\lambda L\rho G(\lambda) : \frac{2\pi\lambda L\rho}{(1-\pi\lambda^2\rho d)^2} , \quad (3)$$

$$g^{(1)}(r) = p_0(\lambda=r)G(\lambda=r) . \quad (4)$$

$G(\lambda)$, “the contact value,” is the radial distribution of hard-spheres evaluated at contact with the surface of the rod excluded-volume [5], and $g^{(1)}(r)$, for $r>\lambda$, is the radial distribution at radius r of the sphere that is *nearest* to the rod [11].

Comparative numerical results were obtained directly by Monte Carlo methods (Figure 3); the numerical details will be reported elsewhere.

4. Conclusions

Evaluation of the statistical thermodynamics of a *long-thin* hard rod in a hard-sphere solvent proceeds on the basis of general quasi-chemical methods, and is simple and successful. This result will be a helpful ingredient to general development of scaled-particle theories of these systems, with intended utility in describing the statistical thermodynamics of solution-filled carbon nanotube forests..

5. Acknowledgments

The current work is funded by the NSF EPSCoR LA-SiGMA project under award #EPS-1003897.

6. References

- [1] B. Widom, *Science* **157**, 375 (1967): “Intermolecular forces and the nature of the liquid state”
- [2] D. Chandler, J. D. Weeks, and H. C. Andersen, *Science* **220**, 4599 (1983): “van der Waals picture of liquids, solids, and phase-transformations”
- [3] E. M. Waisman and J. L. Lebowitz, *Physics Today* **33**, 24 (1980): “Statistical mechanics of simple fluids: beyond van der Waals”
- [4] D. Asthagiri, P. D. Dixit, S. Merchant, M. E. Paulaitis, L. R. Pratt, S. B. Rempe, and S. Varma, *Chem. Phys. Letts.* **485**, 1 (2010): “Ion selectivity from local configurations of ligands in solutions and ion channels”
- [5] H. S. Ashbaugh and L. R. Pratt, *Rev. Mod. Phys.* **78**, 159 (2006): “Scaled-particle theory

and the length scales of hydrophobicity"

[6] H. S. Ashbaugh and L. R. Pratt, *J. Phys. Chem. B* **111**, 9330 (2007): "Contrasting nonaqueous against aqueous solvation on the basis of scaled-particle theory"

[7] L. R. Pratt, R. A. LaViolette, M. A. Gomez, and M. E. Gentile, *J. Phys. Chem. B* **105**, 11662 (2001): "Quasi-chemical theory for the statistical thermodynamics of the hard-sphere fluid"

[8] L. R. Pratt and H. S. Ashbaugh, *Phys. Rev. E* **68**, 021505 (2003): "Self-consistent molecular field theory for packing in classical liquids"

[9] R. P. Feynman, STATISTICAL MECHANICS, A SET OF LECTURES (Benjamin, Reading, 1972). Section 4.7.

[10] L. Tonks, *Phys. Rev.* **50**, 955 (1936): "The complete equation of state of one, two and three-dimensional gases of hard elastic spheres"

[11] P. Zhu, X. You, L. R. Pratt, and K. D. Papadopoulos, *J. Chem. Phys.* **134**, 054502 (2011): "Generalizations of the Fuoss approximation for ion pairing"

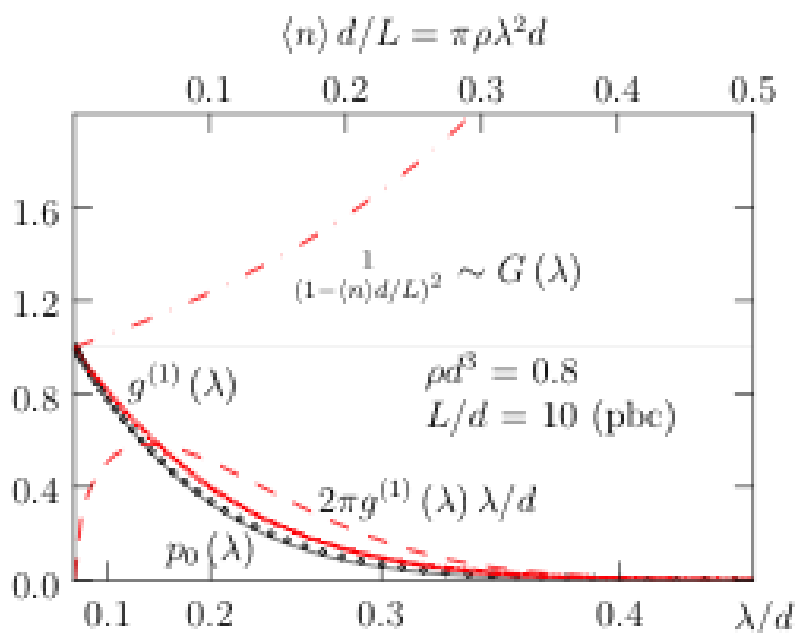


Figure 3: Comparison of quasi-chemical calculation of the statistical thermodynamics of a *long-thin* limiting hard rod in a solvent of hard spheres of diameter d with Monte Carlo results. The circles are the Monte Carlo numerical results of the success probability, $p_0(\lambda)$, for insertion of the rod into the hard-sphere bath. The value $\rho d^3=0.8$ corresponds to a dense fluid thermodynamic state; for liquid Ar this would be just slightly less dense than the triple point. The comparison is encouraging, but note that the contact value $G(\lambda)$ is not larger than 2 here. Consulting Figure 2, we note that $\lambda/d=0.5$ is the physical needle case.

Structural Analysis of Bosch Heated Exhaust Gas Oxygen Sensors after Voltage Treatments

Regina Blackman¹, Arwa Alshowaier², Erica P. Murray²

¹Department of Chemistry, Francis Marion University

²Institute for Micromanufacturing, Louisiana Tech University

Abstract: Heated Exhaust Gas Oxygen Sensors are used to detect the emissions of the everyday vehicle. Applying a voltage to these sensors simulates the conditions that the sensor is under when in a vehicle. Experiments show that when a voltage is applied for a long enough time, blackening occurs around the electrodes. By performing voltage treatments, it is possible to define the conditions that cause blackening. It is also possible to see the changes in the structure of the Yttria Stabilized Zirconia (YSZ) by cutting the sensor and looking at it under a Scanning Electron Microscope. Looking at the cut sensor under an optical microscope allows for the design of the sensor to be examined and measurements to be taken.

Keywords: Heated Exhaust Gas Oxygen (HEGO) Sensor, Yttria Stabilized Zirconia (YSZ), Platinum Electrode, Sensor Side, Heater Side, Blackening

1. Introduction

Heated Exhaust Gas Oxygen (HEGO) sensors are used to detect the oxygen emissions from engines. These sensors help to optimize air-fuel ratio within the engine. The correct air-fuel ratio helps to prevent engine misfire and wasted fuel. HEGO sensors are composed of platinum electrodes encased in an Yttria Stabilized Zirconia (YSZ) electrolyte. When a large voltage is applied to this YSZ, it becomes blackened. Blackening is caused by a strong chemical reduction, or when oxygen is taken from the lattice structure [3,4]. Using an optical and a Scanning Electron Microscope, this change in the lattice structure or blackening can be readily observed.

2. Experimental Procedure

Bosch Heated Exhaust Gas Oxygen (HEGO) Sensor samples were placed in the sensor housing. Ten samples were examined; heat as well as voltage applied to each one as shown in Table 1. The heat was applied using a regulated DC power supply, where the voltage was applied using a single output programmable DC power supply. After the voltage treatment, the samples were cut using a low speed saw. The samples were then examined using X-Ray Diffraction, a Scanning Electron Microscope, and an optical microscope at various magnifications.

Table 1: Voltage, Temperature, and Time of Voltage Treatments for 11 Samples

Sample Number	Voltage (V)	Temperature (°C)	Time Period (hrs)
1	2	400 (9 V)	4
2	Raw Sample (No Voltage Treatment)		
3	2	400 (9 V)	2
4	2	400 (9 V)	3
5	2	400 (9 V)	4
6	3	400 (9 V)	1
7	3	700 (18 V)	0.333
8	2	750 (20 V)	4
9	2.8	750 (20 V)	1
10	2.6	750 (20 V)	3.5
11	2.9	750 (20 V)	2

3. Results and Discussion

Figure 1 displays Sample 6, the first of two samples that were blackened. The right side of the hole is the sensor side, and the left is the heater side. It is apparent that the blackening starts at the heater electrodes and radiates out towards the sensor electrodes. The most significant results achieved were comparing the treated samples to the raw sample. As more samples were treated and examined under the optical microscope, the orientation of the electrodes in the zirconia became clearer. It was noted that at fraction 1 of the sensor, there are 2 platinum electrodes on the heater side, but at fraction 8, there are 4. After the samples are treated, the hole size increases, as shown in Figures 1 and 2. The size difference from figure 1a to 1b is large. In figures 2a and 2b, there is no noticeable difference in size. Figure 4 shows that the counts of YSZ are significantly less in the blackened sample. Figure 5 shows the structural changes seen when looking at YSZ that is not blackened, and also YSZ that is blackened.

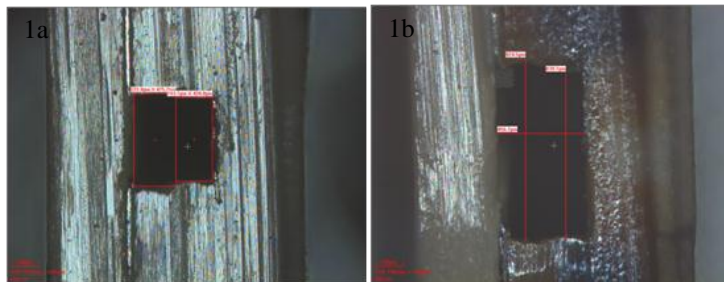


Figure 1 a) and b): Sample 6, fractions 1 and 8 respectively: Noting the difference in hole size as well as color.

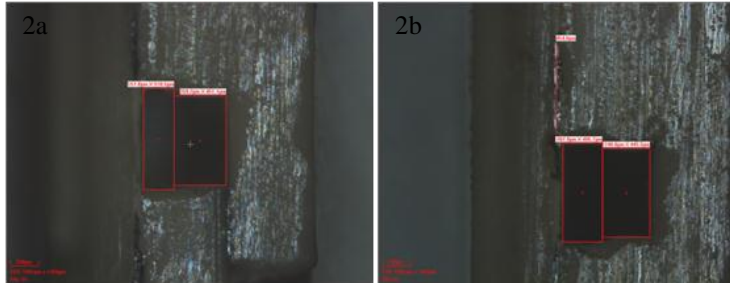


Figure 2 a) and b): Sample 2 (Raw sample), fractions 1 and 8 respectively. There is no noticeable difference in the size of the hole.

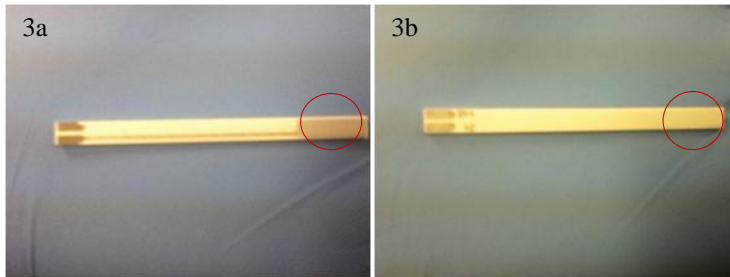


Figure 3 a) Sensor Side and b) Heater Side of a Bosch HEGO sensor. The outlined area is where the blackening occurs (Fraction 8). The opposite end is where the sensor is placed in the housing (Fraction 1).

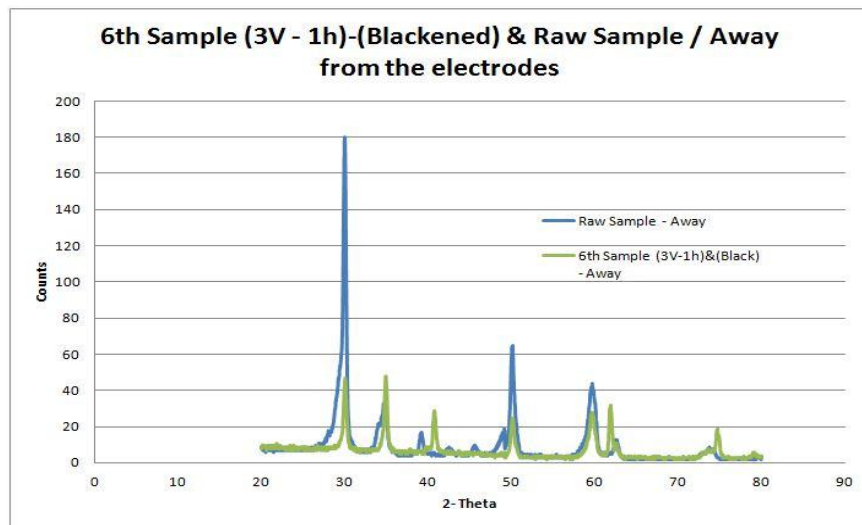


Figure 4: XRD plot comparing the Raw Sample and the Blackened (6th) Sample

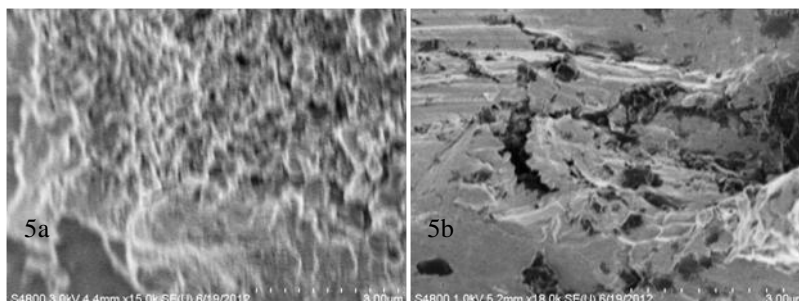


Figure 5: a) SEM image of heater electrode of sample 6, fraction 6 (not blackened) at $3\mu\text{m}$. b) SEM image of heater electrode of sample 6, fraction 8 (blackened) at $3\mu\text{m}$. The structural changes are easily seen.

4. Conclusion

The oxygen that is removed from the lattice structure may affect the functionality of the HEGO sensors. Further research on this will help to define the conditions under which the YSZ becomes blackened. Of the 10 samples that were treated, only two were blackened. From this, it is easy to define the upper threshold of the parameters. When the sensor was treated at 3V, there were signs of blackening, occurring faster and more spread out when the temperature was raised from 400°C to 700°C . Also, the images from the optical microscope help to determine where the blackening is occurring. The blackening is affecting the area around the sensor electrodes. It starts on the inside of the heater electrodes and is blackened through to the opposite side of the sensor electrodes.

5. Acknowledgments

The current work is funded by the NSF EPSCoR LA-SiGMA project under award #EPS-1003897.

6. References

- [1] Butz, B., R. Schneider, D. Gerthsen, M. Schowalter, and A. Rosenauer. "Decomposition of 8.5 Mol.% Y_2O_3 -doped Zirconia and Its Contribution to the Degradation of Ionic Conductivity." *Acta Materialia* 57 (2009): 5480-490. *Science Direct*. Web. 30 May 2012.
- [2] Hattori, Masatoshi, Yasuo Takeda, Yoshinori Sakaki, Akihoro Nakanishi, Satoshi Ohara, Kazuo Mukai, Jin-Ho Lee, and Takehisa Fukui. "Effect of Aging on Conductivity of Yttria Stabilized Zirconia." *Journal of Power Sources* 126 (2004): 23-27. *Science Direct*. Web. 30 May 2012.
- [3] Nazarpour, S., C. Lopez, F. Ramos, and A. Cirera. "Structural and Electrical Properties of Y-doped Zirconia Induced by Electrical Polarization." *Solid State Ionics* 184.1 (2011): 19-22. *Science Direct*. Web. 30 May 2012.
- [4] Nazarpour, S., C. López-Gándara, F. M. Ramos, C. Zamani, A. Cirera, and M. Chaker. "High Temperature Phase Stability and Chemical Analysis of the Highly Doped Yttria-stabilized Zirconia with Alumina." *Ceramics International* 38 (2012): 4813-818. *Science Direct*. Web. 6 June 2012.

Study of the Hydrogen Storage Capability of KMgH_3

Brandon Borill¹, Randall Hall^{1,3}
Fernando Soto², Daniela Mainardi²

¹Department of Chemistry, Louisiana State University

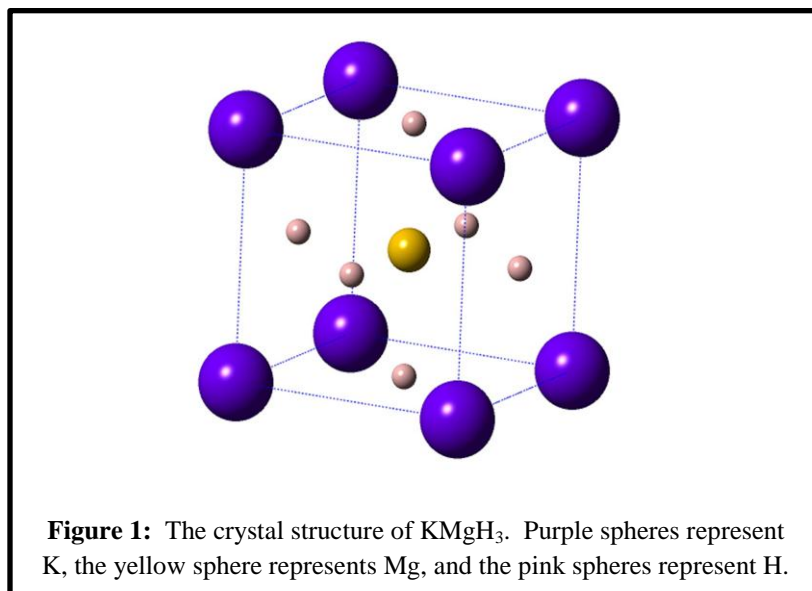
²Department of Chemical Engineering, Louisiana Tech University

³ Department of Natural Sciences and Mathematics, Dominican University of California

Abstract: Grand canonical Monte Carlo simulations were employed in the study of the hydrogen storage capabilities of KMgH_3 . The average number of hydrogen atoms was examined in relation to changes in temperature and pressure and fixed position of metal atoms vs. mobile atoms. The research goals are developing better hydrogen storage materials.

Keywords: Hydrogen storage, Monte Carlo, metal hydride

1. Introduction



Metal hydrides provide one particular avenue of computational and experimental research of solid state hydrogen storage materials. Metal hydrides containing a single metal or multiple metals are targets of hydrogen storage research, though other materials such as carbon nanotubes and metal organic frameworks are also studied as

potential solid state hydrogen storage materials. Some examples of complex metal hydrides studied in hydrogen storage research are LaNi_5H_6 , KMgH_3 , NaMgH_3 , and MgNiH_4 [1, 2, 3]. Figure 1 depicts the crystal structure for KMgH_3 .

Ideal hydrogen storage materials readily accept hydrogen, but do not exhibit high thermodynamic stability. Also of importance for the ideal material are properties such as lower volume and lower mass in addition to being inexpensive. The stated ideal properties are embodied in target values set by the United States Department of Energy [4].

In terms of approaching the ideal hydrogen storage materials, metal hydrides meet the DOE requirements for volumetric capacity [4]. Metal hydrides suffer a setback from ideality due to the issue of high mass density. Some materials such as palladium fail due to expense [5]. A positive for some metal hydrides is their thermodynamic qualities. The enthalpy of hydrogen loss for KMgH_3 is 99.1 kJ mol^{-1} and as low as 30.1 kJ mol^{-1} for LaNi_5H_6 [6, 7].

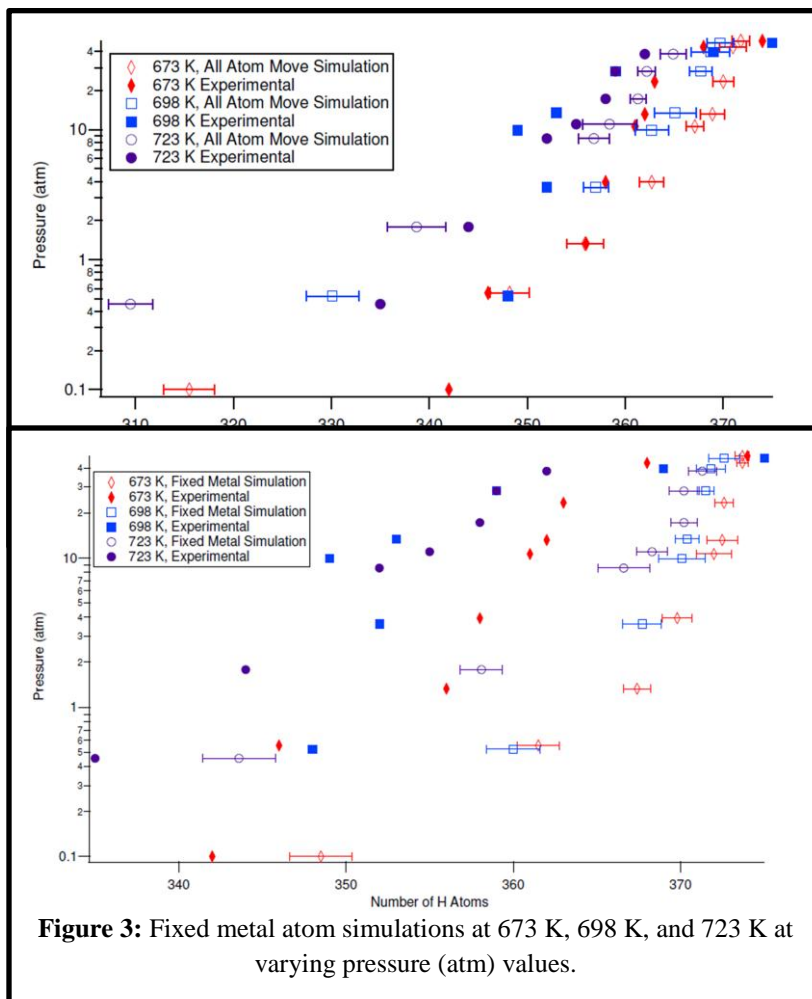
2. Computational Procedure

Calculations included the use of an embedded-atom potential (EAM) similar to that developed for the study of hydrogen in α -iron [8]. Force field parameters were determined using canonical Monte Carlo simulations to minimize the cost function that depended on energies and bulk moduli of K and Mg as well as KMgH_3 . To determine the average fraction of available hydrogen binding sites at different temperatures and pressures, grand canonical Monte Carlo was employed. Simulations were performed using machines provided by the Louisiana Optical Network Initiative (LONI) and the high performance computing resources at LSU.

3. Results and Discussion

Studies on the hydrogen storage properties of KMgH_3 are currently active. Comparisons to the experimental research performed by Komiya et al form the basis of the performed simulations [9]. It is important to note these experimental comparisons are based on digitized plot data from the Komiya paper. Grand canonical Monte Carlo simulations were performed at 673 K, 698 K, and 723 K at varying pressures to determine the average fraction of hydrogen in the $5 \times 5 \times 5$ system of KMgH_3 lattices. At full capacity, there are 375 hydrogen atoms in this system. Also compared was the average fraction of hydrogen in a system where all the atoms were permitted to be mobile (Figure 2) and a system where only the hydrogen atoms were permitted to be mobile (Figure 3).

For the mobile atom simulations, agreement with the experimental data does not occur at low pressures. However, direct comparison with low pressure experimental data is hindered by the fact that decomposition/phase separation occurs at low pressures. Thus, we focus on the higher pressure data when assessing the comparison between simulation and experiment. There is greater statistical agreement with the experimental data at higher pressures. There is much less agreement with the experimental data if the metal atoms are kept fixed during the simulation. Despite the better results with the mobile atom simulations, the current results are still not in quantitative agreement with the experimental data, but appear to be qualitatively correct.



4. Conclusions and Future Work

Currently, the data obtained from the grand canonical Monte Carlo simulations has yet to achieve statistically similar data to the experimental results of Komiya et. al. Research is ongoing to resolve this issue. We seek to improve the sampling method and develop better Monte Carlo sampling to achieve this effort.

5. Acknowledgments

The current work is funded by the NSF EPSCoR LA-SiGMA project under award #EPS-1003897.

This work was performed using the computer resources of the Louisiana Optical Network Initiative (LONI) and high performance computing resources at LSU.

6. References

- [1] Tanaka, S., Clewley, J. D., and Flanagan, Ted B. J. *Phys. Chem.*, 81, 1684 (1977).
- [2] Klaveness, A., Swang, O., and Fjellvag, H. *Europhys. Lett.*, 76, 285 (2006).
- [3] Garcia, G. N., Abriata, J. P., and Sofo, J. O. *Phys. Rev. B*, 59, 11746 (1999).
- [4] Gigras, Ankur, Bhatia, Suresh K., Kumar, A. V. Anil, and Myers, Alan L. *Carbon*, 45, 1043 (2007).
- [5] Crespo, E. A., Ruda, M., and de Debiaggi, S. Ramos. *Int. J. Hydrogen Energy*, 33, 3561 (2008).
- [6] Shinzato, Yoshifumi, Komiya, Kenji, Takahashi, Yoshitaka, Yukawa, Hiroshi, Morinaga, Masashiko, and Orimo, Shinichi. *Adv. Quantum Chem.* 54, 245 (2008).
- [7] Gallagher, Patrick K. *Handbook of Thermal Analysis and Calorimetry, Volume 2: Applications to Inorganic and Miscellaneous Materials*. Elsevier: San Diego, 2003: p. 344.
- [8] Ramasubramaniam, Ashwin, Itakura, Mitsuhiro, and Carter, Emily. *Phys. Rev. B*, 79, 174101 (2009).
- [9] Komiya, K., Morisaku, N., Rong, R., Takahashi, Y., Shinzato, Y., Yukawa, H., Morinaga, M. *J. Alloys Cmpds.*, 453, 157 (2008).

Study of The Spin State of Localized Mn in (GaMn)As and (GaMn)N

R. Nelson^{1,2}, T. Berlijn³, W. Ku³, J. Moreno^{1,2}, and M. Jarrell^{1,2}

¹Department of Physics and Astronomy, Louisiana State University
²Center for Computation and Technology, Louisiana State University

³Condensed Matter Physics & Materials Science Department,
Brookhaven National Laboratory

Abstract: The local density approximation (LDA)+U [1] is applied and combined with a Wannier function-based downfolding method [2] to produce an effective Hamiltonian within the energy windows of interest. The band structure (BS) and density of state (DOS) of (GaMn)As show that the d-orbitals of Mn are very localized and weakly hybridize with As p-orbitals. We conclude that the spin state of Mn in (GaMn)As is 5/2. However, the results for (GaMn)N show that the Mn d-orbitals strongly hybridize with N p-orbitals and the spin state of Mn is between 5/2 and 2.

Keywords: (GaMn)As, (GaMn)N, magnetic semiconductors, LDA, downfolding

1. Introduction

Dilute magnetic semiconductors are ideal candidates for spintronic device applications including non-volatile computer memory. They are promising materials for spintronics because they are able to sustain spin-polarized currents and capable of integration within the standard semiconductor technology [3]. There is a tremendous interest in developing heterostructures and nanostructures made of magnetic semiconductors. However, controlling the properties of magnetic semiconductor nanostructures involves many parameters that are difficult to address experimentally. Often it is faster and cheaper to test new ideas with computer simulations prior to addressing them in the laboratory.

Among dilute magnetic semiconductors (GaMn)As and (GaMn)N are interesting materials to study. Although GaAs and GaN are III-V-based semiconductors and have similar characteristics, their properties change quite differently when impurities are added. Most of the experiments agree that GaAs becomes ferromagnetic when doped with Mn with a Curie temperature (T_c) lower than room temperature [4]. However, there are several controversies about the properties of GaN doped with Mn [5,6,7], including its ferromagnetic transition temperature T_c and the spin state of Mn. Most of theorists and experimentalists believe Mn in (GaMn)As has a spin 5/2 whereas in (GaMn)N is still controversial [8]. Since the localized Mn spin state is important to describe many-body processes in materials, identifying the spin state of Mn is crucial in analyzing the behavior of carriers in these systems. This is the main point we would like to present in this report.

In Sec. 2 the methods are described and, following that, the results and discussions will be given in Sec. 3. And at the end we will conclude our report and describe future works in Sec. 4.

2. Methods

We applied LDA+U [1] to calculate the band structure of the systems. The results were then downfolded using a downfolding method developed by W. Ku, et al. [2].

Local Density Approximation (LDA)+U

LDA+U calculations were performed using the WIEN2K package [9] in the LONI cluster machines. The local coulomb interaction (U) between electrons in d-orbitals and the Hund's coupling (J) were added in order to capture the local correlation effects in Mn d-orbitals. The magnitude of U and J were set to 3.9 and 1.0 eV, respectively. The calculations were not sensitive to the precise value of either U or J. Augmented plane waves (APW) combined with local orbitals (LO) were used as the basis to solve the Kohn-Sham equation.

The Wannier Functions-Based Downfolding Method

The purpose of the downfolding is to obtain an effective Hamiltonian which reproduces the dispersion in the energy window of interest. This method uses Wannier functions as the basis to integrate out all high energy levels and produce an effective Hamiltonian in the low energy region. By definition Wannier functions are

$$|rn\rangle = \frac{1}{\sqrt{l}} \sum_{jk} e^{-ik \cdot r} U_{jn}(k) |kj\rangle, \quad (1)$$

where l is the number of unit cells, whereas $|kj\rangle$ is the Bloch state. The unitary matrix U gives us the freedom to construct the most suitable Wannier functions. In this case we use atomic-based projection operators to construct the U matrix. Matrix elements of the effective Hamiltonian in the Wannier function-basis are then given by

$$\langle r'n'|H|0n\rangle = \sum_{kj} \langle r'n'|kj\rangle \varepsilon_{kj} \langle kj|0n\rangle, \quad (2)$$

where ε_{kj} denote the Kohn-Sham eigenvalues.

3. Results and Discussion

Fig. 1 shows (GaMn)As BS for up and down channels after downfolding to an energy window close to the Fermi energy. Different colors represent different character of the bands. As we can see Mn d-orbitals (red) are very localized and only weakly hybridize with As p-orbitals (light-green). In other words, the charge degree of freedom of Mn is frozen and Mn only keeps its spin degree of freedom. Furthermore, since the valence electrons of Mn are seven ($4s^2 3d^5$) thus, after giving-up its two s-electrons to form a covalent bond with As, it forms a local moment with spin 5/2. Moreover, because in this system Mn basically replaces Ga which has three ($4s^2 4p^1$) valence electrons, every Mn impurity, with localized d-orbitals, ideally provides a hole. This can be seen in the BS for the up channel where we can find a hole-pocket at the Fermi level.

These findings justify previous theoretical works on modeling (GaMn)As with the spin-fermion model [10].

$$H = \sum_k \varepsilon_k c_k^\dagger c_k + J \sum_R \mathbf{S}(\mathbf{R}) \cdot \mathbf{s}(\mathbf{R}) \quad (3)$$

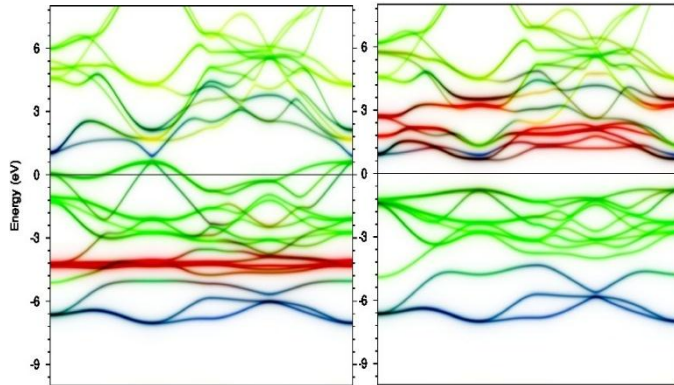


Figure 2. The downfolded band structure of (GaMn)As for up (left) and down (right) spin channels. Mn d-character is indicated by red whereas As p-character by light-green, and Ga s- & p-characters by blue and yellow, respectively.

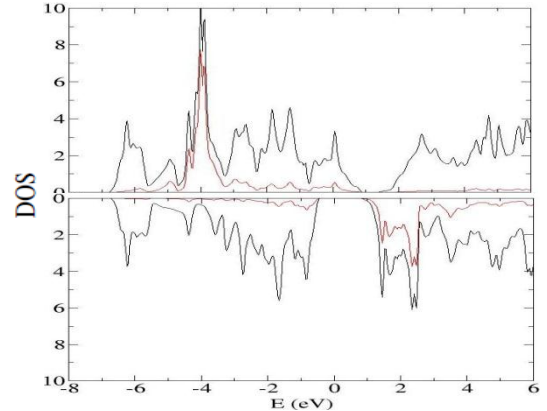


Figure 1. The total density of state (black) of (GaMn)As and Mn d-like band contributions (red) in up (above) and down (below) spin channels.

The spin-fermion model itself is the manifestation of the weak hybridization of Mn d-orbitals with As p-orbitals. A canonical transformation of (GaMn)As effective tight-binding (TB) Hamiltonian gives us the spin-fermion model. In addition to that, the large spin of localized Mn impurities allows its classical treatment. Fig. 2 shows the DOS of (GaMn)As for up and down channels. This figure is further evidence of the presence of the localized Mn d-orbitals.

From the BS and DOS of (GaMn)As we infer different electronic properties for the spin up and down channels. We see no gap in the up channel while a big gap appears in the down channel. It means that (GaMn)As is conducting in one channel but insulating in the other. This property makes (GaMn)As a special kind of material so-called half metallic.

For (GaMn)N the results are quite different. Fig. 3 shows the BS of (GaMn)N for up and down channels. Like (GaMn)As, (GaMn)N is also conducting only in one channel. However, as we can see from the BS Mn d-orbitals (red) strongly hybridize with N p-orbitals (light-green) and some Ga s-orbitals (blue). This means that the charge density of Mn strongly fluctuates. Therefore, unlike (GaMn)As, the effective TB Hamiltonian of (GaMn)N cannot be reduced to the spin-fermion Hamiltonian by a canonical transformation because the low energy excitations include charge fluctuations of the Mn ion between +2 and +3. This also means the spin state of Mn in (GaMn)N is between 5/2 and 2 and the Mn spin should be treated quantum mechanically. The DOS of (GaMn) shown in Fig. 4 gives further evidence. Unlike in (GaMn)As, Mn d-contribution in (GaMn)N is spread over several valence bands indicating strong charge exchange between GaN orbitals and Mn d-orbitals.

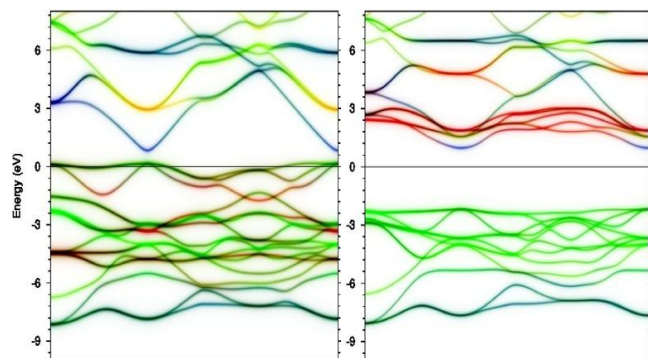


Figure 3. The downfolded band structure of (GaMn)N for up (left) and down (right) spin channels. Mn d-character is indicated by red whereas N p-character by light-green, and Ga s- & p-character by blue and yellow, respectively.

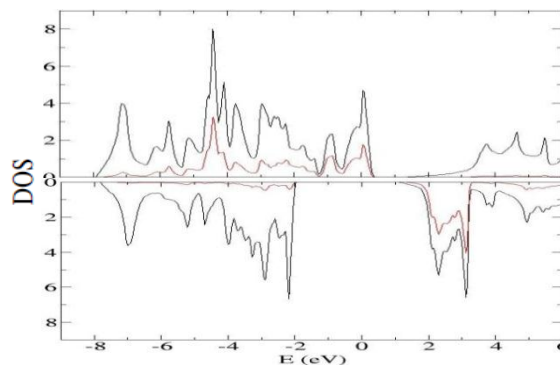


Figure 4. The total density of state (black) of (GaMn)N and Mn d-like band contributions (red) in up (above) and down (below) spin channels.

4. Conclusions and Future Work

We have performed *ab-initio* calculations to study the spin state of Mn in (GaMn)As and (GaMn)N. We have shown that Mn's charge degree of freedom is frozen in (GaMn)As due to its d-orbitals being very localized. We also conclude that Mn has a spin 5/2 and this justifies the use of the spin-fermion model for (GaMn)As. However, Mn in (GaMn)N does not have the charge degree of freedom frozen and thus the spin-fermion model is not reliable to study many-body effects in (GaMn)N. These findings will be applied to many-body calculations in the future especially to end the controversy of the possible ferromagnetism in (GaMn)N.

5. Acknowledgment

This work is supported by the NSF EPSCoR Research Infrastructure Improvement (RII) Award # EPS-1003897.

6. References

- [1] V.I. Anisimov, I.V. Solovyev, M.A. Korotin, M.T. Czyzyk, and G.A. Sawatzky, Phys. Rev. B **48**, 16929 (1993).
- [2] W. Ku, H. Rosner, W.E. Pickett, and R.T. Scalettar, Phys. Rev. Lett. **89**, 167204-1 (2002).
- [3] MacDonald, A.H.; Schiffer, P; and Samarth, N. Nature Materials **4**, 195 - 202, 2005.
- [4] V. Novak et. al., Phys. Rev. Lett. **101**, 077201 (2008).
- [5] T. Dietl, H. Ohno, F. Matsukura, J. Cibert, and D. Ferrand, Science **287**, 1019 (2000).
- [6] S. Sonoda, S. Shimizu, T. Sasaki, Y. Yamamoto, and H. Hori, J. Cryst. Growth **237**, 1358 (2002).
- [7] S. Dhar et. al., Appl. Phys. Lett. **82**, 2077 (2003).
- [8] T. C. Schulthess, et. al., J. Phys.: Condens. Matter **19**, 165207 (2007).
- [9] P. Blaha, K. Schwarz, G. K. H. Madsen, D. Kvasnicka, and J. Luitz, Wien2k, An Augmented Plane Wave + Local Orbitals Program for Calculating Crystal Properties (K. Schwarz, Techn. Universitat Wien, Austria, 2011).
- [10] U. Yu, A.-M. Nili, K. Mielson, B. Moritz, J. Moreno, and M. Jarrell, Phys. Rev. Lett. **104**, 037201 (2010).

Superparamagnetic Iron Oxide Nanoparticles with Variable Size and Iron Oxidation State: Synthesis and Relaxivity Studies

Pavel Kucheryavy¹, Galina Goloverda¹, Cheryl Stevens¹, Leonard Spinu², D. Lenormand², Jibao He³, Vijay John³, Alex Burin³, Charles Johnson⁴, Jackie Johnson⁴ and Vladimir Kolesnichenko¹

¹ Department of Chemistry, Xavier University

² AMRI, University of New Orleans,

³ Departments of Chemical and Biomolecular Engineering and Chemistry, Tulane University

⁴ The University of Tennessee Space Institute

Abstract: Systematic study of the reaction conditions, electrochemistry and complexation was conducted for the synthesis of magnetite in diethylene glycol by high temperature hydrolysis. Cyclic voltammetry and conductivity data indicated the presence of several chloro and alkoxide complexes existing in diethylene glycol solutions of different iron species. The strength of these complexes is compared and discussed in terms of possible reaction mechanisms. The study showed that magnetite nanoparticles can be obtained in high yield regardless of Fe^{II} being used, along with Fe^{III}, in the synthesis or not. The average sizes for the magnetite nanoparticles can be adjusted in the range of 4-7.5 nm by tuning the reaction temperature, solution concentration, and by employing the technique of a sequential growth. Magnetite colloids in diethylene glycol can be reversibly oxidized by molecular oxygen at room temperature into magnetic iron (III) oxide. However, the oxidation state of iron in the nanoparticles causes minimal effect on their relaxivity properties, which is beneficial for the biomedical applications. The larger particles were found to have a higher magnetic susceptibility and T1 relaxivity towards the protons of water or diethylene glycol.

Keywords: magnetite, complexation, cyclic voltammetry, conductivity, relaxivity

1. Introduction

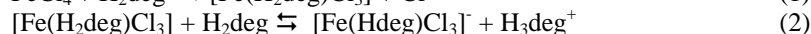
Nanoparticulate metal oxides for a variety of applications are commonly synthesized by solution precipitation reactions. It is a minimum requirement that the products are chemically pure, non-aggregated and have uniform size and shape. In addition, better methods offer control over the size and shape of the nanoparticles [1]. In the first level of control, particle size can be changed when crystal nucleation, growth and coarsening steps are well-separated in time, and the rate of each is a controlled variable. Keeping in mind that all steps of the metal oxide crystallization result from the same chemical reaction, it is clear that achievement of this level of control is not a trivial task. In principle, limitation in the upper side of the size scale can be easily understood, as stability of the colloids is exhausted for progressively growing particles. On the other hand, there are no obvious obstacles for the colloidal stability of the smaller particles or even molecular cage compounds. In this project we are trying to achieve such a level of control over the chemical reaction that would allow us to synthesize the metal oxides in a broad range of the particle sizes, from ultrasmall particles and cage compounds, to relatively large nanoparticles. The mechanism of the metal oxide precipitation reactions is well established for aqueous solutions [2], however, reactions utilized in this work for the synthesis of magnetic metal oxide particles are based on a non-aqueous

solution high-temperature hydrolysis of the chelated metal alkoxide complexes. The mechanism of these non-ionic reactions is not known, nevertheless, its understanding is very important as it can contribute to the finding of a better control over the chemical reaction. In addition to the synthesis and characterization of the magnetite nanoparticles, we report some results shedding light on the nature of several intermediates.

2. Results and Discussion

1. Iron coordination complexes as precursors for magnetic particles.

To evaluate complexation of iron with diethylene glycol we studied solutions of anhydrous FeCl_3 , FeCl_2 and NaFeCl_4 salts in diethylene glycol by the conductivity measurements, cyclic voltammetry (CV) and UV-VIS spectrometry. The CV curves (Fig. 1) for all studied demonstrate several redox processes which points at the presence of more than one component in solution. Most of the processes can be represented by the equations 1 and 2.



Under basic conditions, these complexes undergo deprotonation yielding chelated alkoxide complexes:

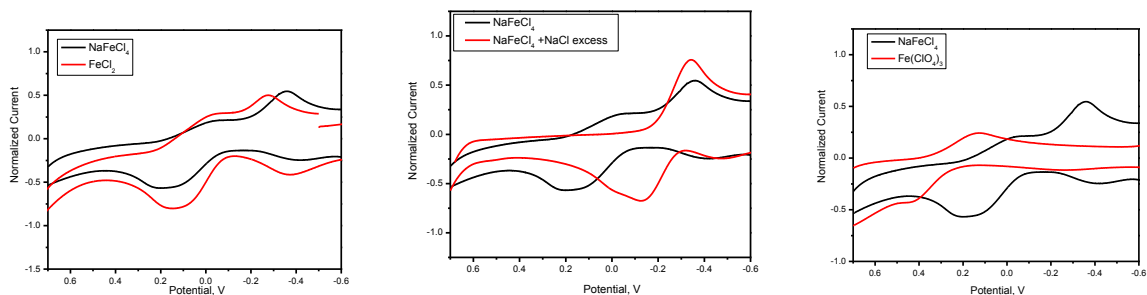


Fig. 1. CV curves for NaFeCl_4 , FeCl_2 , $\text{NaFeCl}_4 + \text{NaCl}$ and $\text{Fe}(\text{ClO}_4)_3$ in diethylene glycol solutions.

High-temperature hydrolysis and reduction of these complexes in diethylene glycol solutions results in formation of magnetite nanoparticles in colloidal form.

2. Synthesis and characterization of magnetic particles

Synthesis of the nanoparticulate iron oxides was accomplished by high-temperature hydrolysis reaction of chelated iron diethylene glycol alkoxides. We have determined that the hydrolysis reactions are indefinitely slow at room temperature, but they are fast at temperatures of 180-200°C, which can be used for the tuning of their rate. Some of the reference reactions specified in equations 4 and 5 represent the general synthesis strategy described in this paper.



Although the reaction products, as written, may be thought as regular iron oxide solids, we have found that different reaction conditions can help to limit the degree of the precursor condensation, which results in obtaining of the magnetic compounds in a form of nanoparticles with variable size. Earlier we reported the synthesis of a single-sized (4-5 nm) magnetite nanoparticles [3,4]. We also showed that larger particles (up to 17 nm) can be obtained by increasing the complexing strength of the reaction mixture by introducing N-donor ligand (N-methyl diethanolamine). In our recent development we aimed at a finer control over the particle size in the same reaction solvent, diethylene glycol, but by varying some other parameters for tuning the rate of the reaction. We employed the injection technique and varied the temperature, time and concentration of the reaction solutions. To produce larger particles, we used the technique of a sequential growth; this allowed us to extend the range of the particle size to 4-7.5 nm (Fig. 2). As we have found, magnetite appears to be the product regardless of whether or not iron(II) is used in the synthesis. It means that diethylene glycol acts as a reducing agent to iron(III) at high temperature. This reaction is reversible in a sense that magnetite diethylene glycol colloids, as well as aqueous colloids, can be oxidized by a molecular oxygen at room temperature to produce magnetic iron(III) oxide, which is commonly thought as maghemite. This oxidation is accompanied by the color change from brown-black to deep-orange (equation 6). Reheating of these colloids after vacuum de-oxygenation, causes the reversed reaction.

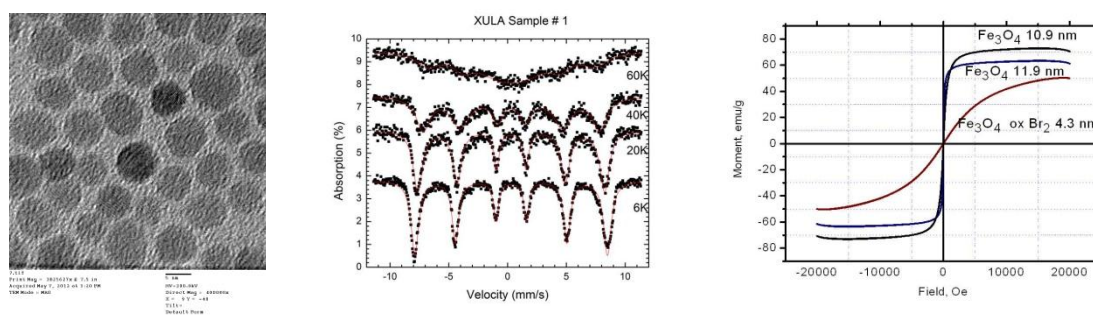
$$4\text{Fe}_3\text{O}_4(\text{H}_2\text{deg}) + \text{O}_2 \rightarrow 4\text{Fe}_3\text{O}_4(\text{Hdeg}) + 2\text{H}_2\text{O} \quad (6)$$


Fig. 2. TEM image, Mössbauer spectrum and room-temperature magnetization plots for Fe_3O_4 particles

3. Relaxivity studies

We measured spin-lattice (T_1) relaxation rates and determined the relaxivity r_1 values for our iron oxide particles that were different in size, oxidation state and surface composition, using NMR. The obtained values for D_2O solutions calculated per metal atom, along with the relaxivity value for gadolinium DTPA complex (magnevist) are presented in table 1. As it can be seen, larger particles demonstrate a greater relaxivity as compared to smaller magnetite particles, and the gadolinium reference compound.

Table 1. The r_1 relaxivity values of iron oxide nanoparticles and GdDTPA in D_2O .

Compound	Ligand	Particle size, nm	r_1 relaxivity, mM^{-1}
Magnetite(a) + O_2	Diethylene glycol	4.2	3.58
Magnetite(b) + O_2	Diethylene glycol	4.8	3.52

Magnetite(c) + O ₂	Diethylene glycol	7.5	10.8
Magnetite(d) + O ₂	Citrate	2.7	4.07
Gd complex (magnevist)	DTPA	n/a	4.81

Table 2. The r_1 relaxivity values of the ligand-free iron oxide nanoparticles in diethylene glycol.

Compound	Particle size, nm	r_1 relaxivity, mM ⁻¹ CH ₂ protons of deg	r_1 relaxivity, mM ⁻¹ OH protons of deg
Magnetite(a)	4.2	0.59	1.65
Magnetite(a) + O ₂	4.2	0.52	1.39
Magnetite(b)	4.8	1.04	2.72
Magnetite(b) + O ₂	4.8	1.22	2.84
Magnetite(c)	7.5	2.24	4.74
Magnetite(c) + O ₂	7.5	2.16	5.97

As it follows from Table 2, iron oxidation state in the iron oxide samples causes only small effect on the relaxivity values. Higher relaxivity value for the 7.5 nm magnetite(c) nanoparticles correlates with its larger magnetic moment (73 emu/g), as compared to 40-50 emu/g measured for other samples.

3. Conclusions

Systematic study have shown that magnetite nanoparticles can be obtained in high yield regardless of Fe^{II} being used in the synthesis or not, along with Fe^{III}. Magnetite diethylene glycol colloids can be reversibly oxidized by molecular oxygen at room temperature into magnetic iron(III) oxide; in other words reheating of these colloids after the vacuum de-oxygenation, causes the reversed reaction.

The average sizes for the magnetite nanoparticles obtained from diethylene glycol solutions can be adjusted to 4-7.5 nm by tuning the reaction temperature, solution concentration and by employing the technique of a sequential growth.

The larger particles were found to have a higher magnetic susceptibility and higher T1 relaxivity towards the protons of water or diethylene glycol. Oxidation state of the iron in the nanoparticles causes minimal effect on their relaxivity properties. This is beneficial for biomedical application, since oxidized particles are less reactive and consequently less toxic.

4. Acknowledgments

The current work is funded by the NSF EPSCoR LA-SiGMA project under award #EPS-1003897, the NIH SCORE grant under award # SC3GM088042, the NIH-RCMI grant under award # 1G12RR026260-01, and by the NSF PREM project under award # DMR-0934111.

5. References

- [1] C. Yang, J. Wu and Y. Hou, *Chem. Commun.*, 2011, 47, 5130.
- [2] J.-P. Jolivet, S. Cassaignon, C. Chanéac, D. Chiche, E. Tronc, *J Sol-Gel Sci Technol*, 2008, 46, 299.
- [3] G. Goloverda, B. Jackson, C. Kidd and V. Kolesnichenko, *JMMM*, 2009, 321, 1372.
- [4] D. Caruntu, G. Caruntu, Y. Chen, C. O'Connor, G. Goloverda, V. Kolesnichenko, *Chem. Mater*, 2004, 5527

Thermal Collapse of N-Isopropyl Acrylamide in Aqueous Solution

Lixin Liu¹ and Henry S. Ashbaugh¹

¹Department of Chemical and Biomolecular Engineering, Tulane University

Abstract: Polymers which undergo a collapse transition at a lower critical solution temperature are potential components to engineered smart-polymers for diverse applications including drug-delivery. The underlying mechanism for this counter-intuitive collapse transition, however, is poorly understood. We report here the results of an extensive replica exchange molecular dynamics simulation of poly-isopropylacrylamide in aqueous solution. Our simulation observes a collapse transition for the polymer with increasing temperature that gets sharper with increasing polymer molecular weight. Our thermodynamic analysis demonstrates thermodynamic signatures indicative of hydrophobic interactions inducing the collapse. An analysis of the correlations between hydrophobic isopropyl side chains confirms the view that the collapse is driven by hydrophobic interactions.

Keywords: N-Isopropyl Acrylamide, Water, Hydrophobic Collapse, Molecular Simulation, Replica Exchange

1. Introduction

The focus of smart polymer engineering mainly relies on achieving the polymer controllable response to the external stimuli such as pH, temperature, irradiation. Lower critical solution temperature (LCST) polymers are thermal responsive polymers that undergo a collapse transition with increasing temperature. Because LCST polymers have been exploited in many areas like drug delivery systems, tissue engineering, and epicardial restraint therapies, significance in understanding, describing and predicting the attractive stimuli-response properties of LCST polymers to engineer the conformational trigger should be shed a light on. PNIPAM (poly-isopropylacrylamide) is one of the most extensively studied LCST polymers with a negative thermal response and has drawn great attention as a drug-delivery polymer. PNIPAM exists as a coil structure at room temperature, but undergoes a dramatic phase transition to a collapsed state above LCST ($\sim 305\text{K}$)¹. Substantial experimental work using tools like FT-IR spectroscopy² and differential scanning calorimeter³ has been done to examine PNIPAM's counter-intuitive coil-to-globule transition and underlying thermodynamic mechanisms. This transition is generally considered to be the competitive results of the hydrophobic interaction of pendent isopropyl group as well as hydrogen bonding association between amide groups with water. However, specific mechanisms leading PNIPAM's collapse are still under debate. One of the promising paths to obtain adequate molecular details is employing Molecular Dynamics (MD) simulations. Previous MD simulation studies^{4, 5} had demonstrated that structure change of PNIPAM from stretched chain to a collapsed one is able to be observed by using OPLS+SPC/E force fields. Nevertheless, molecular level mechanism involved in this structure transition and its thermodynamic explanation is still poorly understood. We report a more in-depth investigation to probe the nature of PNIPAM's counter-intuitive collapse behavior by employing replica exchange simulation⁶ to

ultimately determine the global polymer conformation and multiple data analysis approaches to evaluate solvent intermediated interaction between constituent hydrophobic groups.

2. Simulation Methodology

A series of Replica Exchange MD (REMD) simulations related with PNIPAM homopolymer were conducted under isothermal-isobaric ensemble using GROMACS 4.0.7⁷. Various solutes included propane, Polyacrylamides and PNIPAMs were solvated in water box consisting varying number (1000 to 3113) water molecules. SPC/E⁸ water model and OPLS-AA⁹ force field had been adopted to describe solvent and solute respectively. The Parrinello-Raham barostat was used to maintain pressure at 1 bar and Nose-hoover thermostat was used to maintain temperature for each replicas. A 1fs time step was used to integrate equation of motion. Particle mesh Ewald method was used to calculate long-range electrostatic interaction and L-J interaction was evaluated out of 1.4nm. LINCS algorithm was used to constrain the geometry of water and fix carbon bond length. Temperatures of 15 replicas were assigned using an exponential distribution over a range from 280K to 357K. The replica exchange interval was set 0.25ps (250 steps). Before REMD simulation, each replica was equilibrated for 5ns. An implemented REMD program in GROMACS package was used to perform 50ns REMD simulation for various

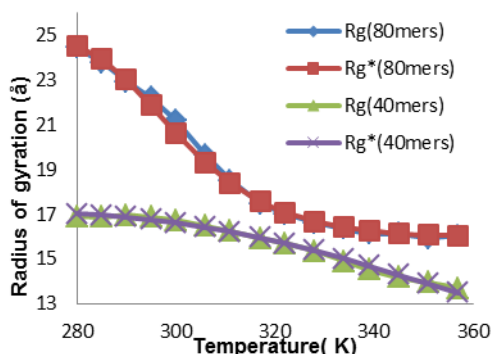


Figure 1. R_g of PNIPAMs with various lengths as function of temperature. R_g^* is the fitted value according the two-state model's prediction.

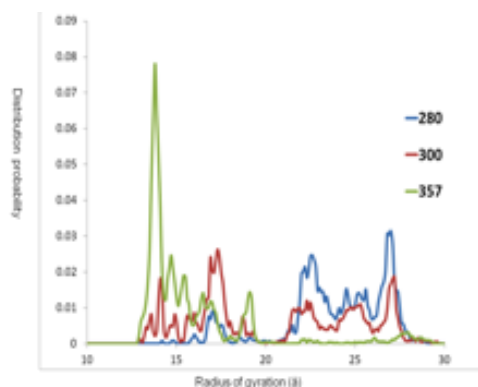


Figure 2. Probability distribution of radius of gyration for 80mers PNIPAM under 280K,300K and 357K.

solutes.

3. Results and Discussions

Using simulation technique mentioned above, radius of gyration (R_g) was calculated from simulation results to characterize the structure of PNIPAMs. Figure 1 presents 80 mers and 40 mers PNIPAM's results which are concluded as the average R_g for each replica. R_g of 80mers PNIPAM display a gradual collapse transition, which had reached a good agreement with previous experimental observation. For 40mers PNIPAM, though the tendency of first-order phase transition is not as obvious as longer chain temperature induced collapse still undergoes. The probability distribution of R_g (Fig 2) was also analyzed in terms of various selected temperatures

and indicated that PNIPAM exhibited a two-state behavior during our simulation which means its conformation preferred to be either at extended state or collapse state but unlikely existed in a transitional state. A two-state model, which usually described protein folding, was adopted to extract thermodynamic driving forces for chain collapse. In the derivation of model, the equilibrium constant of transition between globule and coil state K_{eq} is defined as ratio of P_C , the probability of coil state, and P_G , the probability of globule state, and the free energy involved in the transition process can be calculated based on following equation: $\Delta G = -RT \ln K_{eq}$. In order to describe the relationship between free energy and temperature, we can introduce a thermodynamic empirical equation to fit results derived from simulation by using least square fitting method,

$$\Delta G = a + b(T - T_0) + cT \ln(T/T_0) \quad (1)$$

As results showing in Figure 3, values obtained from equation fitted well with simulation data with T_0 set as 300K. Increasing temperature lead free energy change from negative to positive which means a conversion between extended states to collapse state. By using fitted data, A predicted R_g value (R_g^* in Figure 1) which reflected transition straightforwardly can also be obtained through reversely derivation of two-state model under the assumption that R_g^2 is in a linear relation with P_C .

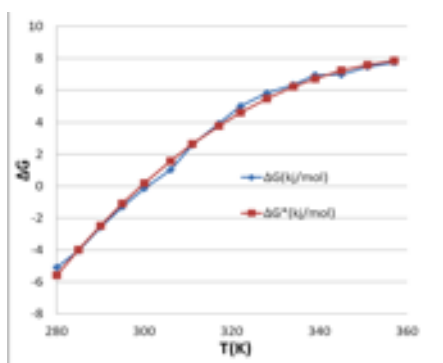


Figure 3. Free energy (80mers PNIPAM) as function of temperature, blue line is summarized from the simulation data while the red line is from thermodynamic empirical equation fitting.

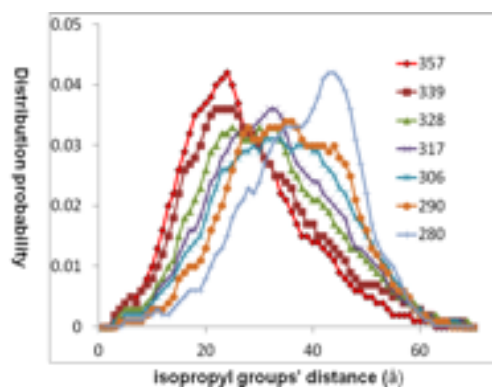


Figure 4. Probability distribution of isopropyl groups' distance within 40 monomers length under various temperatures' conditions.

One of the known factors promoting free energy is entropy increase due to increasing temperature resulting in a reduction of the total number of water molecule structured around the hydrophobic solutes. Therefore the hydrophobic interaction arisen by isopropyl pending groups of PNIPAM take an important role in understanding theoretical background of its collapse which inspire our multiple comparative simulations and their related analysis. First analysis we conducted is to study the isopropyl groups' distance within various length of monomers. In Figure 4, statistical results of the distance's distribution of isopropyl group within a 40mers' length manifested the hydrophobic groups became approach within closer distance with temperature increasing, which can also be interpreted as a phenomenon of stronger interaction. To evaluate collapse behavior's dependence of hydrophobic groups, REMD simulation was performed for polyacrylamide, which is the similar polymer as PNIPAM but substituting the isopropyl group with hydrogen, reducing the hydrophobicity. Analysis of average R_g of 40mers and 80mers polymers indicated there was no occurrence of obvious thermal-responsive collapse as

PNIPAM's. To take a quantitative evaluation of hydrophobic groups' response with temperature, another REMD simulation of pure propane solvating with water as long as its analysis of radial distribution function to compare with PNIPAM's results was undertaken. As shown in Figure 5, even though the scale of $g(r)$ of PNIPAM's alpha carbon on isopropyl group is higher than alpha carbon of propane due to larger amount of PNIPAM's isopropyl group and stronger restriction of their spatial coordination, the quantitative ratios of first $g(r)$'s peaking value at 357K and one at 280K are 1.6 for both two simulations. Results elucidated that PNIPAM's isopropyl group behave more interacted with each other in a similar way as known propane aggregation phenomenon due to temperature strengthening hydrophobic interaction.

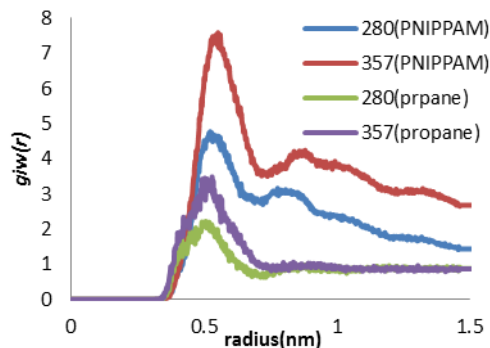


Figure 5. Radius distribution function for alpha-carbons of isopropyl group of PNIPAM (red & blue) and propane (purple & green) respectively at highest and lowest temperature.

4. Conclusion

Our simulation work for PNIPAM polymers has reproduced the thermal induced collapse transition over a broad range of temperature. A two-state model was applied to fit our simulation data and extract the thermodynamic driving forces for PNIPAM's collapse behavior. Analysis of distance distribution of isopropyl groups exhibited that the hydrophobic isopropyl groups' thermal-responsive interaction grew stronger as temperature increase. On the other hand R_g results from REMD simulation of polyacrylamide doesn't show obvious collapse behavior as PNIPAM's simulation. Further comparative analysis of radial distribution function for propane groups' carbon atoms displayed consistent thermal responsive change in magnitude between propane solution and PNIPAM. In all, we suggest hydrophobic group of PNIPAM make the main contribution for PNIPAM's thermal-responsive collapse behavior.

5. Acknowledgments

The current work is funded by the NSF EPSCoR LA-SiGMA project under award #EPS-1003897.

6. References

- [1] Wu, C.; Wang, X. H., *Phys. Rev. Lett.* **1998**, *80* (18), 4092-4094.
- [2] Sun, S. T.; Hu, J.; Tang, H.; Wu, P. Y., *J. Phys. Chem. B* **2010**, *114* (30), 9761-9770.
- [3] Otake, K.; Inomata, H.; Konno, M.; Saito, S., *Macromolecules* **1990**, *23* (1), 283-289.
- [4] Walter, J.; Ermatchkov, V.; Vrabec, J.; Hasse, H., *Fluid Phase Eq.* **2010**, *296* (2), 164-172.
- [5] Algaer, E. A.; van der Vegt, N. F. A., *J. Phys. Chem. B* **2011**, *115* (46), 13781-13787.
- [6] Earl, D. J.; Deem, M. W., *Phys. Chem. Chem. Phys.* **2005**, *7* (23), 3910-3916.
- [7] Hess, B.; Kutzner, C.; van der Spoel, D.; Lindahl, E., *J. Chem. Theory Comp.* **2008**, *4* (3), 435-447.
- [8] Berendsen, H. J. C.; Grigera, J. R.; Straatsma, T. P., *J. Phys. Chem.* **1987**, *91* (24), 6269-6271.
- [9] Jorgensen, W. L.; Maxwell, D. S.; TiradoRives, J., *J. Am. Chem. Soc.* **1996**, *118* (45), 11225-11236.

Toward Improved Meta-Generalized Gradient Approximations: Variations on a Density Functional Theme

Adrienn Ruzsinszky¹ and John P. Perdew¹

¹Department of Physics and Engineering Physics, Tulane University

Abstract: We have improved the revised or revTPSS meta-GGA (MGGA) for the exchange-correlation energy, which provides excellent atomization energies and lattice constants. For other properties, however, even revTPSS does not give the desired accuracy. Examples are the energy differences between different geometries for the same molecular formula, and the related non-barrier-height chemical reaction energies. These failures are related to the order-of-limits anomaly or to the uncontrolled interpolation between the one-electron and large-gradient limits. The same problems might lead to inaccurate energy differences between different crystal structures, and to inaccurate cohesive energies of insulating solids. (1) Here we show a possible way to remove the order-of-limits anomaly. The new regularized or regTPSS gives atomization energies comparable to revTPSS and preserves its accurate lattice constants as well. For other properties, regTPSS gives at least the same performance as the revTPSS meta-GGA. (2) The formation of the intershell region between the outermost core and the valence regions of an atom within a solid is associated with an increase of the variable α and a decrease of the gradient. This observation leads to a simple MGGA exchange functional, which interpolates in a controlled way between the single-orbital regime, where $\alpha=0$, and the slowly-varying density regime, where $\alpha = 1$, and then extrapolates to $\alpha \rightarrow \infty$. This resulting MGGA performs equally well for atoms, molecules, surfaces, and solids, and respects a tight Lieb-Oxford bound.

Keywords: density functional, meta-generalized gradient approximation

1. Introduction

The ascent of the ladder of nonempirical density functionals generally results in better performance, although for several properties of bulk solids the second rung, the PBE GGA, can be less accurate than the simpler local spin density approximation (LSDA). Predicting lattice constants more accurately than LSDA remained a challenge for a long time, even for state-of-the-art meta-GGA's. The nonempirical TPSS meta-GGA only achieves a moderate improvement upon PBE GGA. Recently, we have used the PBEsol idea to develop a revised TPSS or revTPSS meta-GGA [1] for atoms, molecules, solids, and surfaces. The basic idea of the PBEsol density functionals is to restore the second-order gradient expansion for exchange over a wide range of slowly or moderately varying densities. The revTPSS meta-GGA preserves all the correct constraints of TPSS, keeps its good surface and atomization energies, but yields lattice constants as good as those of the GGA's designed for solids. The revTPSS was designed to be a "workhorse density functional" for atoms, molecules, and solids.

Meta-GGA's are computationally not much more expensive than GGA's. It is expected that LSD and GGA users in condensed matter physics and quantum chemistry will switch to the meta-GGA, which can accurately describe both solids and molecules, at little extra cost. All nonempirical meta-GGA functionals discussed here can be written in the form:

$$E_{xc}[n_{\uparrow}, n_{\downarrow}] = \int d^3r n_{xc}(n_{\uparrow}, n_{\downarrow}, \nabla n_{\uparrow}, \nabla n_{\downarrow}, \tau_{\uparrow}, \tau_{\downarrow}), \quad (1)$$

where $n = n_{\uparrow} + n_{\downarrow}$ and τ_{σ} is the Kohn-Sham kinetic energy density of σ -spin electrons defined by

$$\tau_{\sigma}(r) = \frac{1}{2} \sum_i |\nabla \varphi_{i\sigma}(r)|^2. \quad (2)$$

The $\varphi_{i\sigma}$ are the occupied Kohn-Sham orbitals. The meta-GGA exchange energy keeps $\varepsilon_x^{unif}(n) = -3(3\pi^2 n)^{1/3} / 4\pi$, the exchange energy per electron for the uniform electron gas of density n , and adds inhomogeneity parameters beyond the uniform electron gas by the enhancement factor F_x :

$$E_x^{mGGA}[n] = \int d^3r n \varepsilon_x^{unif}(n) F_x^{mGGA}(p, z). \quad (3)$$

Here $p = s^2 = |\nabla n|^2 / [4(3\pi^2)^{2/3} n^{8/3}]$ is the square of the dimensionless density gradient s , and $z = \tau_w / \tau$ is an inhomogeneity parameter that arises beyond GGA. Regions of one- or two-electron density may be recognized by the condition $\tau = \tau_w$, where $\tau_w = |\nabla n|^2 / 8n$ is the Weizsäcker kinetic energy density. The parameter z falls in the range $0 \leq z \leq 1$. $z = 1$ for one- and two-electron densities while $z = 5p/3 + O(\nabla^4) \rightarrow 0$ for slowly-varying densities, for which the kinetic energy density has a second-order gradient expansion.¹ With these two limits of $z = 0$ or $z = 1$, the revTPSS satisfies two paradigms, the slowly-varying limit relevant to condensed matter physics, and the iso-orbital (one- or two-electron) limit relevant to quantum chemistry. In our recent meta-GGA development [1], F_x is reduced for $z = 0$, and is kept at the TPSS limit at large s or for $z = 0$. With these constraints we preserve the good lattice constants and surface properties and accurate atomization energies and enthalpies of formation at the same time.

2. Improvement beyond revTPSS

In TPSS and revTPSS, F_x is constructed using both $\alpha = (5p/3)[1/z - 1]$ and z . But in this equation z has an unintended and unphysical order-of-limits anomaly:

$$\lim_{p \rightarrow 0} \lim_{\alpha \rightarrow 0} z = 1, \quad \lim_{\alpha \rightarrow 0} \lim_{p \rightarrow 0} z = 0. \quad (4)$$

The different approach to zero in both α and p could lead to different limits of z , and therefore different F_x values ($\lim_{p \rightarrow 0} F_x(p, \alpha = 0) = 1.1470$ and $\lim_{\alpha \rightarrow 0} F_x(p = 0, \alpha) = 1.0143$). There is a similar problem in TPSS and revTPSS correlation. This problem was noticed in early molecular tests of TPSS, where it seemed to be harmless. But it may not be harmless in systems where important single-bond regions have both small α and small p (around the bond critical points). Single bonds are common in covalent molecules and in insulating solids, where each atom may have a large number of nearest neighbors with which it can form bonds. This is why the order-of-limits anomaly is particularly relevant for these solids and covalent molecules. The order-of limits anomaly does not arise when α is zero but p is large, i.e, in an atom or in lone molecular orbitals filled by one or two electrons.

The order-of-limits problem can be the source of several failures in describing material properties. The revTPSS did not perform as well as expected for the energy differences between different geometries for the same molecular formula, and for the related non-barrier-height chemical reaction energies. This problem seems similar to the problem of the energy differences between different crystal structures, and the problem of the cohesive energies of the insulating solids. We found [2] that the order-of limits problem can be removed by a weighted difference of the revTPSS F_x at $\alpha=0$ and ordinary α values:

$$F_{xregTPSS}(s, \alpha) = F_{xrevTPSS}(s, \alpha) + f(\alpha) \exp(-cs^2) [F_{xrevTPSS}(s, \alpha = 0) - F_{xrevTPSS}(s, \alpha)] \quad (5)$$

where $f(\square) = (1 - \alpha)^3 / (1 + (d\alpha)^2)^{1.5}$ and $c = 3$, $d = 1.475$. The factor $f(\square)$ is designed to preserve the exact fourth-order gradient expansion of the revTPSS. In this new F_x , the natural ingredient is α instead of z . The values of the c and d parameters were set by two criteria: the order-of-limits anomaly does not arise for $s > 1$, so we set the value of $f(\alpha) \exp(-cs^2) = 0.001$ for $s = 1$. The second criterion was chosen to obtain a flat $F_{xregTPSS}$ surface for $s < 1$ and $\square > 1$ values.

For $\alpha = 0$ we recover F_x of revTPSS for the iso-orbital region. For $\alpha \approx 1$ the form of F_x becomes the F_x of revTPSS. The form above regularizes the revTPSS exchange close to those regions where both α and the gradient are small. The single bond in H_2 , which has $\alpha = 0$, will then not be affected by the change from revTPSS to regTPSS, but other single bonds, including bonds to H, should be strengthened. The regTPSS also provides a way to control the interpolation between the one-electron and large-gradient limits.

In separate work [3], we have proposed a simple exchange enhancement factor, which puts α and p (square of the gradient) on an equal footing, and a new paradigm density, the ground state fully spin-polarized six-electron hydrogenic density ($1s2s2p^33s$) (FP6EH), to guide the functional from $\alpha = 0$ to $\alpha \approx 1$. The enhancement factor reads now:

$$F_x^{int}(p, \alpha) = F_x^1(p) + f(\alpha) [F_x^0(p) - F_x^1(p)] \quad (6)$$

where $F_x^1(p) = F_x^{int}(p, \alpha = 1) = 1 + \kappa - \kappa / (1 + \mu^{GE} p / \kappa)$ and $F_x^0(p, \alpha) = F_x^{int}(p, \alpha = 0) = 1 + \kappa - \kappa / (1 + (\mu^{GE} p + c) / \kappa)$. Eq. (6) interpolates between $F_x^0(p)$ and $F_x^1(p)$ through the factor $f(\alpha) = (1 - \alpha^2)^3 / (1 + \alpha^2 + \alpha^3)$ which (along with $c = 0.28771$ and $\kappa = 0.29$) is chosen to guarantee for the

functional the second- order gradient expansion (represented by μ^{GE}) for a wide range of densities, good jellium surface exchange energies, and the exchange energy of the new paradigm density. The small $\kappa \ll 0.804$ corresponds to a tightened Lieb-Oxford bound.

3. Conclusion

The meta-GGA form contains rich possibilities for further improvement. We have explored two here: (1) removal of the nonphysical order-of-limits problem, and (2) alternative interpolations between the iso-orbital ($\alpha=0$) and slowly-varying ($\alpha=1$) limits.

4. Acknowledgments

The current work is funded by the NSF EPSCoR LA-SiGMA project under award #EPS-1003897, and by NSF under Grant No. DMR-0854769.

5. References

- [1] J.P. Perdew, A. Ruzsinszky, G.I. Csonka, L.A. Constantin, and J. Sun., Phys. Rev. Lett. **103**, 026403 (2009).
 - [2] A. Ruzsinszky, J. Sun, B. Xiao, and G.I. Csonka, J. Chem. Theory Comput. **8**, 2078, (2012).
 - [3] J. Sun, B. Xiao, and A. Ruzsinszky, submitted.
-

LA-SIGMA Poster Session			
Number	Name	University Affiliation	Title of Poster
1	Lucy Kiruri	Louisiana State University	A DFT Study of the Reaction of Chlorinated Phenols with Copper Oxide Clusters
2	Lawrence Pratt	Tulane University	Ab Initio Molecular Dynamics Simulation of a Propylene Carbonate-filled Uncharged Nanotube Forest
3	Cheri McFerrin	Louisiana State University	Ab Initio Study of Iron Oxide Clusters and their Reactions with Phenol, 2-Chlorophenol and 4-Chlorophenol and Force Field Development for Copper Oxide Systems
4	Alex Burin	Tulane University	Advanced Quantum Chemistry Approach to the Ground State Spin of Iron Oxide Clusters
5	Wei Zhang	Tulane University	Charge Transfer from a Carbon Nanotube Electrode to Tetramethyl Ammonium Ions Investigated by Ab Initio Molecular Dynamics Simulation
6	Paige Nelson	Xavier University of Louisiana	Colloid and Surface Chemistry of Magnetic Iron Oxide Nanoparticles
7	Fernando Soto	Louisiana Tech University	DFT Study of Complex Metal Hydrides for On-Board Hydrogen Storage
8	Chinedu Ekuma	Louisiana State University	Dynamical Cluster Approximation – Typical Medium Theory Approach to Disordered System
9	Zi Yang Meng	Louisiana State University	Dynamical Embedding of the Dual Fermion Dynamical Cluster Approach for Strongly Correlated system
10	John DiTusa	Louisiana State University	Electrical Transport in a Magnetic Semiconductor Nanowire
11	Neelima Ranjitkar	Louisiana Tech University	Electronic and Conductive Properties of Polythiophene containing Cobaltabisdicarbollide Structures
12	John Perdew, Adrienn Ruzsinszky & Jianman Tao	Tulane University	Everything You Always Wanted to Know about the van der Waals Interaction (But Were Afraid to Ask)
13	Jin Hu	Tulane University	Ferromagnetism in CuFeSb: Evidence of Competing Magnetic Interactions in Fe-based Superconductors
14	Supada Laosooksathit	Louisiana Tech University	GPGPU Performance Modeling
15	Conrad Moore	Louisiana State University	GPU Accelerated Hirsch-Fye Quantum Monte Carlo
16	Kasra Fattah-Hesary	Louisiana State University	Hybrid MD-continuum Simulation Methodology with Capability of Handling Two-Phase Flows with Application in Biomolecular Systems
17	Ling Cui & Erica Murray	Louisiana Tech University	Impedance Characterization of YSZ based NOx Sensor
18	Zhiqiang Mao	Tulane University	Interplay Between Magnetism and Superconductivity in Iron Chalcogenides
19	Ayorinde Hassan	Louisiana Tech University	Investigations of RuO2 and SnO2 Nanoclusters as Potential Lithium Ion Battery Electrode Materials
20	Sanjay Kodiyalam	Southern University at Baton Rouge	Molecular Dynamics Simulation and Visualization of Thermal Barrier Coatings
21	Kai Xia	Louisiana State University	Molecular Dynamics Simulation Study of the Effect of Electric Field on DNA Mononucleotides Dynamics in Nanoslits
22	Brian Novak	Louisiana State University	Molecular Dynamics Simulations of the Interaction of a PLGA Nanoparticle with a Lipid Bilayer
23	Alexander Burin	Tulane University	Molecular Magnet Based on Iron Oxide Clusters
24	Divya Elumalai	Louisiana Tech University	Molecular Transport in Nanotubes
25	Michael Benissan	Southern University at Baton Rouge	Multi-scale Thermal Model for In-Service Performance of Thermal Barrier Coatings
26	Ye Fang	Louisiana State University	Multi-spin Coding Parallel Tempering Monte Carlo Simulation of Ising Spin Glass with CUDA
27	Vishwa Poddaturi	Louisiana Tech University	Nanoparticle Uptake by the Tumor Tissue through its Capillary Pores
28	Fei Han	Louisiana Tech University	Numerical Simulation of Hydrogen Absorption/Desorption in Metal-Hydride Reactors
29	Amin Azizi	Tulane University	Optimization of Electroless Deposition of CoNiFeB Thin Films for Application in Magnetic Recording Media
30	Scott Grayson	Tulane University	Preparation and Characterization of Amphiphilic, Biocompatible Cyclic Block Copolymers
31	Diola Bagayoko	Southern University at Baton Rouge	Self-consistent Calculations of Electronic Properties of Systems with Energy or Band Gaps
32	Lawrence Pratt	Tulane University	Simulation of Propylene Carbonate Solutions for Electrochemical Double-layer Capacitors
33	Lawrence Pratt & Hank Ashbaugh	Tulane University	Statistical Mechanics of a Hard Rod in the Hard Sphere Fluid
34	Brandon Borrill	Louisiana State University	Study of the Hydrogen Storage Capability of KMgH3
35	Ryky Nelson	Louisiana State University	Study of the Spin State of Localized Mn in (GaMn)As and (GaMn)N
36	Vladimir Kolesnichenko & Pavel Kucheryavy	Xavier University of Louisiana	Superparamagnetic Iron Oxide Nanoparticles with Variable Size and Iron Oxidation State: Synthesis and Relaxivity Studies
37	Cynthia Sisson	Louisiana State University at Shreveport	The Online Scientific Teaching Institute at LA-SIGMA
38	Lixin Liu	Tulane University	Thermal Collapse of N-Isopropyl Acrylamide in Aqueous Solution
39	Adrienn Ruzsinszky & John Perdew	Tulane University	Toward Improved Meta-Generalized Gradient Approximations: Variations on a Density Functional Theme

REU/RET Poster Session			
Number	Name	Affiliation	Title of Poster
1	Thaddeus Howard & Joseph McPherson	REU/Tulane University	Carbon Nanotube-based Supercapacitor
2	David Anderson	RET/Tulane University	Deep Zooms into the Mandelbrot Set using NVIDIA CUDA CProgramming
3	Adam Wang	REU/University of New Orleans	Dependency on eposition Conditions and Substrates on Epitaxial Growth of Single Crystal Iron
4	Nathan Keilbart	REU/Louisiana State University	EELS Study of Phenol on TiO2
5	David Howe	REU/Louisiana Tech University	Efficient Hydrogen Saturation and Transfer Rate Simulation in Metallic Rods
6	Juan Arrendondo	REU/Southern University at Baton Rouge	Electrical Properties of Fluoropolymer-Carbon Nanotubes
7	Victoria Bamburg	REU/Louisiana Tech University	Nucleosome Binding in Highly Occupied Sequences
8	Allyssa Massie	REU/Xavier University of Louisiana	Epoxyaconitic Acid as Prospective Capping Ligand for Magnetite Nanoparticles: Synthesis and Complexation with Magnetite
9	Andrea Rice	REU/University of New Orleans	Fabrication and Magnetic Characterization of Nickel Nanowires
10	Adam Wang	REU/University of New Orleans	Growth and Characterization of Single Crystal Films
11	Donald Pleshinger	REU/Louisiana State University	iBook on 3D+ Visualization
12	Aditya Das	REU/Louisiana Tech University	Investigations of RuO2 and SnO2 Nanoclusters as Potential Lithium Ion Battery Anode Coatings
13	Ellie Rodebeck	REU/Tulane University	Modeling Tau Protein Aggregation
14	Madeline Reed	REU/Louisiana State University	Molecular Dynamics Simulation of the Interaction Between Cholates and Cholesterol
15	Ronald Brown	REU/Louisiana Tech University	Geometric Analysis of DNA in Molecular Dynamics Simulations of Nucleosomes
16	Sheldon Williams	REU/University of New Orleans	Pig Liver Esterase Enantioselectivity
17	Chris Kieren	REU/Louisiana State University	Searching for Helimagnetic Ordering through the Synthesis of Ternary Non-Centrosymmetric Crystal Structures
18	Cole Vanderlick	REU/Southern University at Baton Rouge	Stereographic Visualization of Molecular Configurations in a CAVE
19	Regina Blackman	REU/Louisiana Tech University	Structural Analysis of Bosch Heated Exhaust Gas Oxygen Sensors After Voltage Treatments
20	Matthew Kornfield	REU/Southern University at Baton Rouge	Synthesis and Structural Characterization of Lanthanum Strontium Calcium Manganate
21	Kevin Willis	REU/Xavier University of Louisiana	Synthesis of Novel Iron-Oxide-Based Superparamagnetic Nanoparticles for MRI Contrasting Agent
22	Brad Burkman	RET/Louisiana State University	Teaching HPC in High Schools
23	Alys Reed	REU/Louisiana State University	The Preparation of Liposomes
24	Julia Russ	REU/Tulane University	Transport Properties of Hydrogenated VO2 Thin Films

2012 Symposium Attendees

Last name	First name	Affiliation
Aamodt	Stephanie	Louisiana State University Shreveport
AbuAsal	Sameer	Center for Computation and Technology - LSU
Adams	Stephanie	DAC
Anderson	David	RET - Tulane University
Arredondo	Juan	REU - Southern University - Baton Rouge
Ashbaugh	Hank	Tulane University
Azizi	Amin	Tulane University
Bagayoko	Diola	Southern University - Baton Rouge
Bamburg	Victoria	REU - Louisiana Tech University
Benissan	Michael	Southern University
Bishop	Tom	Louisiana Tech University
Blackman	Regina	REU - Louisiana Tech University
Borill	Brandon	Louisiana State University
Boudreaux	Alicia	Louisiana Tech University
Brown	Ronald	REU - Louisiana Tech University
Burin	Alexander	Tulane University
Burkman	Brad	RET - Louisiana State University
Butler	Les	Louisiana State University
Capenter	Jenna	DAC
Carman	Kevin	Louisiana State University
Chowriappa	Pradeep	Louisiana Tech University
Cruthirds	Rachel	Xavier University of Louisiana
Cui	Ling	Louisiana Tech University
D'Amour	Gene	Xavier University of Louisiana
Das	Aditya	REU - Louisiana Tech University
Deng	William	Columbia University
Derosa	Pedro	Grambling State University-Louisiana Tech University
Devireddy	Ram	Louisiana State University
Domingue	Jessica	Louisiana Board of Regents
Dunn	Cindi	Office of Educational Innovation and Evaluation -Kansas State University
Ekuma	Chinedu	Louisiana State University
Elkholy	Karim	Baton Rouge Community College (BRCC)
Elumalai	Divya	Louisiana Tech University
Fang	Ye	Louisiana State University
Fattah Hesary	Kasra	Louisiana State University
Gershey	James	Louisiana Board of Regents
Goloverda	Galina	Xavier University of Louisiana
Grayson	Scott	Tulane University
Guice	Les	Louisiana Tech University
Hall	Randall	Dominican University of California

2012 Symposium Attendees

Last name	First name	Affiliation
Han	Fei	Louisiana Tech University
Hassan	Ayorinde	Louisiana Tech University
Howard	Thaddeus	REU - Tulane University
Howe	David	REU - Louisiana Tech University
Hu	Jin	Tulane University
Hunt	Rayla	LA-SiGMA
Hynes	Chris	Louisiana School for Math, Science, and the Arts
Jana	Amitava	Southern University
Jarrell	Mark	Louisiana State University
Jernigan	Susan	Louisiana Board of Regents
Jones	DiOnetta	DAC
Keilbart	Nathan	REU - Louisiana State University
Khonsari	Michael	Louisiana Board of Regents
Kieren	Chris	REU - Louisiana State University
Kiruri	Lucy	Louisiana State University
Kodiyalam	Sanjay	Southern University
Kolesnichenko	Vladimir	Xavier University of Louisiana
Kornfield	Matthew	REU - Southern University - Baton Rouge
Kucheryavy	Pavel	Xavier University of Louisiana
Lange	Sheila	DAC
Laosooksathit	Supada	Louisiana Tech University
Lee	Shelley	Louisiana State University
Lester, Jr.	William A.	University of California, Berkeley
Li	Guoqiang	Southern University
Lin	Jieqiong	Louisiana State University
Liu	Lixin	Tulane University
Mainardi	Daniela	Louisiana Tech University
Mao	Zhiqiang	Tulane University
Massie	Allyssa	REU - Xavier University of Louisiana
McCall	Valon	Louisiana Tech University
McFerrin	Cheri	Louisiana State University
McKoy	Vincent	California Institute of Technology
McPherson	Joseph	REU - Tulane University
Meng	Zi Yang	Center for Computation and Technology - LSU
Mensah	Lydia	Xavier University of Louisiana
Merchant	Mark	McNeese State University
Montes	Carlos	Louisiana Tech University
Moore	Conrad	Louisiana State University
Moreno	Juana	Louisiana State University
Murray	Erica	Louisiana Tech Univeristy
Nelson	Paige	Xavier University of Louisiana
Nelson	Ryky	Louisiana State University

2012 Symposium Attendees

Last name	First name	Affiliation
Nikitopoulos	Dimitris	Louisiana State University
Nilov	Denis	Xavier University of Louisiana
Novak	Brian	Louisiana State University
Parameswaran	Sreeja	University of New Orleans
Paudyal	Anjana	Louisiana Tech University
Perdew	John P.	Tulane University
Pesika	Noshir	Tulane University
Pleshinger	Donald	REU - Louisiana State University
Podduturi	VishwaPriya	Louisiana Tech University
Poobal	Karthik	Louisiana Board of Regents
Pratt	Lawrence	Tulane University
Ramachandran	B. Ramu	Louisiana Tech University
Ramanujam	J. Ram	Louisiana State University
Ranjitkar	Neelima	Louisiana Tech University
Reed	Alys	REU - Louisiana State University
Reed	Madeline	REU - Louisiana State University
Rice	Andrea	REU - University of New Orleans
Robinson	Anne	Tulane University
Rodebeck	Ellie	REU - Tulane University
Russ	Julia	REU - Tulane University
Ruzsinszky	Adrienn	Tulane University
Schrader	Laura	Tulane University
Silverman	Harold	Retired
Sinnott	Susan	University of Florida
Sisson	Cynthia	Louisiana State University Shreveport
Soto	Fernando	Louisiana Tech University
Spinu	Leonard	University of New Orleans
Spruger	Phillip	Louisiana State University
Steen-Sighinolfi	Melanie	Xavier University of Louisiana
Tao	Jianmin	Tulane University
Tohline	Joel	Louisiana State University
Townsend	Leigh	Louisiana State University
Traxler	Kathryn	Center for Computation and Technology - LSU
Vanderlick	Cole	REU - Southern University - Baton Rouge
Wang	Adam	REU - University of New Orleans
Whittenburg	Scott	University of New Orleans
Williams	Sheldon	REU - University of New Orleans
Willis	Kevin	REU - Xavier University of Louisiana
Xia	Kai	Louisiana State University
Yun	Zhifeng	Louisiana State University
Zhang	Boyu	Tulane University
Zhang	Wei	Tulane University